

R78-1  
JANUARY 1978

N78-25321  
CR-151733

FINAL REPORT ON THE  
**ELECTROMECHANICAL  
FLIGHT CONTROL ACTUATOR**

VOLUME 1

CONTRACT NAS 9-14952

Submitted to  
NATIONAL AERONAUTICS and SPACE ADMINISTRATION  
L.B. Johnson Space Center  
Houston, Texas

 **Delco Electronics**

General Motors Corporation  
- Santa Barbara Operations  
Santa Barbara, California

R78-1  
JANUARY 1978

FINAL REPORT ON THE  
**ELECTROMECHANICAL  
FLIGHT CONTROL ACTUATOR**

VOLUME 1

CONTRACT NAS 9-14952

Submitted to  
NATIONAL AERONAUTICS and SPACE ADMINISTRATION  
L.B. Johnson Space Center  
Houston, Texas



**Delco Electronics**

*General Motors Corporation  
- Santa Barbara Operations  
Santa Barbara, California*



FOREWORD

This report is divided into three volumes. Volume 1 is the body of the report, Volume 2 contains Appendices A through I, and Volume 3 contains Appendices J through L.

## CONTENTS

<u>Section</u>		<u>Page</u>
I	INTRODUCTION	1-1
II	CONCLUSIONS AND RECOMMENDATIONS	2-1
	2.1 Conclusions	2-1
	2.2 Recommendations	2-3
III	SYSTEM FUNCTIONAL DESCRIPTION	3-1
	3.1 Four-Channel System Functional Description	3-1
	3.1.1 System Operation	3-3
	3.1.2 Current Source Power Converter	3-5
	3.2 Single-Channel Power Electronics Breadboard Functional Description	3-10
IV	EQUIPMENT DESCRIPTION	4-1
	4.1 Delco Breadboard System Description	4-1
	4.1.1 Power Source	4-1
	4.1.2 System Description	4-1
	4.2 NASA Four-Channel System Description	4-11
	4.2.1 Differential Gearbox	4-11
	4.2.2 Motor Assembly	4-20
	4.2.3 Control Electronics	4-27
	4.2.4 Cabling	4-34
	4.3 Single-Channel Power Electronics Breadboard Description	4-36
V	EQUIPMENT MECHANIZATION	5-1
	5.1 Four-Channel System Mechanization	5-1
	5.1.1 Current Command Rate Limiter	5-4
	5.1.2 Power Converter Control	5-6
	5.1.3 Low-Level Electronics	5-16
	5.1.4 Power Electronics	5-16

<u>Section</u>	<u>Page</u>
5.2 Single-Channel Power Electronics	
Breadboard Mechanization	5-17
5.2.1 High Power Motor Driver	5-17
5.2.2 Base Driver Power Supply	5-19
5.2.3 Base Driver Circuit	5-19
VI ANALYTICAL STUDIES	6-1
6.1 Introduction	6-1
6.2 Servo Analyses	6-1
6.2.1 Simplified Single-Channel Analyses	6-1
6.2.2 Detailed Single-Channel Linear Analysis	6-18
6.2.3 Two-Channel Linear Analysis	6-24
6.2.4 Single-Channel Nonlinear Analysis	6-42
6.3 Chopper Circuit Analysis	6-51
6.3.1 Motoring Mode	6-51
6.3.2 Regenerative Braking Mode	6-54
6.4 Commutation Analysis	6-57
VII TESTS AND TEST RESULTS	7-1
7.1 Motor Tests	7-1
7.2 Efficiency Tests	7-1
7.3 Electronics Tests	7-3
7.3.1 Low-Level Electronics Tests	7-3
7.3.2 Power Converter Tests	7-3
7.4 Design Verification Tests	7-3
7.4.1 Design Verification Test Plan	7-3
7.4.2 Design Verification Test Configuration	7-3
7.4.3 Design Verification Test Results	7-4
7.5 Comparison of Analytical and Test Results	7-7
7.6 Power Component Tests	7-7
7.7 Single-Channel Power Electronics Breadboard Tests	7-15
VIII FINAL STATUS	8-1

Appendices

A	System Schematics
B	Gear Design Data
C	NASA Statement of Work
D	Operations Manual
E	Motor Tests
F	Efficiency Tests
G	Low-Level Electronics Tests
H	Power Converter Waveform Tests
I	Design Verification Test Plan
J	Design Verification Test Results
K	Power Component Tests
L	Single-Channel Power Electronics Breadboard Tests

## SECTION I

### INTRODUCTION

A technology program has been conducted to investigate the feasibility of using electromechanical devices as primary flight control actuators for aerospace vehicles. This program was initiated after studies of electrohydraulic and electromechanical systems had indicated that a highly efficient battery-powered electromechanical actuation system had potentially significant advantages over the electrohydraulic actuation system. In addition to its potential weight reduction (extremely important in many aircraft, missile and spacecraft applications) the electromechanical actuator shows great promise in terms of reliability and maintainability. However, before such an approach could be seriously considered, hardware feasibility of electromechanical actuator concepts suitable for aerospace vehicle applications had to be demonstrated.

The purpose of the Electromechanical Flight Control Actuator Program is to develop an electromechanical actuator that will follow a proportional control command with minimum wasted energy, and demonstrate the feasibility of meeting space vehicle actuator requirements using advanced electromechanical concepts. The approach was restricted to a four-channel redundant configuration (Figure 1-1). Each channel has independent drive and control electronics, a brushless electric motor with brake, and velocity and position feedback transducers. A differential gearbox sums the output velocities of the motors. Normally, two motors are active and the other two are braked. A 270 Vdc battery powers the actuator.

The most unique feature of the electromechanical actuator (EMA) is its use of a brushless self-synchronous motor having a permanent magnet rotor. The stator of this machine is similar to that of a conventional three-phase synchronous or induction motor, and is simple in construction and windings. The rotor has permanent magnet poles made of samarium cobalt, which is an extremely effective magnetic material, resulting in a lightweight, low-inertia machine with very high efficiency. Brushes and commutator are eliminated in this motor through

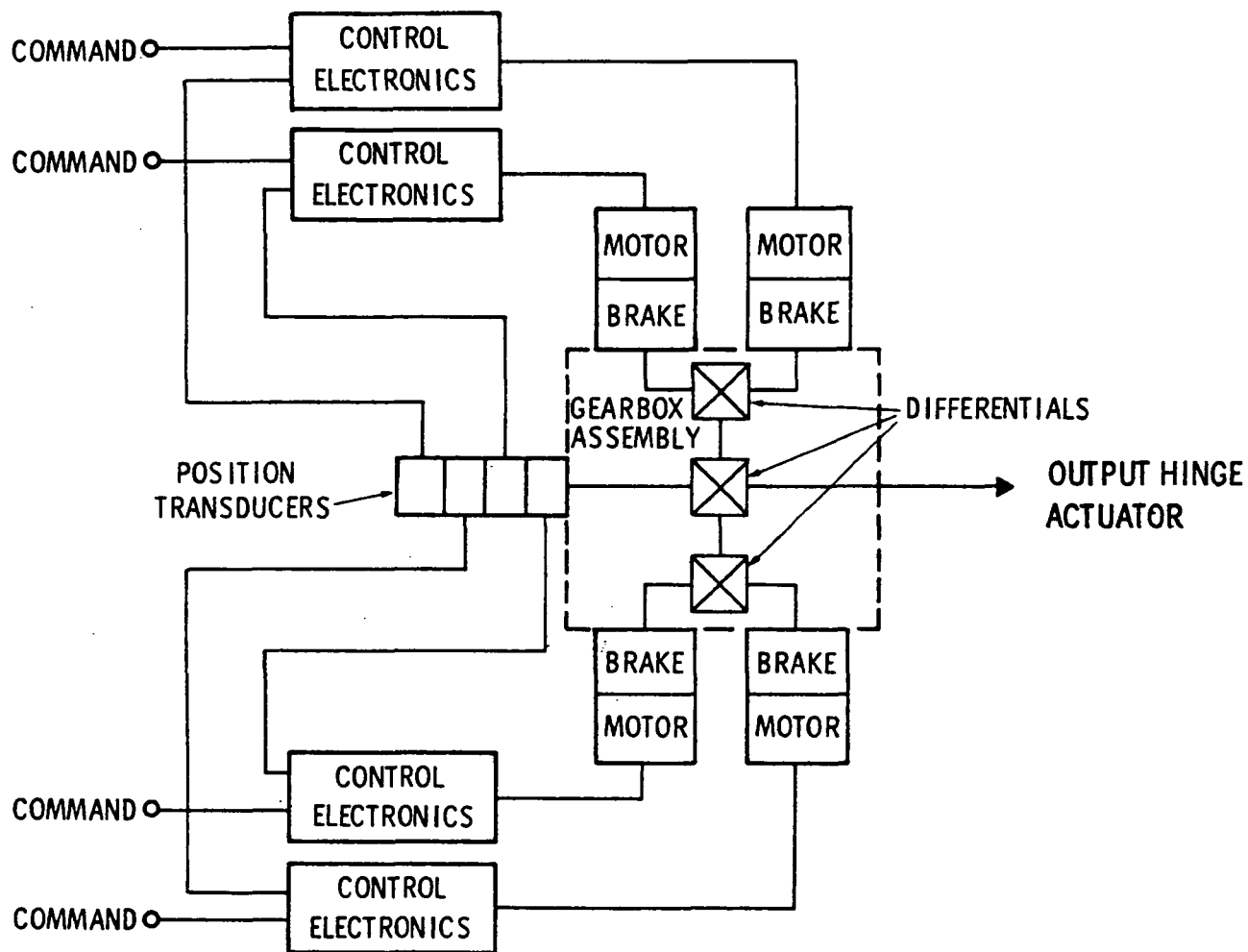


Figure 1-1. Electromechanical Actuator Block Diagram

the use of a rotor position sensor (RPS) and solid-state electronics. The stator windings are excited by three-phase waveforms to create a rotating magnetic field. As the rotor moves, the RPS sends signals to the control electronics to indicate which windings should receive excitation to produce the torque required by the load. Thus, the machine operates in a manner similar to a conventional dc motor, except that the conventional commutator and brushes are replaced by the RPS and control electronics.

The design goals for the system were established in the NASA Statement of Work for the program (Ref. Appendix C). The major tasks for this effort included:

- Design and fabrication of the four-channel actuator
- Design and installation of necessary test instrumentation
- Modification of the NASA-furnished actuator test stand
- Development of mathematical models of the actuator and its major subsystems
- The design, fabrication and testing of a state-of-the-art single-channel power electronics breadboard
- Planning and conducting design verification tests of the four-channel actuator
- Participation in formal program reviews
- Documentation of the program with plans, reports and an operations manual.

#### Acknowledgments

Although a number of individuals have made significant contributions to this program, the efforts of several key personnel merit special recognition. Messrs. F. Bourbeau and A. Barrett were instrumental in the electronics design, Mr. E. Sawyer was largely responsible for the motor design, Messrs. W. Gully and F. Pavlics contributed to the mechanical design, and Mr. J. Anselmi provided significant analytical support. Mr. J. T. Edge of NASA/JSC, the Technical Monitor for this program, contributed direction, enthusiasm and technical support.

## SECTION II

### CONCLUSIONS AND RECOMMENDATIONS

#### 2.1 CONCLUSIONS

The Electromechanical Flight Control Actuator Program has clearly demonstrated the feasibility of meeting stringent space vehicle flight control actuator performance requirements using advanced motor, gearbox and power electronics concepts.

A four-channel redundant electromechanical actuator (EMA) has been developed and tested which exceeded virtually all its design goals. The displacement linearity design goal is 1% of full travel, and the worst-case measured deviation was found to be 0.22%. The threshold design goal is 0.0275 degree, and all combinations of two active channels easily met this requirement. The position null design goal is 0.275 degree. This requirement was also easily met. The hysteresis design goal is 0.0275 degree. The worst-case measured hysteresis was less than one-third of the goal. Velocity tracking tests showed that all combinations of two active channels had steady-state speeds which were in agreement within 3% of the maximum motor speed (thus meeting the design goal for the system). The frequency response characteristics also exceeded the EMA design goals. The -4 dB bandwidth was typically 9.5 Hz compared with a design goal of 3.0 Hz.

The phase characteristics of the EMA also exceeded the design goals (for example, the  $-45^{\circ}$  phase shift frequency is 3.4 Hz compared to a design goal of 3.0 Hz). The step response characteristics were the only ones which did not exceed the EMA design goals. At small step amplitudes (less than 2% of full travel, or 1.1 degree) the step response met the design goals. At larger amplitudes (from 2% to 5% of full travel) the step response overshoot slightly exceeded the design goal of 25% (the worst-case overshoot was 30%). For a 5% step command, the EMA exceeded the time allowed to reach 85% of full travel (0.160 second compared to a design goal of 0.145 second). For step commands of 4% or less, the response reached 85% of the steady-state motion in less time than the design goal of 0.145 second.



To aid the understanding and evaluation of the test results, analytical models of the EMA were developed. The models were also used to finalize and optimize the system design. The analytical models which were developed include:

- Simplified single-channel servo models
- Detailed single-channel servo models
- Detailed dual-channel servo models
- Detailed dual-channel servo models
- Nonlinear servo models
  - Simplified
  - Detailed.

The simplified models take into account the dominant parameters of the system and are very useful in gaining an understanding of the basic system characteristics. The detailed analyses take into account all of the major system parameters including load characteristics. In general, the complexity of the detailed models is such that it was most expedient to develop computer programs for use with these models.

In addition to the servo models, analyses were made of several EMA subsystems. The transient conditions which occur during motor current commutation were analyzed, and an analysis was made of the current source (chopper) which supplies the motor current. These analyses are important in understanding the electrical stresses which occur in the power electronics.

The agreement between the analytical models and the actual hardware test results has been found to be very good, thus providing a high degree of confidence that system performance characteristics predicted from the models actually can be achieved.

The four-channel EMA power electronics used Integrated Hybrid Transistor Switches (IHTS), developed by Texas Instruments for the U. S. Army. These devices are rated at 60 A, and are the limiting element in establishing the output power capability of the actuator. With operating margins which assure safe transistor conditions, the four-channel power electronics is capable of

developing two-thirds of the motor's rated output power. Since the development of the IHTS, power transistor technology has advanced considerably. As one of the tasks in this program, a single-channel power electronics breadboard was developed (using state-of-the-art power transistors) which has been tested to demonstrate full rated motor power (17 hp). This single-channel power electronics breadboard has been extensively tested and clearly demonstrates the feasibility of driving the EMA motor at full power with very safe transistor design margins.

## 2.2 RECOMMENDATIONS

Several efforts can be recommended on the basis of the results which have been achieved in this program:

- Make technical improvements to the EMA subsystems
- Design, build and test a prototype EMA suitable for flight testing.

Improvements have been made in the magnetic properties of samarium cobalt since the EMA was designed. An improved EMA motor should be developed utilizing these newer materials to achieve improved performance characteristics and higher power density. The rotor position sensor should be replaced by one having greater resolution, and more sophisticated commutation angle control should be incorporated in the EMA design to provide improved performance and efficiency. The power electronics should be improved by making use of the latest power transistors. This would provide greater output power, while retaining adequate design margins in the power electronics design.

The feasibility of the EMA has been demonstrated during this program. The next recommended major effort is the design, fabrication and testing of a prototype unit suitable for flight testing. This effort would establish the size, weight and environmental characteristics of a state-of-the-art electro-mechanical actuator concept, and would also demonstrate the performance capabilities which can be achieved. After laboratory tests have been made (including flight simulation tests), actual flight tests should be conducted. These tests should be made on an aircraft having sufficient space available for monitoring and recording the behavior of the actuator under the full range of flight conditions typical of high-performance aircraft.

## SECTION III

## SYSTEM FUNCTIONAL DESCRIPTION

3.1 FOUR-CHANNEL SYSTEM FUNCTIONAL DESCRIPTION

The electromechanical actuator (Figure 3-1) is composed of four independent servo-controlled channels. Each channel consists of control and drive electronics, a brushless electric motor with brake, and velocity and position feedback transducers. The four electric motors are driven into a differential gearbox which has a common double-ended output which is coupled to the NASA-supplied rotary actuators (planetary gear reducers). The output velocity of the gearbox is proportional to the sum of the velocities of the motors. In the normal mode of operation, two of the four motors are driving and the other two are braked. Each motor has independent control and drive electronics, providing servo control and power control for motoring and electrical braking modes of operation. The electromechanical actuator (EMA) is powered from a battery which has a nominal terminal voltage of 270 V.

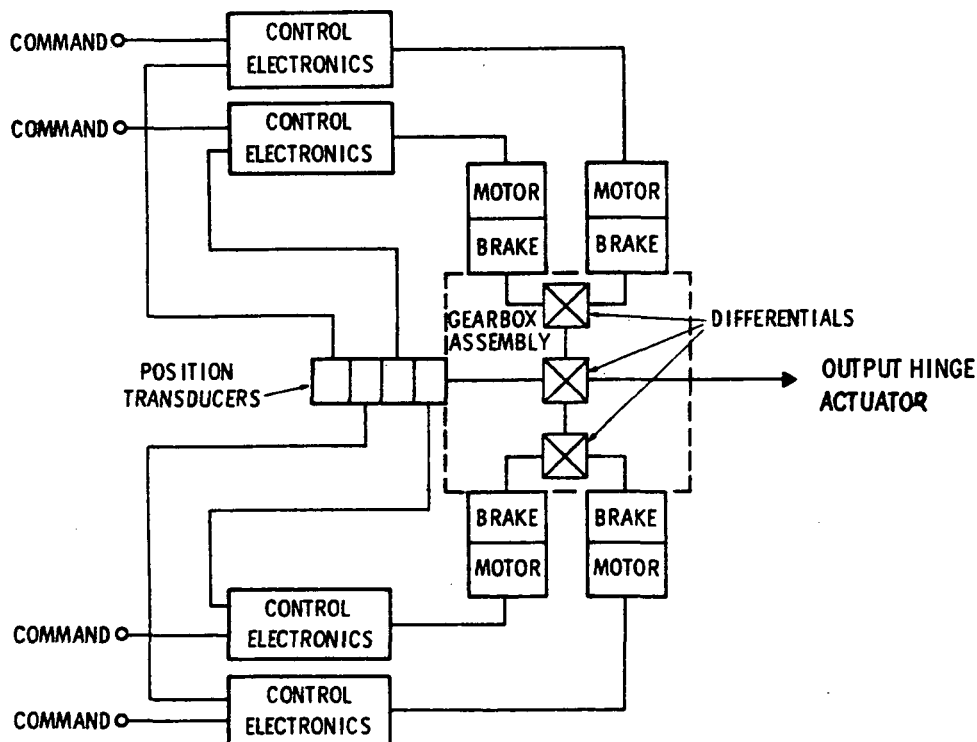


Figure 3-1. Electromechanical Actuator Block Diagram

The most unique feature of the EMA is its use of a brushless synchronous motor having a permanent magnet rotor. The stator of this machine is similar to that of a conventional three-phase synchronous or induction motor, and is simple in construction and windings. The rotor has permanent magnet poles made of samarium cobalt, which is an extremely effective magnetic material, resulting in a lightweight, low-inertia machine with very high efficiency. The ceramic-like magnets are bonded to a solid steel shaft. A fiberglass band is wrapped around the rotor to aid in resisting centrifugal forces, and provides a smooth, cylindrical rotor surface to minimize windage losses. Brushes and commutator are eliminated in this machine through the use of the rotor position sensor (RPS) and solid-state electronics. The stator windings of the motor are excited by three-phase waveforms to create a rotating magnetic field. As the rotor moves, the RPS sends signals to the control electronics to indicate which windings should receive excitation to produce the torque required by the load. Thus, the machine operates in a manner similar to a conventional dc motor, except that the conventional commutator and brushes are replaced by the RPS and control electronics. The resulting machine is capable of operating at much higher speeds than one having rotor windings and a commutator. Because the permanent magnet rotor has virtually no losses, the thermal problems associated with cooling the machine are greatly simplified. Virtually all losses in the machine occur in the stator; therefore, cooling is easily accomplished by allowing air to flow through the stator slots which are only partially filled by the machine's windings.

The power control electronics for the machine are relatively simple. For servo control purposes it is very convenient to provide a controlled torque mode of operation. This is easily accomplished in the permanent magnet motor because its output torque is proportional to the current in the stator windings. For a given rotor position, two of the stator windings receive excitation. Idealized motor phase currents are shown in Figure 3-2. For example, at electrical angles between 0 and  $60^{\circ}$ , the motor current flows into winding A and out through winding B. During the next interval, from  $60$  to  $120^{\circ}$ , the current continues to flow into winding A, but out through winding C. The current is thus commutated at intervals of 60 electrical degrees to provide three-phase

current waveforms. The magnitude of the current is controlled to produce the desired torque, and the rotor position sensor and control electronics switch the controlled current through the appropriate pair of windings.

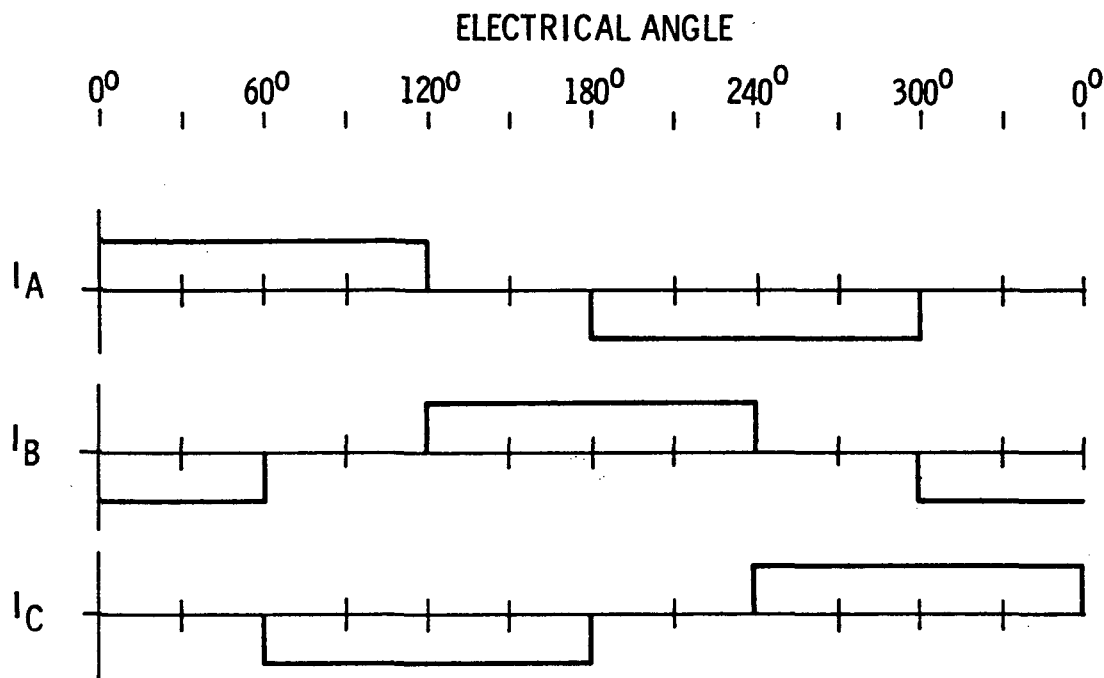


Figure 3-2. Idealized Motor Phase Currents

### 3.1.1 SYSTEM OPERATION

Figure 3-3 is a simplified system block diagram of a single channel of the actuator. For convenience, all torque, inertia, and motion variables are referenced to the load. Linearized load effects (viscous damping, load spring and steady-state hinge moments) are represented, and the velocity and position feedback paths are shown.

The position command and position feedback signals are compared to form a position error signal. This signal is amplified and combined with the velocity feedback signal to develop a current command signal. The current source

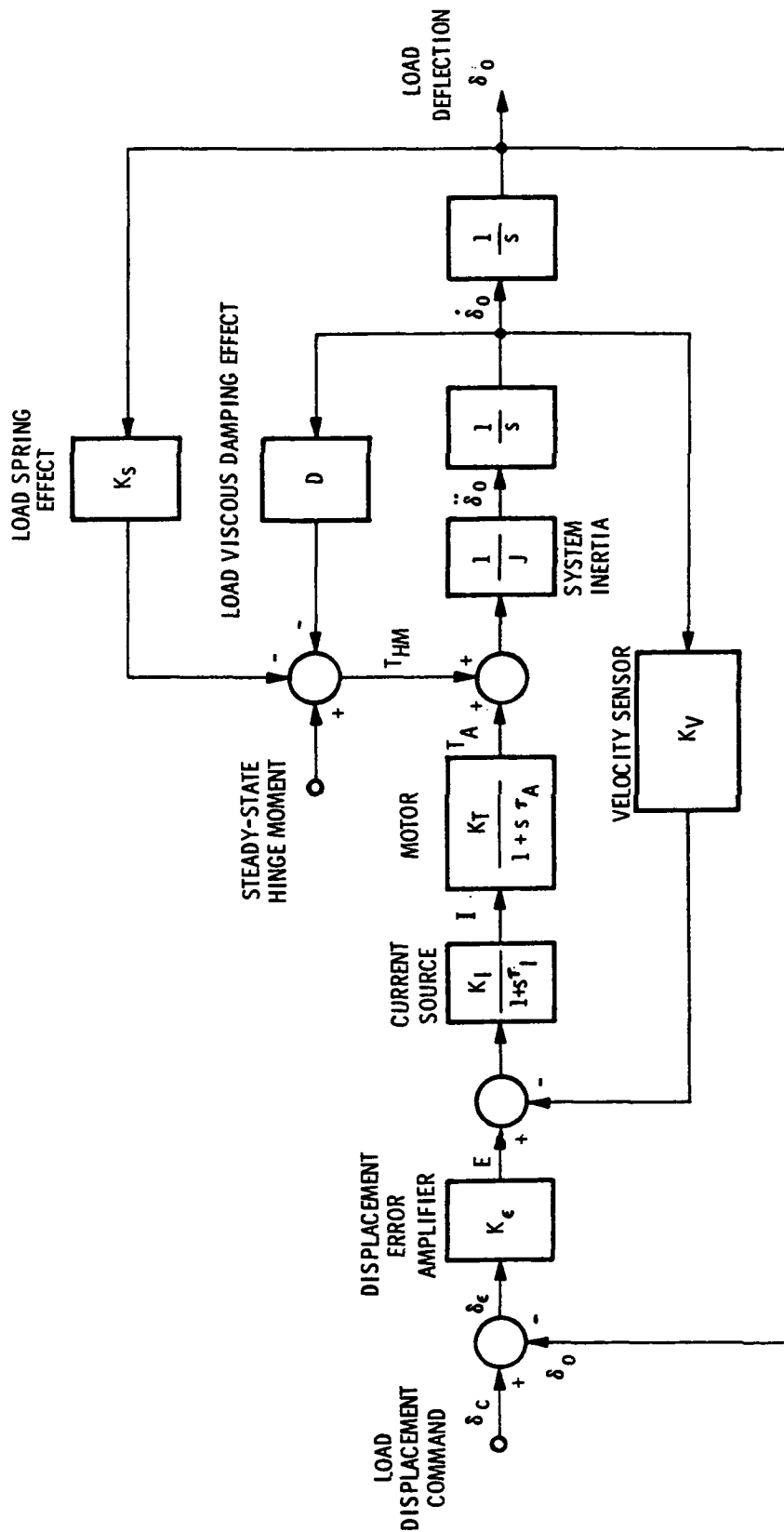


Figure 3-3. Single Channel Simplified Functional Diagram

develops a motor current in response to the current command signal. The motor current produces a torque which accelerates the reflected inertia of the system and overcomes the reflected hinge moment of the load.

In normal operation, two channels of the actuator are active (Figure 3-4). Each motor is controlled in essentially the manner described in the preceding paragraphs, but a velocity correction loop is also included. The tachometer outputs of the two active channels are compared to form a velocity error signal. If the two motors are not rotating at the same angular velocity, the error signal causes the slower motor to speed up, and the faster motor to slow down. In this manner, under idealized operation, each motor would operate at the same speed, produce the same torque, and thus share the load equally with the other motor.

The servo aspects of the actuator design are given in Paragraph 6.3.

### 3.1.2 CURRENT SOURCE POWER CONVERTER

The brushless, self-synchronous motor is driven by a current source power converter. The current source power converter is achieved with an inductor-coupled pulse width modulator (chopper) and inverter (Figure 3-5). The chopper establishes a dc current level with an acceptable ripple component in the coupling inductor in response to a torque error signal. The inductor current is processed by the inverter to form a six-step motor current waveform (Figure 3-6).

The current source power converter is implemented with the Integrated Hybrid Transistor Switch (IHTS)\* as a basic building block. This unit contains two power transistors and antiparallel power diodes, together with over-temperature, over-current, and control logic interface circuits.

---

\* The IHTS is described in:

1. Texas Instruments Bulletin No. DL-S 7311988, April 1973.
2. D. Balthasar, E. Reimers, "The Integrated Hybrid Transistor Switch," IEEE Conf. Rec. of the 1972 IAS Meeting, 72CHO-8-1A, pp. 495-503.

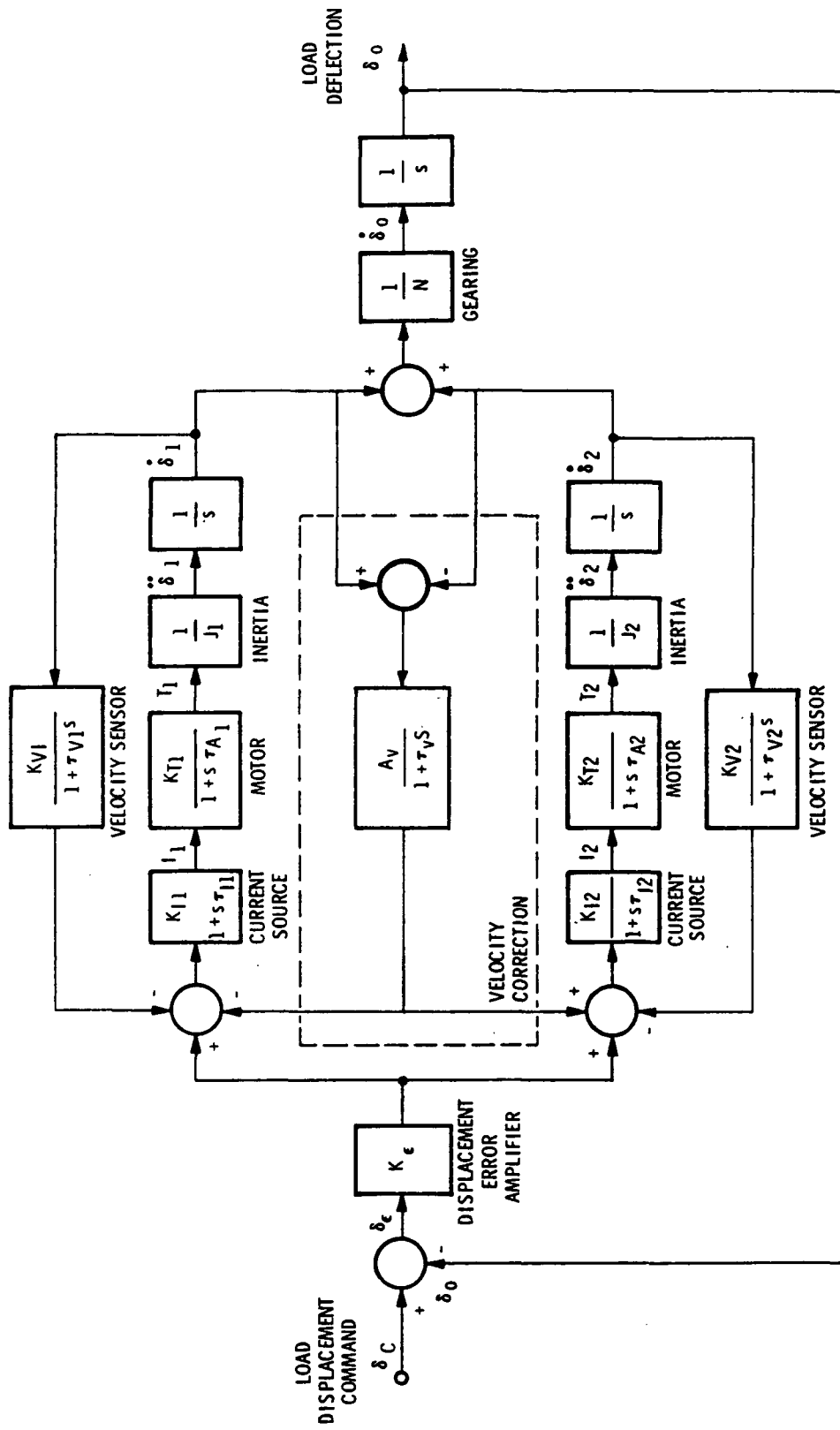


Figure 3-4. Two-Channel Operation Simplified Functional Diagram



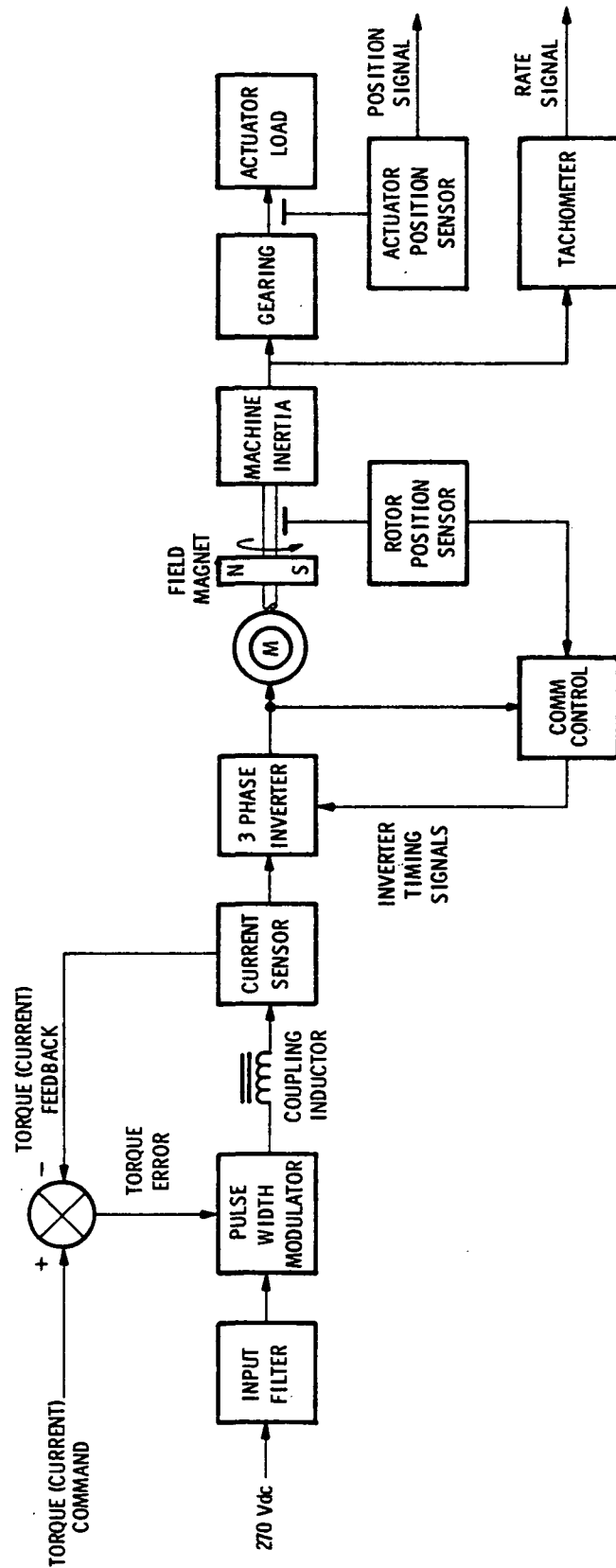


Figure 3-5. Controller Block Diagram

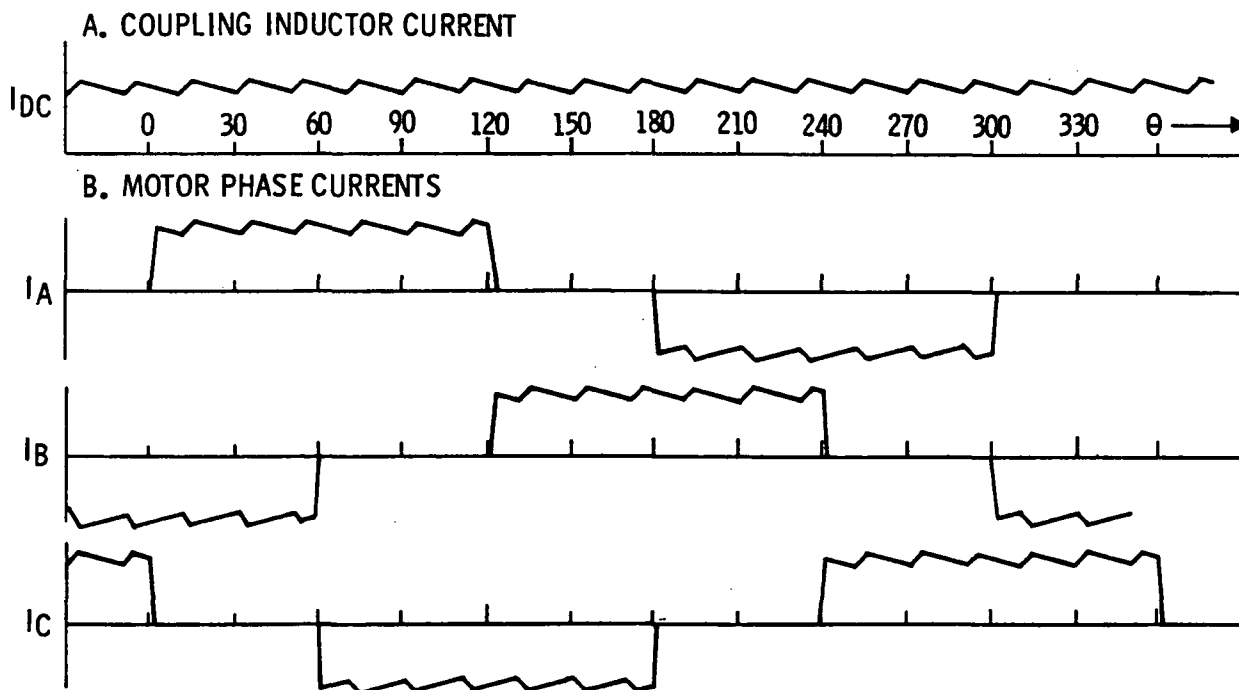


Figure 3-6. Typical Power Converter Waveforms

### 3.1.2.1 Torque Control, Motoring Mode

Figure 3-7 is a simplified schematic diagram of the power converter.  $Q_1$  through  $Q_6$  are connected to form a three-phase inverter. The inverter controls the currents in the motor stator windings. Idealized motor phase current waveforms are shown in Figure 3-2. Switch  $Q_M$  controls the current through the inverter during motoring operation, and  $Q_B$  controls the inverter current during regenerative braking.

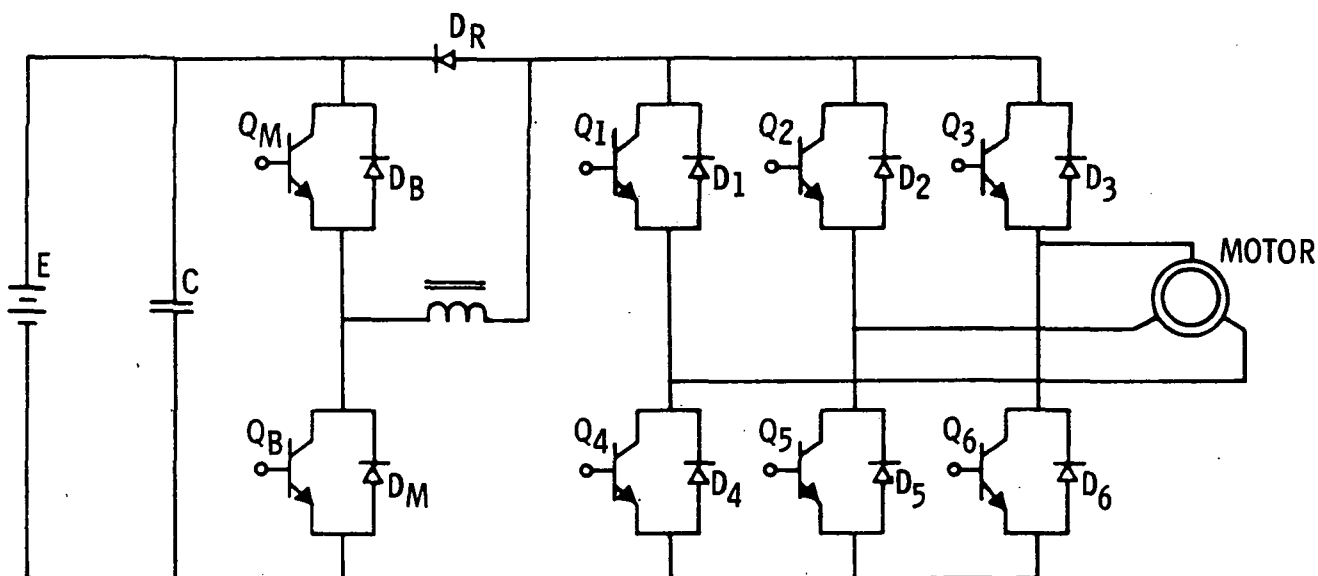


Figure 3-7. Power Electronics Schematic

During motoring operation, if the current in the current source inductor is less than the commanded value,  $Q_M$  is turned on; this applies full battery voltage to the input terminal of inductor L. Therefore, current increases in the inductor as indicated in Figure 3-6. Hysteresis in the control circuit allows the current to build up to a preestablished level which is slightly greater than the commanded current. At this point,  $Q_M$  is turned off. The

current which is flowing through the inductor at the switching time then flows through diode  $D_M$ . The current then decreases to a value slightly below the commanded current, at which point  $Q_M$  is again turned on, thus restarting the cycle. Figure 3-6 shows the coupling inductor current waveform, as well as the motor phase currents.

The current in the inductor is routed through the proper motor windings by the inverter transistors  $Q_1$  through  $Q_6$ . These transistors are turned on and off by signals which are derived from the RPS.

### 3.1.2.2 Torque Control, Regenerative Mode

When the load is capable of returning energy to the battery, the power converter operates in a regenerative mode. In this mode, the inverter transistors ( $Q_1$  thru  $Q_6$  in Figure 3-7) are all turned off. Their antiparallel diodes,  $D_1$  through  $D_6$ , then act as a three-phase full-wave rectifier load on the motor (which is acting as a permanent-magnet generator). Current through the coupling inductor is controlled by transistor  $Q_B$  and the braking diode,  $D_B$ . If the current in the coupling inductor is less than the commanded current,  $Q_B$  is turned on. Again, hysteresis designed into the control circuitry allows the current to build up in the inductor to a level slightly greater than the commanded value. At this point,  $Q_B$  is turned off, and the current which is flowing in the inductor now flows through diode  $D_B$  back into the battery. When the current decreases to a value somewhat lower than the commanded value,  $Q_B$  is again turned on, thus restarting the current control cycle.

## 3.2 SINGLE-CHANNEL POWER ELECTRONICS BREADBOARD FUNCTIONAL DESCRIPTION

The single-channel power electronics breadboard performs essentially the same function as the power converter described in Paragraph 3.1.2, but is designed to provide substantially greater currents (and therefore much larger power output levels). A simplified schematic diagram of the motor driver is given in Figure 3-8. During motoring, the current is controlled by transistors  $QM1$  and  $QM2$ , diode  $DRM$  and the motoring inductor,  $LM$ .  $QM1$  and  $QM2$  operate alternately, controlling the current in  $LM$  (and thus the motor current). The

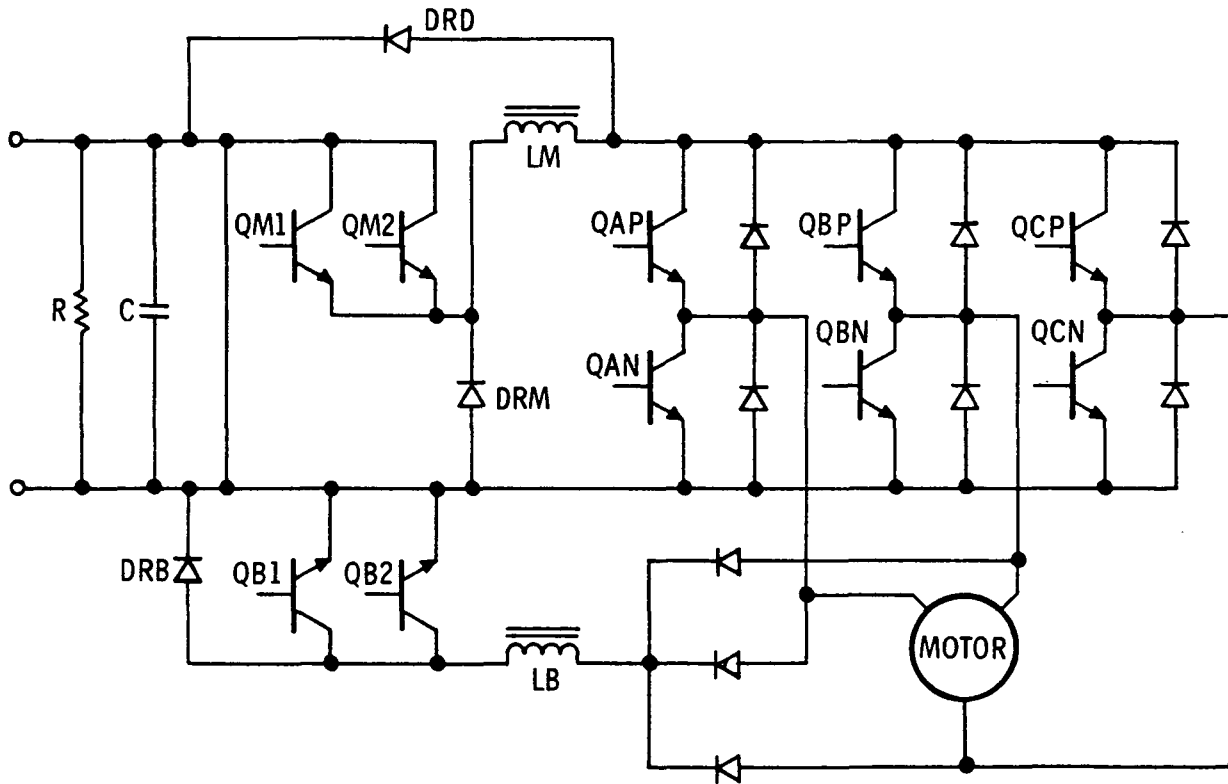


Figure 3-8. High Power Single-Channel Motor Driver

inverter is formed by transistors  $QAP$ ,  $QAN$ ,  $QBP$ ,  $QBN$ ,  $QCP$ ,  $QCN$ , and their associated antiparallel diodes.

During regenerative braking, the inverter transistors are all turned off, and the current is controlled by transistors  $QB1$  and  $QB2$ , diode  $DRB$  and inductor  $LB$ . The high-power, single-channel power electronics breadboard switches are discrete devices (rather than the Integrated Hybrid Transistor Switches discussed in Paragraph 3.1.2). A more detailed description of the High Power Motor Driver and its related driver and power supply circuits is presented in Paragraph 5.2.

## SECTION IV

### EQUIPMENT DESCRIPTION

#### 4.1 DELCO BREADBOARD SYSTEM DESCRIPTION

The Delco breadboard system was used during the company-funded design development phase. The following paragraphs describe the breadboard system and indicate how it was used to develop the EMA.

##### 4.1.1 POWER SOURCE

As indicated in Section III, the high-voltage power for the electromechanical actuator (EMA) is obtained from a battery (270 V nominal). For development purposes, Delco utilized a battery bank consisting of 24 heavy duty batteries (Figure 4-1). Quick-disconnect cables were used to allow the battery voltage to be tapped at selected levels. The battery is connected through cables and protective switchgear to the Electromechanical Actuator Development Laboratory which is located approximately 150 feet from the battery bank. The batteries power both the Delco breadboard and the NASA four-channel actuator system.

Figure 4-2 shows the battery charger which was used with the system. A simple Variac control was used to adjust the charger output voltage and control the battery charging rates.

##### 4.1.2 SYSTEM DESCRIPTION

The Delco breadboard system consists of a single channel of electronics, a motor, a gear train, and position and velocity feedback transducers. The assembly which was used in developing the basic circuitry for the EMA is shown in Figure 4-3. The electronics rack includes a variety of instrumentation used to monitor motor currents and various system voltages. Torque transducer and r/min instrumentation is also mounted in the rack along with an electronic wattmeter. The electromechanical assembly (Figure 4-4) is mounted on the laboratory bench and consists of a baseplate on which are fastened the synchronous motor, dynamometer, gear train and associated electromechanical assemblies.

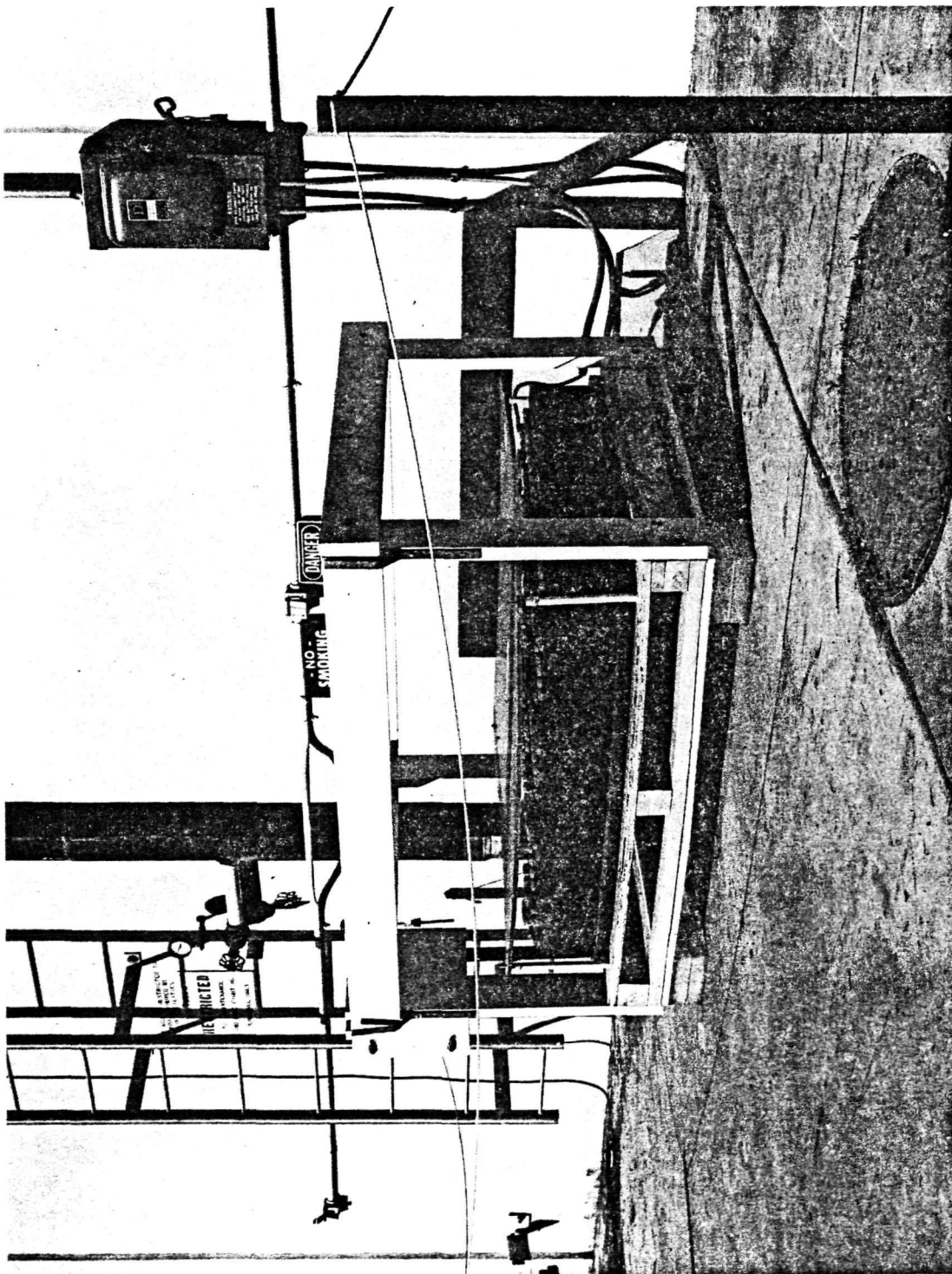


Figure 4-1. Battery Bank

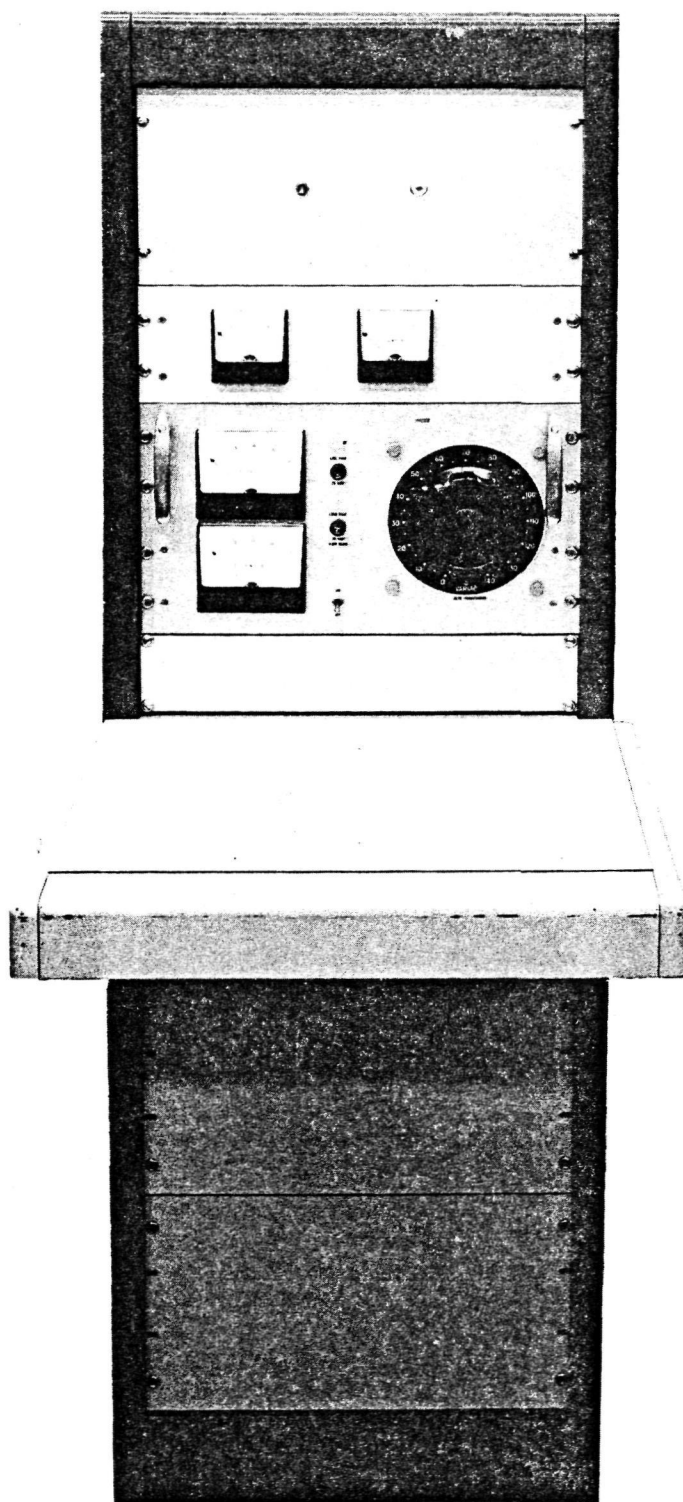


Figure 4-2. Battery Charger



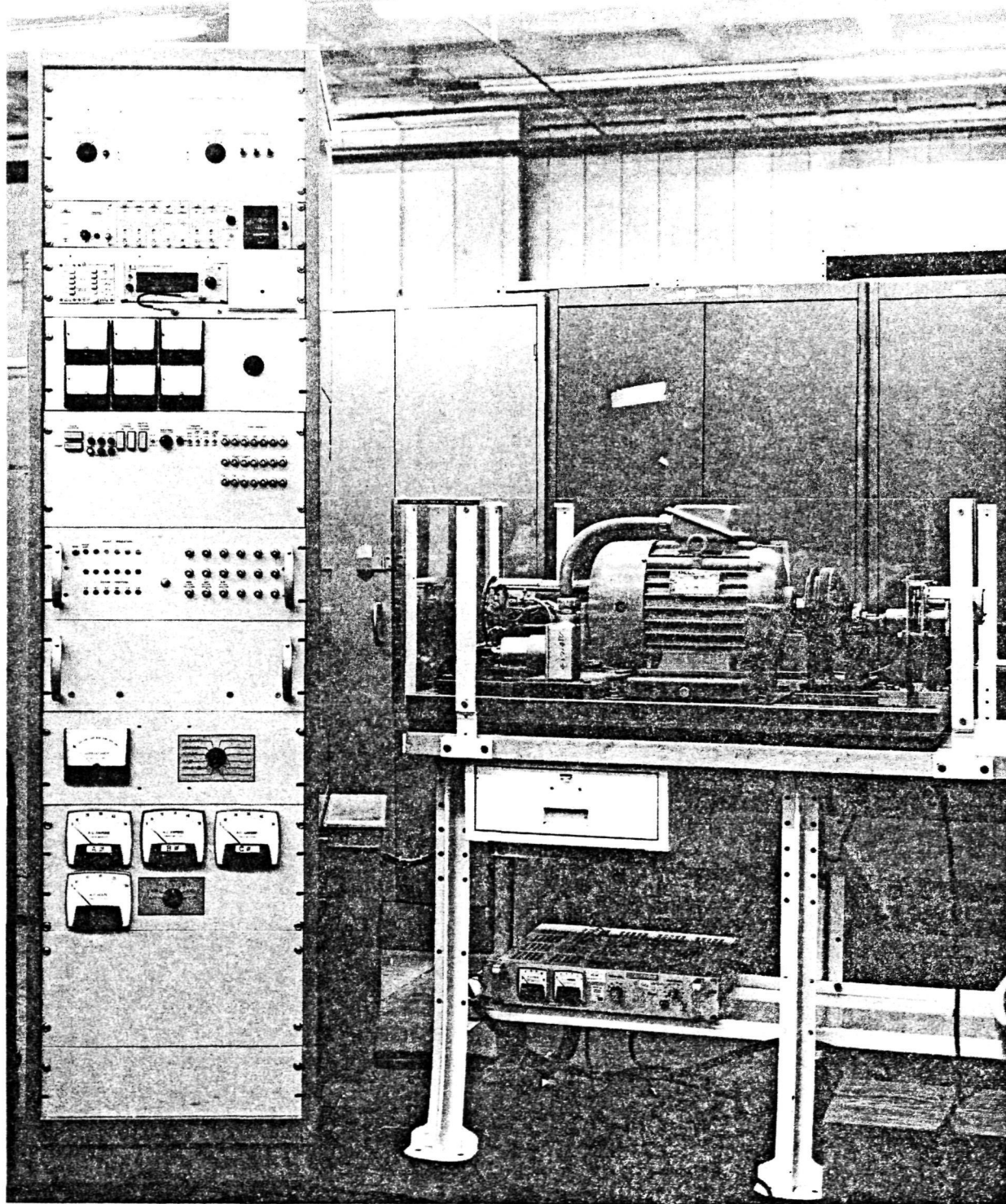


Figure 4-3. Delco Breadboard System

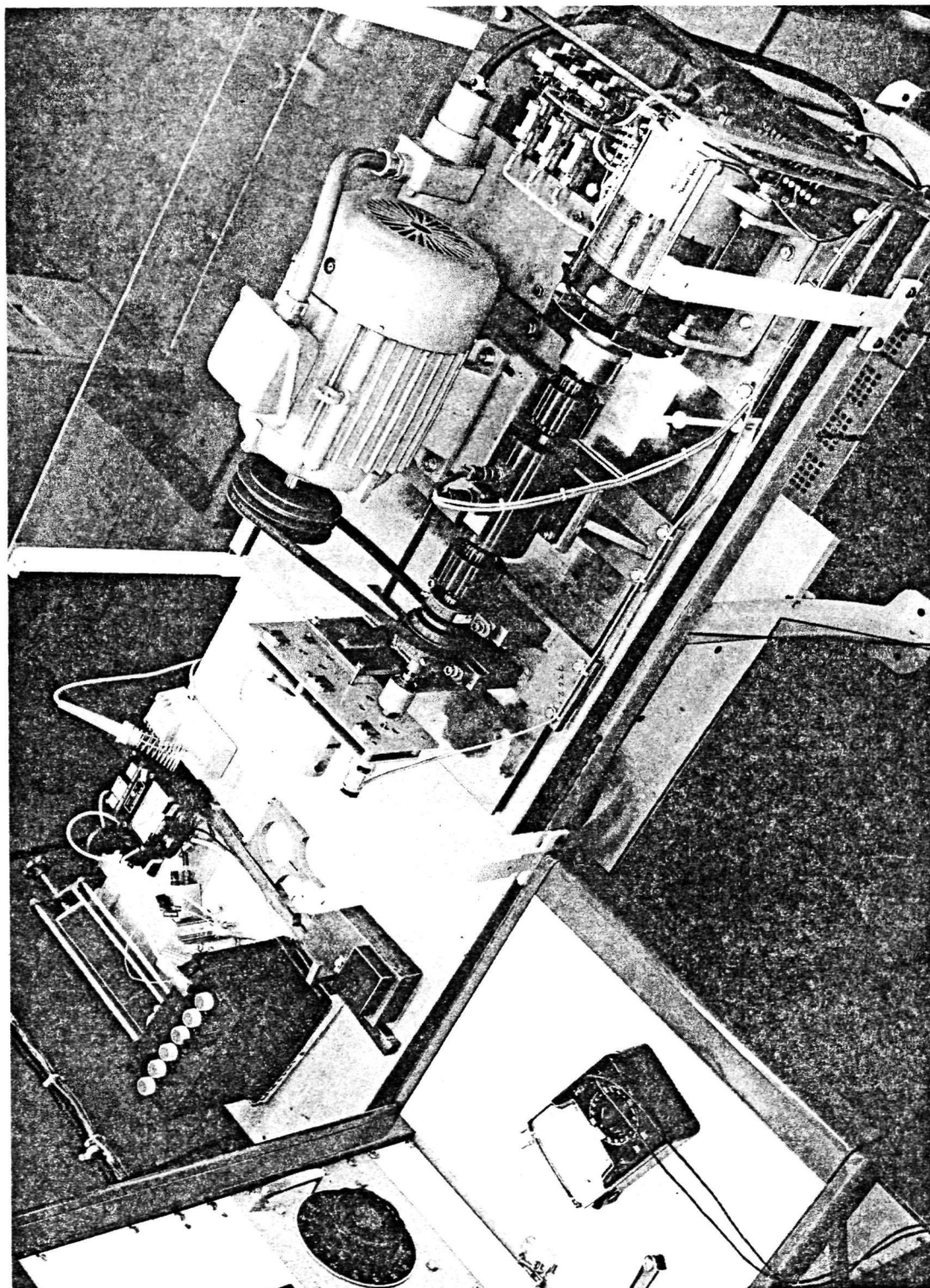


Figure 4-4. Delco Electromechanical Assembly

At this stage of the program, the permanent magnet motor had not yet been developed; the actuator motor shown in the lower right-hand corner of Figure 4-4 is a five kilowatt wound-rotor, self-synchronous motor which is operated with fixed field excitation. The motor is coupled to a torque transducer which also provides an r/min indication by means of a toothed wheel and permanent magnet pulse generator arrangement. The motor assembly is coupled to the large induction machine with a V-belt.

The induction motor was used to drive the assembly when the actuator motor was operating as a generator, and as a dynamometer when the actuator was under test in its motoring mode.

The system also drives a servo-type gear reducer which is mounted at the left end of the baseplate. The gear reducer drives a tachometer at the high-speed end and a position transducer potentiometer at the low-speed end of the gear train. This arrangement was used to aid in system development before the final motor was designed. After the permanent magnet motor was designed, it was incorporated in the same basic breadboard assembly as shown in Figure 4-5. Here, a dc machine, coupled to the EMA by means of a toothed belt, is used to load or drive the actuator system. The dc machine's field and armature circuits were available for loading and control purposes. When operated as a generator, the dc machine supplied power to a resistive load bank.

Figure 4-6 shows the breadboard electromechanical assembly at a later time. The large dc machine has approximately the same power rating as the actuator motor, but its speed is one third that of the permanent magnet machine. Figure 4-7 is a closer view of the same equipment. Figure 4-8 shows the Delco EMA motor with a digital shaft encoder coupled to the right end of the motor. As part of a continuing company-funded development effort, Delco developed a digital rotor position sensor (RPS). The RPS uses a three-bit encoder (Figure 4-9). One bit provides an absolute reference (once per revolution), and the other two bits allow the RPS to determine the rotor position with a resolution of 0.25 degree. Figures 4-10 and 4-11 are front and rear views of the RPS electronics housing. Digital decoding and control allow the



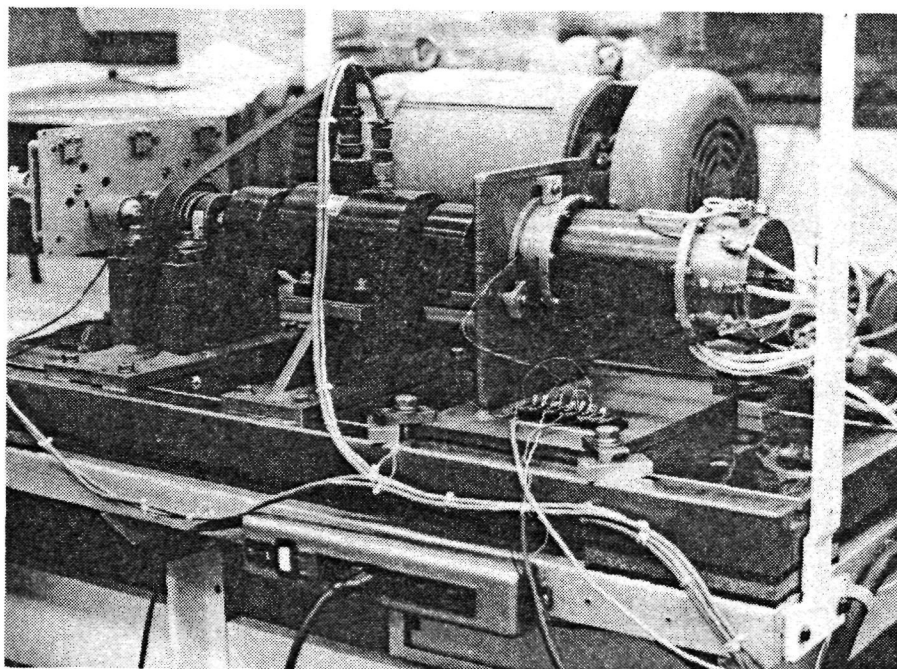


Figure 4-5. Delco Electromechanical Assembly

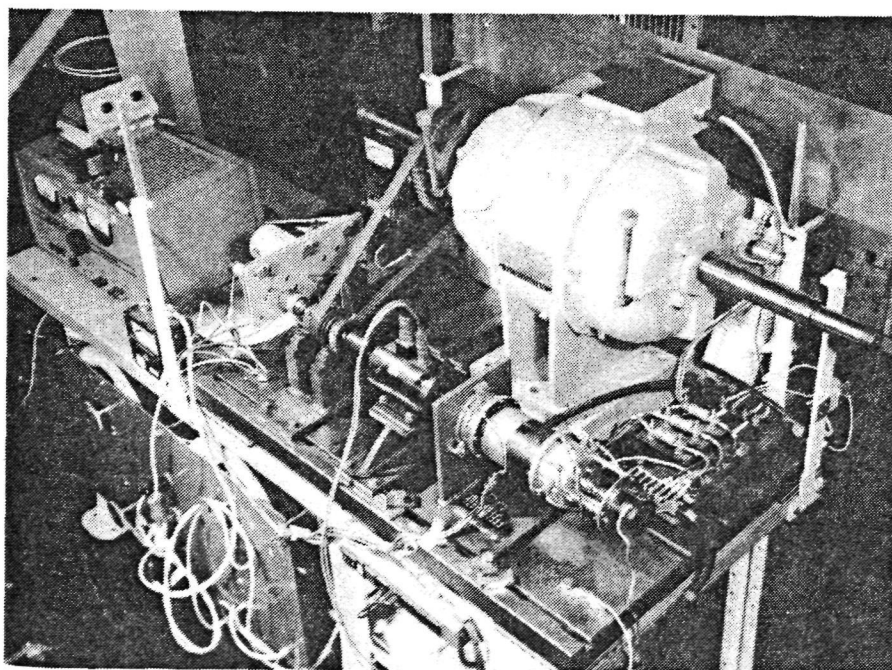


Figure 4-6. Delco Dynamometer Stand

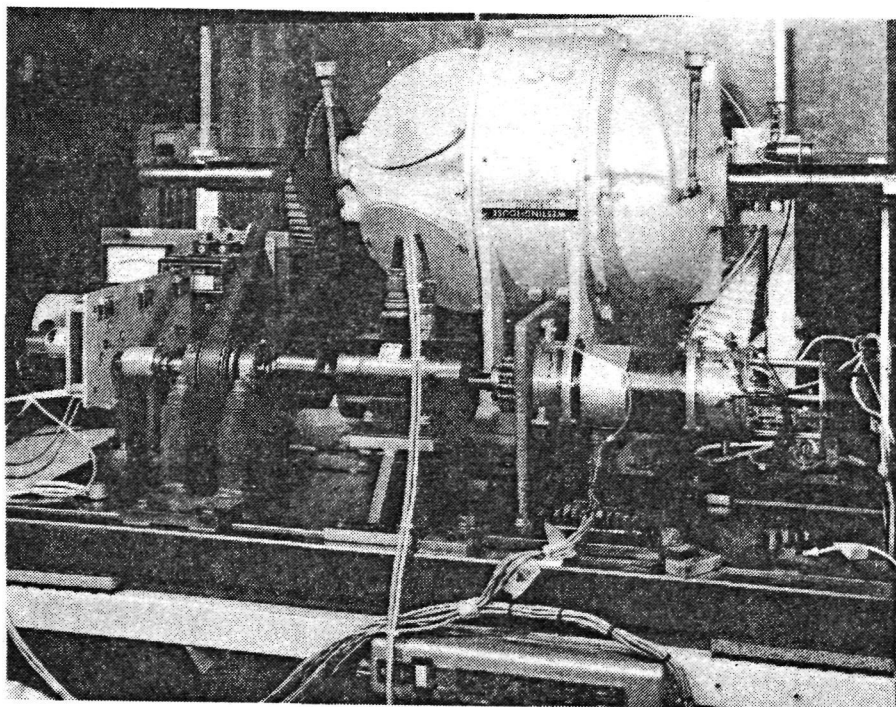


Figure 4-7. Close-Up View of Delco Dynamometer

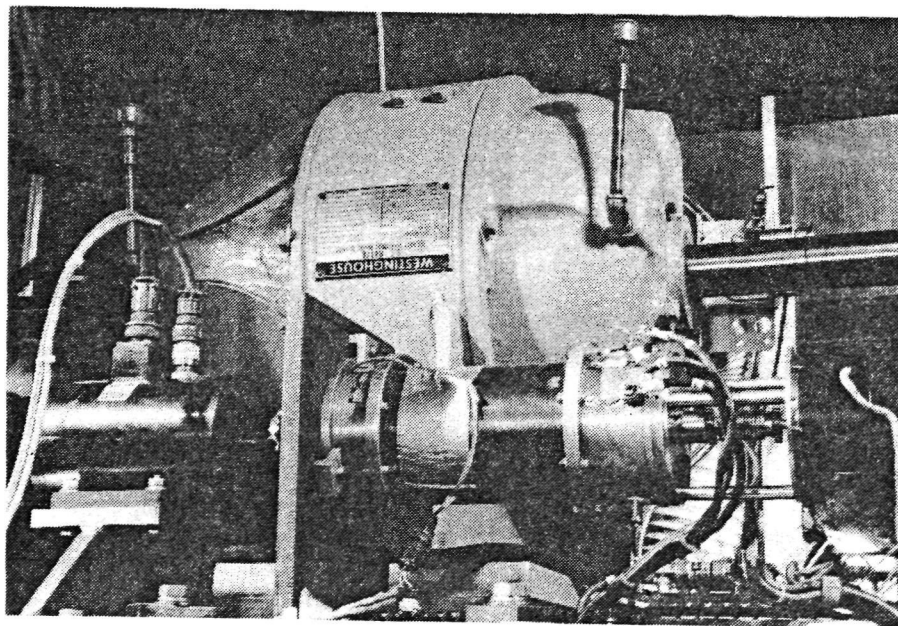


Figure 4-8. Delco EMA Motor with Shaft Encoder

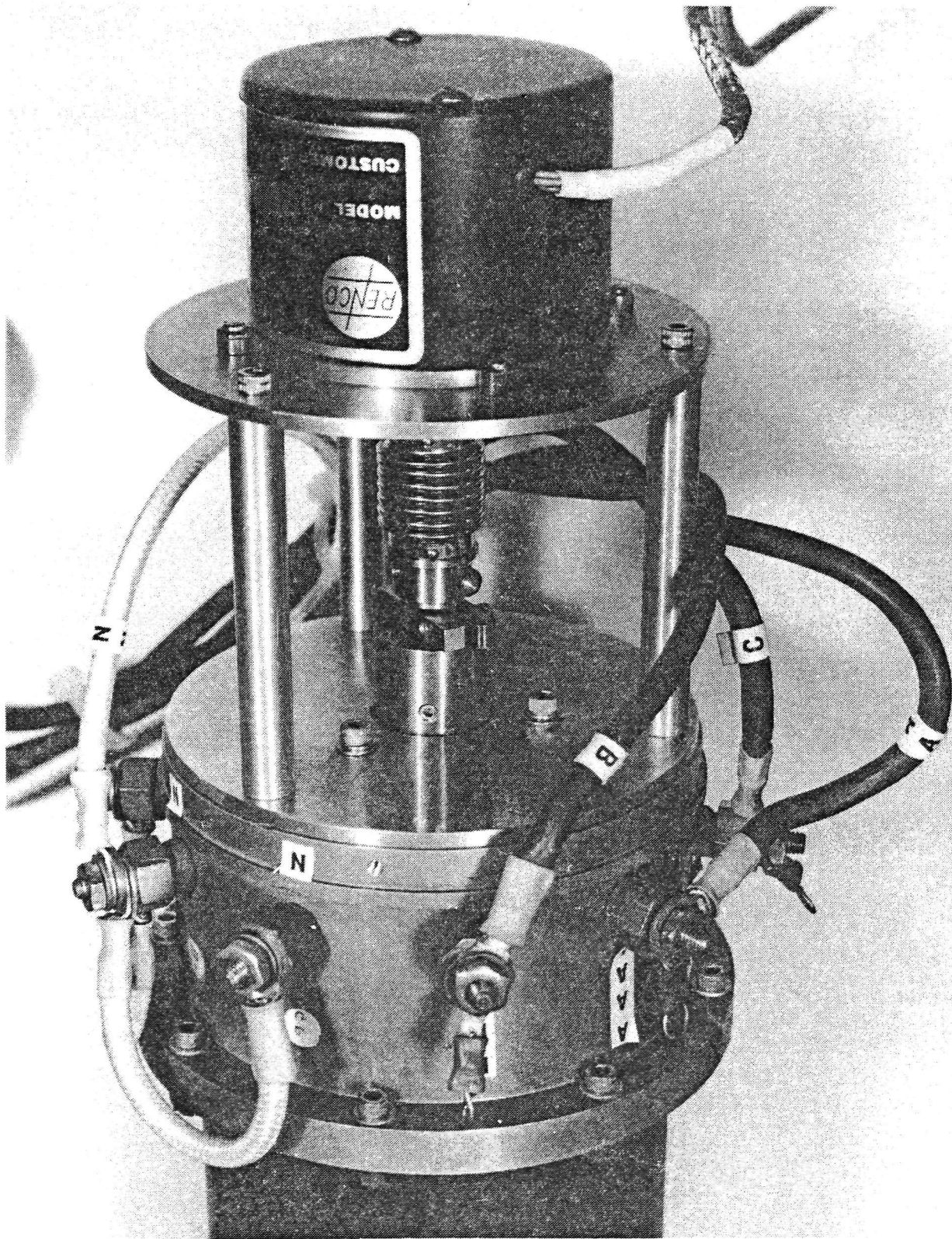


Figure 4-9. Digital Shaft Encoder



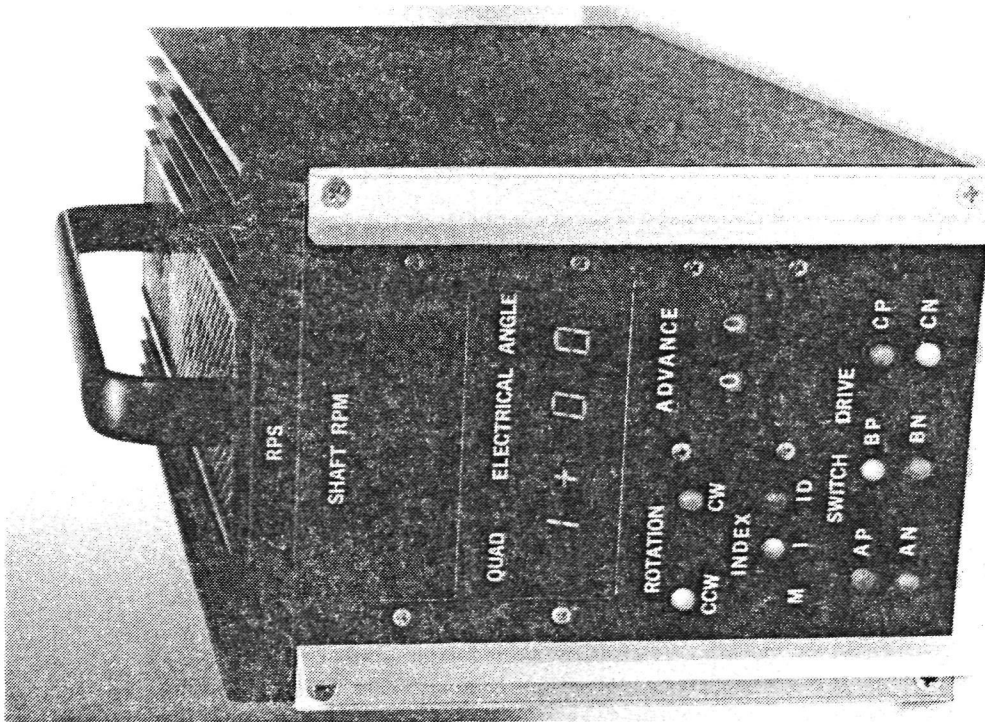


Figure 4-10. Delco Rotor Position Sensor Electronics (Front View)

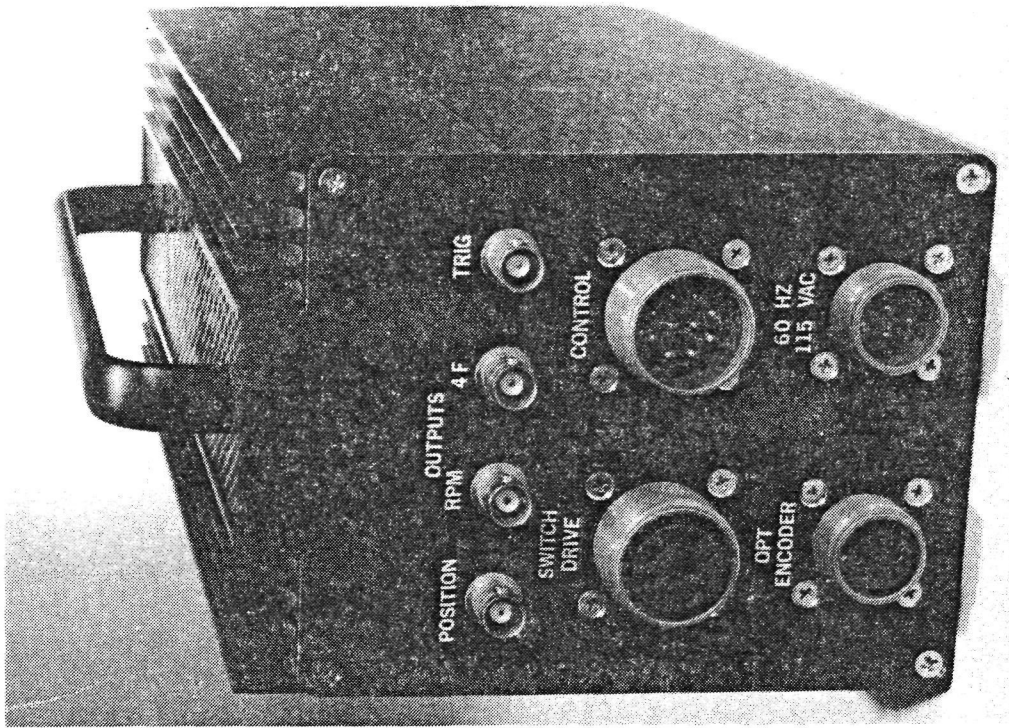


Figure 4-11. Delco Rotor Position Sensor Electronics (Rear View)

motor's commutation angle to be varied through an electrical angle of 59 degrees, and the RPS also provides speed and direction of rotation information.

#### 4.2 NASA FOUR-CHANNEL SYSTEM DESCRIPTION

The four-channel motor/gearbox assembly was mounted on the NASA-developed test stand (Figure 4-12) which consists of two large spring assemblies located at each end of the stand. The springs are coupled by means of a clevis arm into the rotating portion of the stand. A 238.71:1 gear reducer is used to reduce the gearbox output speed to that of the simulated control surface motion.

Figure 4-13 is a closer view of the load stand, showing the clevis arm and load spring. A rear view of the EMA test stand is given in Figure 4-14. This shows the electrical cabling and the compressed air filter, manifold and hoses which provide cooling air to the system.

Figure 4-15 is a close-up view of the motor/gearbox assembly, and clearly shows the position feedback potentiometers (mounted on the right rear corner of the gearbox) and the tachometers (mounted on the motors). Figure 4-16 shows the motor/gearbox assembly and also the torque transducers which are mounted between the EMA gearbox and the planetary gear reducers. Figure 4-17 is a rear view of the motor/gearbox assembly, showing the cable arrangement.

##### 4.2.1 DIFFERENTIAL GEARBOX

###### 4.2.1.1 Power Train

The differential gearbox sums the velocities of the individual servo motors and provides a common output shaft. The gearbox also furnishes the required gear reduction ratio between the motor shaft and the rotary hinge actuator. A schematic of the system is shown in Figure 4-18.

The maximum motor speed is approximately 9000 r/min and the overall gear reduction ratio is about 2700:1, resulting in a control surface rate of 20 degrees/s. Since the rotary hinge actuator (not part of the differential gearbox) reduction is 238.71:1, the differential gearing must provide a reduction of about 11.30:1.



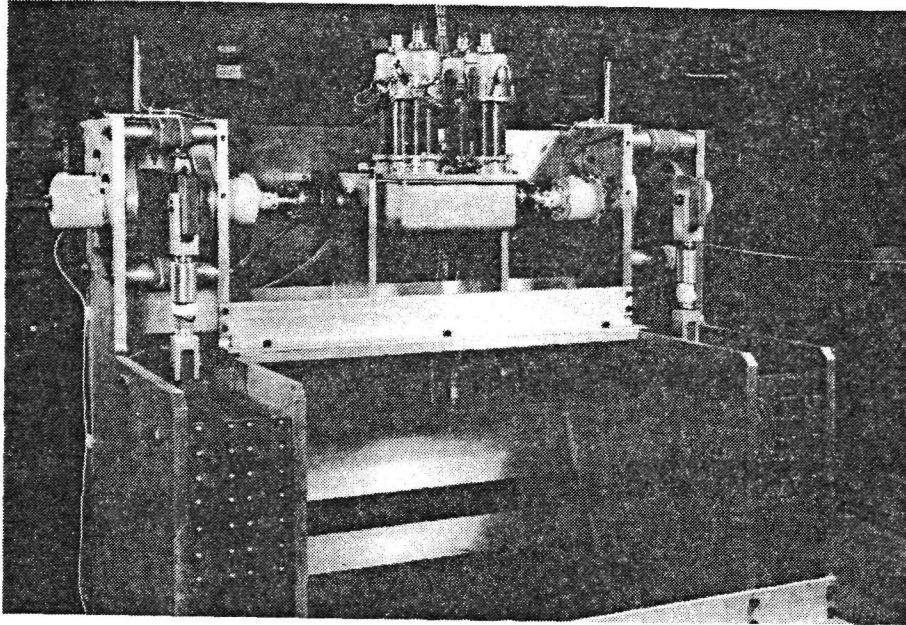


Figure 4-12. EMA Test Stand

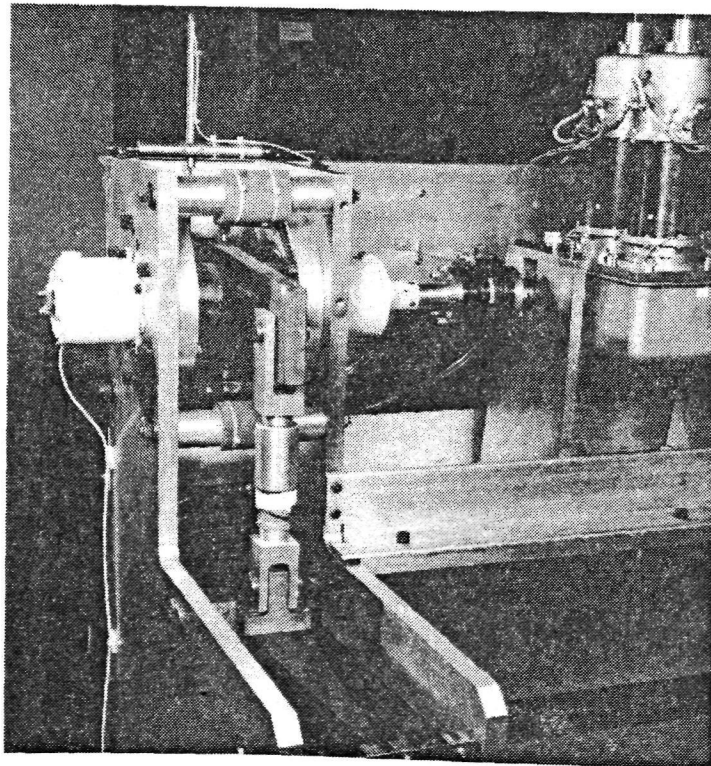


Figure 4-13. Clevis Arm and Load Spring

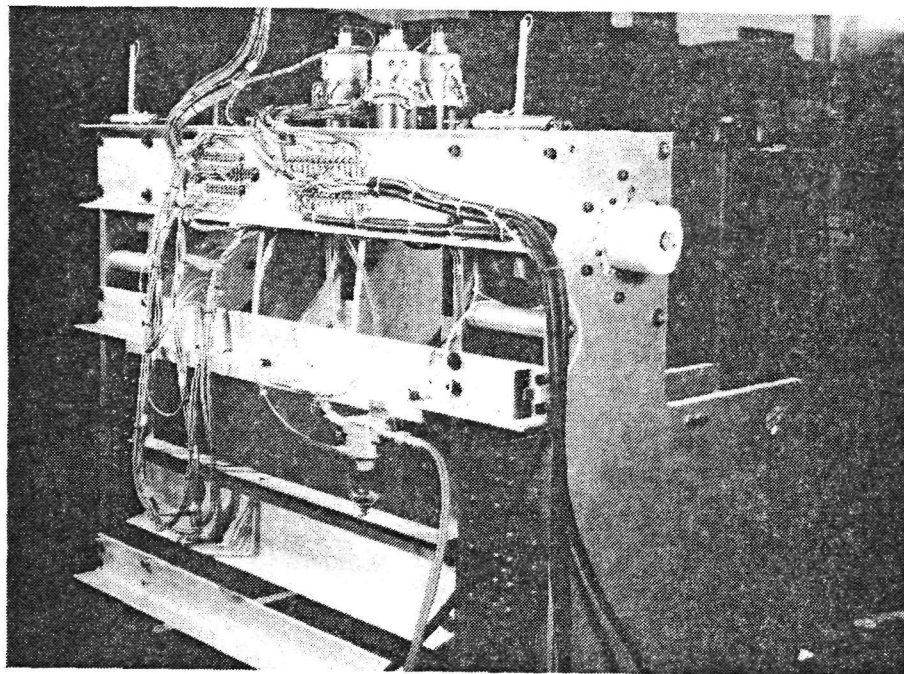


Figure 4-14. EMA Test Stand (Rear View)

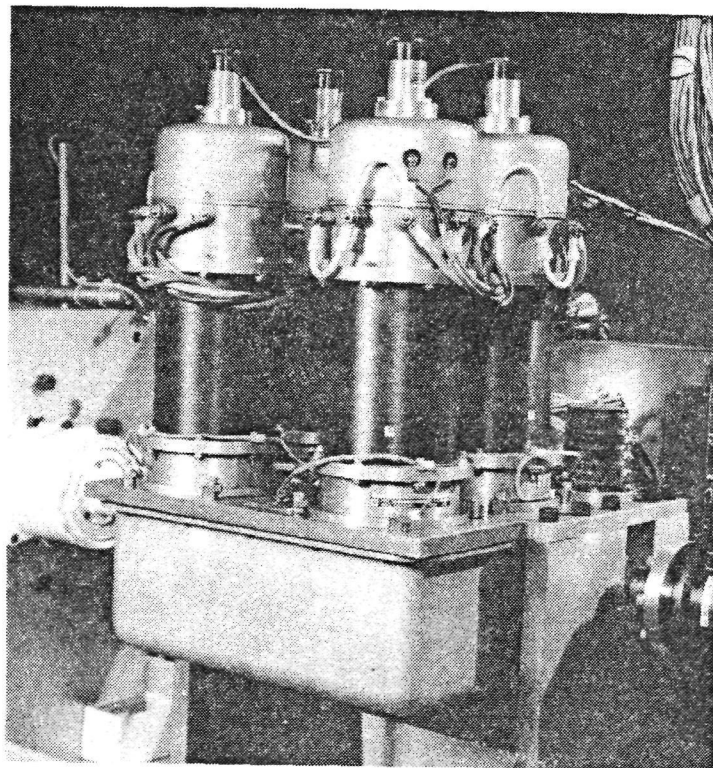


Figure 4-15. Motor/Gearbox Assembly

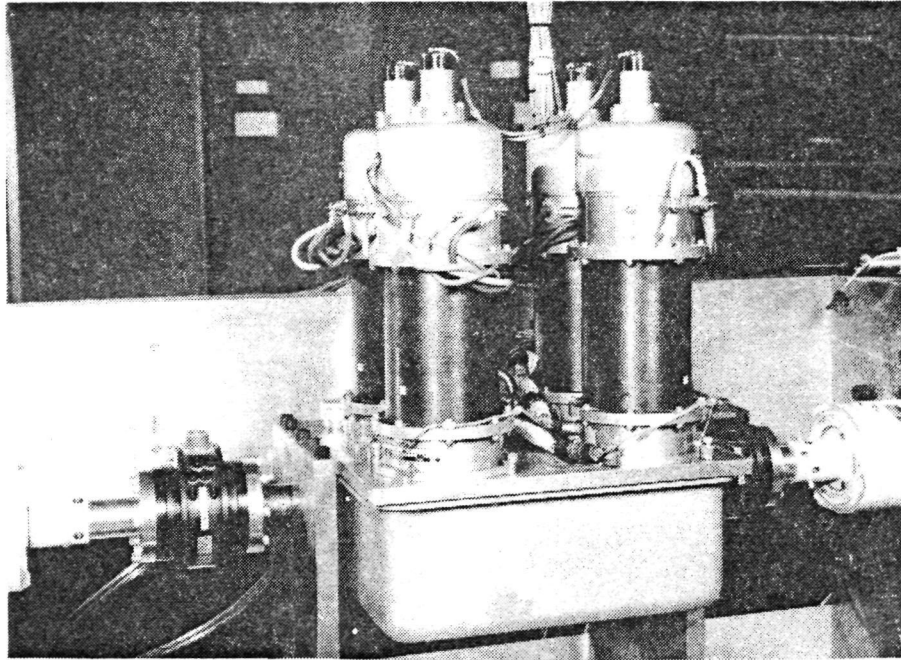


Figure 4-16. Motor/Gearbox Assembly and Torque Transducers

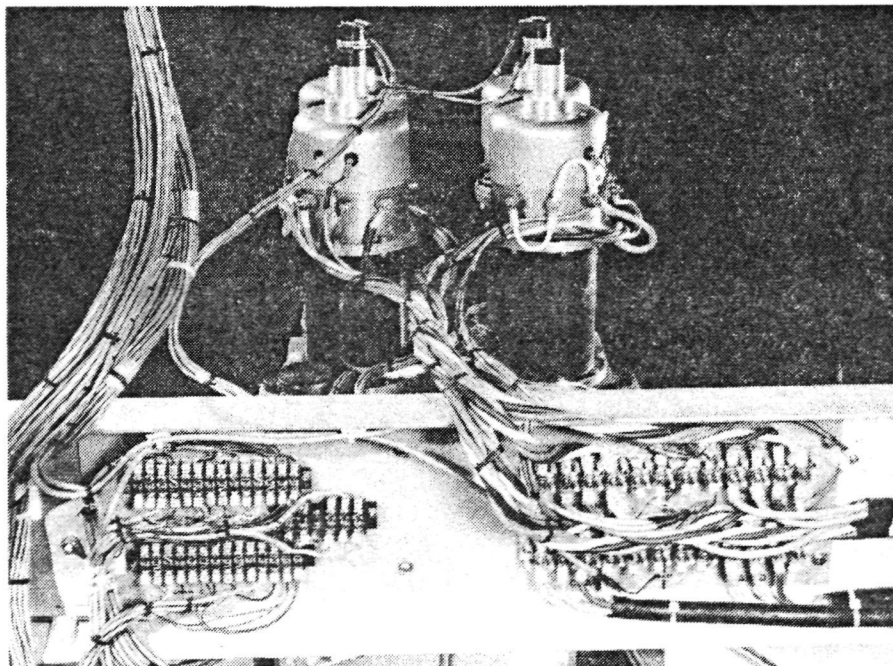


Figure 4-17. Motor/Gearbox Assembly (Rear View)

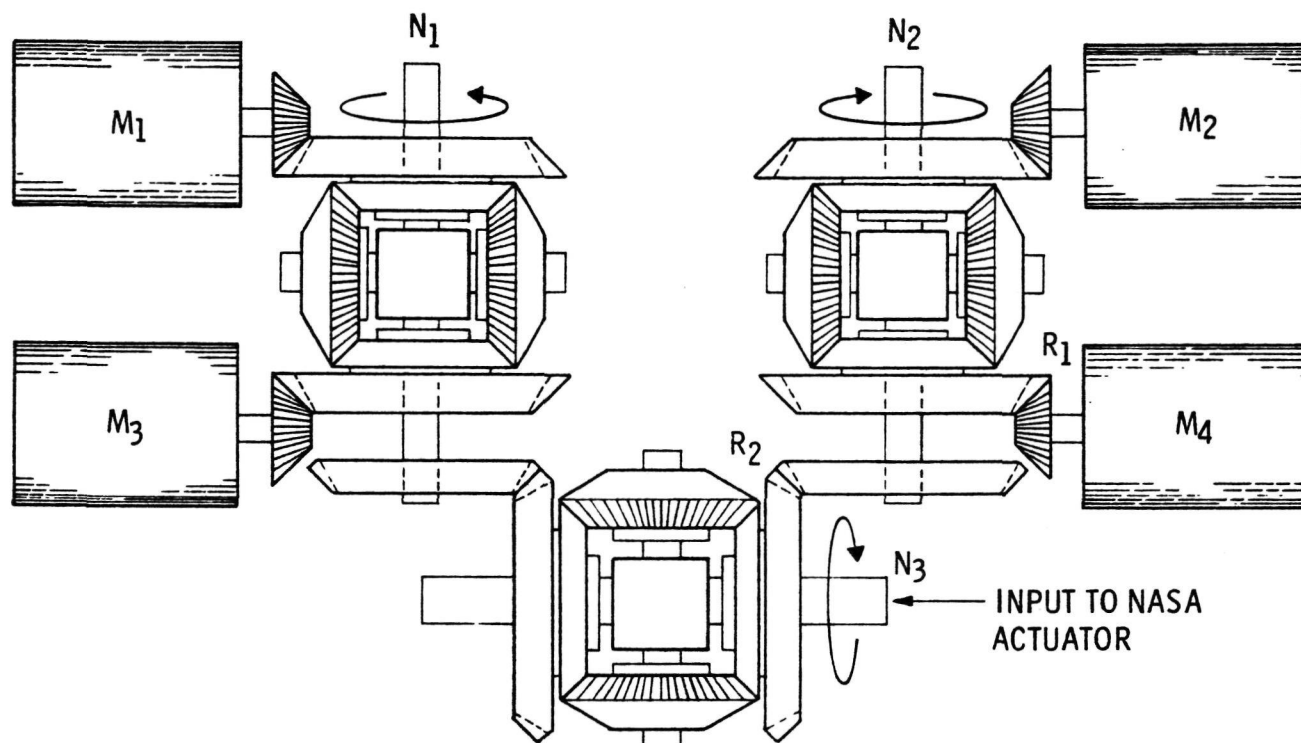


Figure 4-18. Differential Gearbox Arrangement

When any two of the four motors are operating, the differential gear arrangement inherently has a 2:1 reduction; therefore, only a 5.65:1 additional gear reduction is required. This is accomplished in two stages: 3.75:1 between the motors and the first stage differential inputs, and 1.5:1 between the first and second stage differential inputs. By applying the larger reduction at the motor, the moment of inertia effect of the gear train is minimized.

#### 4.2.1.2 Position Transducer Gear Train

The position transducer is coupled to the output of the gearbox by means of precision servo gearing (The mounting hole for the position transducer assembly can be seen in the lower left-hand corner of Figure 4-19). A worm gear (shown in Figure 4-19) drives an anti-backlash gear which is mounted on the position transducer shaft. The gear ratio of this train provides 5.189 degrees of position transducer motion for each degree of load motion (based on a gear reduction of 238.71:1 in the NASA-furnished rotary hinge actuator). With



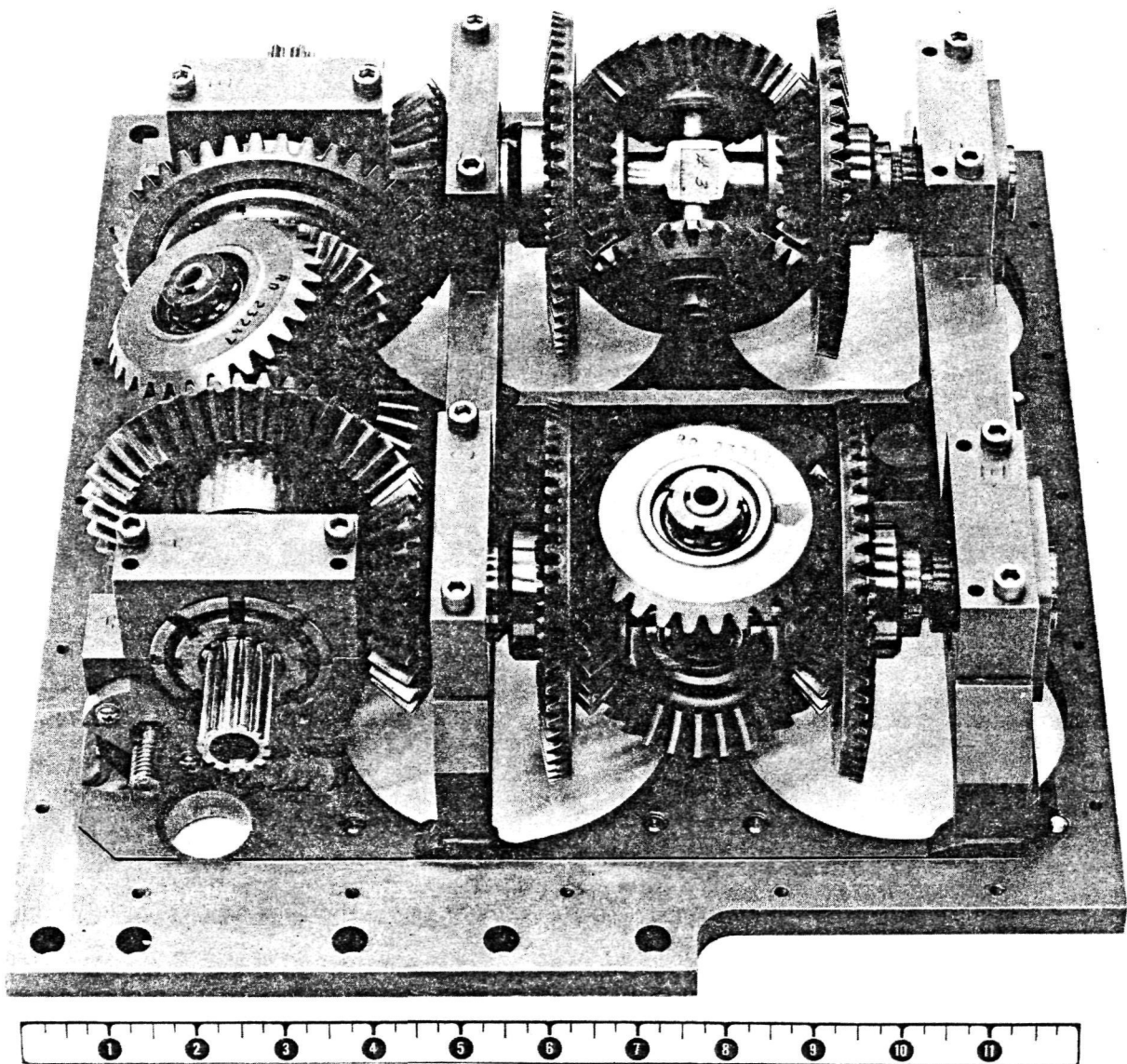


Figure 4-19. Differential Gearbox

typical adjustment, the position transducer motion as a function of load angle would be as illustrated in Figure 4-20.

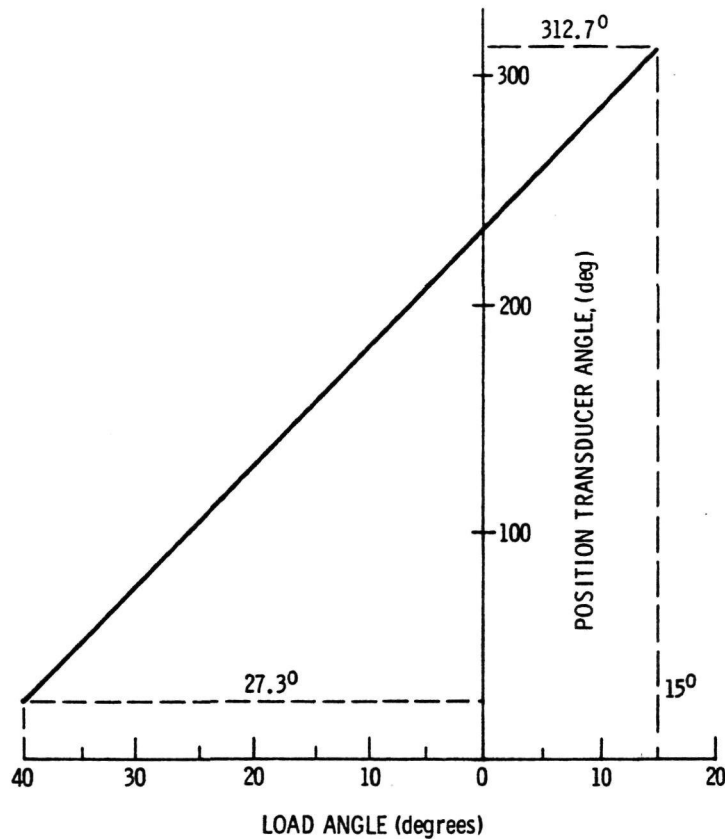


Figure 4-20. Position Transducer Motion

#### 4.2.1.3 Position Transducer

The position transducer consists of four precision servo potentiometers ganged on a single shaft. The transducers utilize a film resistive element to achieve virtually infinite resolution. Some of the major features of the position transducer are:

Diameter	2.0 in.
Resistance (each element)	20K ohms
Linearity	0.25%
Electrical Travel	340°
Standard Life Expectancy	10 M revolutions

#### 4.2.1.4 Physical Characteristics

The differential gearbox assembly (Figure 4-21) consists of three identical bevel gear differentials of the type often used in precision instruments. Input rotations are applied to the gears at either end of the bevel gear set. The output speed is taken off the "spider" or cage shaft.

The differential gear assembly is shown in Figure 4-19. All gears are ground spiral bevel gears specifically developed for this application and fabricated from high-quality gear steel as recommended by AGMA standards. "Zero1" spiral bevel gears (spiral gears with zero spiral angle) have been selected for this design to provide smooth operation, continuous pitch line contact, superior performance with low number of pinion teeth, and low axial bearing loads. Adjustment capability is provided to control gear mesh clearance and backlash. Basic gear sizing along with gear and pinion bending and contact stresses have been determined by the Gleason Works (See Appendix B for detail gear data). Antifriction bearings of instrument quality are used throughout. Angular contact bearings have been chosen for uses when both axial and radial loads are present.

The gearbox housing is made of aluminum, welded and machined after welding. Oil splash type lubrication is provided for the gears.

The major gearbox power train performance characteristics are summarized below.

Maximum input speed	9000 r/min
Average input speed	2250 r/min
Maximum input torque	120 in. lb
Maximum output torque	2700 in. lb
Maximum input power per motor	17 hp
Average input power per motor	5 hp
Maximum output speed	800 r/min
Gear ratio (two motors operating)	11.25:1

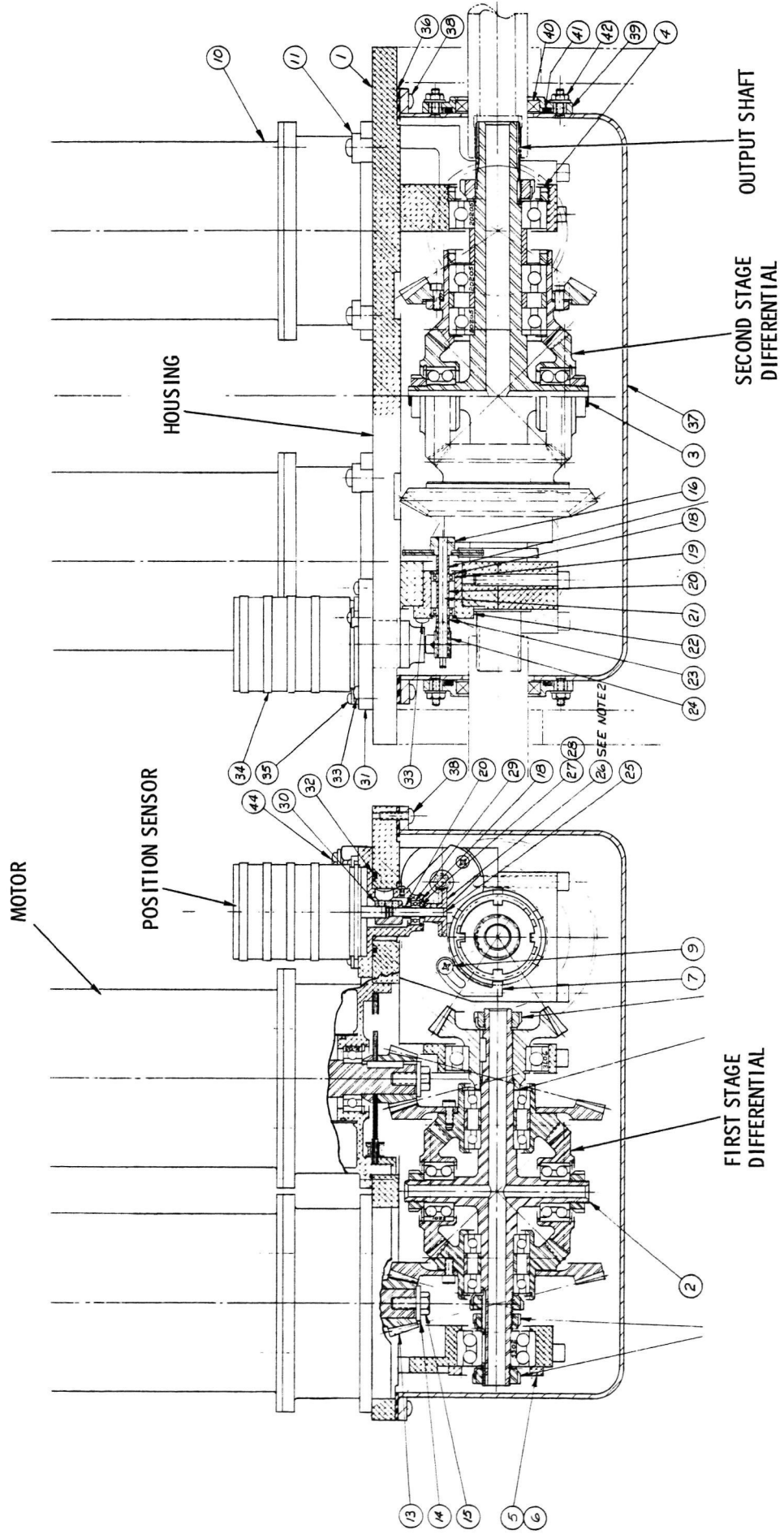


Figure 4-21. Four-Channel EMA Assembly



#### 4.2.2 MOTOR ASSEMBLY

Figure 4-22 shows the motor mechanical arrangement. The motor output pinion is shown at the left-hand end of the figure. The rotor position sensor is also located at the left side of the machine. The sensor consists of nine coils on a laminated stator which works in conjunction with a laminated rotor.

The rotor has four lobes (equal to the number of pairs of rotor poles). The stator coils form three groups, each of which has a one excitation coil (at the center of the group) and two secondary coils that are connected so that their outputs buck each other when either the rotor lobe or rotor slot is centered at the excitation coil. Excitation for the sensor is provided by a 30 kHz oscillator. The output of the secondary coils is processed by phase-sensitive detectors to produce rotor position signals which determine the rotor location with a resolution of 60 electrical degrees. The rotor position sensor is very rugged and can withstand the same temperature extremes as the motor. The RPS rotor stack is made very short to minimize its inertia. The stator stack is longer than the rotor stack to minimize false signals which could be caused by rotor axial motion or wobble. The stator is centered on the rotor stack to provide overhang at both ends.

The motor rotor is an eight-pole permanent magnet assembly described later in more detail. Compressed air is used to cool the motor. The air enters one end of the stator assembly. The stator winding partially fills the stator slots so that the air can flow through the stator assembly slots and out the exit outlet at the far end. The rotor is coupled to a brake disc assembly and to a dc tachometer which provides velocity feedback in the actuator system. The brake consists of both a permanent magnet and an electromagnet. If the electromagnet is deenergized, the permanent magnet pulls the brake disc into contact with the stationary brake shoe, thus stopping the rotor. To release the brake, the electromagnet is energized, thus cancelling the field of the permanent magnet. A small spring pushes the brake disc away from the brake shoe to allow free rotation.

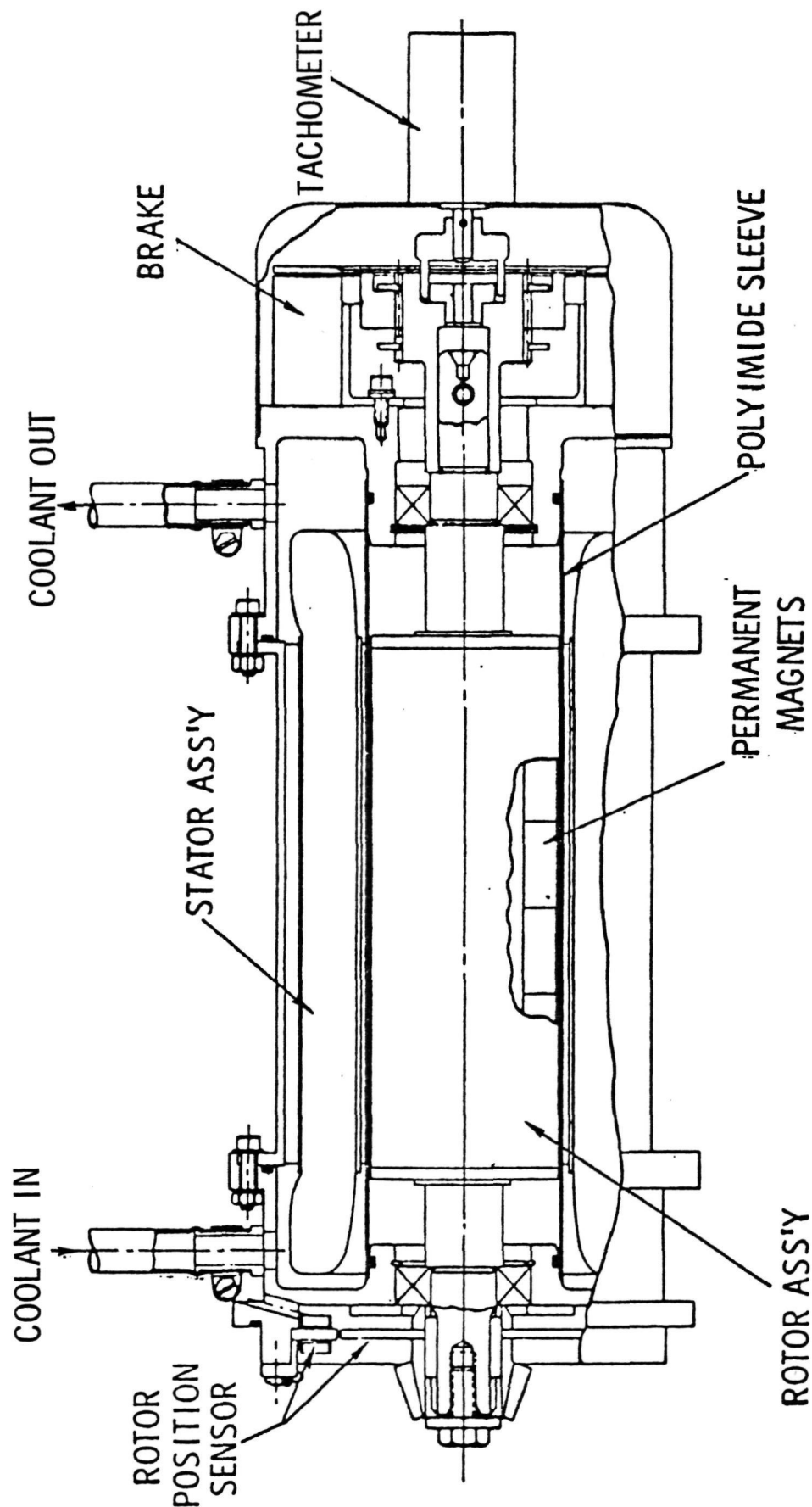


Figure 4-22. EMA Motor Design

Figure 4-23 shows the motor shaft before the permanent magnets are attached. Since the motor is an eight-pole machine, the central portion of the shaft has an octagonal cross section. Figure 4-24 shows the rotor with the samarium cobalt magnets attached. The samarium cobalt material has a high energy product (18 million gauss oersteds). The magnetic blocks, approximately 7/8 inch long, are bonded to the rotor shaft and then ground to a cylindrical form. Brass end discs are bonded to the magnet assembly and retained by snap rings (Figure 4-25).

The end discs provide material which can be removed during dynamic balancing; they also reduce windage losses and provide a termination point for the rotor banding. The banding is a high-strength glass filament winding which is wound under tension using SCG 150 I/O 1Z HTS901 fiberglass, with Ferro Corp. CE 9020 adhesive, 60% solids, 40% acetone, cured at 350°F for 1-1/2 hours. The banded rotor (Figure 4-26) is ground to provide an accurate diameter for mechanical clearance in the stator bore.

A special test fixture (Figure 4-27) was used during system development to spin up the rotor. A high-speed motor is located at the left end of the fixture. The spin tests were conducted in a chamber which consisted of two plywood boxes, one inside the other with the void filled with sand (Figure 4-28). The rotor was spun at speeds greater than 30,000 r/min without failure; this is better than three times the rated speed of the motor (9,000 r/min).

The stator is shown in Figure 4-29; the stator laminations are 7 mils thick and are Vanadium Permendur.

Figure 4-30 shows the rotor position sensor for the wound rotor machine which was used during the early development stages; the unit is mounted on a precision indexing stand for caliabration purposes.

The tachometer is directly coupled to the motor shaft. It has a highly linear speed/voltage characteristic, operates bidirectionally, and is designed for long operating life. Important specifications for the tachometer are listed in Table 4-1.

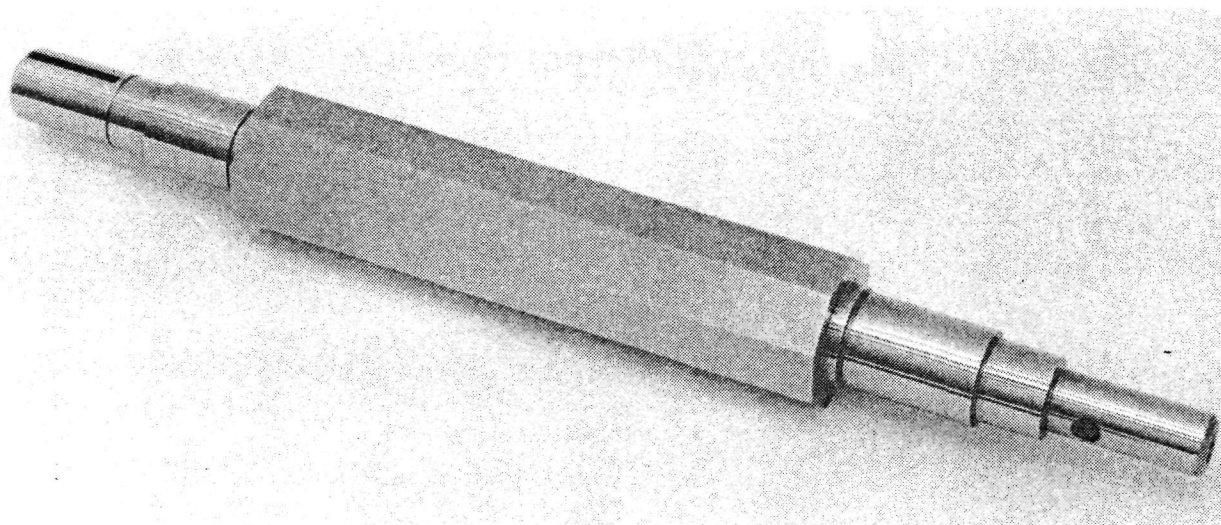


Figure 4-23. Motor Shaft

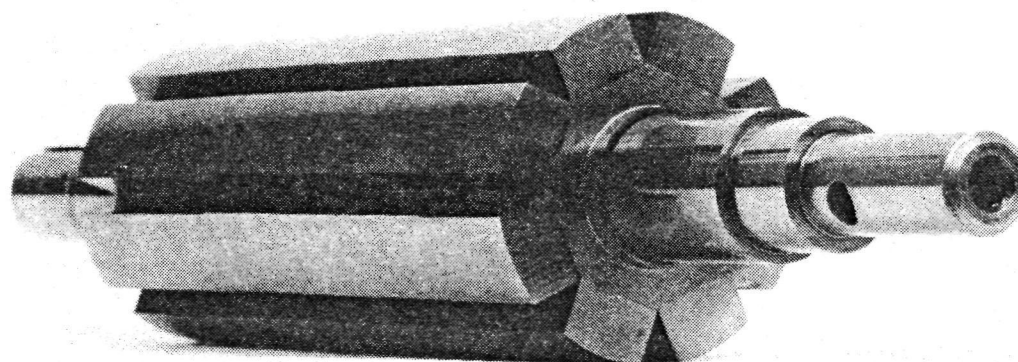


Figure 4-24. Rotor

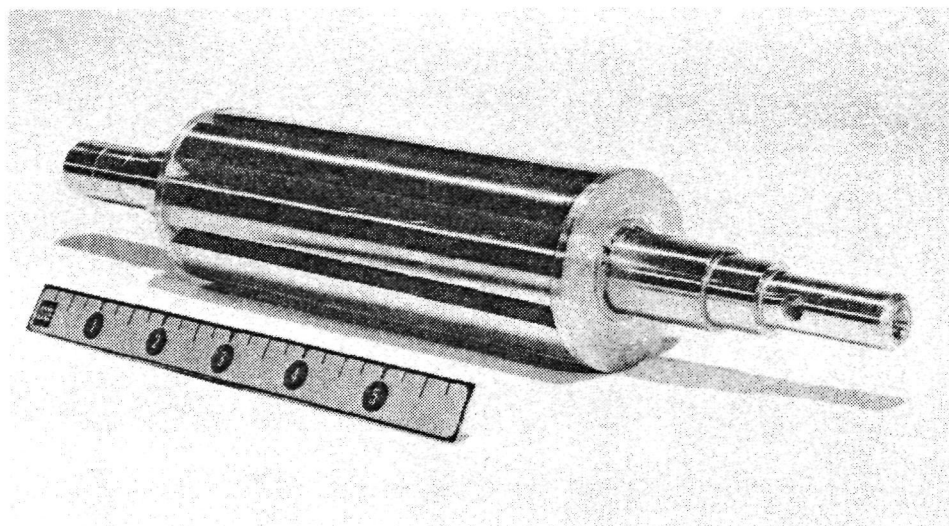


Figure 4-25. Rotor Before Banding

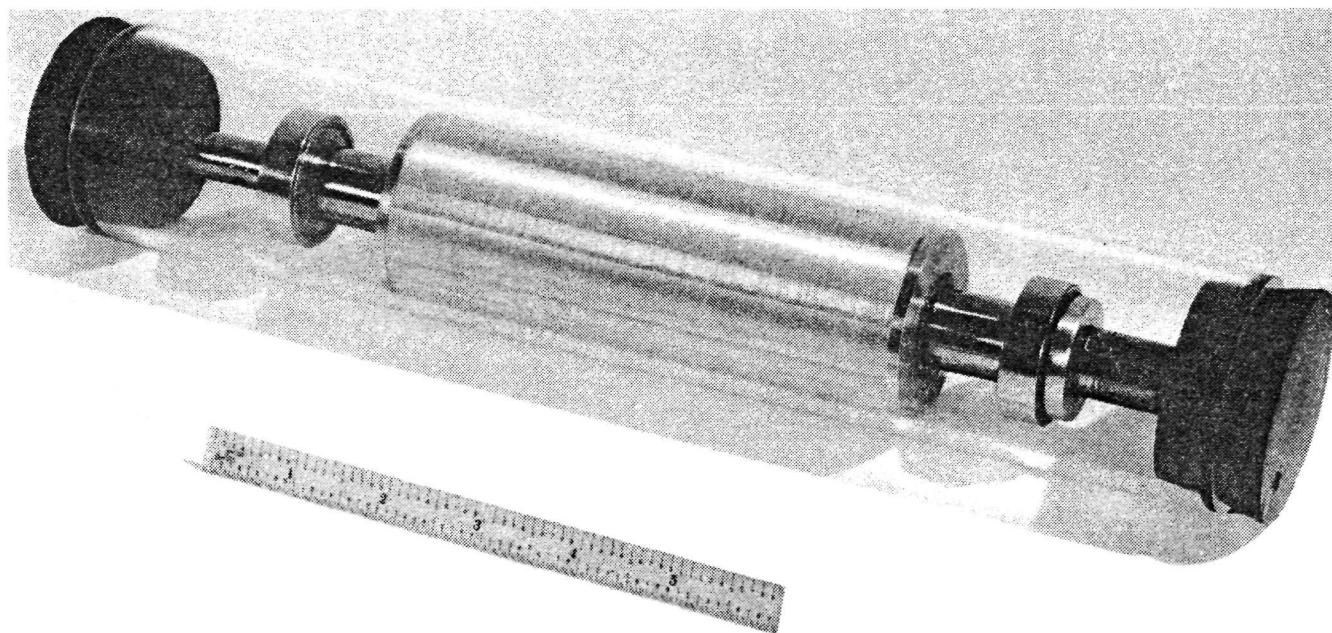


Figure 4-26. Rotor After Banding



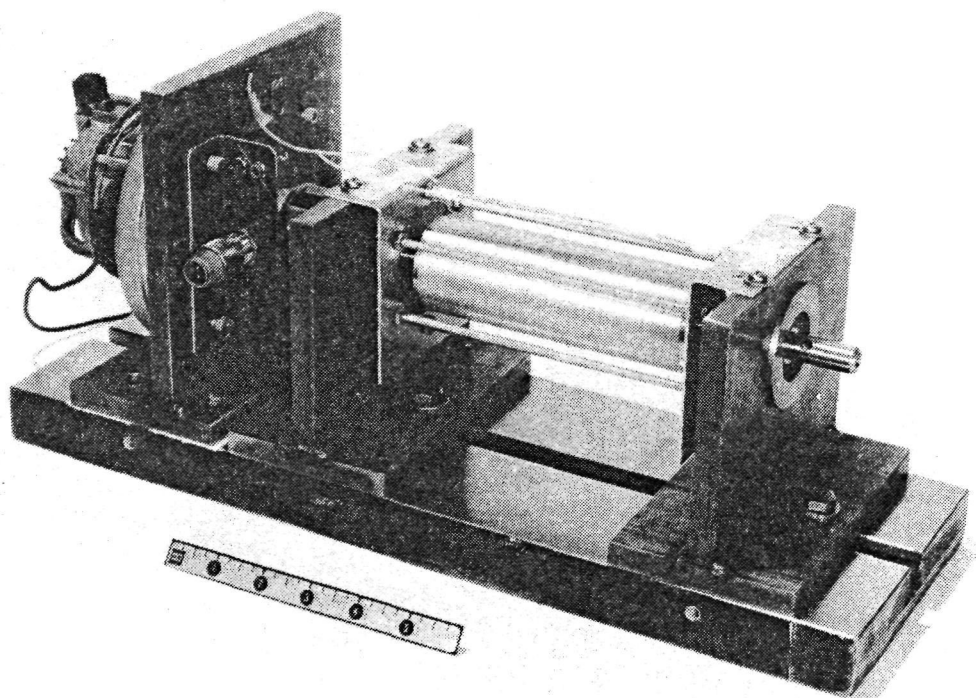


Figure 4-27. Rotor Spin Test Fixture

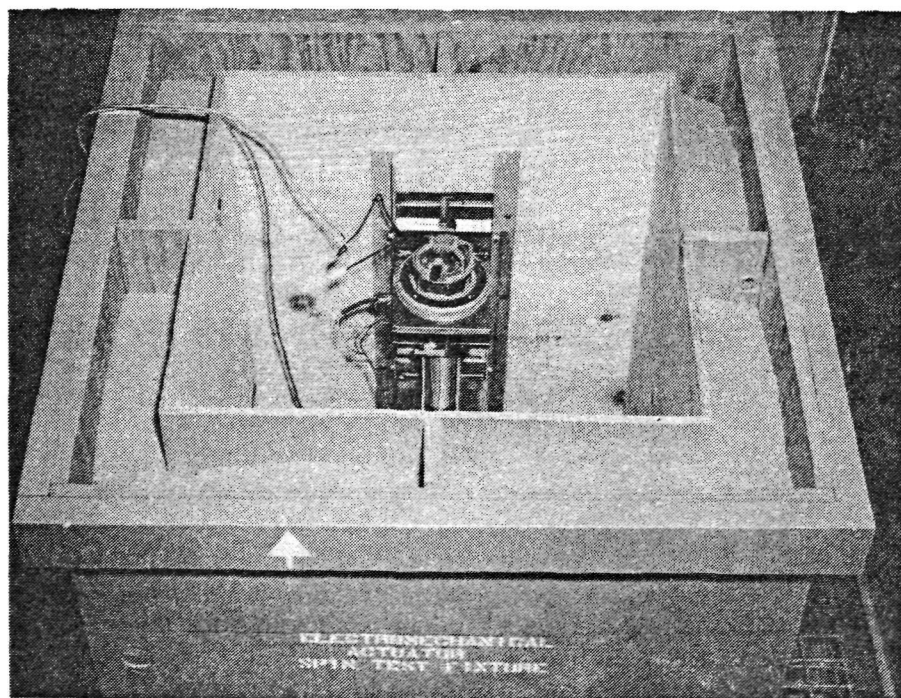


Figure 4-28. Rotor Spin Test Chamber

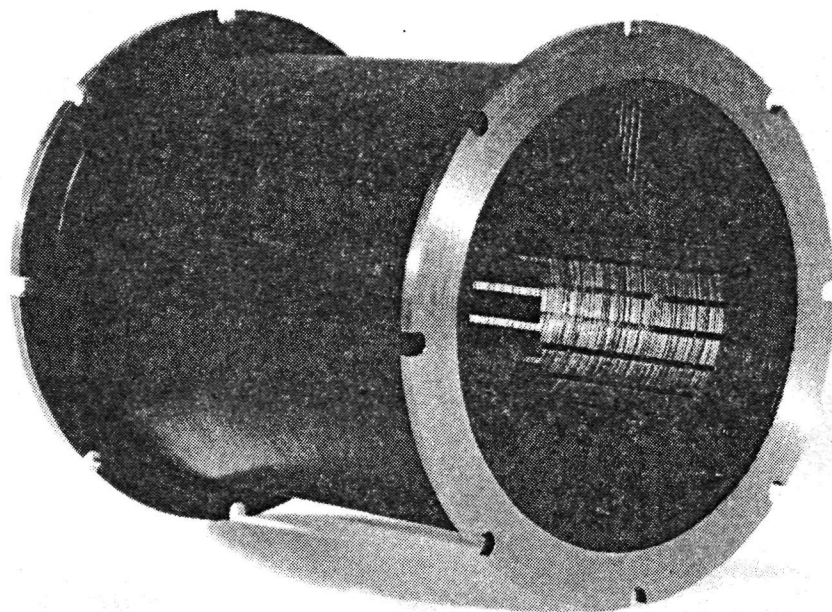


Figure 4-29. Stator

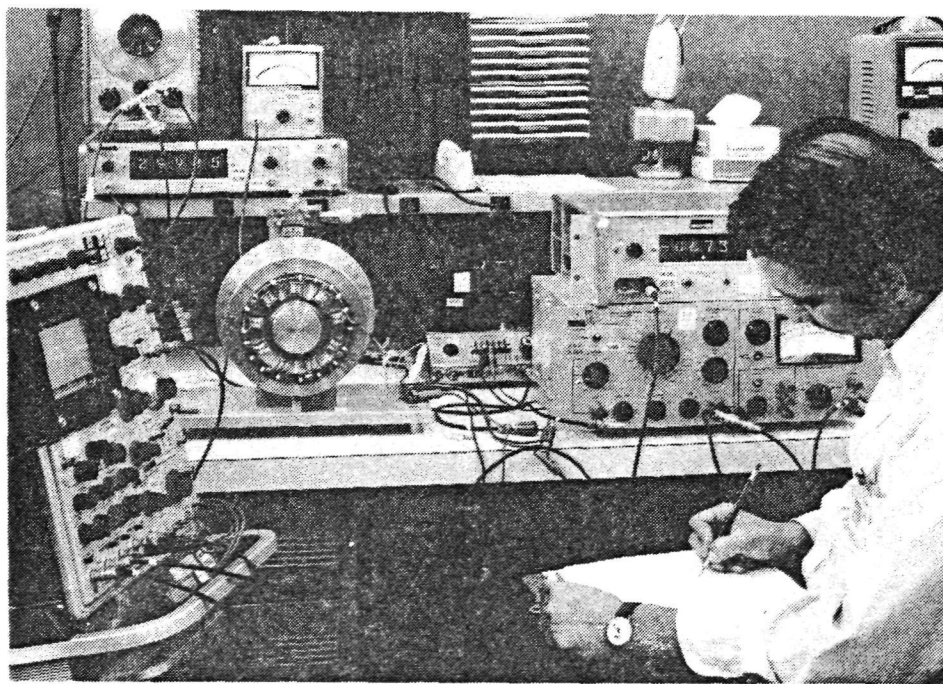


Figure 4-30. Rotor Position Sensor Calibration

Output voltage gradient	7.0 V/1000 r/min
Output impedance, maximum	350 ohms
Output linearity, 100 to 6,000 r/min	0.1%
Ripple voltage, maximum rms	3%
Bidirectional output voltage error	0.25%
Maximum speed	12,000 r/min
Friction torque, maximum	0.25 oz-in.
Armature inertia, maximum	6.5 gm-cm <sup>2</sup>
Weight, maximum	3.0 oz
Mechanical natural frequency, minimum	1800 Hz
Life expectancy at 3600 r/min	10,000 hr

Table 4-1. Tachometer Specifications

The motor assembly has the following physical characteristics:

Length over brake	11.25 in.
Diameter of motor frame	3.75 in.
Weight of motor, RPS and cable	17.2 lb
Weight of brake, tachometer and coupling	2.7 lb

#### 4.2.3 CONTROL ELECTRONICS

##### 4.2.3.1 Physical Arrangement

The electronics for the four-channel EMA are housed in a conventional equipment rack (Figure 4-31). The power control electronics are located at the top. The volume immediately below the power control panel is presently empty, but it is anticipated that the redundancy management electronics would eventually be housed here. Below this area are two drawers of control electronics, each of which contains two channels of low-level electronic equipment. The main power electronics assembly is located immediately below the control drawers. The bottom part of the rack contains the power contactors, 28 Vdc power supply for the system, and the brake control electronic chassis.



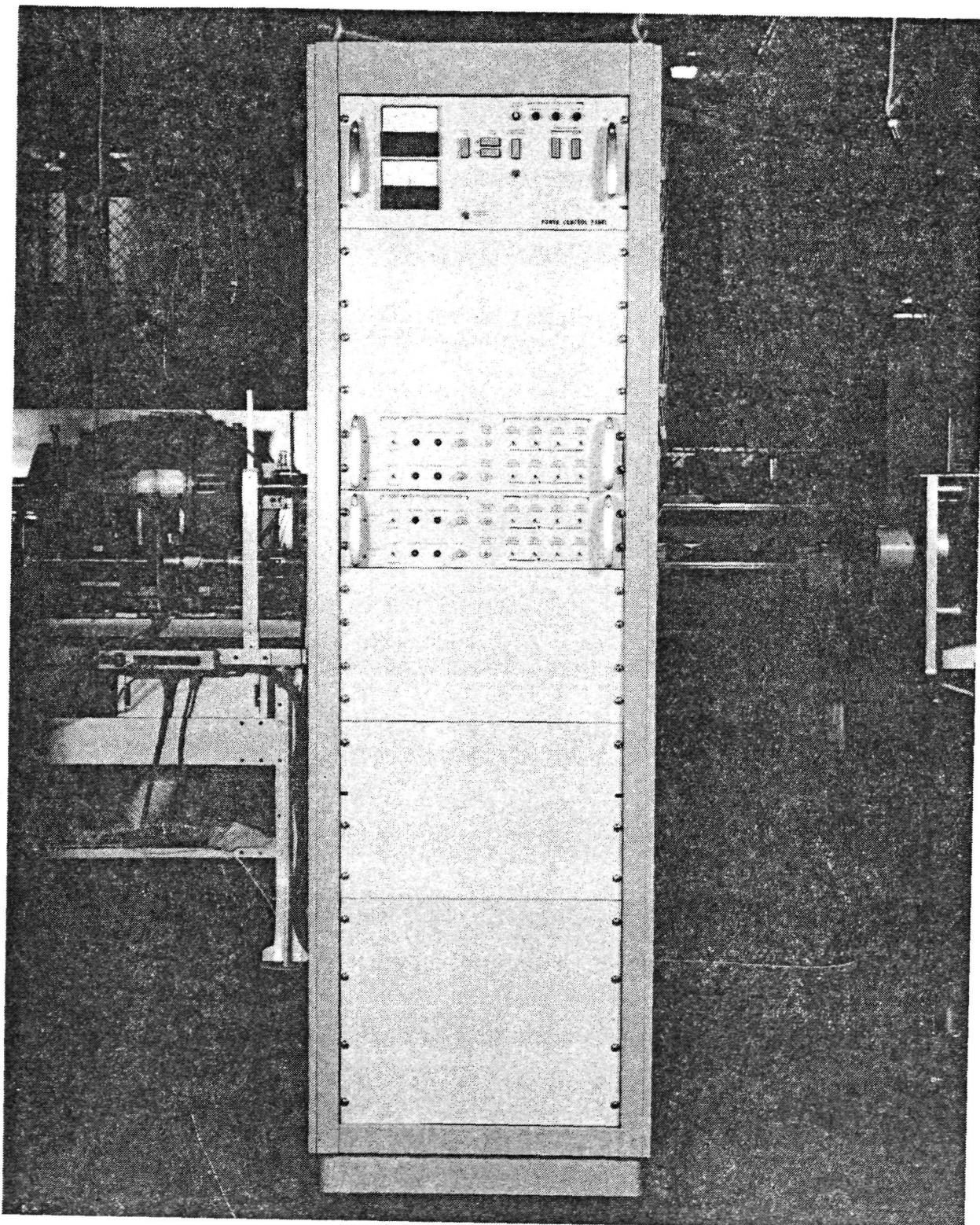


Figure 4-31. Electronics Rack

Figure 4-32 is a close-up view of the power control panel. The power control panel provides the necessary sequencing switches to turn power on or off in the system, displays high voltage on-off and cooling system status, and contains the battery voltage and current meters. Figure 4-33 shows the front panels of the low-level electronics drawers.

The control panels on the front of the low-level electronics drawers allow each channel to be placed in either an active or standby mode, via a two-position toggle switch. Over-current sensing indicators are provided for each channel. The indicators remain illuminated after an over-current condition is detected until reset by means of a momentary push button. A position offset adjustment is also available on the panel (a locking, screwdriver-adjustable potentiometer is used for this purpose). Failure simulation switches are provided for future redundancy management studies, but they are not presently wired into the control circuits.

#### 4.2.3.2 Low-Level Electronics

The low-level electronics (Figures 4-34 through 4-36) consist primarily of dual-in-line packages (DIP's). Where necessary discrete components are mounted on special adapters and plugged into the major assembly. Connections to other parts of the electronics rack are made through connectors on the rear of the drawer. The digital logic is CMOS which operates from a 12 V supply. The low-level analog circuitry operates from  $\pm 12$  V. Figure 4-35 shows one of the circuit boards in the upright position. The connections are wire-wrapped to allow circuit changes to be made easily, and are very convenient for brassboard development. In addition, the wire wrap posts allow ready access to any of the circuit nodes; this is very valuable during system check-out and testing.

#### 4.2.3.3 Power Electronics

The power source used for the power electronics is the same as that described for the Delco Breadboard System (Ref. paragraph 4.1.1). Figures 4-37 through 4-39 show the power electronics drawer. The four power circuits are mounted

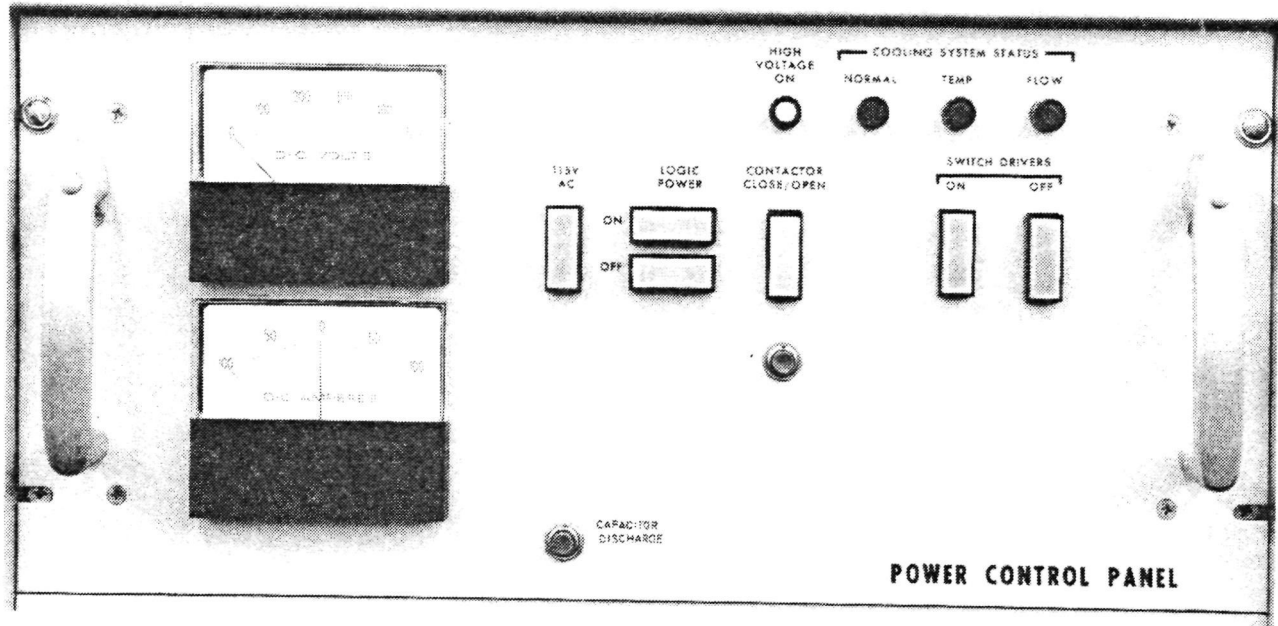


Figure 4-32. Power Control Panel

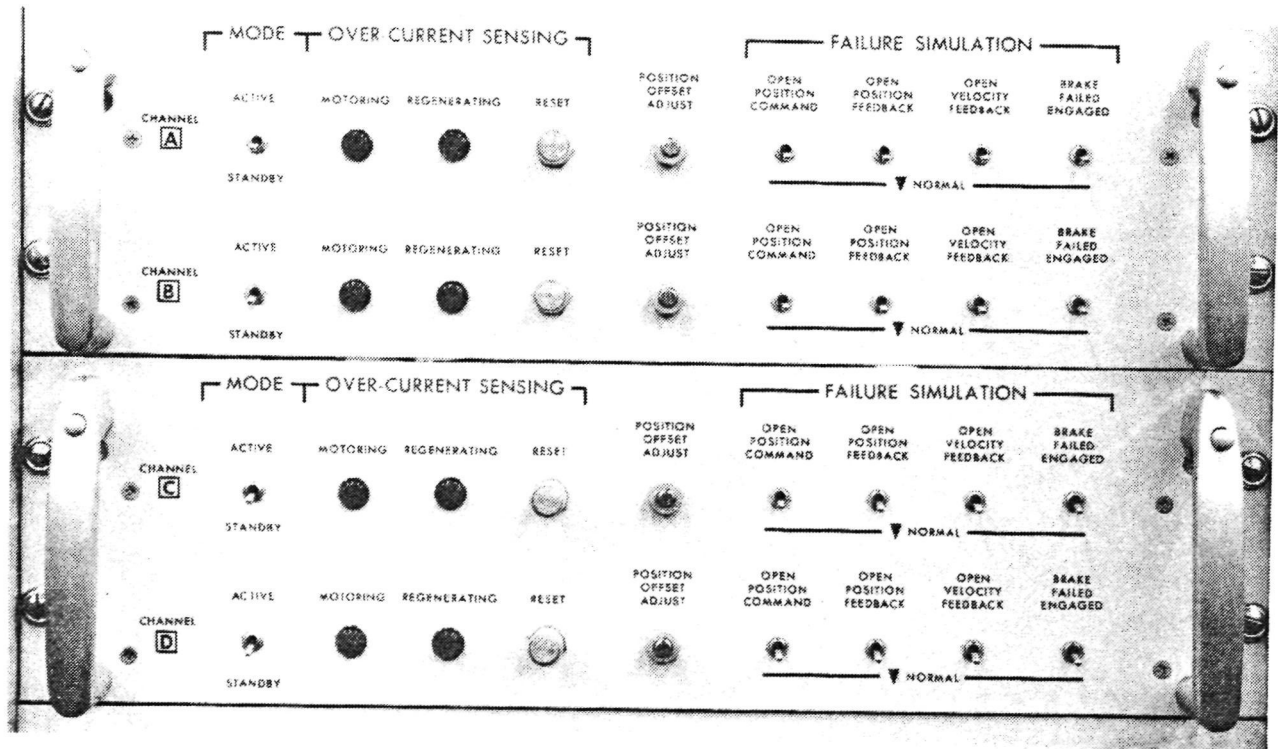


Figure 4-33. Low-Level Electronics Drawer

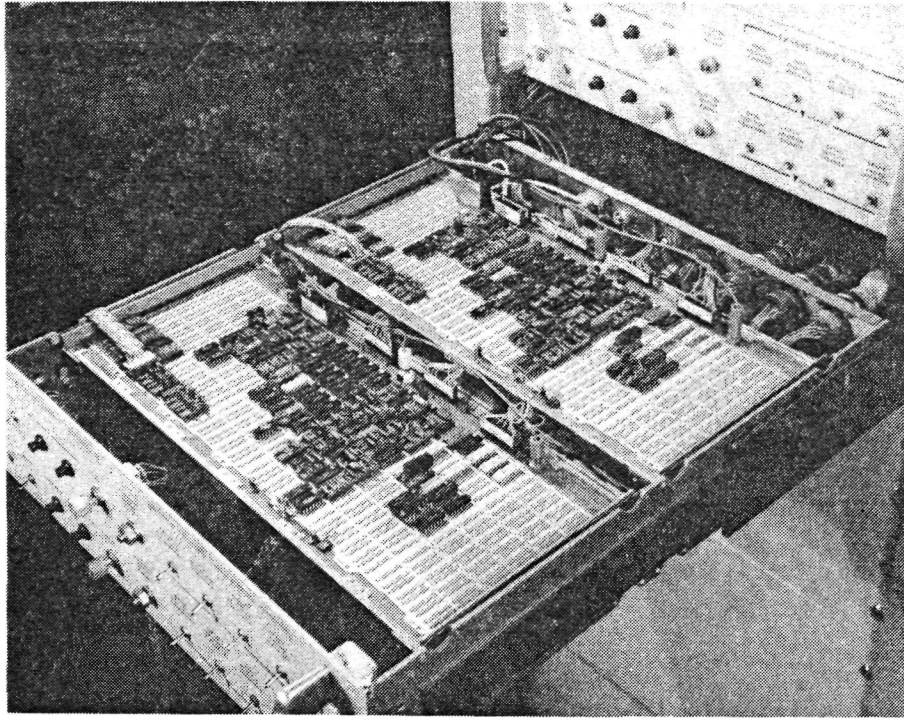


Figure 4-34. Low-Level Electronics Drawer  
(Component Side of Boards)

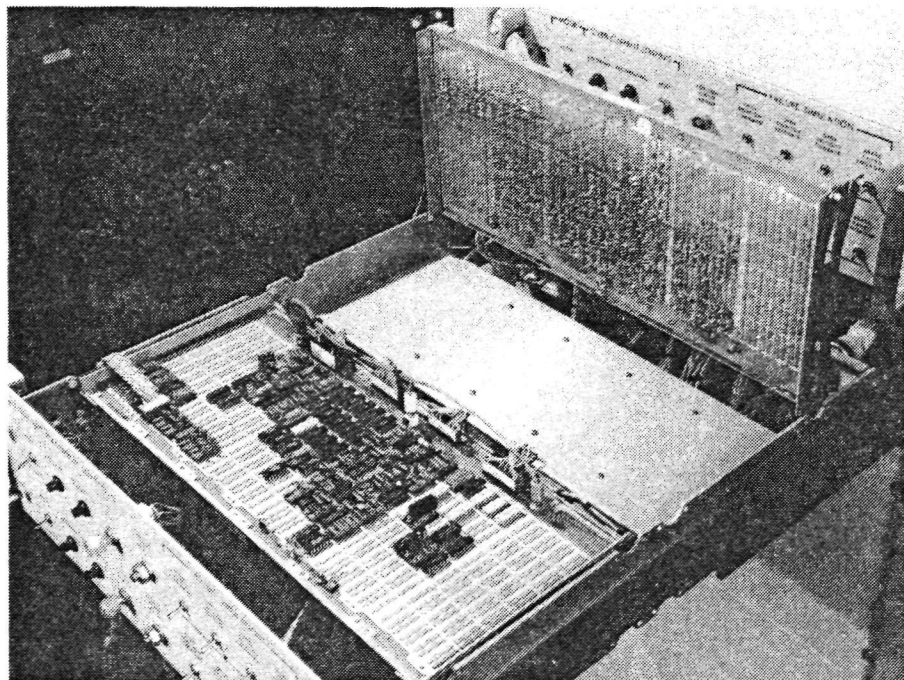


Figure 4-35. Low-Level Electronics Drawer  
(Rear Board Showing Wire-Wrap Side)



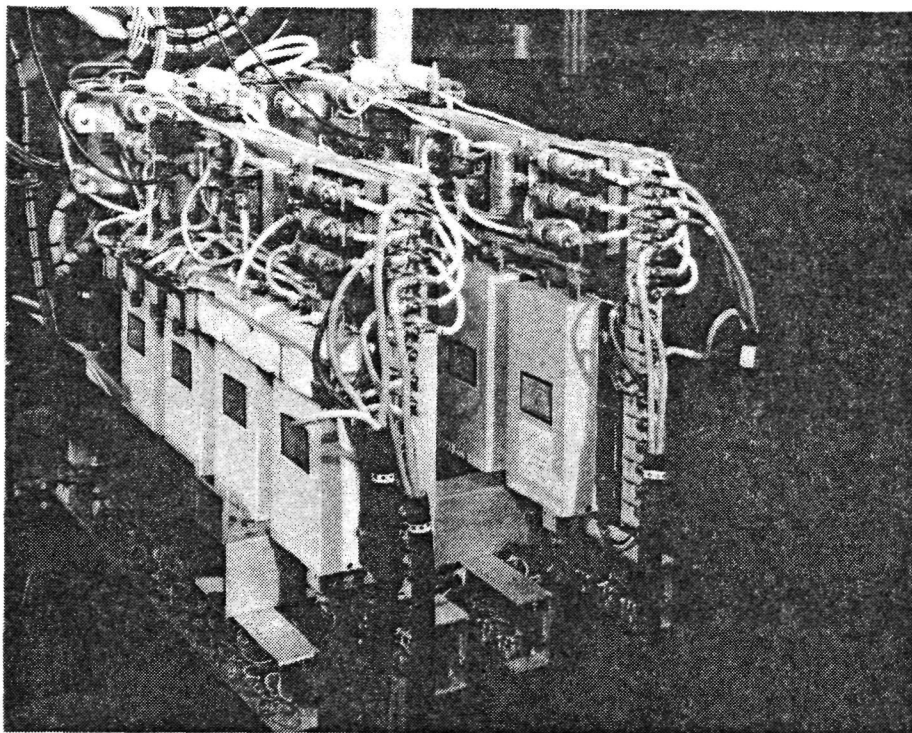


Figure 4-36. Low-Level Electronics Drawer (Rear View)

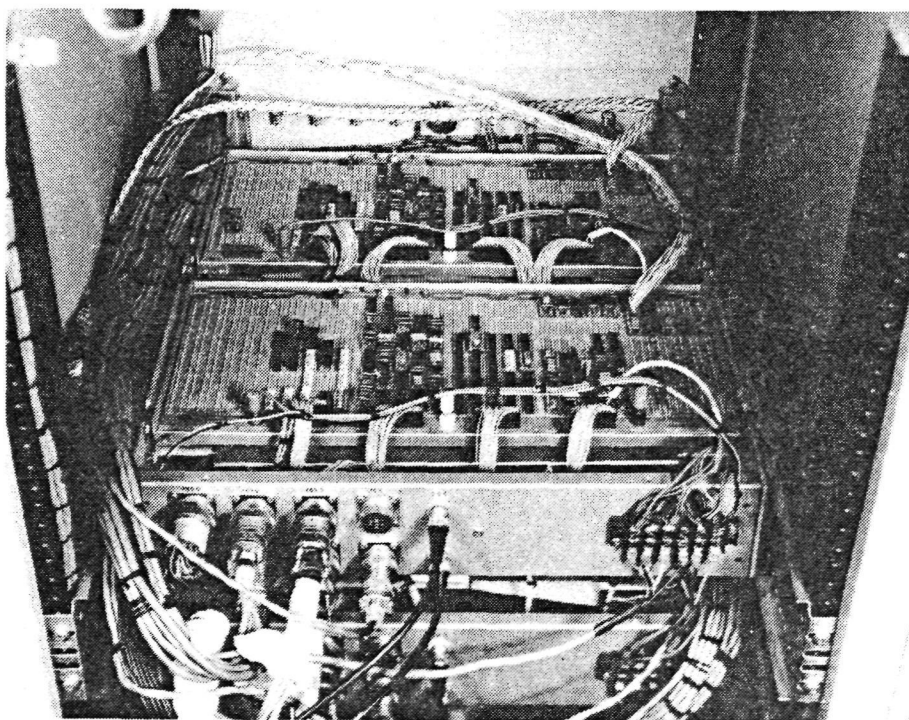


Figure 4-37. Power Electronics Drawer

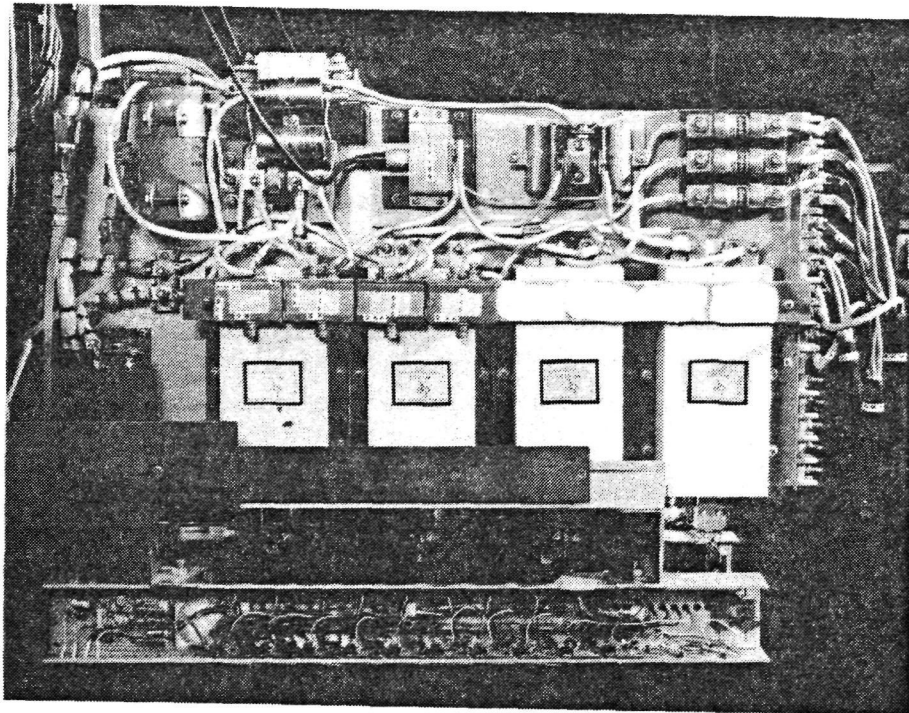


Figure 4-38. Power Electronics Channel A

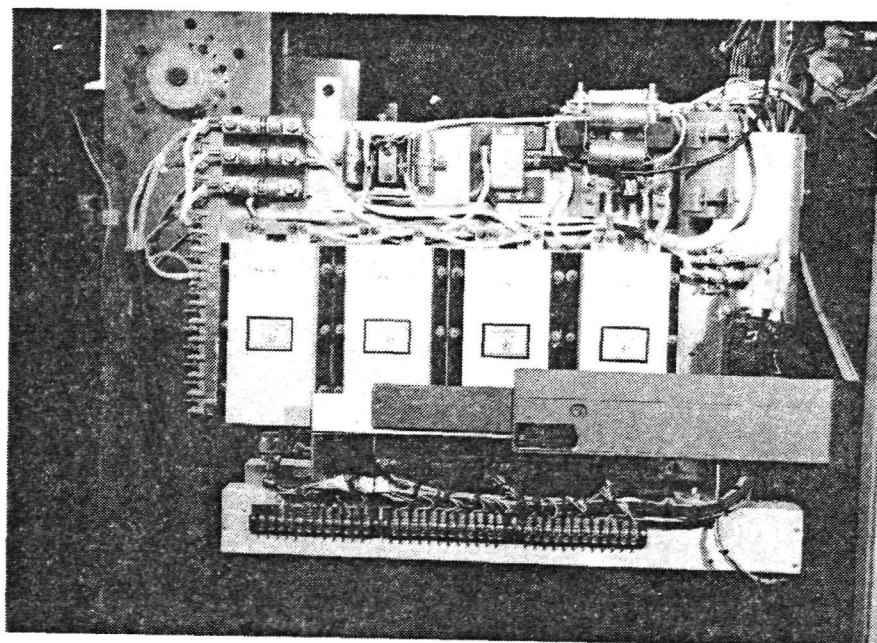


Figure 4-39. Power Electronics Channel D

on two heatsinks. Each of the four power converters uses four power switch assemblies (dual integrated power switches, Texas Instruments, Inc.). Also mounted on the drawer are the inductor, filter capacitors, and the current shunt used to measure the current being sent through the power converter. Fuses for the three motor leads are shown on the upper right-hand corner of the heatsink assembly (Figure 4-38). Liquid cooling lines are brought in at the upper left-hand corner of the assembly and provide coolant flow through the heatsink structure. Although liquid cooling was used in some of the early system tests, all design verification tests were run without liquid cooling, and the heatsink temperature rise was never significant.

The power supplies for the power switches are mounted in the channel shown at the bottom of Figure 4-38. These isolated supplies provide necessary logic power for the power switches.

The dual integrated power switches, rated at 60 A, 390 V, are designed for use in precision power conversion equipment. Typical switching time at rated current is 0.5  $\mu$ s. Each dual switch contains two identical circuits which may be connected together for a single push-pull output or operated as two independent switches. It features optically coupled isolation between input circuitry and power system. Internal circuitry turns off each switch within approximately 2  $\mu$ s if its load is short-circuited. Approximately 2.5 ms after turnoff caused by a short circuit, the switch becomes operational again. Should the short circuit still exist, the switch will turn off again and re-cycle at a frequency of approximately 400 Hz until the short circuit condition is removed. Protection is also provided against overheating; the signal for this condition is fed into a Schmitt trigger which, because of its hysteresis, assures that the temperature recovers by a safe margin before operation resumes.

#### 4.2.4 CABLING

The interconnecting cables are brought into the rear of the electronics rack. Figure 4-40 shows the general cabling arrangement. The 270 Vdc and 115 Vac power cables enter the lower panel. Figure 4-41 is a closer view of this area. The power cables to the EMA motors are terminated on the power electronics



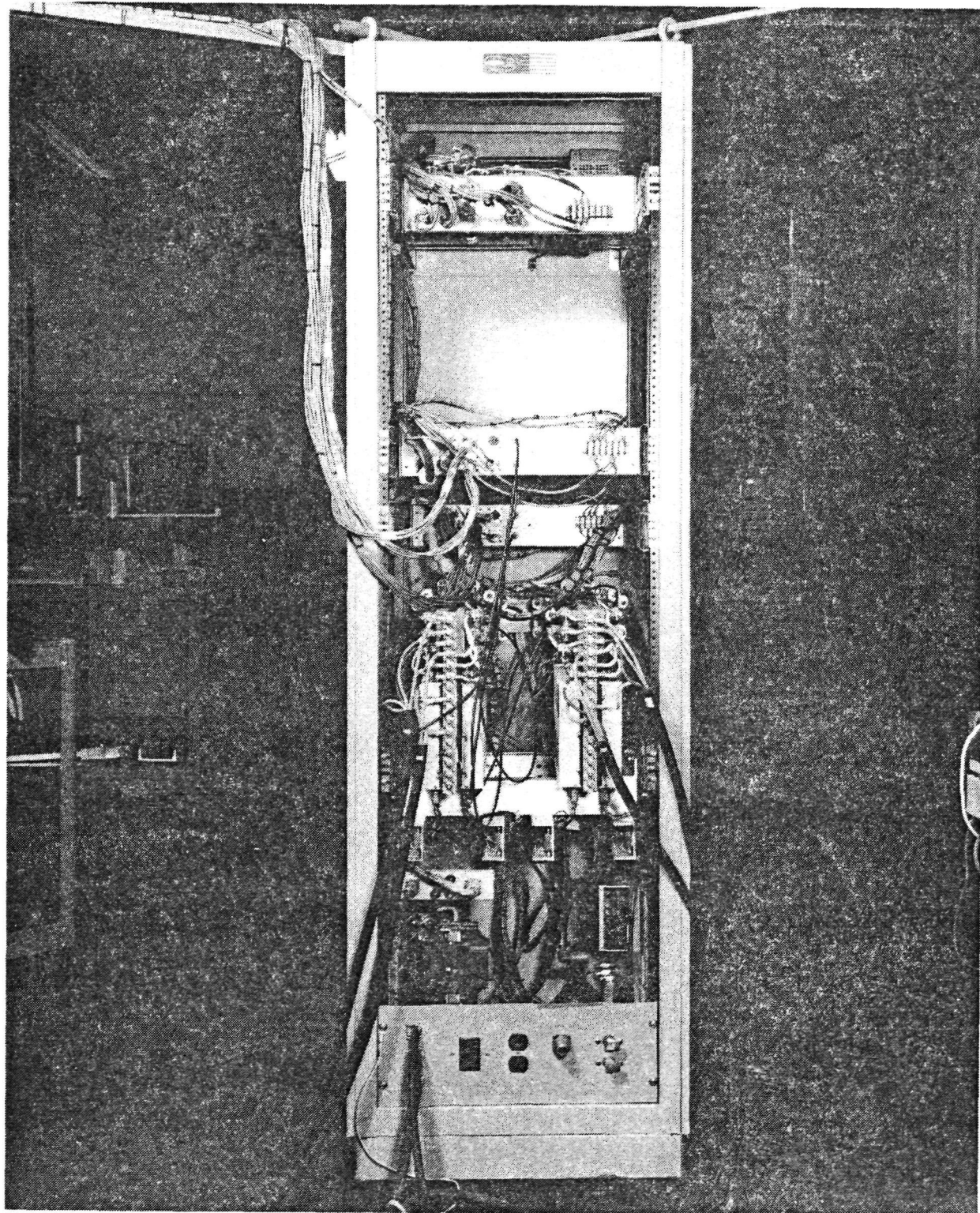


Figure 4-40. Electronics Rack (Rear View)



drawer. Figure 4-42 is a rear view of the top portion of the electronics rack.

#### 4.3 SINGLE-CHANNEL POWER ELECTRONICS BREADBOARD DESCRIPTION

The single-channel power electronics breadboard test set-up is shown in Figure 4-43. The power electronics assembly is on the table in the foreground, along with the three low-level electronics enclosures. Delco's motor/dynamometer stand and Variac-controlled voltage source are in the rear of the lab. During most of the testing the variable-voltage supply was used, rather than the battery bank, because the Variac allowed convenient control of the supply voltage.

A closer view of the power electronics assembly is presented in Figure 4-44. The power transistors are mounted on the heat sinks which are located on the top side of the assembly. Figure 4-45 shows the reverse side of the power electronics assembly. This view shows the power transistor driver circuit cards. Close-up views of this card are presented in Figure 4-46. The power oscillator circuit card assembly is shown in Figure 4-47.

The low-level electronics is contained in the three enclosures shown in Figures 4-48 and 4-49. The middle box contains Delco's rotor position sensor electronics, and the other two boxes control the chopper and inverter power switches. As can be seen in these figures, test jacks are available on the panels, and the RPS panel displays the motor shaft speed, the rotor angle, and the inverter switch drive conditions.

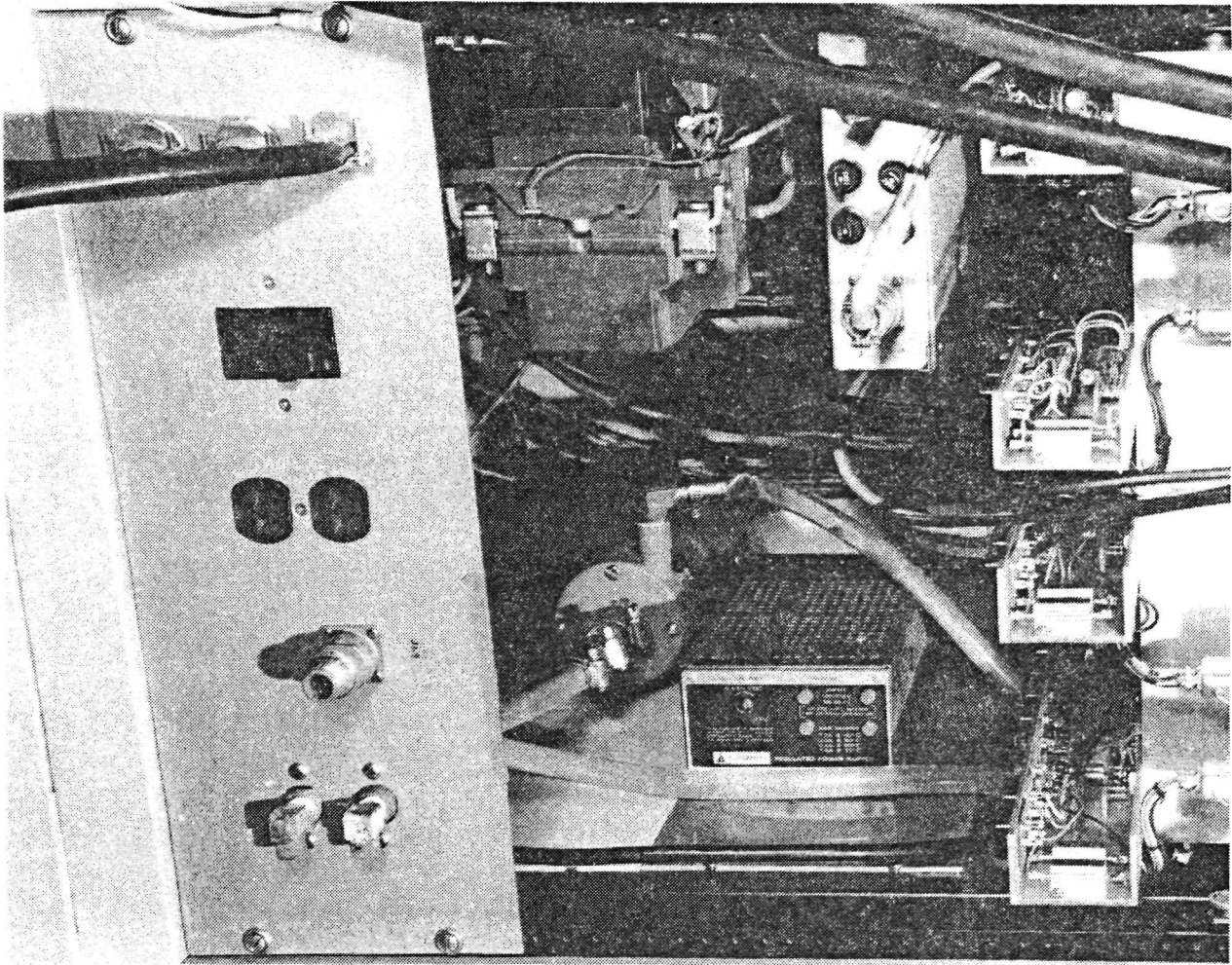


Figure 4-41. Power Entry Panel

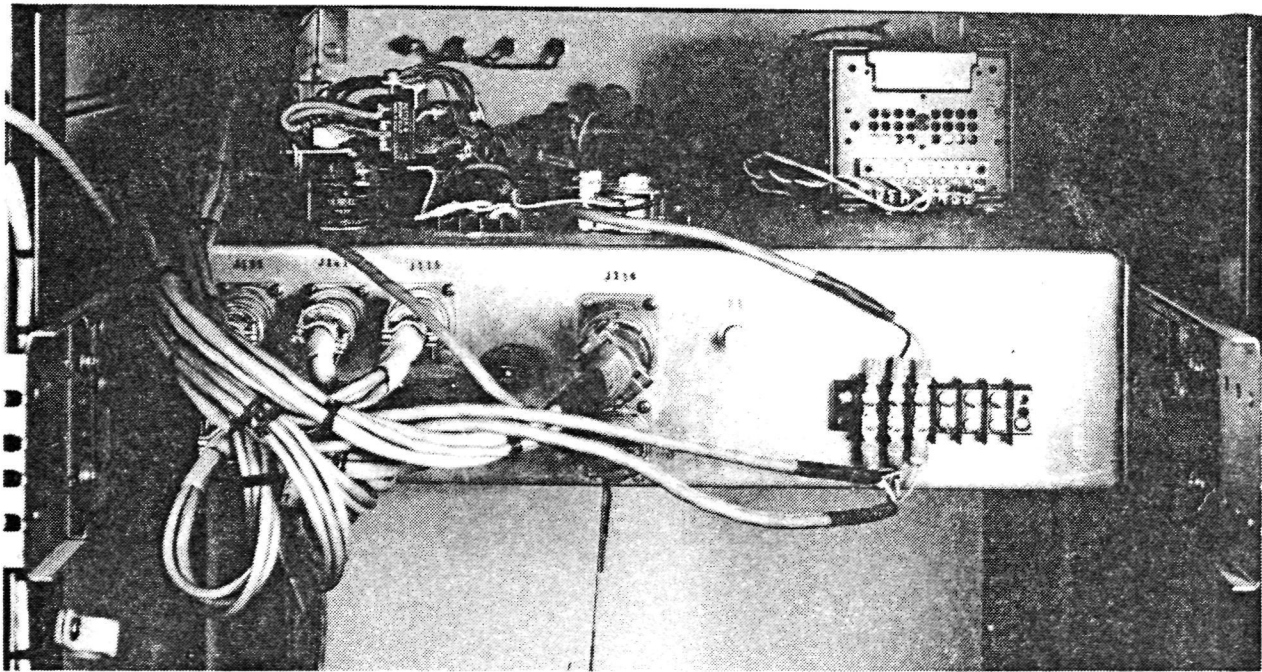


Figure 4-42. Rear View of Top Drawer

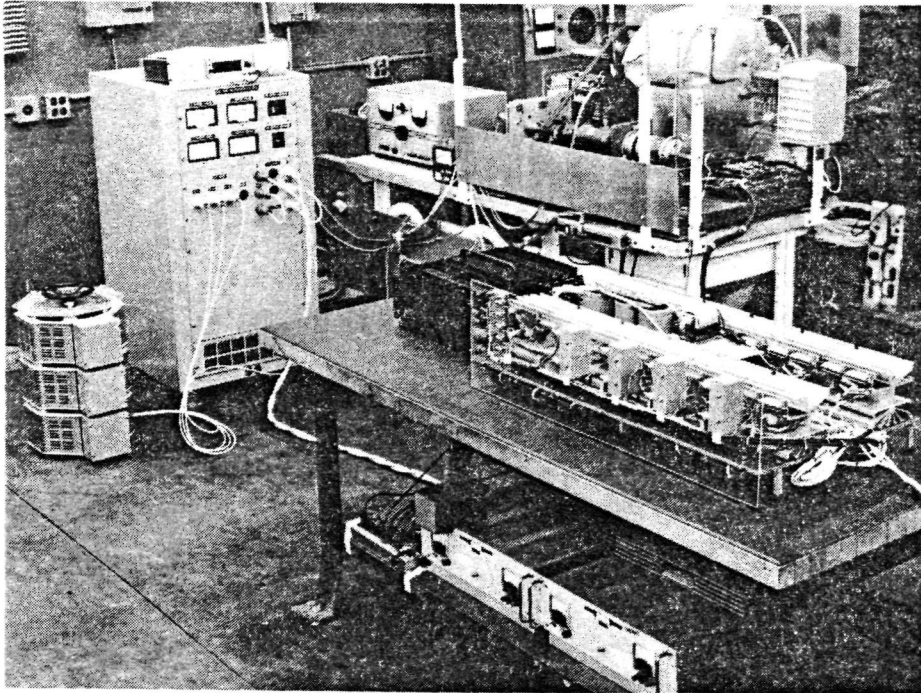


Figure 4-43. Single-Channel Power Electronics Test Setup

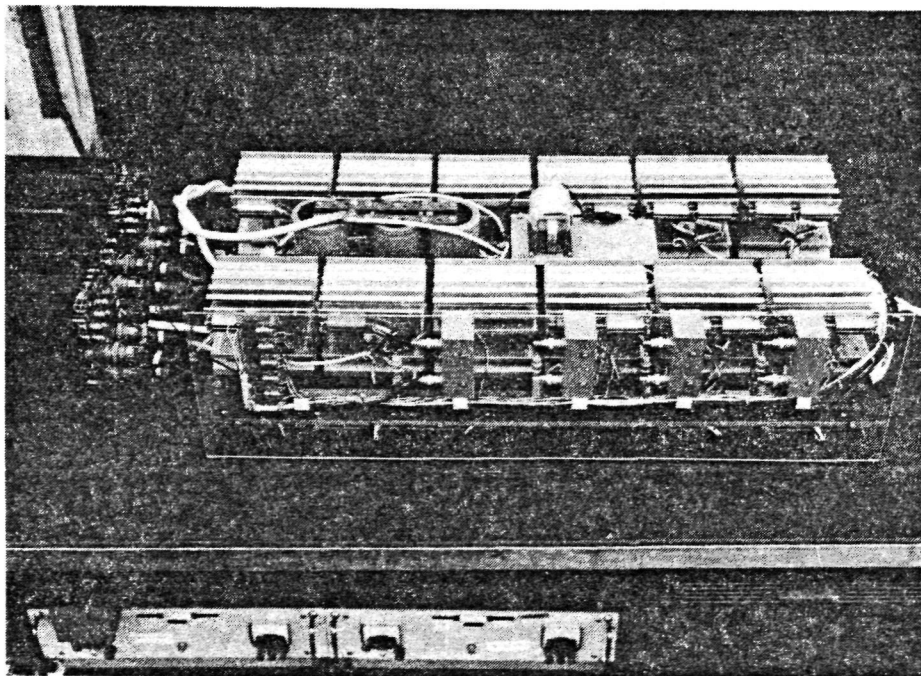


Figure 4-44. Single-Channel Power Electronics Assembly, Power Transistor Side



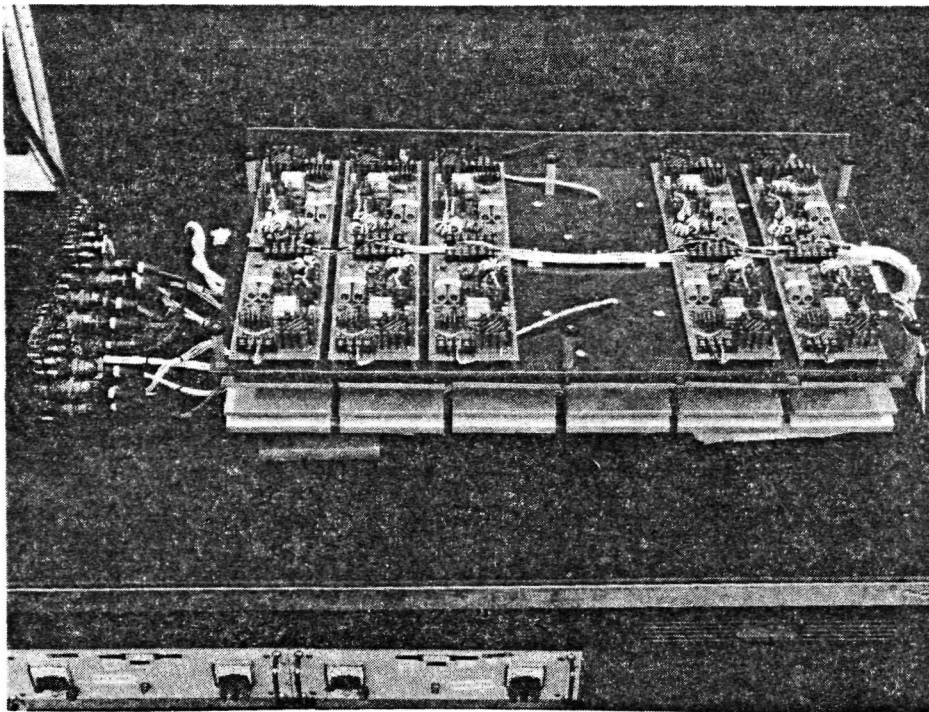


Figure 4-45. Single-Channel Power Electronics Assembly, Driver Side

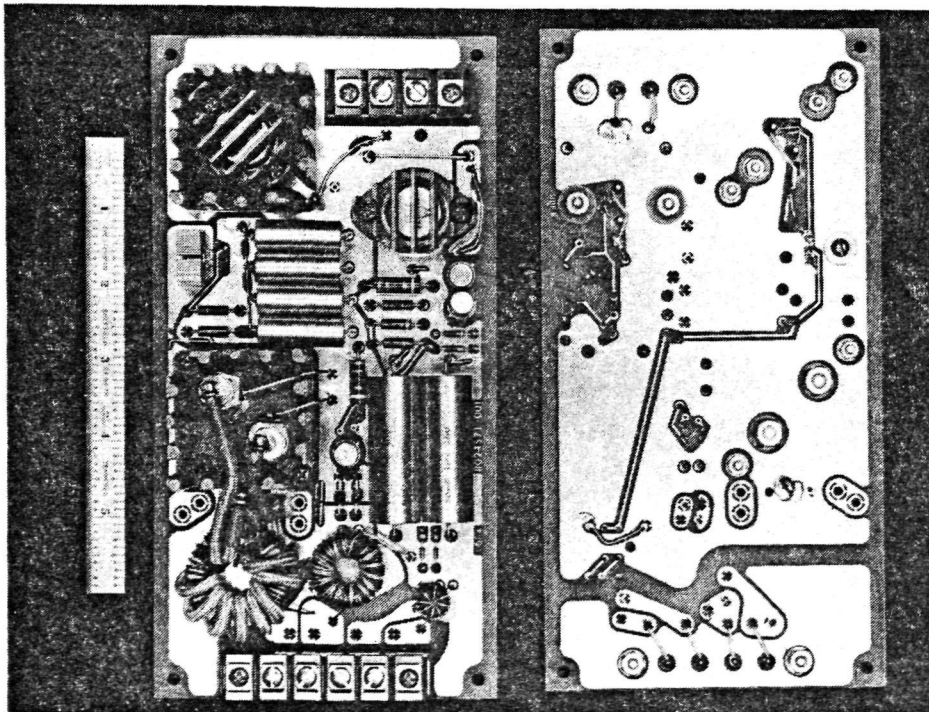


Figure 4-46. Transistor Base Drive Power Output Circuit Card Assembly

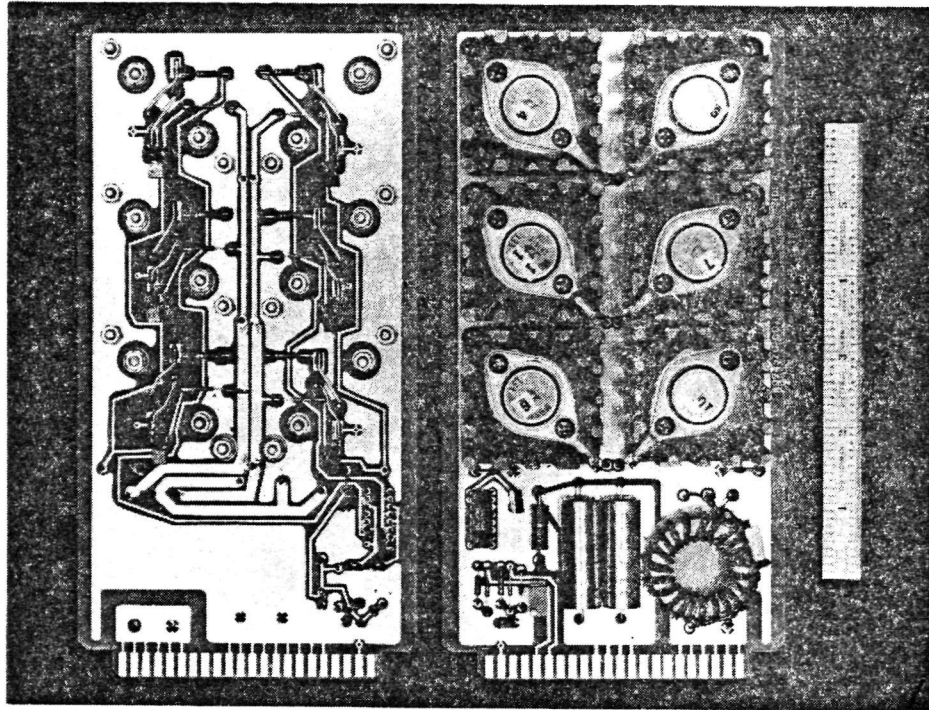


Figure 4-47. Transistor Base Drive Power Oscillator Circuit Card Assembly

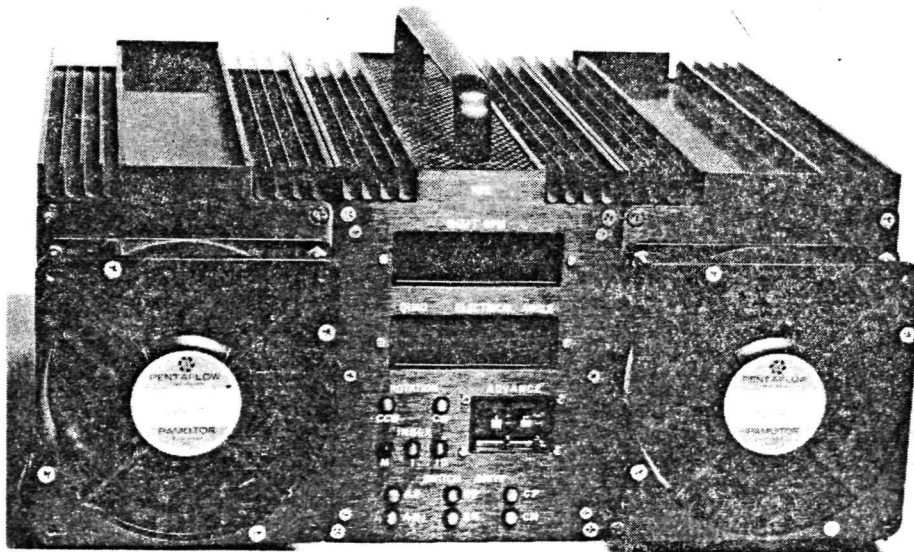


Figure 4-48. Low-Level Electronics Enclosures, Rear View

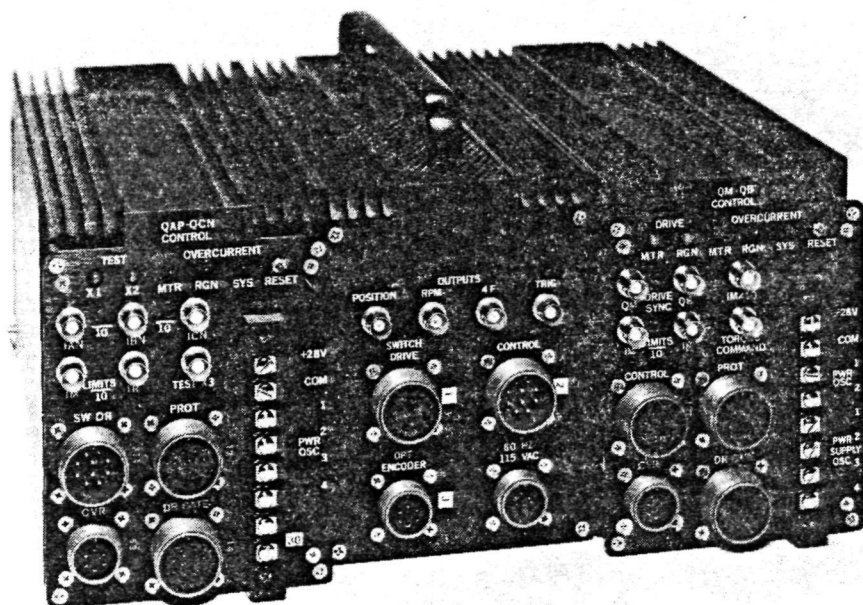


Figure 4-49. Low-Level Electronics Enclosures, Front View

## SECTION V

## EQUIPMENT MECHANIZATION

5.1 FOUR-CHANNEL SYSTEM MECHANIZATION

The electromechanical actuator (EMA) is a positioning servo system, and its output motion is proportional to an input command. An idealized block diagram of a single channel of the EMA is shown in Figure 5-1. Table 5-1 defines the symbols used in this diagram. Both position and velocity feedback are used for control purposes, and the motor is controlled by means of its armature current. In the idealized case, the deflection command is compared with the actual output position to provide a position error. Velocity feedback is also used, and the resulting system error signal is used to provide a motor current command. The idealized current controller forces the motor current to follow the command, resulting in motor output torque. This output torque accelerates the system inertia and produces output motion.

Figure 5-2 is a block diagram showing the actual EMA mechanization. Most of the transfer functions are self-explanatory. The definitions for the symbols used in this system are given in Table 5-1. For convenience in locating the various circuits in the system schematics, reference designations have been included for all major signal outputs. For example, the upper left block in Figure 5-2 with the designation "AMPL D2-1" indicates that the output signal for this amplifier will be found in area D2 of the Augat board on pin 1. The gain adjustment resistor for KE is located in Augat area D3 between pins 11 and 6.

Scaling for the various control signals is also indicated on Figure 5-2. For example, if the current command, ICMD, is 20 A, the signal shown as ICMD/5 would be 4.0 V. The various gains and time constants are easily changed if desired (by replacing resistive or capacitive components).

All of the four channels are mechanized in an identical manner. Whenever two (and only two) channels are in an ACTIVE mode (as established by the ACTIVE/

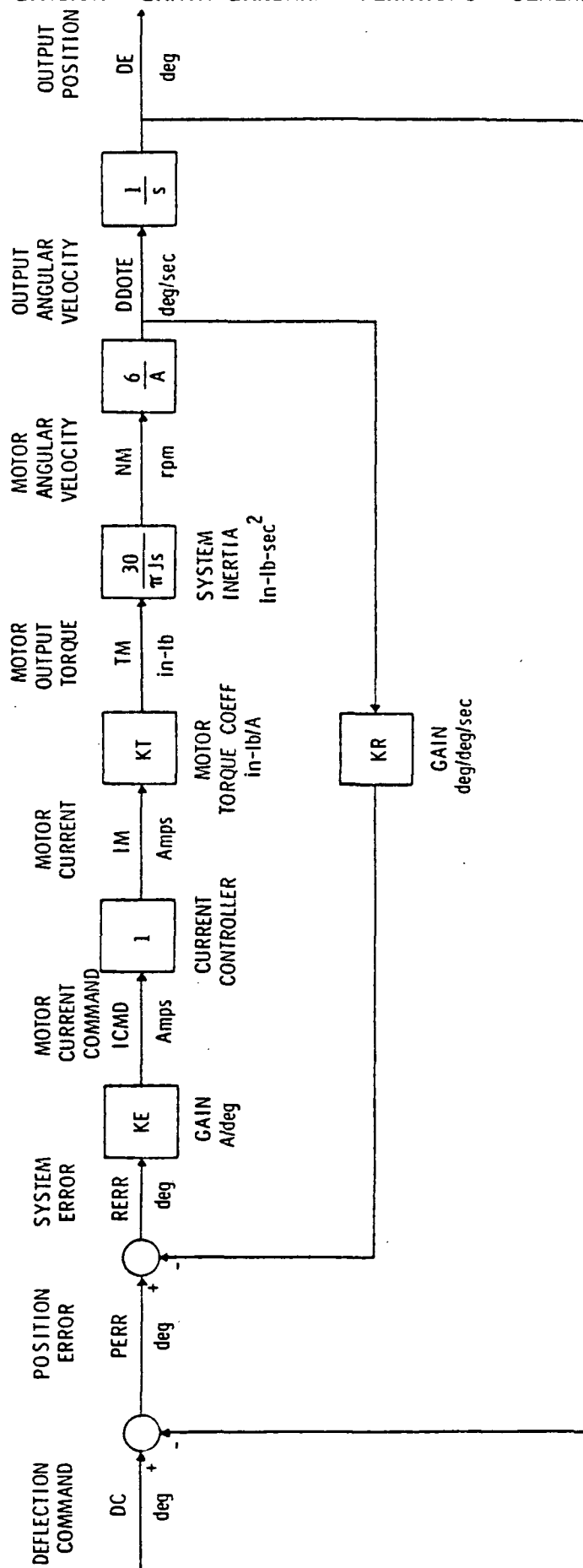


Figure 5-1. Idealized EMA Block Diagram





STANDBY switch located on the front panel of the low-level electronics control drawer), a velocity error correction loop is used to force the two active channels to operate at almost the same velocity. This is accomplished by comparing the velocities of the two active channels (Figure 5-3) to develop an error signal. This signal is passed through a lowpass filter and is then sent back to each of the ACTIVE channels (inverted, if required) where it is combined with the other error signals (position and velocity) to provide a motor current (or torque) command.

<u>SYMBOL</u>	<u>DEFINITION</u>
DC	Load deflection command, deg
PERR	Load position error, deg
DE	Load deflection angle, deg
KE	Gain coefficient, A/deg
KR	Gain coefficient, A/deg/s
ICMD	Current command (prior to limiting), amperes
ICMD1	Current command (after command rate limiting), amperes
ICMDL	Current command (after amplitude limiting), amperes
IMC	Motoring current command, Amperes
$A_1$	Gear ratio, motor-to-load deflection
$A_2$	Gear ratio, position pickoff potentiometer-to-load
IM	Motor current (current into inverter), amperes
DDOTE	Angular velocity of load, deg/s

Table 5-1. Definitions

Although most of the subsystems shown in Figure 5-2 are straightforward, several are somewhat complex, and are therefore discussed in some detail in the following paragraphs.

#### 5.1.1 CURRENT COMMAND RATE LIMITER

The current command rate limiter, shown in block diagram form in Figure 5-4, prevents sudden changes in the commanded control current.

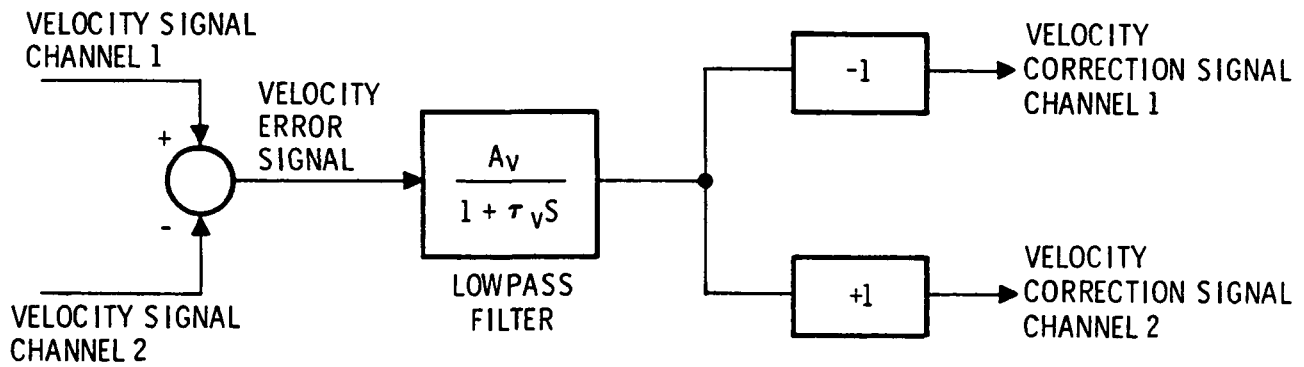


Figure 5-3. Two-Channel Velocity Correction Block Diagram

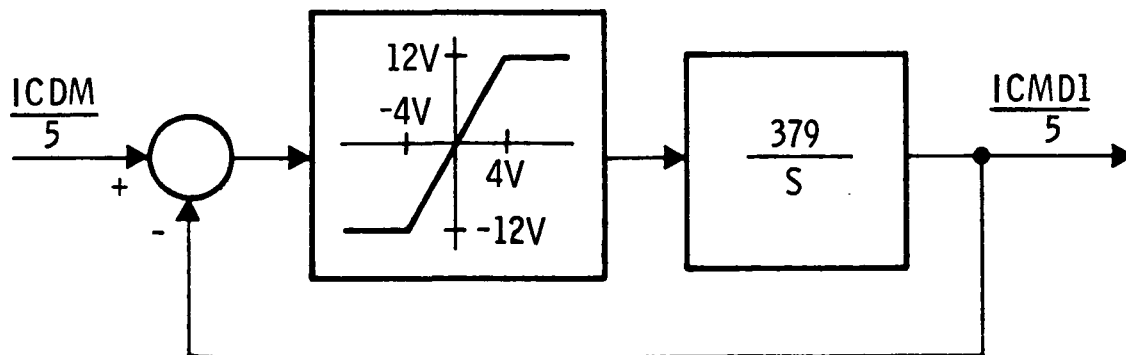


Figure 5-4. Current Command Rate Limiter

When the system is operating in its linear region, its transfer function is

$$\frac{E_{out}}{E_{in}} = \frac{1}{1 + Ts}$$

where  $T = 1/(3) (379) = 0.00088 \text{ s}$

When limiting action takes place (for example, if a sudden large change in current command should occur), the output voltage changes at a rate given by

$$\dot{E}_{out} = 12 \times 379 \text{ V/s} = 4548 \text{ V/s}$$

With the scaling used in this circuit, 1 V represents 5 amperes; therefore, the current command rate limit is

$$\dot{i}_{command} = 5 \times 4548 = 23 \times 10^3 \text{ A/s} = 23 \text{ A/ms}$$

Changes to the current command rate limit or the linear-region time constant are easily made by changing resistor or capacitor values.

#### 5.1.2 POWER CONVERTER CONTROL

The EMA operates in three different modes:

- Motoring
- Plugging
- Regenerating.

These basic operating regions are illustrated in Figure 5-5. In the first quadrant, the torque produced by the machine is in the same direction the rotor is turning, resulting in normal motoring operation. If the motor is operating at low speed in the second quadrant, the motor torque opposes the velocity, and plugging operation results. At higher speeds in the second quadrant, a regenerative braking mode is used during which energy from the system is returned to the battery. Similar modes are indicated in Figure 5-5 for the third and fourth operating quadrants.

The power converter is shown in Figure 5-6. Since it operates somewhat differently in each operating region, it is necessary for the low-level control circuits to establish which region is currently being encountered. This is

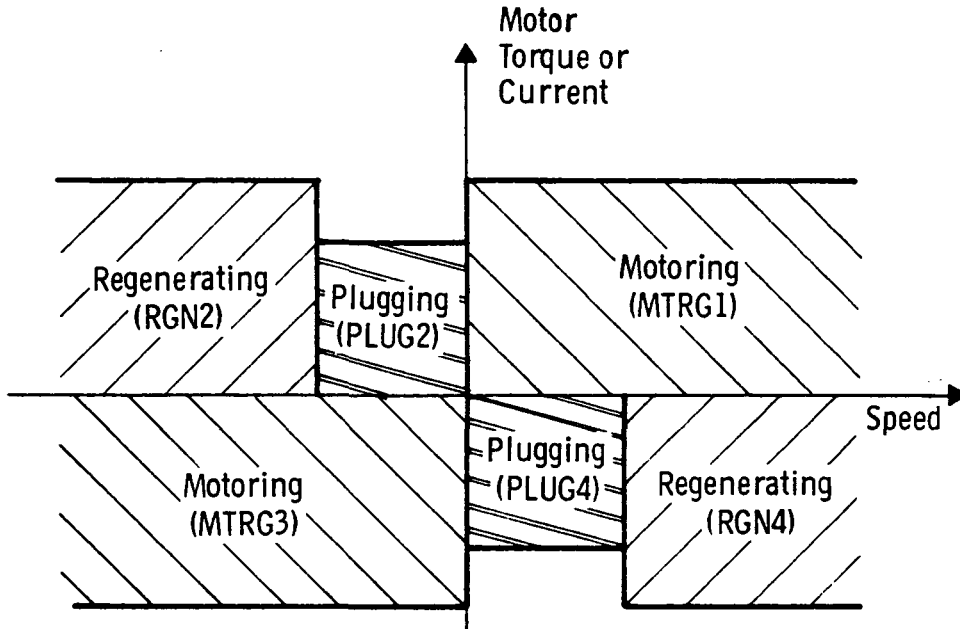


Figure 5-5. EMA Operating Regions

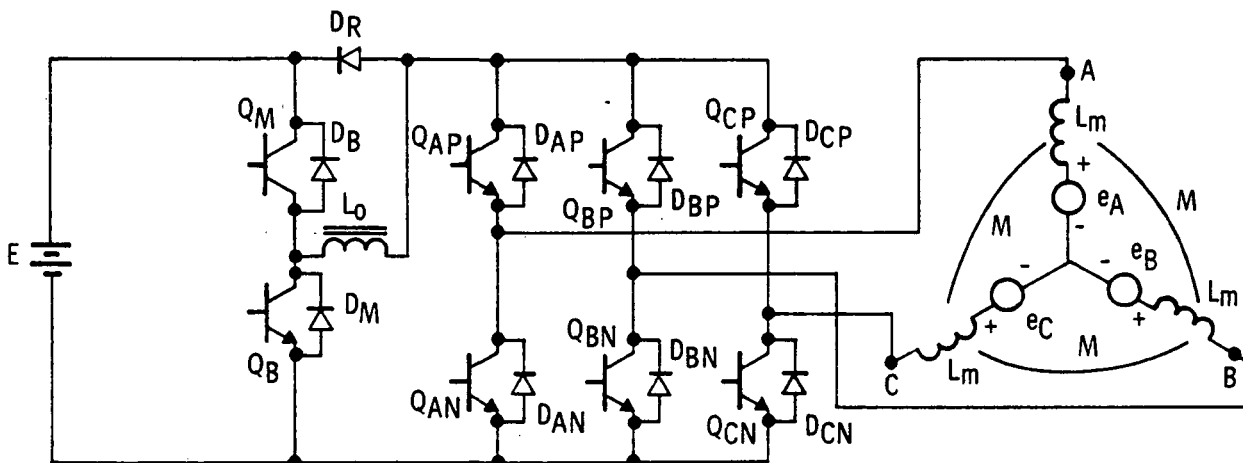


Figure 5-6. Power Converter Schematic

accomplished by comparators which establish which one of the following speed regimes (as illustrated in Figures 5-7 and 5-8) exists:

- SPDHI
- SPDLO
- SPDNEG
- SPDPOS

In addition, the current command is tested by a comparator to establish which of the following regions (Figure 5-9) is active.

- TPOS
- TNEG

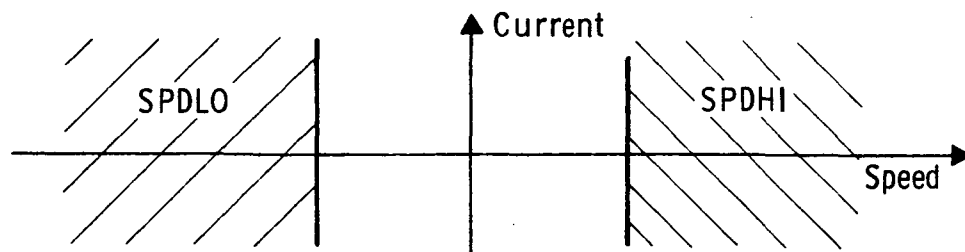


Figure 5-7. SPDHI and SPDLO Conditions

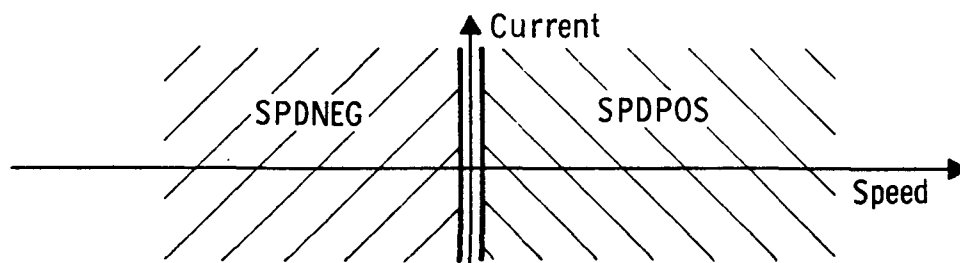


Figure 5-8. SPDPOS and SPDNEG Conditions

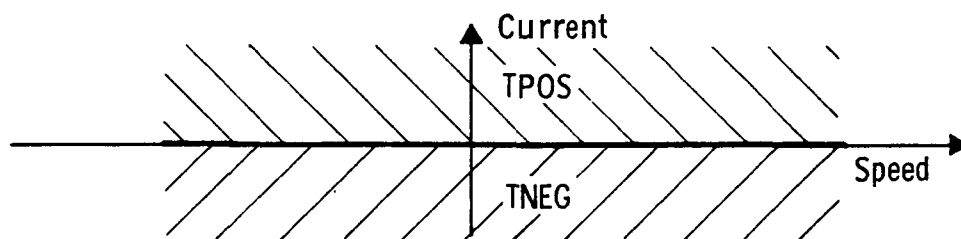


Figure 5-9. TPOS and TNEG Conditions

The regenerative and plugging modes are then determined using the following Boolean relationships:

$$\begin{aligned}
 \text{RGN2} &= \text{TPOS} \cdot \text{SPDLO} \\
 \text{RGN4} &= \overline{\text{TPOS}} \cdot \text{SPDHI} \\
 \text{RGN} &= \text{RGN2} + \text{RGN4} \\
 \text{PLUG2} &= \text{TPOS} \cdot \text{SPDNEG} \cdot \overline{\text{SPDLO}} \\
 \text{PLUG4} &= \overline{\text{TPOS}} \cdot \text{SPDPOS} \cdot \overline{\text{SPDHI}} \\
 \text{PLUG} &= \text{PLUG2} + \text{PLUG4}
 \end{aligned}$$

#### 5.1.2.1 Current Limiting

Two different current limits are used in the EMA. During motoring or regeneration, the motor current is limited to 40 A. However, during plugging, circulating currents occur in the inverter which do not appear in the current source inductor. Therefore, the motor current in the plugging mode is limited to 25 A. These limits were selected to permit the IHTS's to operate well within their current ratings (60 A). The current limiting mode switching is indicated in Figure 5-2. Solid-state analog switches are used to mechanize this subsystem.

#### 5.1.2.2 Chopper Control

In controlling the choppers, comparators are used to determine whether the motor current is greater or less than the commanded value. The motoring transistor comparator is in its high state if the motor current, IM, is less than the commanded value, IMC. In equation form this is related by

$$QMC \geq IM < |IMC|$$

Similarly, the braking transistor comparator is described by

$$QBC \geq IM > -|IMC|$$

A continuous check is also made of the motor current to assure that its magnitude does not become excessive. The equations for these two comparators are

$$IMHI \geq IM > KIH I$$

$$IMLO \geq IM < -KIL O$$

During all of the final EMA system tests, KIH I and KIL O were set at 60 A.

Another comparator is used in initializing the system, and it remains in its high state for about one second after logic power is turned on. Therefore, it is described by

$$INIT \geq TIME < 1 \text{ second}$$

For convenience, all of the relationships describing the comparators are summarized in Table 5-2. Almost all of the comparators (except IMHI and IMLO) have built-in hysteresis to minimize toggling on noise.

Whenever the ACTIVE/STANDBY switch for the channel is in the ACTIVE mode,

LOCATION	HIGH OUTPUT CONDITION	COMMENTS
D18-1	SPDHI $\Rightarrow$ DDOTEX $>$ KSPDHI	Indicates large positive velocity
D18-2	SPDLO $\Rightarrow$ DDOTEX $<$ -KSDPDLO	Indicates large negative velocity
D18-16	SPDNEG $\Rightarrow$ DDOTEX $<$ -KSPDNEG	Indicates negative velocity
D18-15	SPDPOS $\Rightarrow$ DDOTEX $>$ KSPDPOS	Indicates positive velocity
D22-2	TPOS $\Rightarrow$ ICMD1 $>$ 0	Indicates positive torque command
B3-2	QMC $\Rightarrow$ IM $<$  IMC	Turn-on signal for motoring switch, QM
B3-16	QBC $\Rightarrow$ IM $>$ - ICMDL	Turn-on signal for braking switch, QB
B12-16	IMHI $\Rightarrow$ IM $>$ KIH1	Indicates large positive motor current
B12-15	IMLO $\Rightarrow$ IM $<$ - KILO	Indicates large negative motor current
B3-15	INIT $\Rightarrow$ TIME $<$ 1 second	Signal used to initialize logic

Table 5-2. Comparator Outputs



a logic signal called CHANXON will be high. Thus

$$\text{CHANXON} = \text{ACTIVE}$$

If the switch drivers are turned on (using the POWER CONTROL PANEL switch) a logic signal, DRIVEON, will be high.

If a motoring overcurrent is sensed, a flip-flop, labeled IMHIL, is set. Similarly, a regenerative overcurrent will set IMLOL. The overload indicators are reset by

$$\text{IRESET} = \text{RESET} + \text{INIT}$$

where RESET is made high by pressing a momentary push button on the front of the low-level electronics drawer.

A logic signal called IHIX is high whenever an overcurrent occurs, or if the IRESET comparator has not timed out. Thus

$$\text{IHIX} = \text{IMHIL} + \text{IMLOL} + \text{IRESET}$$

If an overcurrent is sensed or if the channel is not active, the brakes for that channel are turned on, hence

$$\text{BRAKEONX} = \overline{\text{CHANXON}} + \text{IHIX}$$

If the brakes are on, or if the switch drivers are not turned on, a signal, SWOFF, will be high. Therefore

$$\text{SWOFF} = \text{BRAKEONX} + \overline{\text{DRIVEON}}$$

All of the inverter switches are turned off if the EMA is in a regenerative mode or if the SWOFF signal is high. Thus

$$\text{QIOFF} = \text{RGN} + \text{SWOFF}$$

The motoring chopper turn-on signal, QMON, is high if

$$\text{QMON} = \text{QMC} \cdot \overline{\text{QIOFF}}$$

Similarly, the braking chopper turn-on signal, QBON, will be high if

$$\text{QBON} = \text{QBC} \cdot \overline{\text{SWOFF}} \cdot \text{RGN}$$

These relationships are summarized in Table 5-3, along with notes which indicate the location and meaning of the various logic signals used in the system.

#### 5.1.2.3 Inverter Control

The inverter section of the power converter (Figure 5-10) consists of switches QAP, QAN, QBP, QBN, QCP, QCN, and their antiparallel diodes. These switches are actuated by signals developed from the rotor position sensor. During motoring or plugging, two switches are on, thus allowing current to flow into one motor winding and out through a second winding. In regeneration, all of the inverter switches are open, but the diodes DAP, DAN, DBP, DBN, DCP, and DCN act as three-phase, full-wave rectifiers for the voltages generated by the machine.

Figure 5-11 shows the idealized rotor position sensor signals and the open-circuit line-to-neutral armature voltage waveforms of the EMA, with the motor moving in the forward direction.

Figure 5-12 shows the idealized rotor position sensor signals and motor currents for both forward and reverse motoring conditions. The inverter switch turn-on conditions can be found to be:

$$\begin{aligned} QAP1 &= \overline{AB}F + \overline{AC}\overline{F} \\ QAN1 &= \overline{AB}F + A\overline{C}\overline{F} \\ QBP1 &= \overline{BC}F + \overline{AB}F \\ QBN1 &= \overline{BC}F + \overline{AB}\overline{F} \\ QCP1 &= \overline{QAP1} \cdot \overline{QBPI} \\ QCN1 &= \overline{QAN1} \cdot \overline{QBN1} \\ QAPON &= QAP1 \cdot \overline{QIOFF} \\ QANON &= QAN1 \cdot \overline{QIOFF} \\ QBPON &= QBN1 \cdot \overline{QIOFF} \\ QBNON &= QBN1 \cdot \overline{QIOFF} \\ QCPON &= QCP1 \cdot \overline{QIOFF} \\ QCNON &= QCN1 \cdot \overline{QIOFF} \end{aligned}$$

where the symbols and notation are those indicated in Table 5-4.

LOCATION	EQUATION	COMMENTS
C13-3	$RGN2 = TPOS \cdot SPDLO$	Regenerative mode, second quadrant
C13-4	$RGN4 = \overline{TPOS} \cdot SPDHI$	Regenerative mode, fourth quadrant
C13-13	$RGN = RGN2 + RGN4$	Regenerative mode
D26-11	$PLUG2 = TPOS \cdot SPDNEG \cdot SPDLO$	Plugging mode, second quadrant
D26-6	$PLUG4 = \overline{TPOS} \cdot SPDPOS \cdot SPDHI$	Plugging mode, fourth quadrant
D26-12	$PLUG = PLUG2 + PLUG4$	Plugging Mode
B7-2	$CHANXON = ACTIVE$	Status of ACTIVE/STANDBY switch (front panel)
G9-2	DRIVEON	Status of DRIVERS ON switch (Power Control Panel)
B15-2	IMHIL	Flip/flop set by IMHI (motoring overcurrent)
B15-9	IMLOL	Flip/flop set by IMLO (regenerative overcurrent)
B1-15	RESET	Status of RESET switch (front panel)
B20-6	$IRESET = RESET + INIT$	Signal to reset overload indicators
B20-10	$IHX = IMHIL + IMLOL + IRESET$	Motor overcurrent condition
B19-12	$BRAKEONX = \overline{CHANXON} + IHX$	Signal to turn brake on
C8-12	$SWOFF + BRAKEONX + \overline{DRIVEON}$	Power converter switch control signal
C9-6	$QIOFF = RGN + SWOFF$	Signal to turn off all inverter switches
C12-2	$QMON = QMC \cdot \overline{QIOFF}$	Signal to turn on motoring chopper switch, QM
C12-4	$QBON = QBC \cdot \overline{SWOFF} \cdot RGN$	Signal to turn on braking chopper switch, QB

Table 5-3. Boolean Equations for EMA Control

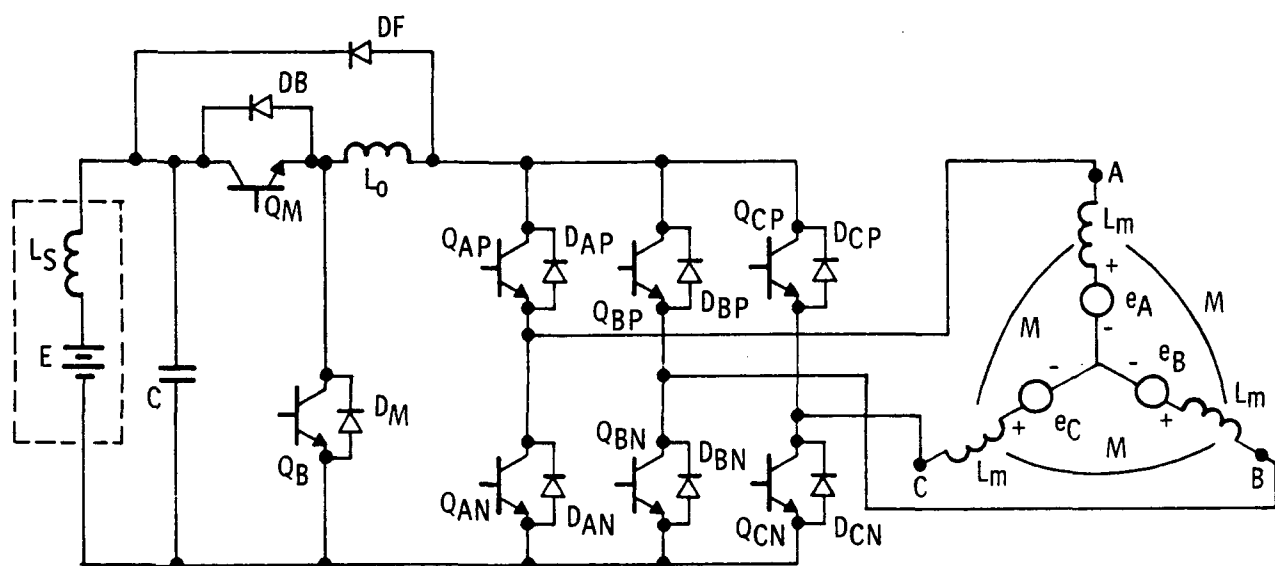


Figure 5-10. Power Electronics Schematic

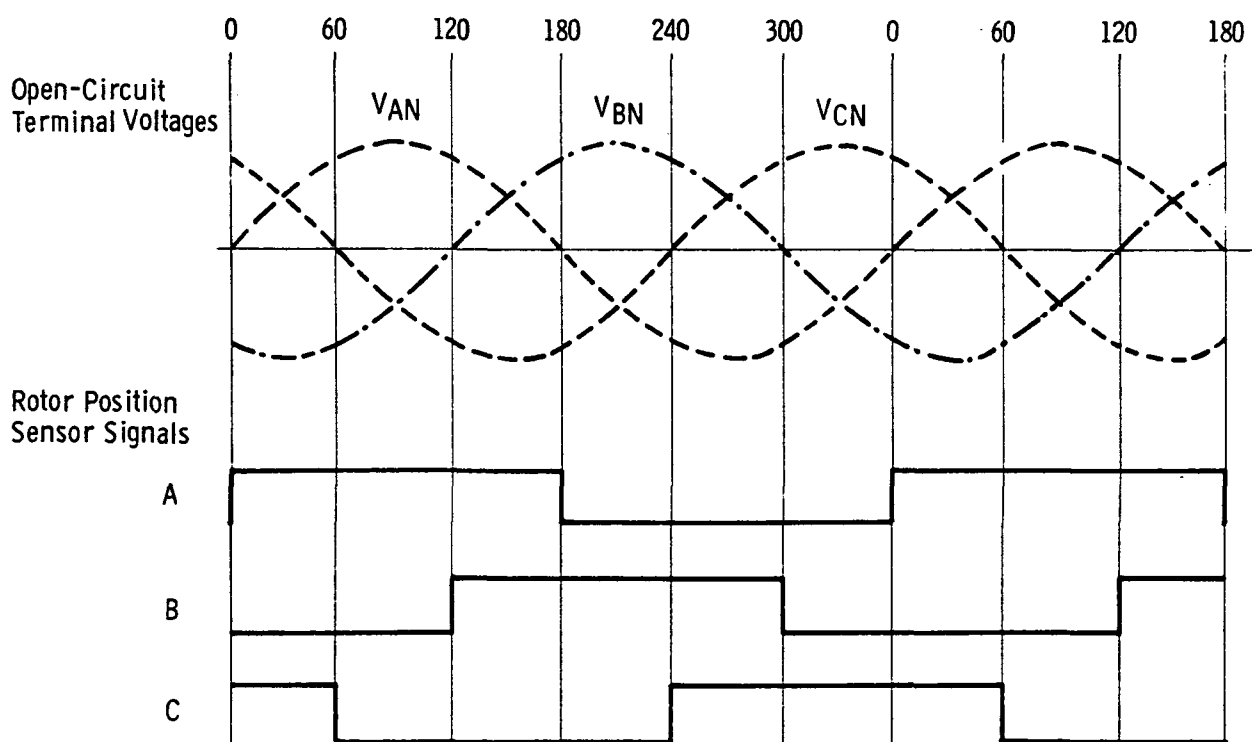


Figure 5-11. Idealized Motor Voltages and Rotor Position Sensor Signals

Mechanical Angle

0 15 30 45 60 75 90

Electrical Angle

0 60 120 180 240 300 0

Rotor Position  
Sensor Signals

A  
B  
C

Motor Currents in  
Forward Direction

I<sub>A</sub>

0

I<sub>B</sub>

0

I<sub>C</sub>

0

Motor Currents in  
Reverse Direction

I<sub>A</sub>

0

I<sub>B</sub>

0

I<sub>C</sub>

0

Figure 5-12. Rotor Position Sensor Signals and Motor Currents

<u>Symbol</u>	<u>Definition</u>
A = RPSA	Rotor position sensor output signal, phase A
B = RPSB	Rotor position sensor output signal, phase B
C = RPSC	Rotor position sensor output signal, phase C
F = TPOS	Foward direction command
QAP1	Signal to turn on transistor QAP
QAN1	Signal to turn on transistor QAN
QBP1	Signal to turn on transistor QBP
QBN1	Signal to turn on transistor QBN
QCP1	Signal to turn on Transistor QCP
QCN1	Signal to turn on transistor QCN
QIOFF	Signal to turn off all inverter transistors
QAPON	Drive signal for transistor QAP
QANON	Drive signal for transistor QAN
QBPON	Drive signal for transistor QBP
QBNON	Drive signal for transistor QBN
QCPON	Drive signal for transistor QCP
QCNON	Drive signal for transistor QCN

Table 5-4. Inverter Logic Signal Definitions

### 5.1.3 LOW-LEVEL ELECTRONICS

Complete schematics for the four-channel EMA are presented in Appendix A. The low-level logic is CMOS which operates from +12 Vdc. The analog circuits use + 12 Vdc. Most of the low-level circuitry is mounted on wire-wrap boards in the control drawers, as was indicated in Paragraph 4.2.3.2.

### 5.1.4 POWER ELECTRONICS

The schematics for the power converter (SK 001228), the brake control system (SK 001230), the isolated power supplies (SK 001229), and the power control system (SK 001227) are also included in Appendix A. Photographs of these subsystems are given in Paragraph 4.2.3.3.

## 5.2 SINGLE-CHANNEL POWER ELECTRONICS BREADBOARD MECHANIZATION

As indicated in Paragraph 3.2, the single-channel power electronics breadboard performs the same function as the power converter for the four-channel system, but is designed to handle substantially larger power output levels. The following paragraphs describe the three major subsystems which form the single-channel power electronics breadboard.

### 5.2.1 HIGH POWER MOTOR DRIVER

The schematic diagram of the motor drive circuit is given in Figure 5-13. The inverter uses six power transistors (QAP, QAN, QBP, QBN, QCP, AND QCN). During motoring, the current through the motoring inductor, LM, is controlled by the two motoring chopper transistors, QM1 and QM2. It is possible to drive QM1 and QM2 in several ways, but in this system they are time-shared, operating alternately. Braking current through LB is controlled by the two braking chopper transistors QB1 and QB2. Noninductive current viewing resistors (CVR's) are used to sense currents IMB, IAN, IBN, and ICN. Motoring and braking control circuits use the signals from these CVR's for control purposes, and the motor phase currents are also instrumented using broadband current transformers TA, TB, and TC.

In mechanizing the power switches, several alternatives were considered. The use of paralleled devices would require that they all turn on and off simultaneously. The required matching of turn-on, storage, and static operating characteristics is very difficult to achieve, thus making it desirable to avoid the use of paralleled devices. The use of Darlington's in parallel creates further problems, because the input stage must absorb most of the high energy associated with turn-off if the device is operated in a saturated mode. For these reasons, it was clear that the use of a single, large-geometry device was most desirable in mechanizing the power switch. Three very different large-geometry devices were tested for use in this application, and the results summarized in EE-22T-EMA-022 (Appendix K). Of the three devices tested, two were found suitable for the EMA switching. However, the Westinghouse D60T type transistor was selected because its characteristics were slightly better than the other device for the EMA application.





### 5.2.2 BASE DRIVER POWER SUPPLY

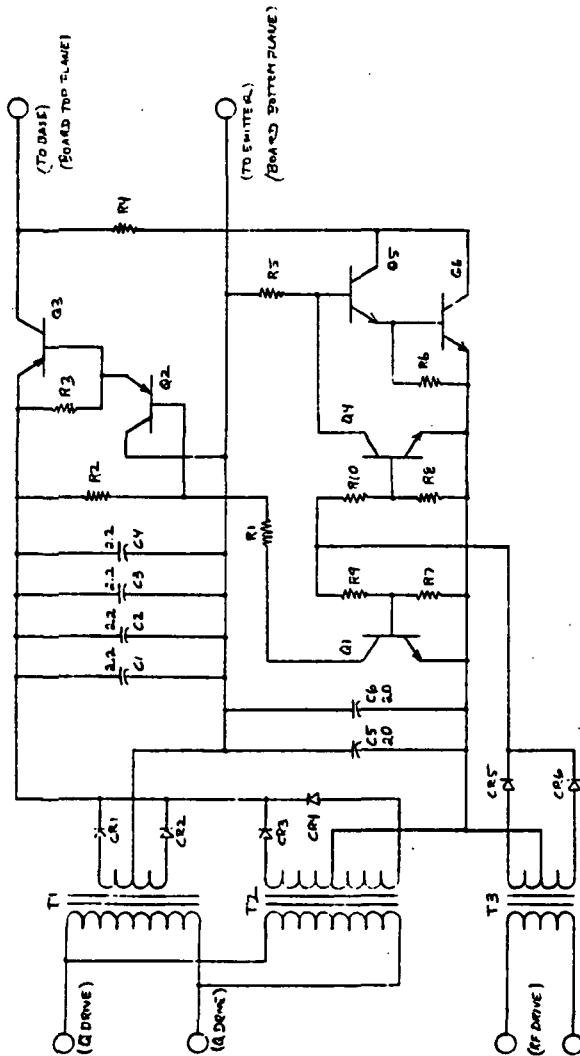
The schematic diagram of the base driver power supply is given in Figure 5-14. The output of the circuit is a 250 kHz square wave (QDRIVE AND  $\overline{\text{QDRIVE}}$ ) which is used to control the currents in the base driver circuit (described in the next paragraph). The output is transformer-coupled through T1. The primary of T1 is center-tapped, and this point is connected to the 28 Vdc supply. In operation, the two ends of T1's primary are alternately grounded by the power FET's. Q1 through Q3 operate in parallel to drive one side of T1, while Q4 through Q6 drive the other side of T1. The FET's are excellent devices for this application, since they are easily driven by CMOS logic buffers, are very fast, and tend to act as a current source when operating under heavy loads. The hex buffer U1 drives the FET's, and the amount of drive which is provided is controlled by potentiometer R8. Zener diodes CR7 and CR8 assure that the drain voltages on the FET's cannot exceed 75 V. Diodes CR10 and CR11 assure that the logic signals driving the hex buffer U1 do not exceed safe input limits for U1. The input control signals (QIN and  $\overline{\text{QIN}}$ ) are square waves with an exact 50% duty cycle established by counting down a higher frequency waveform.

### 5.2.3 BASE DRIVER CIRCUIT

The schematic diagram of the base driver circuit is given in Figure 5-15. This circuit uses the QDRIVE and  $\overline{\text{QDRIVE}}$  signals from the base driver power supply, and an RF drive signal for control. The RF drive signal is a 500 kHz waveform, synchronous with the 250 Hz QDRIVE waveform. When the RF drive signal is present, the base driver turns on the power transistor it controls. When the RF drive signal is absent, the base driver turns the power transistor off.

The QDRIVE waveforms are coupled into the circuit through transformers T1 and T2. The rectified outputs of these transformers result in a nominal 4 V across capacitors C1 through C4, and 10 V across C5 and C6. When the RF drive signal is present, transistors Q1 and Q4 are turned on. The turn-on of Q1 results in Q2 and Q3 being turned on, thus placing a positive voltage on the base of the power transistor which is being driven by the circuit. While the RF drive signal is present, Q4 is on, and Q5 and Q6 are off. When the RF drive





PARTS LIST

C1-C4	6.2M/30VDC, K12A225KSC, CRC
C5, C6	20M/30VDC, M12A206KSC, CRC
C1, C2	1N5831, SCHOTTKY RECT, MOTOROLA, 10-32 STD
C3, C4	1N8077, SUPER FAST REC. SE RECT., SENTERN
Q1, Q4, Q5	2N5320, PNP, TO-5, RCA
Q2	2N5333, PNP, TO-5, TI
Q3	2N6377, PNP, TO-3, MOTOROLA
Q6	2N6274, NPN, TO-3, MOTOROLA
R1, R5	330, 1W, 5%, CARBON RESISTOR
R2, R3, R6	75, 1/2W, 5%, " "
R4	200, 1/4W, 5%, CARBON RESISTOR
R7, R8	1K, 1/2W, 5%, " "
R9, R10	1K, 1/2W, 5%, " "

NOTES

- T1 IS DELCO DESIGN XT77005
- T2 IS DELCO DESIGN XT77006
- T3 IS DELCO DESIGN XT77007
- C1, C2, C3, C4 MOUNTED WITH ANAM 436-435 HEATSINK
- Q1, Q2 MOUNTED WITH ANAM 436-435 HEATSINK
- Q3 MOUNTED WITH ANAM 436-435 TO3 AND ANAM 435 HEATSINK
- Q6 MOUNTED WITH ANAM 435 HEATSINK
- AND WAFIELD 177-3-62 B.O. INSULATOR
- USE HEATSINK THERMAL COMPOUND IN MOUNTING C1, C2, C3, Q3, AND Q6

CONSTRUCT 12 BOARDS  
PCB DESIGNATION - ALL DRIVER

DELCO ELECTRONICS		GENERAL MOTORS CORPORATION, SANTA BARBARA CALIF.	
NASA 4.6 V DRIVER BASE DRIVER -		DRIVER OUTPUT (10 REQUIRED)	
SC-EMATIC DIAGRAM		REV	
DATE	3/6/72	SCALE	1 OF 1
DESIGNED BY	W. J. H. H.	CHECKED BY	W. J. H. H.
APPROVED BY	W. J. H. H.	DATE	3/6/72
SIZE	13160	SCALE	1 OF 1
REV	1	DATE	3/6/72

Figure 5-15. Base Driver Circuit

signal is removed, Q4 turns off, and Q5 and Q6 are turned on. This causes the base of the power transistor to be about -10 V with respect to its base, thus turning it off.

The driver provides excellent control of the power transistor. At turn-on, the base-emitter voltage rises very quickly, and the base current rises rapidly. After turn-on, the driver maintains a base current into the power transistor of about 15 A to assure that the power transistor remains conductive. At turn-off, the base is rapidly driven to -10 V, and base charge is quickly removed to minimize turn-off time. Diodes CR1 and CR2 provide the base drive current during the "on" state. Schottky rectifiers have been selected for this application to minimize circuit losses.

## SECTION VI

### ANALYTICAL STUDIES

#### 6.1 INTRODUCTION

Various analyses were conducted to obtain a clearer understanding of the EMA and help finalize its design. These analyses covered both linear and nonlinear servos (on both single- and two-channel systems), the chopper circuits, and analytical studies of the commutation transients. These analyses are summarized in the following paragraphs.

#### 6.2 SERVO ANALYSES

##### 6.2.1 SIMPLIFIED SINGLE-CHANNEL ANALYSES

##### 6.2.1.1 Simplified Linear Servo Analysis

A simplified, linearized block diagram of the EMA is given in Figure 6-1. Although this diagram ignores all system lags other than those associated with the motor/current source, it is very useful for analyzing the affects of major system gains, inertias, and gear ratios. In the diagram,  $\delta_o$ , is the output motion of the load (degrees),  $\omega_o$  is the angular velocity of the load (degrees/second),  $N_M$  is the motor angular velocity (r/min),  $T_M$  is the motor torque (inch-lb),  $I_A$  is the motor armature current (amperes), and  $I_c$  is the commanded armature current (amperes). The commanded load deflection,  $\delta_c$  (degrees) is compared with the actual load deflection,  $\delta_o$ , and the error signal is amplified (with gain  $K_E$ ) to provide control signal E. The velocity feedback signal, V, is subtracted from E to form the current command,  $I_c$ . For this analysis, the current source and motor effects are represented by a single first-order lag with time constant  $\tau$  (seconds). The motor torque coefficient,  $K_T$  (in-lb/A), converts the armature current to a torque which is applied to the inertia of the system,  $J$  (in-lb-s<sup>2</sup>), reflected to the motor shaft. The integrated acceleration (with appropriate scaling) results in a motor r/min,  $N_M$ . The gear ratio,  $a$ , (and proper scale factor) converts the motor angular velocity to load angular velocity. This is integrated to obtain the output (load) deflection,  $\delta_o$ .

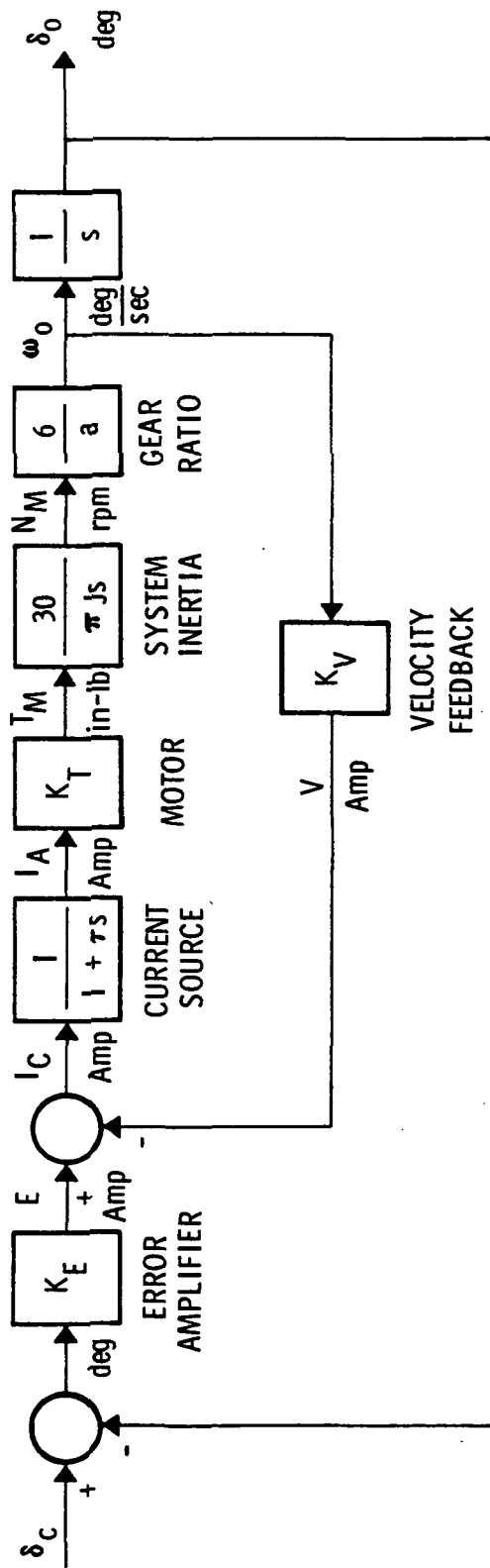


Figure 6-1. EMA Actuator Block Diagram

$K_E$  Amp/deg  
 $\tau$  sec  
 $K_T$  in-lb / Amp  
 $J$  in-lb-sec<sup>2</sup>  
 $a$  dimensionless  
 $K_V$  Amp / deg / sec

$$K_I = \frac{180 K_T}{\pi J a}$$

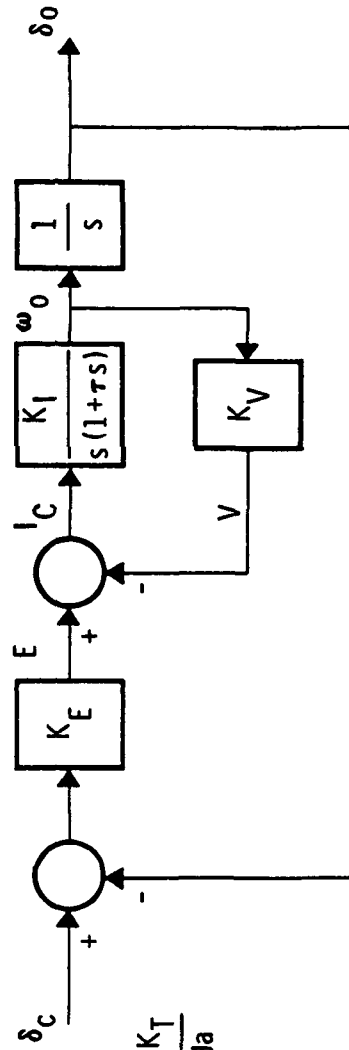


Figure 6-2. EMA Simplified Block Diagram



For convenience, let

$$K_1 = \frac{180 K_T}{\pi J a} \quad (6-1)$$

The system block diagram can then be simplified to that shown in Figure 6-2.

#### 6.2.1.1.1 Inner Loop Transfer Function

From an analysis of the simplified system diagram, the inner loop transfer function is found to be:

$$\frac{\omega_o}{E} = \frac{\frac{K_1}{\tau}}{s^2 + \frac{1}{\tau}s + \frac{K_1 K_v}{\tau}} \quad (6-2)$$

$$= \frac{\frac{1}{K_v}}{1 + \frac{s}{K_1 K_v} + \frac{\tau s^2}{K_1 K_v}} \quad (6-3)$$

A root locus plot for this loop is given in Figure 6-3. For gains such that

$$K_1 K_v \leq 1/4\tau \quad (6-4)$$

it can be seen that the loop has two real poles. For higher gains, the loop has complex poles.

The natural frequency of the inner loop is

$$\omega_n = \sqrt{K_1 K_v / \tau} \quad (\text{rad/s}) \quad (6-5)$$

and its damping ratio is

$$\zeta = \frac{1}{2\tau\omega_n} \quad (6-6)$$

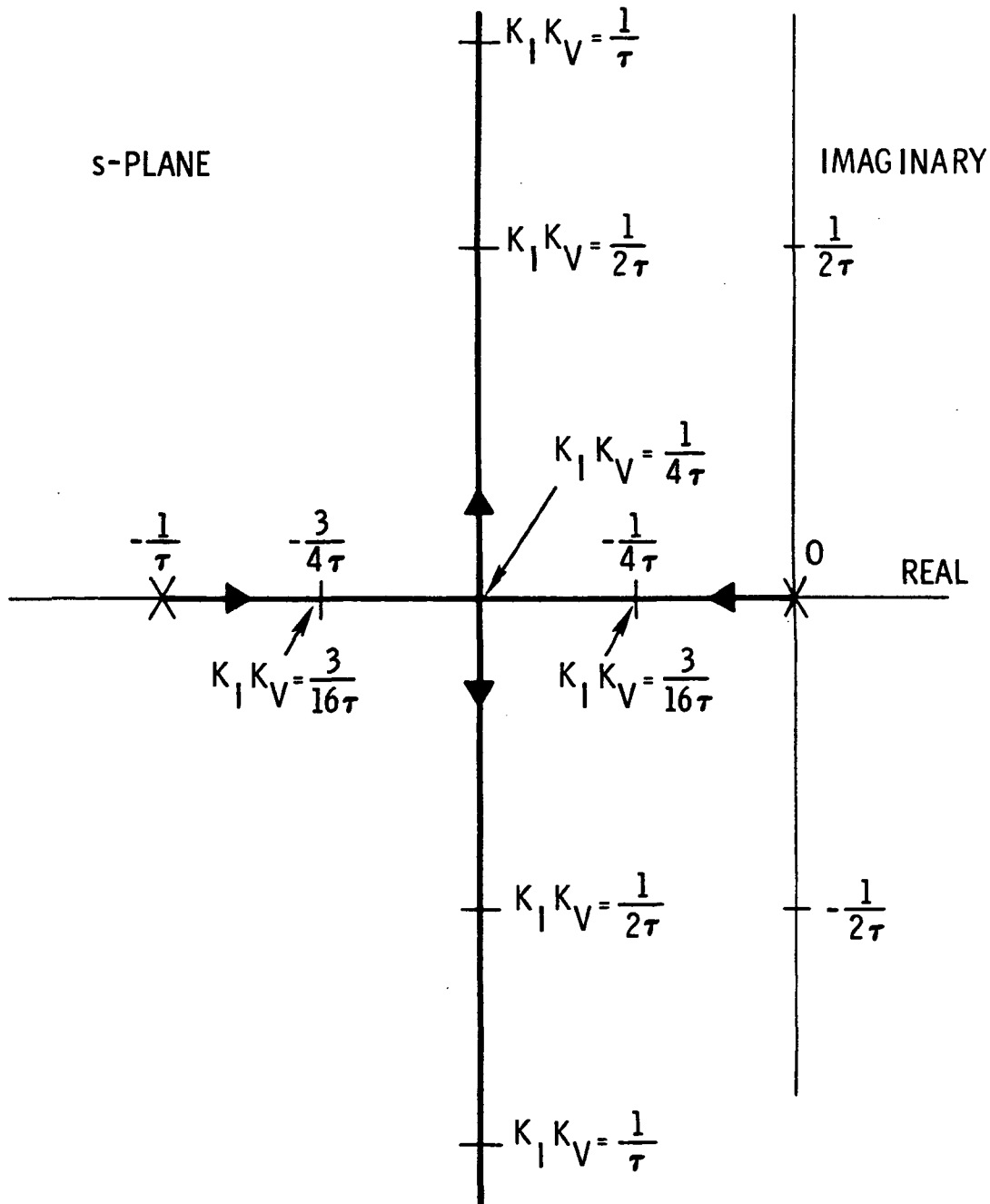


Figure 6-3. Inner Loop - Root Locus

Figure 6-4 shows asymptotic Bode plots for the inner loop. The natural frequency and damping ratio of the inner loop as a function of the loop gain,  $K_1 K_V$ , is shown in Table 6-1.

$K_1 K_V$	$\omega_n$	$\zeta$
$\frac{1}{4\tau}$	$\frac{1}{2\tau}$	1
$\frac{1}{2\tau}$	$\frac{\sqrt{2}}{2} \frac{1}{\tau}$	$\frac{\sqrt{2}}{2} = 0.707$
$\frac{1}{\tau}$	$\frac{1}{\tau}$	$\frac{1}{2} = 0.5$
$\frac{2}{\tau}$	$\frac{\sqrt{2}}{\tau}$	$\frac{1}{2\sqrt{2}} = 0.354$
$\frac{4}{\tau}$	$\frac{2}{\tau}$	$\frac{1}{4} = 0.250$
$\frac{16}{\tau}$	$\frac{4}{\tau}$	$\frac{1}{8} = 0.125$

Table 6-1. Inner Loop Natural Frequency And Damping

#### 6.2.1.1.2 Outer Loop Transfer Function

The closed-loop transfer function for the system shown in Figure 6-2 is given by

$$\frac{\delta_o}{\delta_c} = \frac{1}{1 + \frac{K_V s}{K_E} + \frac{s^2}{K_1 K_E} + \frac{\tau s^3}{K_1 K_E}} \quad (6-7)$$

$$= \frac{\frac{K_1 K_E}{\tau}}{s^3 + \frac{s^2}{\tau} + \frac{K_V K_1 s}{\tau} + \frac{K_1 K_E}{\tau}} \quad (6-8)$$

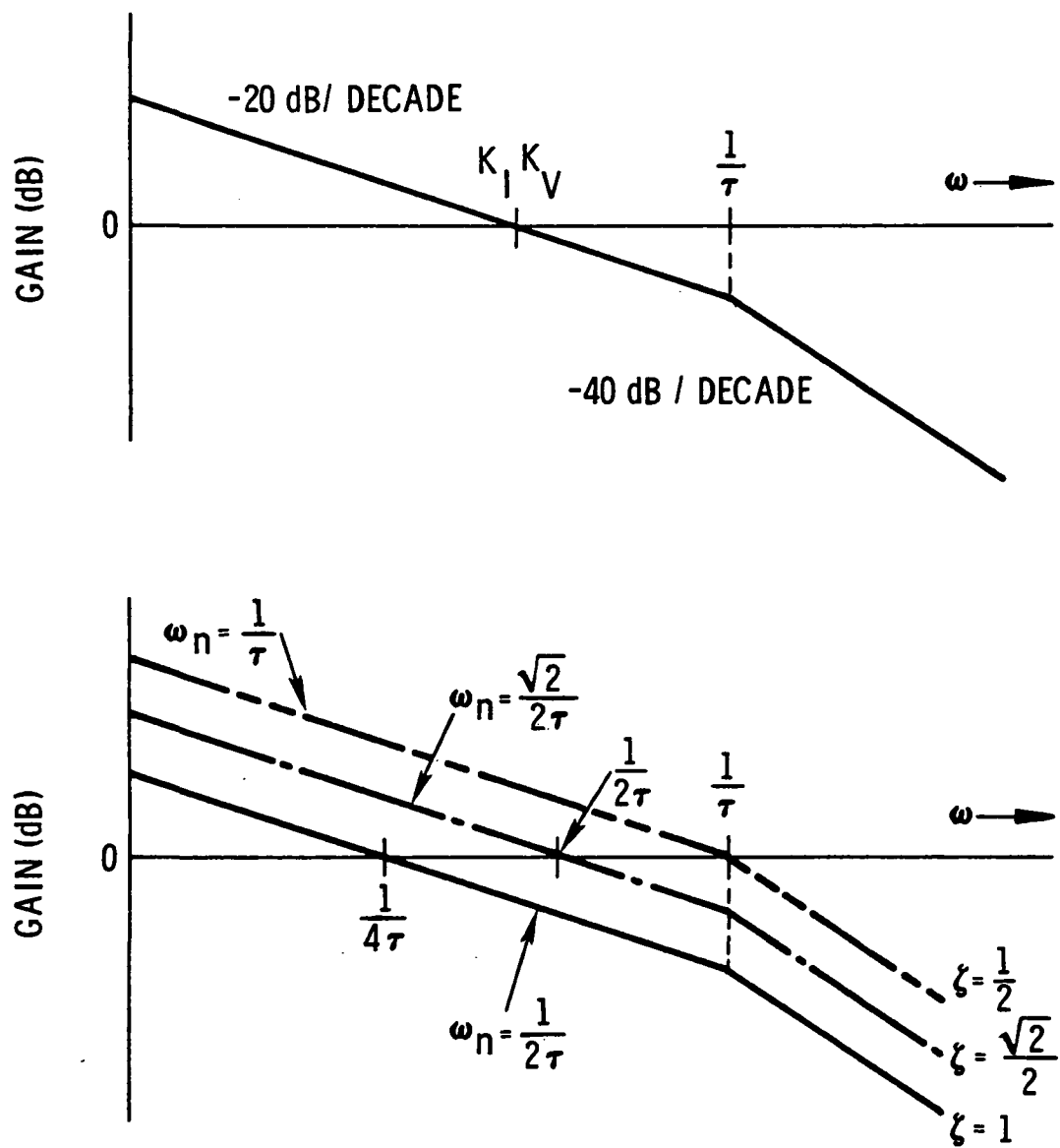


Figure 6-4. Inner Loop Gain Bode Plots

The Routh table for the characteristic equation of the system is

$s^3$	1	$\frac{K_v K_1}{\tau}$
$s^2$	$\frac{1}{\tau}$	$\frac{K_1 K_E}{\tau}$
$s^1$	$\left( \frac{K_1 K_v}{\tau} - K_1 K_E \right)$	
$s^0$	$\frac{K_1 K_E}{\tau}$	

The system will be stable if all elements in the left-hand column of the array are positive. This requires that  $\tau$ ,  $K_1$  and  $K_E$  all be positive and that

$$K_E < \frac{K_v}{\tau} \quad (6-9)$$

When  $K_E = \frac{K_v}{\tau}$ , the characteristic equation of the system becomes

$$s^3 + s^2/\tau + K_v K_1 s/\tau + K_v K_1/\tau^2 = 0 \quad (6-10)$$

For this condition, the roots are

$$s_1 = -\frac{1}{\tau} \quad (6-11)$$

and

$$s_2, s_3 = \pm j \sqrt{\frac{K_v K_1}{\tau}} \quad (6-12)$$

Root locus plots for the outer loop can have the two general characteristics shown in Figures 6-5 and 6-6. When the open-loop poles are all real (Figure 6-5), the root locus for the system shows that the closed-loop poles will all be real when the loop gain is low. At higher gains, the two lower frequency poles merge and break away from the real axis forming complex pairs.

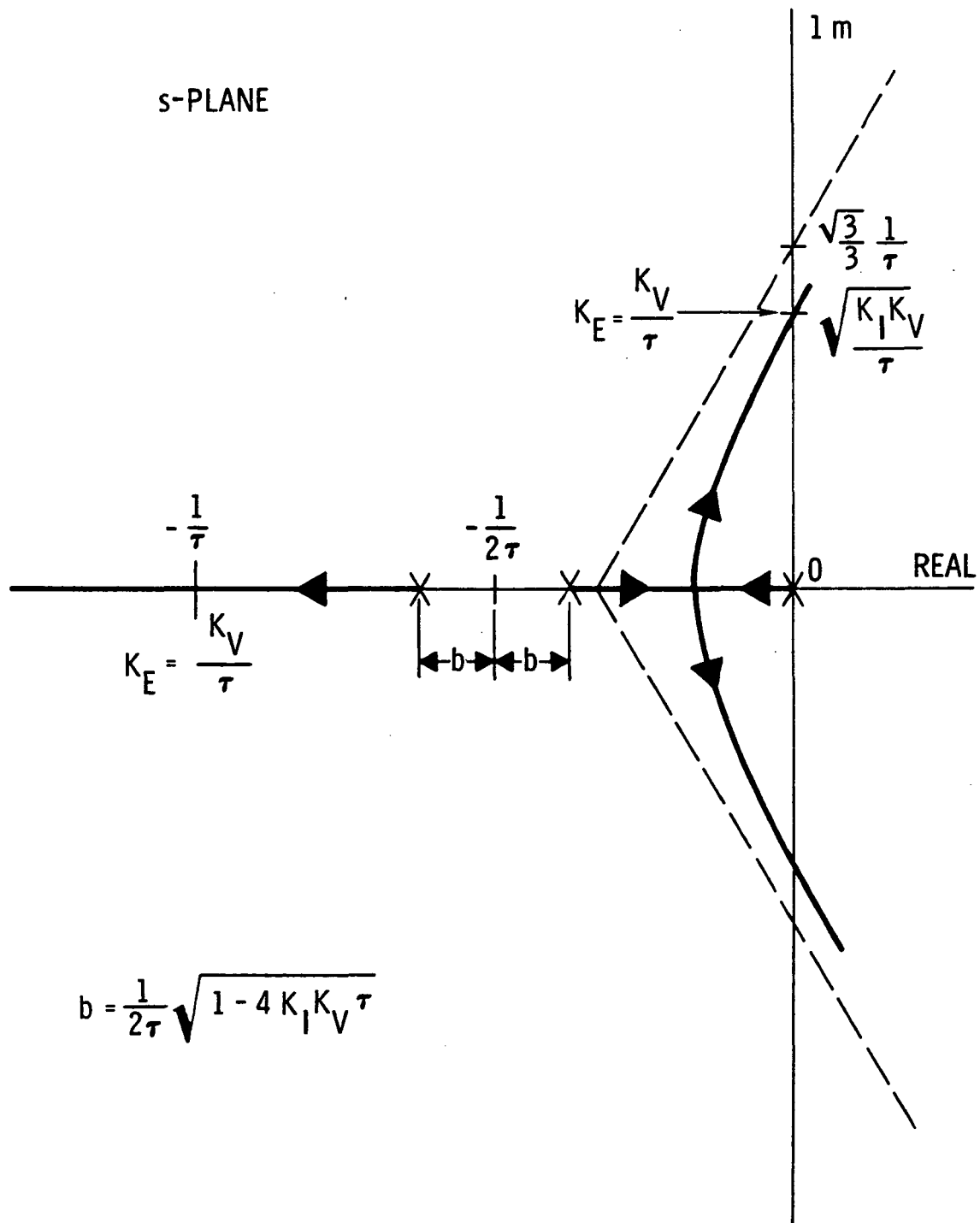


Figure 6-5. Root Locus - Three Real Open-Loop Poles



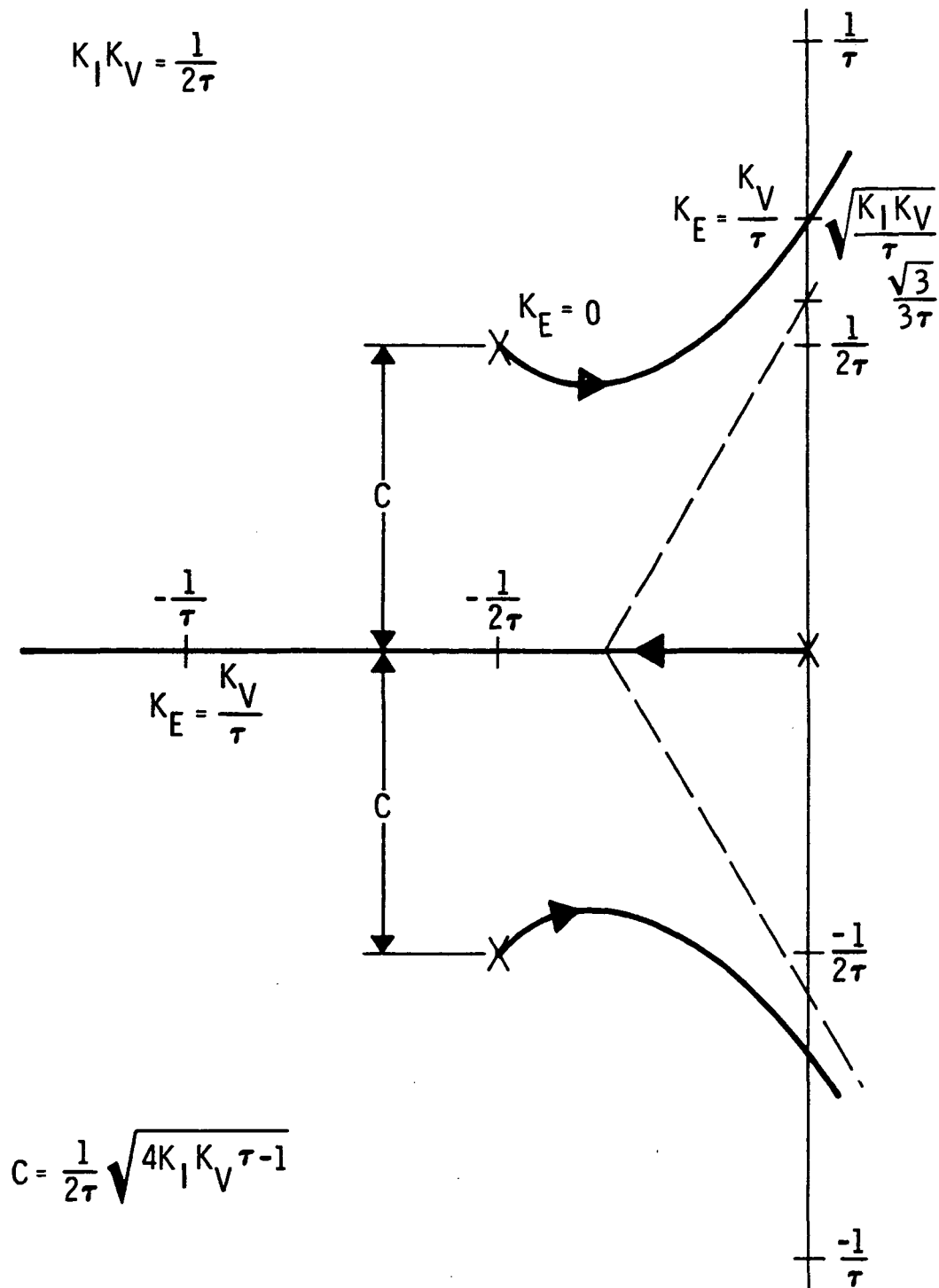


Figure 6-6. Root Locus - One Real and Two Complex Open-Loop Poles

If the open-loop poles include a complex pair (Figure 6-6), the closed loop will have one real pole and two complex conjugate poles. Typical asymptotic Bode plots for the two possible open-loop conditions are shown in Figure 6-7.

As a special case which provides very important insights as to the affects of system parameters, consider the case where the system's dominant time constant,  $\tau$ , is small enough to be neglected. For this case, the closed-loop transfer function of Eq. 6-7 can be simplified to:

$$\frac{\delta_o}{\delta_c} = \frac{1}{1 + \frac{K_V}{K_E} s + \frac{s^2}{K_1 K_E}} \quad (6-13)$$

For this case, the natural frequency of the actuator is

$$\omega_N = \sqrt{K_1 K_E} = \sqrt{\frac{180 K_T K_E}{\pi J a}} \quad (\text{rad/s}) \quad (6-14)$$

and the damping ratio is

$$\zeta = \frac{\omega_N}{2} \frac{K_V}{K_E} = \frac{K_V}{2} \sqrt{\frac{K_1}{K_E}} = \frac{K_V}{2} \sqrt{\frac{180 K_T}{J a K_E}} \quad (6-15)$$

These equations clearly indicate the affects of system gains, inertia, and gear ratio on the linear response characteristics of the system. Although this analysis is too over-simplified to provide a quantitative representation of the system's characteristics, it does represent the ideal situation which would be achieved if all system lags were negligible. More accurate analyses must include the affects of all dominant poles and zeroes, and must also take into consideration such nonlinear affects as torque limiting, velocity limiting, and gear backlash.

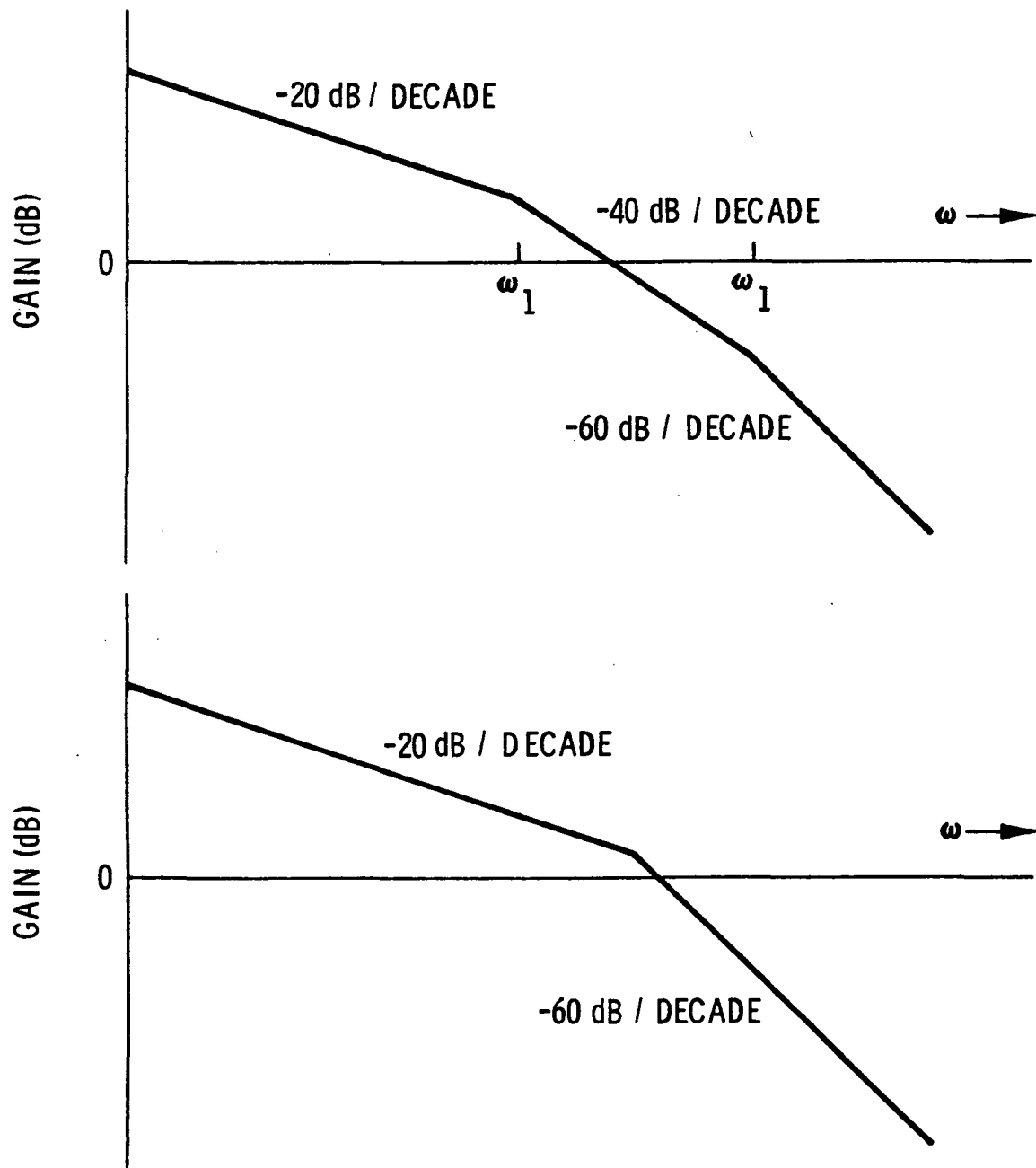


Figure 6-7. Asymptotic Bode Plots

### 6.2.1.2 NONLINEAR ANALYSES

#### 6.2.1.2.1 Step Response with Torque and Velocity Limiting

If the actuator were ideal, except for velocity and torque limiting, its behavior when responding to a step command would be as shown in Figure 6-8 (assuming all loading effects other than the system's inertia are negligible). During the initial portion of the step response, the motor would operate at full torque, thus achieving a constant acceleration. After the velocity limit is reached, the motion continues with constant velocity. As the load approaches the commanded position, full negative torque would be applied, decelerating the system inertia to its commanded position without overshoot. This idealized behavior can be analyzed using the following notation:

<u>Symbol</u>	<u>Description, units</u>
$I_M$	Maximum motor current, amperes
$J$	System inertia reflected to motor axis, in-lb-s <sup>2</sup>
$K_T$	Motor torque coefficient, in-lb/A
$N_M$	Motor maximum speed, r/min
$T_M$	Maximum motor torque, in-lb
$t_A$	Time to accelerate to maximum velocity, seconds
$\alpha$	Motor angular acceleration, rad/s <sup>2</sup>
$\omega$	Motor angular velocity, r/min
$\theta$	Motor angular position, degrees
$\theta_A$	Motor travel in accelerating to maximum velocity, degrees
$\theta_T$	Total motor travel, degrees
$\delta_E$	Load angular position, degrees
$\delta_{E_A}$	Load angular motion required in accelerating to maximum velocity, degrees

The time required to accelerate the load to maximum velocity is given by

$$t_A = \frac{\pi}{30} \frac{N_M J}{K_T I_M} = \frac{\pi}{30} \frac{N_M J}{T_M} \quad (s) \quad (6-16)$$

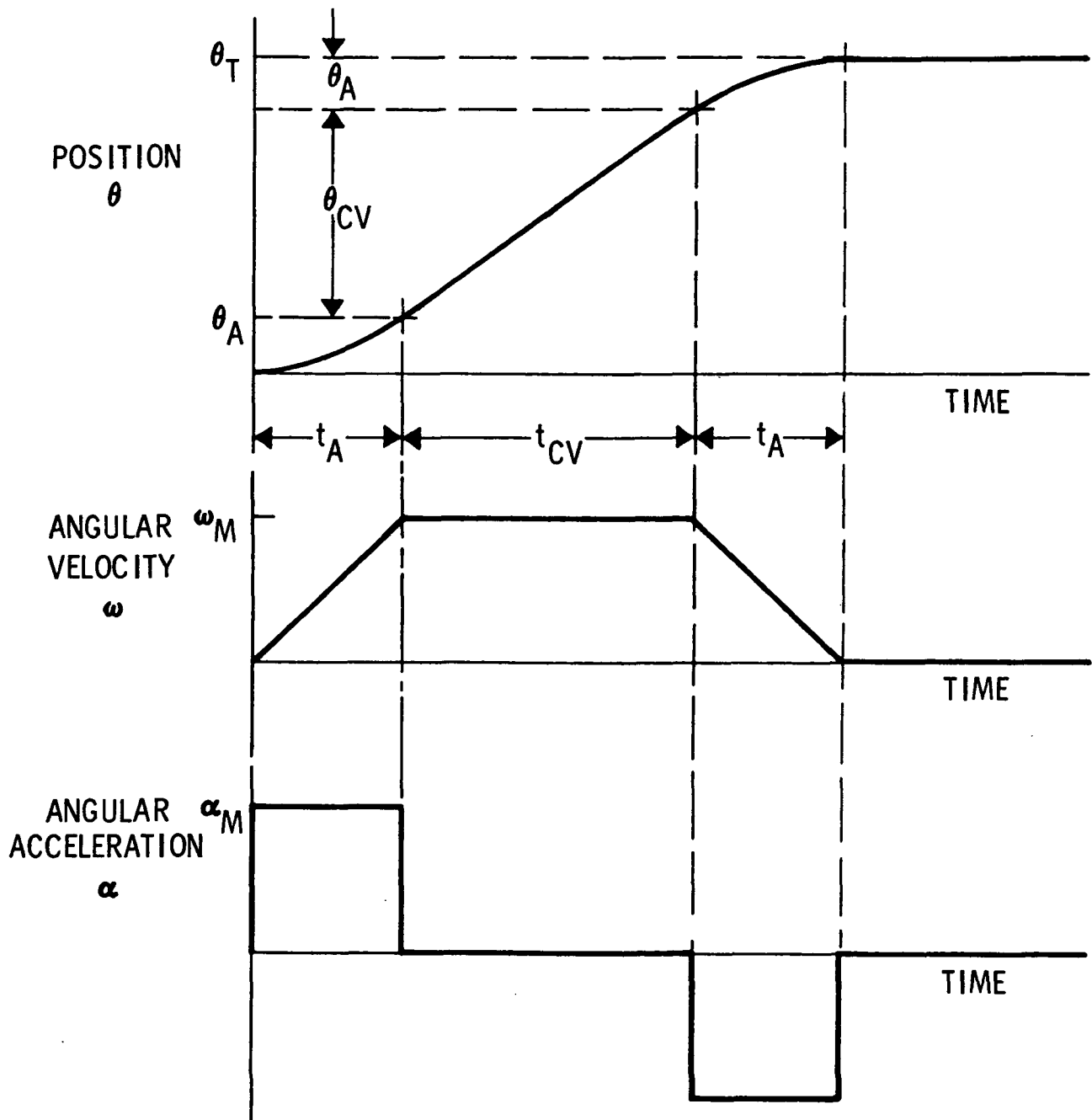


Figure 6-8. Step Response of Idealized Actuator with Velocity Acceleration Limiting

The angle traveled in reaching full speed is found to be:

$$\theta_A = \frac{\pi J N_M^2}{10 T_M} \quad (\text{deg}) \quad (6-17)$$

The time required to traverse a large angle (the case where velocity limiting occurs) is

$$t_T = \frac{\theta_T}{6 N_M} + \frac{\pi}{30} \frac{N_M J}{T_M} \quad (\text{s}) \quad (6-18)$$

The time required to travel through a small angle (without reaching velocity limiting) is

$$t_T = \sqrt{\frac{\pi \theta_T J}{180 T_M}} \quad (\text{s}) \quad (6-19)$$

where

$$\theta_T \leq 2\theta_A \quad (\text{deg}) \quad (6-20)$$

or

$$\theta_T \leq \frac{\pi}{5} \frac{N_M^2 J}{T_M} \quad (\text{deg}) \quad (6-21)$$

As a design example, if the maximum motor speed is 9000 r/min (corresponding to a load angular velocity of 20 deg/s), the step command is 2.0 degrees at the load, and

$$\begin{aligned} J &= 0.006 \text{ in-lb-s}^2 & \theta_T &= 5400 \text{ deg} \\ T_M &= 120 \text{ in-lb} & N_M &= 9000 \text{ r/min} \end{aligned}$$

then

$$t_A = \frac{\pi}{30} \frac{(9000)(.006)}{120} = 0.0471 \quad (\text{s})$$

$$\theta_A = \frac{\pi}{10} \frac{(9000^2)(.006)}{120} = 1272 \quad (\text{deg})$$

$$\delta_{EA} = 1272 \left[ \frac{20}{9000 \times 6} \right] = 0.471 \quad (\text{deg})$$

$$t_T = \frac{5400}{6(9000)} + \frac{\pi}{30} \left[ \frac{9000 \times .006}{120} \right] = 0.1471 \quad (\text{s})$$

Thus, a step load command of 2.0 deg. is completed in 0.1471 s. The load reaches maximum velocity in 0.0471 s. During this time the load has traveled 0.471 deg (and the motor has rotated 1272 deg).

For the same design example conditions, velocity limiting would be reached for step angular commands (referred to the motor axis) greater than:

$$\theta_T = \frac{\pi}{5} \frac{(9000)^2 (0.006)}{120} = 2545 \quad (\text{deg})$$

which would correspond to a load deflection of

$$\delta_E = 2545 \left[ \frac{20}{9000 \times 6} \right] = 0.942 \quad (\text{deg})$$

Figure 6-9 shows idealized step response characteristics for the same design example when traveling 1.1 deg and 2.75 deg.

Although the preceding analysis is considerably simplified, it provides an ideal response against which the actual system characteristics can be compared. The actual step response of the system can be made to approach the idealized response, but can never exceed it. A more thorough analysis of the nonlinear step response of the system is presented in Paragraph 6.2.4.

#### 6.2.1.2.2 Sinusoidal Motion with Torque and Velocity Limiting

If the load is moving sinusoidally,



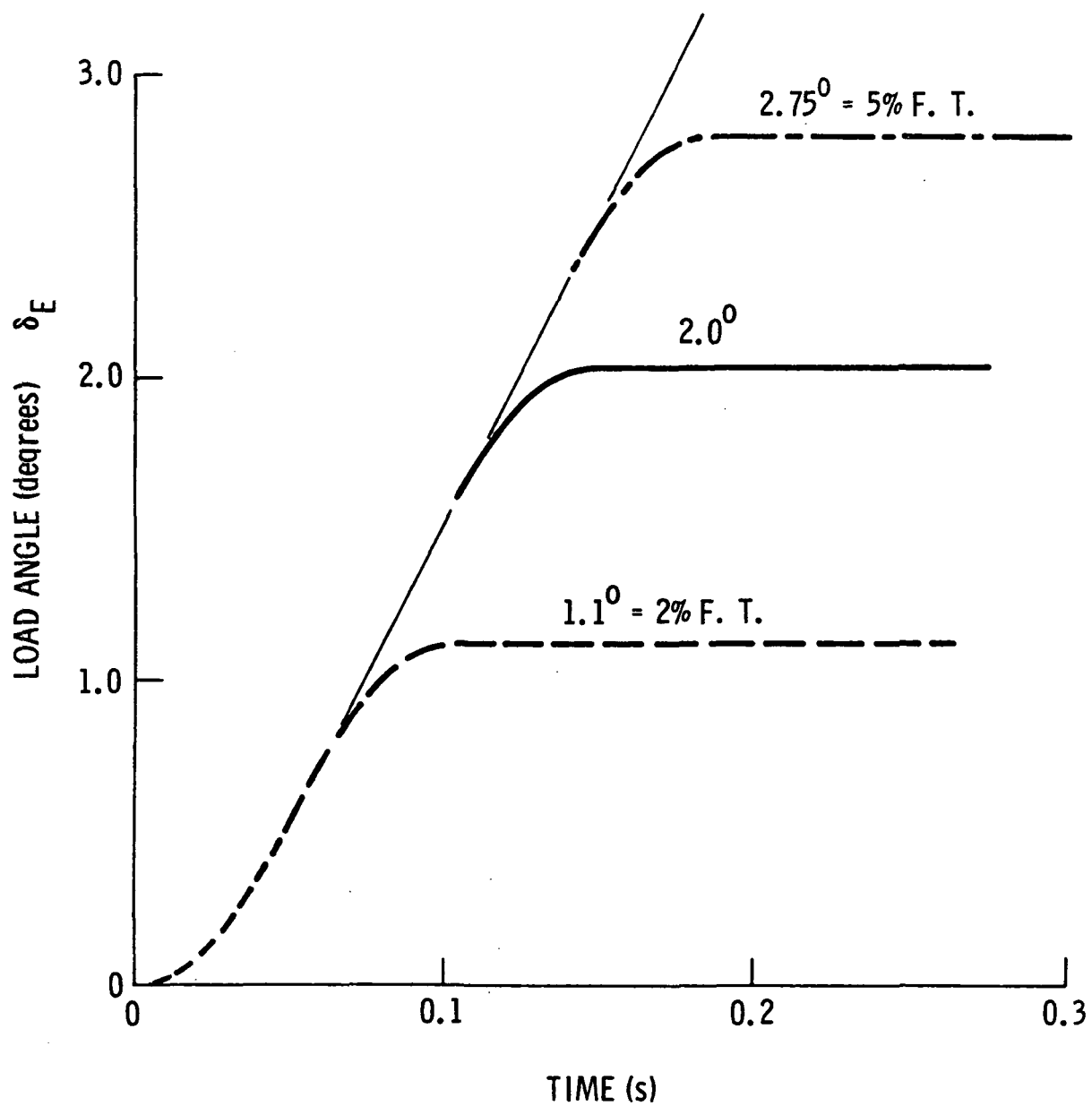


Figure 6-9. Step Response with Torque and Velocity Limiting

$$\delta = A \sin 2\pi ft \quad (\text{deg}) \quad (6-22)$$

$$\omega = \dot{\delta} = 2\pi f A \cos 2\pi ft \quad (\text{deg/s}) \quad (6-23)$$

$$\alpha = \dot{\omega} = -4(\pi f)^2 A \sin 2\pi ft \quad (\text{deg/s}^2) \quad (6-24)$$

where A is the amplitude of the load motion (degrees),  $\delta$  is the load deflection (degrees),  $\omega$  is the load angular velocity (degrees/second),  $\alpha$  is the load angular acceleration (deg/s/s), and f is the frequency of the sinusoidal motion (Hz). If the ratio of the motor speed to load speed is G, the peak angular velocity of the motor is

$$\omega_M = \frac{2\pi f G A}{6} \quad (\text{r/min}) \quad (6-25)$$

Therefore, if the motor speed can be no greater than  $N_M$  (r/min), velocity limiting will occur if the amplitude of the motor exceeds

$$A_V = \frac{3N_M}{\pi G f} \quad (\text{deg}) \quad (6-26)$$

Similarly, if the maximum motor torque is  $T_M$  (in-lb) and the system inertia reflected to the motor shaft is J (in-lb-s<sup>2</sup>), the maximum motor acceleration is

$$\alpha_M = \frac{T_M}{J} \left[ \frac{\text{rad}}{\text{s}^2} \right] \left[ \frac{180}{\pi \text{rad}} \text{ deg} \right] \quad (\text{deg/s}^2) \quad (6-27)$$

Therefore, acceleration (torque) limiting will occur if

$$\frac{180 T_M}{\pi J} = 4\pi^2 f^2 G A \quad (\text{deg/s}^2) \quad (6-28)$$

Therefore, the amplitude of the motion which results in acceleration limiting is given by

$$A_A = \frac{45 T_M}{\pi^3 f^2 G J} \quad (\text{deg}) \quad (6-29)$$

For the same design example used above, with

$$T_M = 120 \text{ in-lb} \quad (J = 0.006 \text{ in-lb-s}^2)$$

$$G = 2700 \quad (N_M = 9000 \text{ r/min})$$

$$A_v = \frac{3}{\pi} \frac{(9000)}{(2700)f} = \frac{3.18}{f} \quad (\text{deg})$$

and

$$A_A = \frac{45 (120)}{\pi^3 (2700)(0.006)f^2} = \frac{10.75}{f^2} \quad (\text{deg})$$

Figure 6-10 shows the velocity and acceleration limits for this design example. For this case, velocity limiting will be encountered before acceleration limiting for frequencies less than 3.4 Hz. At higher frequencies, the motion will be constrained by acceleration limiting.

## 6.2.2 DETAILED SINGLE-CHANNEL LINEAR ANALYSIS

The simplified linear analysis presented in Paragraph 6.2.1.1 is highly useful in showing how the dominant gains, time constants, and system parameters of the EMA affect the natural frequency and damping of the system. However, in examining the servo characteristics in greater detail it is necessary to consider all of the system parameters. In addition, it is desirable to have a computerized analysis available so that the effects of parameter variations can readily be evaluated. The following analysis was therefore conducted at a relatively early stage in the program. A later analysis (presented in Paragraph 6.2.3) was expanded to incorporate two operating channels, and is therefore even more useful for analyzing the EMA.

The single-channel linear analysis was conducted using the block diagram shown in Figure 6-11. The variables used in the computer program are shown next to the blocks which they represent. The equations used in developing the model are derived from the system block diagram. The inner loop gain is given by

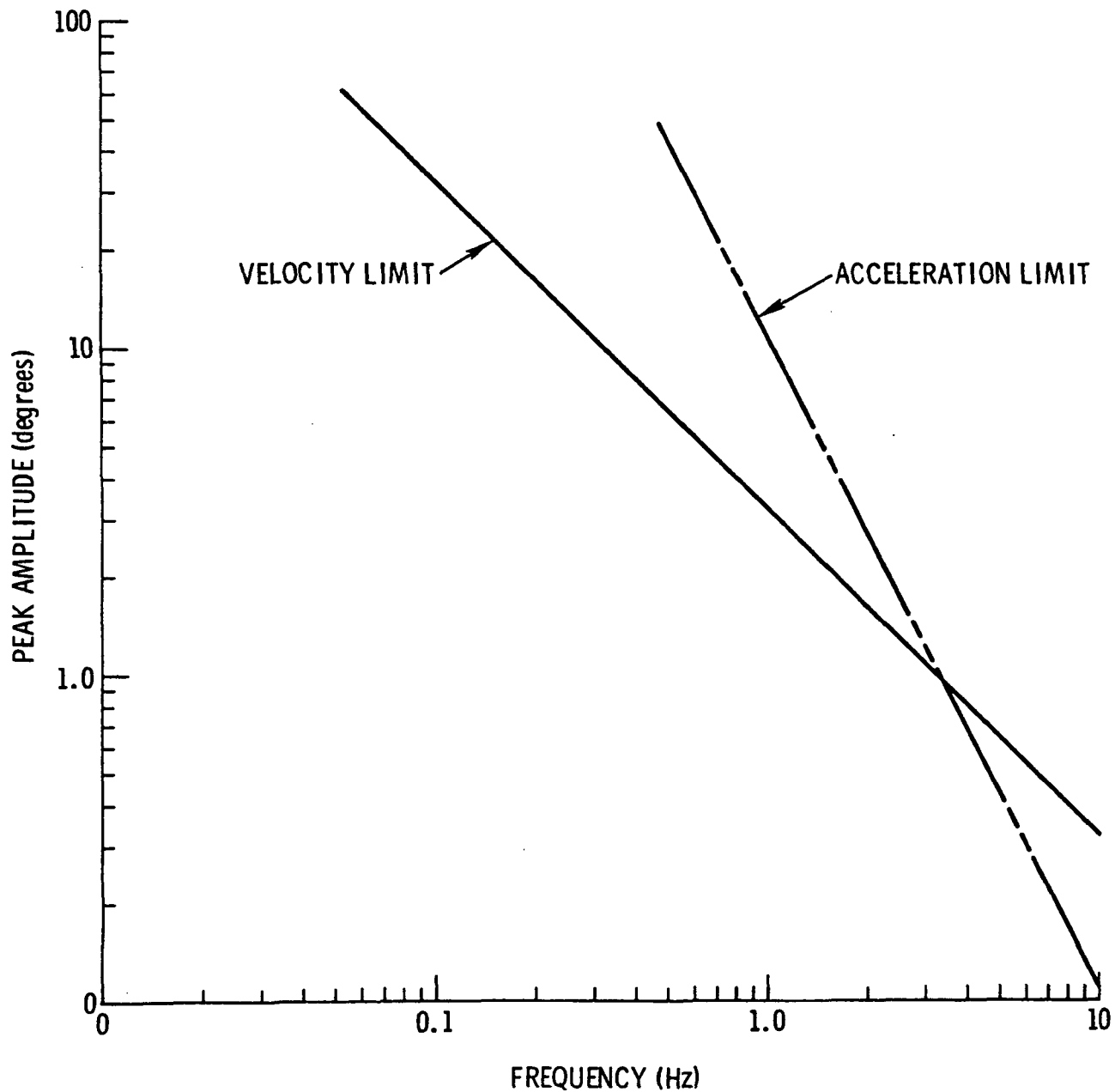


Figure 6-10. Limiting Amplitude of Sinusoidal Motion

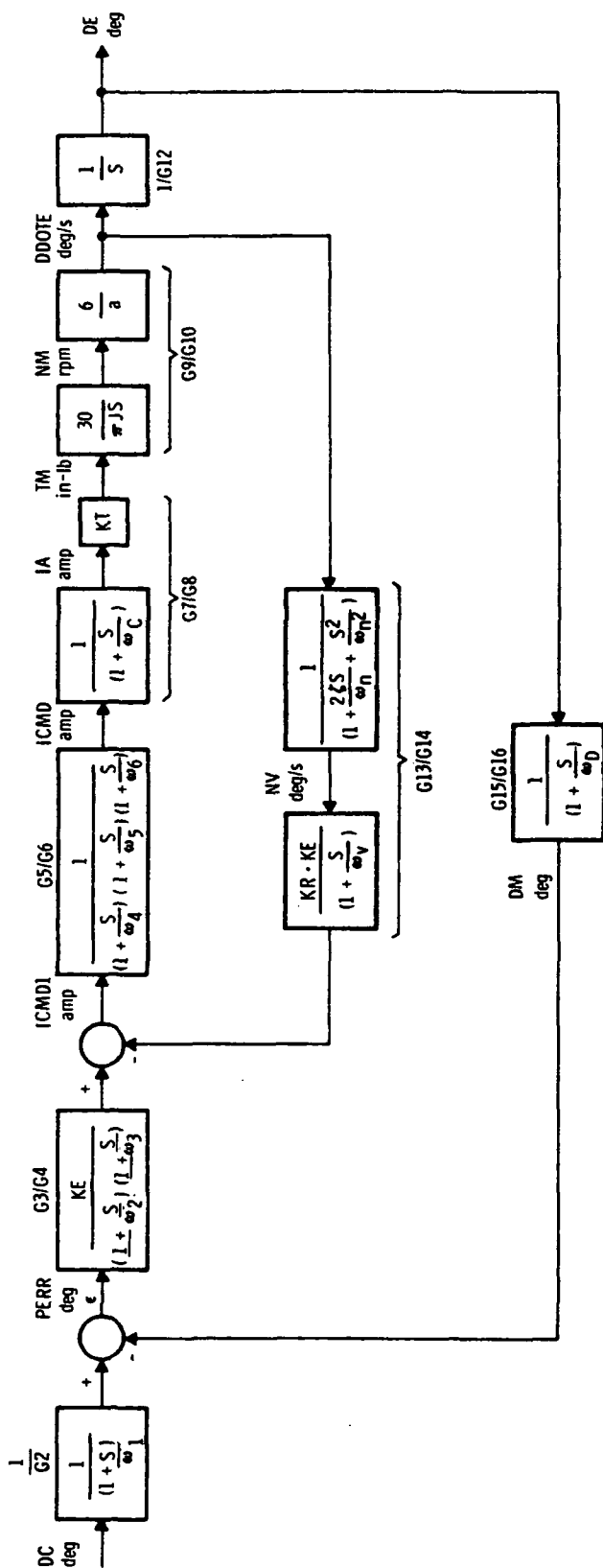


Figure 6-11. Single-Channel Linear Analysis Block Diagram

$$L_1 = - \frac{G_5}{G_6} \frac{G_7}{G_8} \frac{G_9}{G_{10}} \frac{G_{13}}{G_{14}}$$

and the outer loop gain is

$$L_2 = - \frac{G_3}{G_4} \frac{G_5}{G_6} \frac{G_7}{G_8} \frac{G_9}{G_{10}} \frac{1}{G_{12}} \frac{G_{15}}{G_{16}}$$

The characteristic expression for the system is

$$\begin{aligned} CE &= 1 - L_1 - L_2 \\ &= 1 + \frac{G_5}{G_6} \frac{G_7}{G_8} \frac{G_9}{G_{10}} \frac{G_{13}}{G_{14}} + \frac{G_3}{G_4} \frac{G_5}{G_6} \frac{G_7}{G_8} \frac{G_9}{G_{10}} \frac{1}{G_{12}} \frac{G_{15}}{G_{16}} \\ &= \left[ G_4 G_6 G_8 G_{10} G_{12} G_{14} G_{16} + G_5 G_7 G_9 G_{13} G_4 G_{12} G_{16} \right. \\ &\quad \left. + G_3 G_5 G_7 G_9 G_{15} G_{14} \right] / LCD \\ &= CHAREQ / LCD \end{aligned}$$

where LCD is defined to be

$$LCD = G_4 G_6 G_8 G_{10} G_{12} G_{14} G_{16}$$

The open loop transfer function for the inner loop is given by

$$GI\emptyset L = \frac{G_5}{G_6} \frac{G_7}{G_8} \frac{G_9}{G_{10}} \frac{G_{13}}{G_{14}}$$

and the closed-loop transfer function for the inner loop is

$$GICL = \frac{G_5 G_7 G_9 G_{14}}{(G_6 G_8 G_{10} G_{14} + G_5 G_7 G_9 G_{13})}$$

The open loop gain for the outer loop is found to be

$$G\emptyset\emptyset L = \frac{G_3 G_5 G_7 G_9 G_{14} G_{15}}{G_4 G_6 G_8 G_{10} G_{12} G_{14} G_{16} + G_4 G_5 G_7 G_9 G_{12} G_{13} G_{16}}$$

and the corresponding closed loop transfer function is given by

$$G_{\theta CL} = \frac{G_3 G_5 G_7 G_9 G_{14} G_{16}}{CHAREQ}$$

The transfer function relating the position error to the displacement command is given by

$$\frac{\varepsilon}{\delta_c} = \frac{\frac{1}{G_2} [1 - L_1]}{CHAREQ/LCD}$$

or

$$G_{EDC} = \frac{G_4 G_{12} G_{16} (G_6 G_8 G_{10} G_{14} + G_5 G_7 G_9 G_{13})}{G_2 CHAREQ}$$

The various gains and transfer functions of Figure 6-11 (using the parameter values at an early stage in the program) are given by

$$\begin{aligned} G_2 &= s/12409. + 1 \\ G_3 &= 100. \\ G_4 &= (s/452.4+1) * (s/213.6 + 1) \\ G_5 &= 1. \\ G_6 &= (s/999. +1) *(s/2488. + 1)*(s/879.7 + 1) \\ G_7 &= 2.0 \\ G_8 &= s/502.7 + 1 \\ G_9 &= 1.796 \\ G_{10} &= s \\ G_{12} &= s \\ G_{13} &= 5.0 \\ G_{14} &= s/1061.9 + 1 \\ G_{15} &= 1.0 \\ G_{16} &= s/213.6 + 1 \end{aligned}$$

A complete program listing for the model is presented in Table 6-2. As can be seen, several parameter changes were used for  $G_3$ ,  $G_4$ ,  $G_{13}$ , and  $G_{16}$ .

```

C      EPSN(10,1)
0      EPSN(11,1)
C      EMA      SINGLE MOTOR MODEL      LINEAR
C
0
0      G2 = (S/12409. + 1)
0      G3 = 1.0
0      G3 = 100.
0      G3 = 800.
0      G4 = (S/452.4 + 1)*(S/213.6 + 1)
0      G4 = (S/904.8 + 1)*(S/427.2 + 1)
0      G5 = 1.
0      G6 = (S/999. + 1)*(S/2488. + 1)*(S/879.7 + 1)
0      G7 = 2.0
0      G8 = (S/502.7 + 1)
0      G9 = 1.796
0      G10 = S
0      G12 = S
0      G13 = 1.0
0      G13 = 5.0
0      G13 = 25.0
0      G14 = (S/1061.9 + 1)
0      G15 = 1.0
0      G16 = (S/213.6 + 1)
0      G16 = (S/427.2 + 1)
1
0
C      CHARACTERISTIC EQUATION INNER AND OUTER LOOPS
C
0      GCEQ = G4*G6*G8*G10*G12*G14*G16 + G5*G7*G9*G13*G4*G12*G16 +
0      1 G3*G5*G7*G9*G15*G14
0      G00L = G3*G5*G7*G9*G14*G15/(G4*G6*G8*G10*G12*G14*G16 +
0      1 G4*G5*G7*G9*G12*G13*G16)
C
0      INNER LOOP RESPONSE ( OPEN LOOP )
C
0      G10L = G5*G7*G9*G13/(G6*G8*G10*G14)
0      FREQ( , .,1,1.,.1,1.,50.,1.,50.,250.,5.,G10L,CYC)
C
0      INNER LOOP RESPONSE ( CLOSED LOOP )
C
0      G1CL = (G5*G7*G9*G14/(G6*G8*G10*G14 + G5*G7*G9*G13))*25.279
0      FREQ( , .,1,1.,.1,1.,50.,1.,50.,250.,5.,G1CL,CYC)
C
0      OUTER LOOP RESPONSE ( OPEN LOOP )
C
0      FREQ( , .,1,1.,.1,1.,50.,1.,50.,250.,5.,G00L,CYC)
C
0      OUTER LOOP RESPONSE ( CLOSED LOOP )
C
0      G0CL = G3*G5*G7*G9*G14*G16/GCEQ
0      FREQ( , .,1,1.,.1,1.,50.,1.,50.,250.,5.,G0CL,CYC)
C
0      CLOSED LOOP POSITION ERROR TO POSITION COMMAND
C
0      GEDC = G4*G12*G16*(G6*G8*G10*G14 + G5*G7*G9*G13)/(G2*GCEQ)
0      FREQ( , .,1,1.,.1,1.,50.,1.,50.,250.,5.,GEDC,CYC)

```

Table 6-2. Single-Loop Analysis Program Listing



A root locus analysis of the inner loop was conducted, and a plot of the results is presented in Figure 6-12. Since the dominant complex poles dictate most of the system response, a gain was chosen to provide a damping ratio of 0.707. From the open loop response the gain and phase margins were found to be:

Phase margin =  $62.6^{\circ}$  at 14 Hz

Gain margin = 13 dB at 48 Hz

Figure 6-13 illustrates the resulting inner loop, closed loop response. Its -3 dB bandwidth is 27 Hz.

Using the inner loop gains established above, the outer loop root locus was determined (Figure 6-14). The dominant complex poles (near the origin) are strongly influenced by the 213.6 rad (34 Hz) double filter lags. With the gain adjusted to give a damping ratio of 0.707, it was found that the closed-loop phase shift was greater than the design goal. To improve the closed-loop characteristics, the filter lag frequencies were doubled. A root locus plot for this condition is shown in Figure 6-15. For  $K_p = 800$ , the damping ratio of the dominant closed-loop complex pair is 0.6. Corresponding roots are indicated on the root loci by the rectangular symbols. The closed-loop gain and phase characteristics for the system are given in Figure 6-16 and Figure 6-17, respectively. For comparison purposes, the design goals for the gain and phase characteristics are also plotted in these figures, and it can be seen that the design goals are exceeded. The outer loop phase and gain margins from this analysis are:

Phase margin =  $61^{\circ}$  at 5 Hz

Gain margin = 10 dB at 15 Hz.

### 6.2.3 TWO-CHANNEL LINEAR ANALYSIS

The single-channel linear analysis which was presented in the preceding section is very useful in establishing system characteristics, but does not take into account the load characteristics or the effects of having two channels operating simultaneously. The analysis of the two-channel linear system described in the following paragraphs takes both of these factors into account.

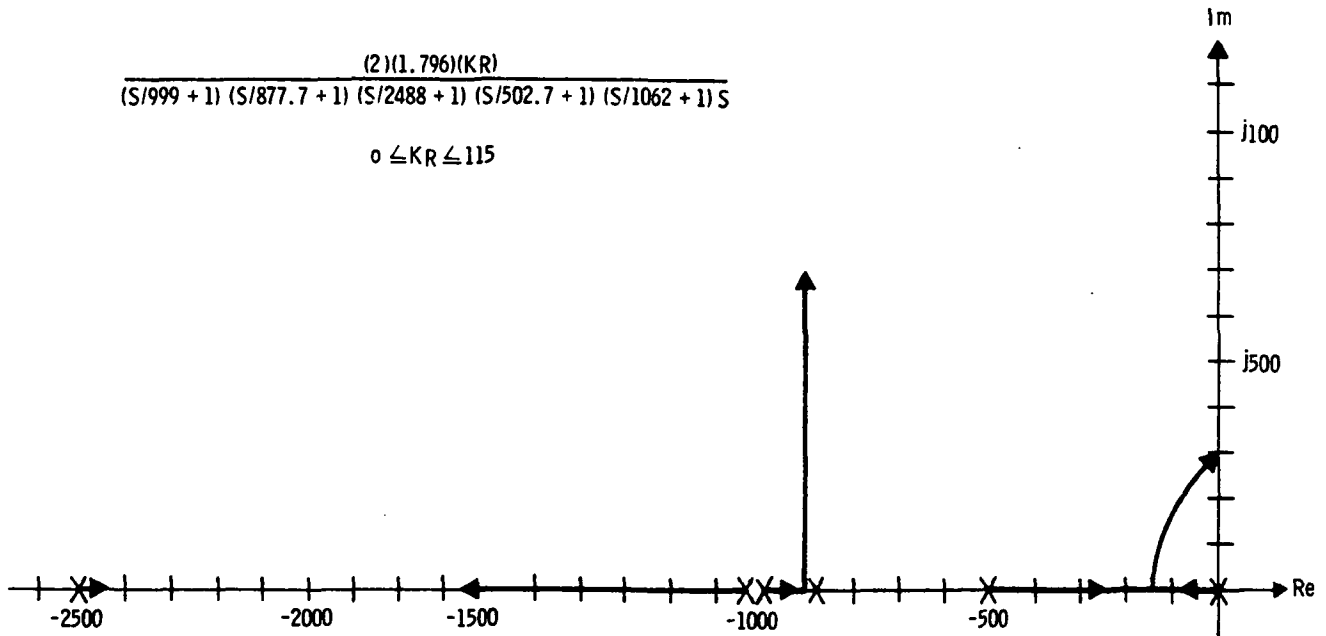


Figure 6-12. Root Locus for Inner Loop

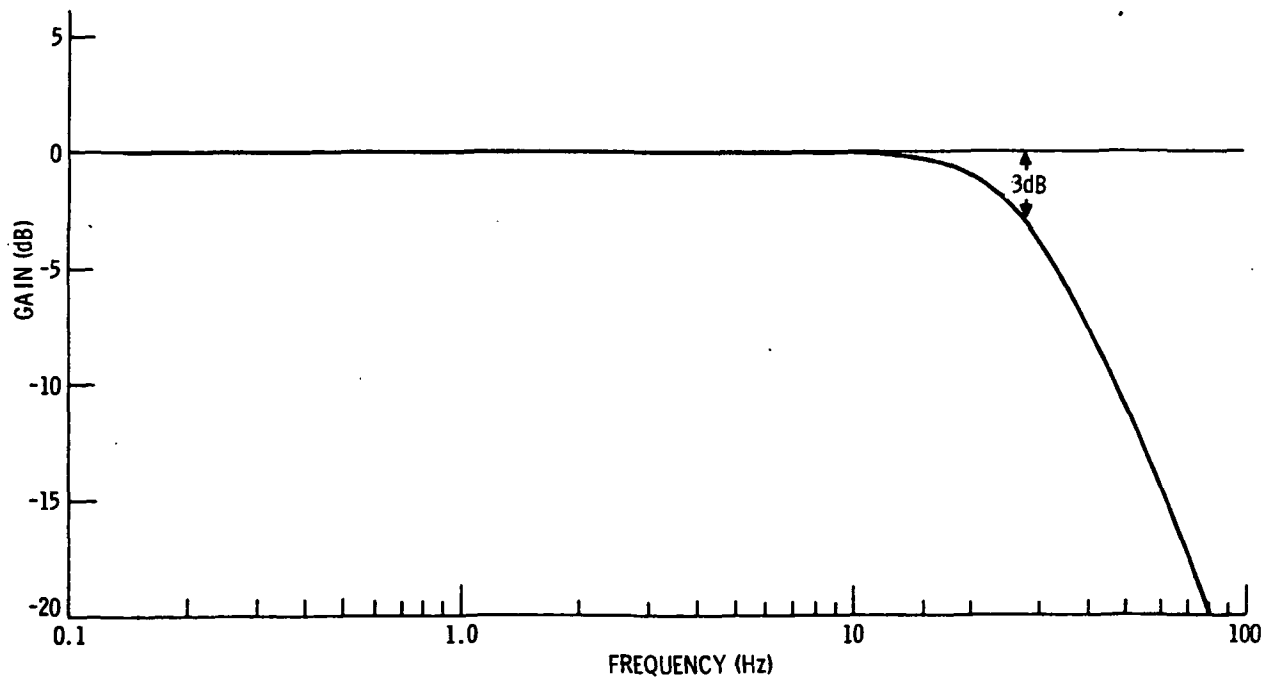


Figure 6-13. Closed-Loop Response for Inner Loop

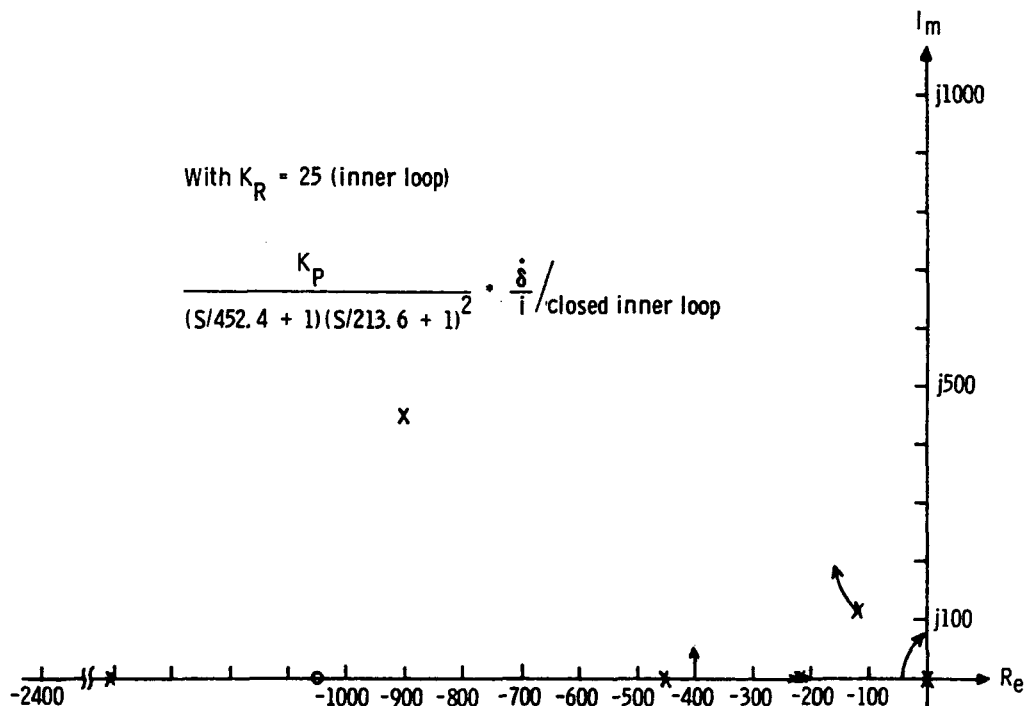


Figure 6-14. Root Locus Plot for Narrowband Outer Loop

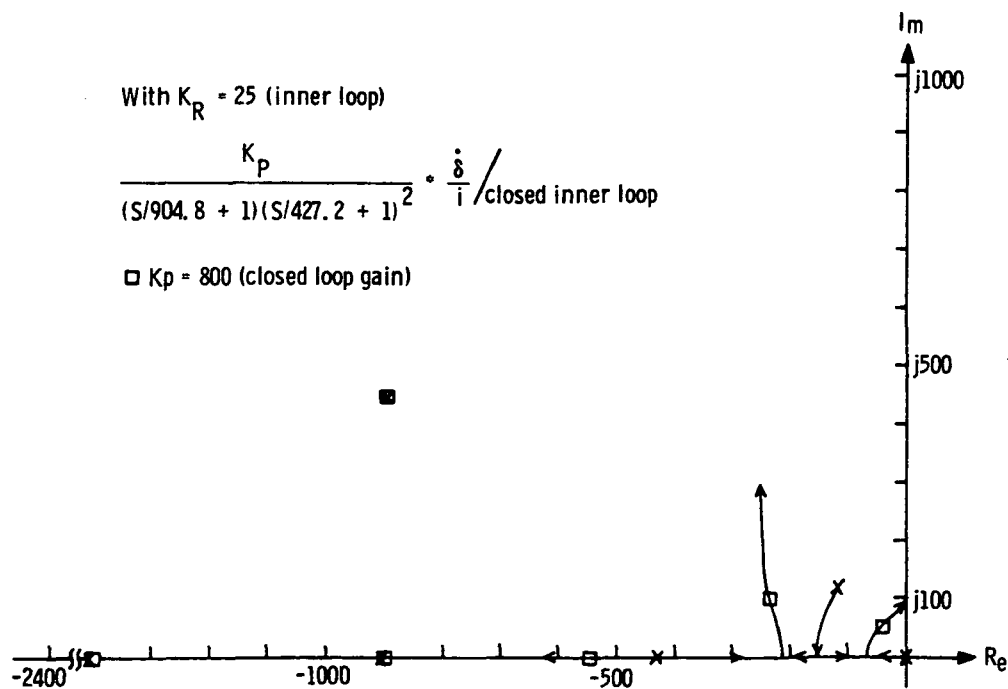


Figure 6-15. Root Locus Plot for Wideband Outer Loop

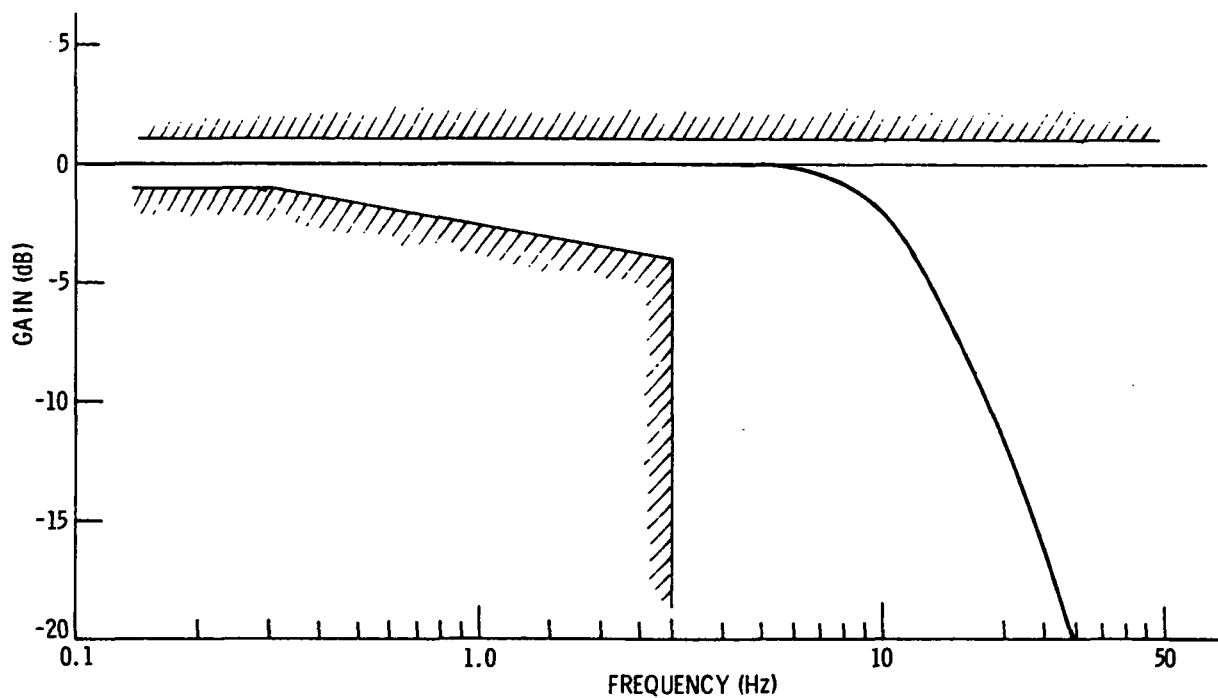


Figure 6-16. Closed Outer Loop Gain Characteristic

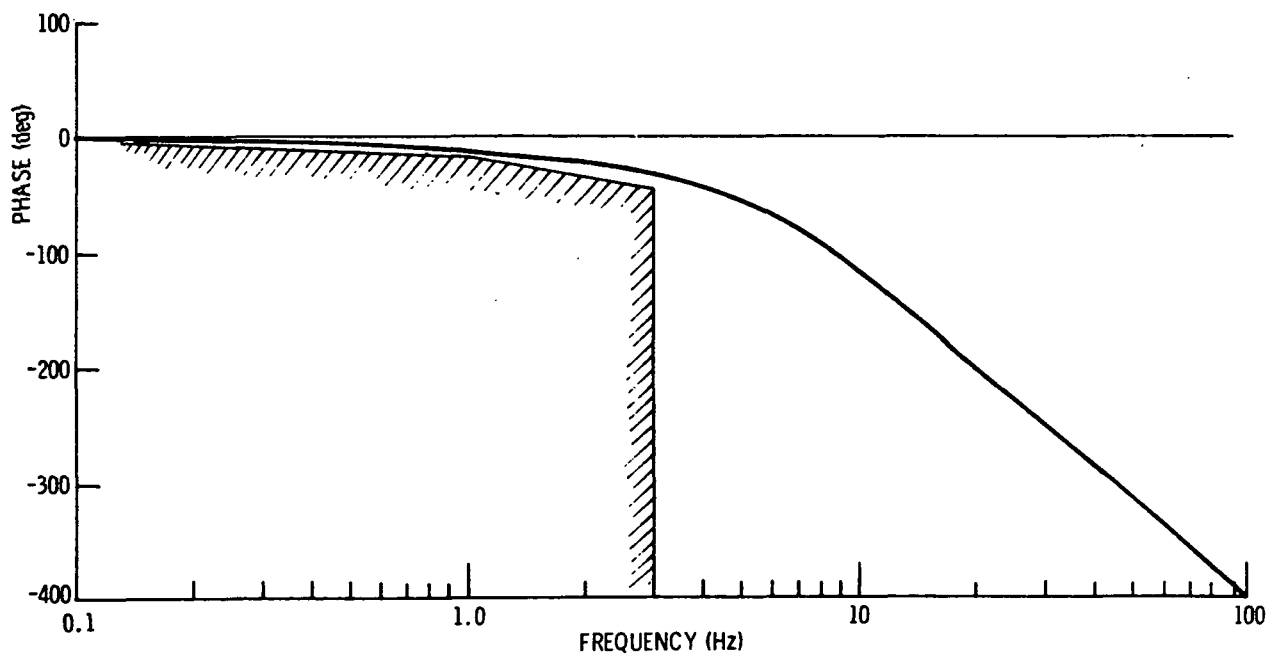


Figure 6-17. Closed Outer Loop Phase Characteristic

In analyzing the two-channel system there are six possible combinations of two motors. The one that was chosen for analysis considers two motors sharing the load through one of the primary differentials. The remaining primary differential is locked up, thereby allowing torque transmission through the final differential. The other possible combinations of two motors could be analyzed in a similar manner. Figure 6-18 shows the two motors, the differentials, and the system load. Table 6-3 presents the symbols and related data for the variables used in the analysis. For this model, all of the compliances associated with the actuator are lumped together at the output shaft.

A block diagram of the two-channel system is given in Figure 6-19. In this representation the inertias of the first gear stages are reflected to the motor shafts, and the inertias of the remaining stages are neglected. The actuator load is modelled as a simple inertia which is accelerated by the EMA output torque magnified by the gear ratio  $n_3$  and opposed by damping and spring load torques. The complete model block diagram includes tachometer, velocity correction and position feedback loops as shown in Figure 6-19.

Programming was facilitated by block diagram manipulation of the load dynamics. The load dynamics were included in the feedback torque loop and added open loop to the output of the actuator motion. Figure 6-20 represents the computer model block diagram (which is of course dynamically identical to the model in Figure 6-19). All responses run with this model are with respect to the EMA output shaft. Since the load dynamics can be neglected for a stiff system such as the load stand, the test stand motion is related to the EMA output shaft motion by

$$\frac{\theta_F}{\theta_O} = \frac{1}{n_3}$$

Therefore, any of the responses which follow can readily be converted to test stand motion.

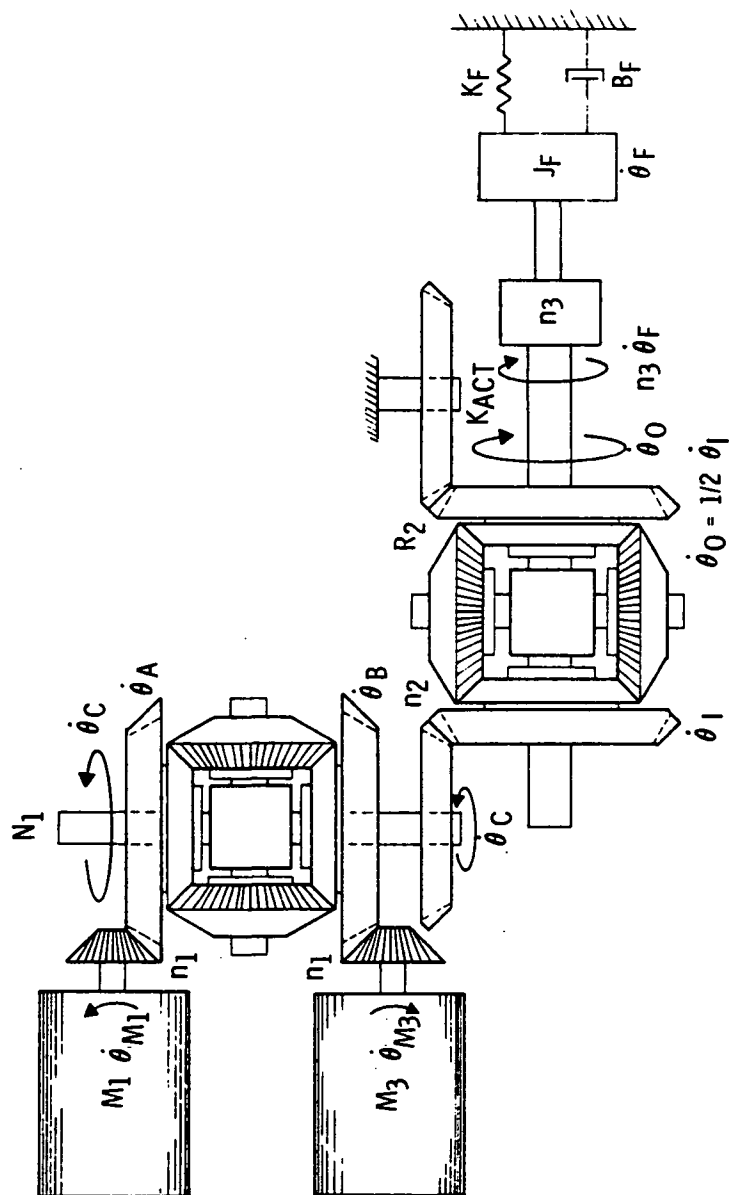


Figure 6-18. EMA Dual-Channel Model 1 Showing Motors, Differential and Load

Table 6-3. Model Parameters

<u>SYMBOL</u>	<u>UNITS</u>	<u>VALUE</u>	<u>DESCRIPTION</u>
$\delta_C$	radians	Variable	Commanded Position
$K_E$	volts/rad	170.4*	Position forward loop gain
$F_{C(s)}$	See Figure 6-19		Position loop compensation
$K_I$	A/volt	1.0	
$K_T$	in-lb/A	2.0	Nominal motor torque constant
$J_{M1}, J_{M3}$	in-lb-s <sup>2</sup>	0.00842	Motor inertia including reflected gear
$K_{V1}, K_{V3}$	volts/rad/s	0.2694*	Tachometer feedback gain
$\eta_1$		3.75	Gear ratio, motor-to-primary differential
$\eta_2$		1.5	Gear ratio, primary-to-secondary differential
$\eta_3$		238.71	NASA actuator gear ratio
$\dot{\theta}_{M1}$	rad/s	Variable	Motor velocity (#1 motor)
$\dot{\theta}_{M3}$	rad/s	Variable	Motor velocity (#3 motor)
$\dot{\theta}_A$	rad/s	Variable	Primary differential input
$\dot{\theta}_B$	rad/s	Variable	Primary differential input
$K_{ACT}$	in-lb/rad	100,000	Combined actuator/mount stiffness
$J_F$	in-lb-s <sup>2</sup>	96.46	NASA load inertia
$B_F$	in-lb/rad/s	1821.6	NASA load damping
$K_F$	in-lb/rad	$8.6 \times 10^5$ *	NASA load spring rate
$T_1, T_3$	in-lb	Variable	Commanded motor torque
$K_{VC} \begin{cases} K_P \\ K_I \end{cases}$	volts/rad/s	0.178*	Proportional velocity comparator gain
	volts/rad	4.48*	Integral velocity comparator gain
$\theta_F$	radians	Variable	NASA test stand load position
$\theta_F / \theta_O$	rad/rad		$1/\eta_3$ (if load dynamics neglected)
$\theta_O$	radians	Variable	EMA output shaft position

\* Typical value used in the analysis

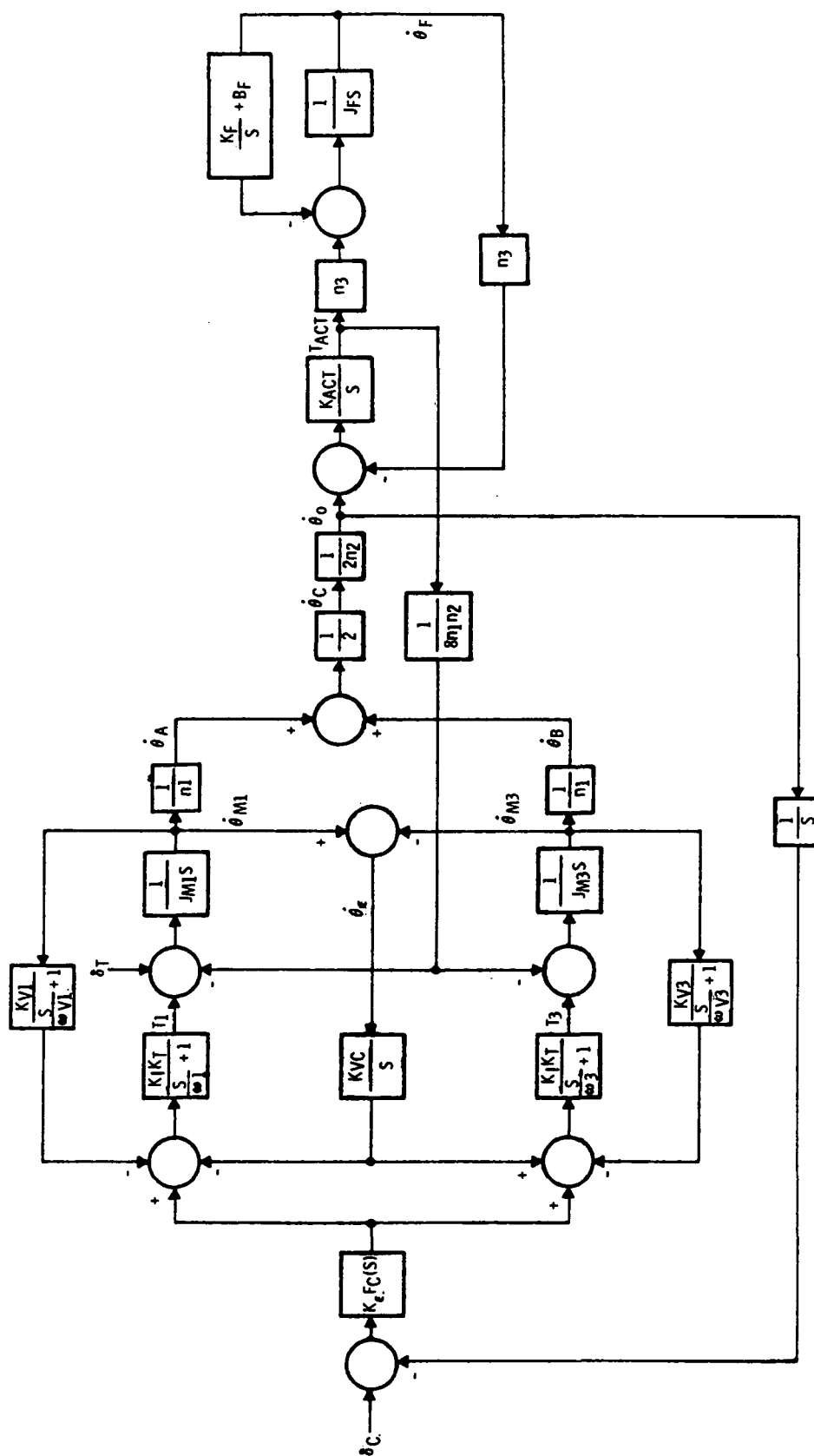


Figure 6-19. Two-Channel Model Block Diagram



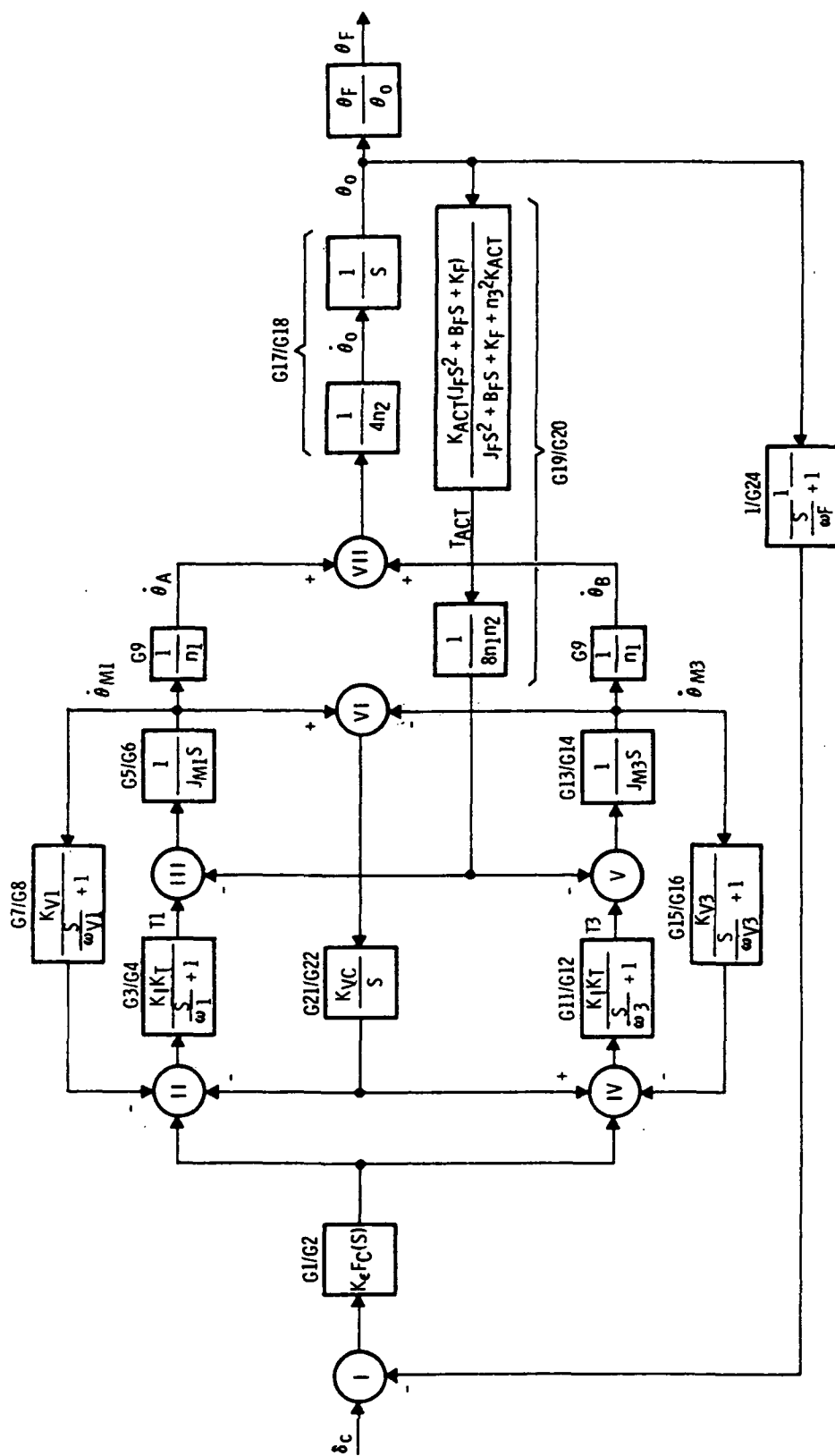


Figure 6-20. Two-Channel Computer Model Block Diagram

The program developed from the model in Figure 6-20 allows stability analyses to be conducted for all compensation loops, and calculates frequency responses and transient responses of all expected system errors with respect to command inputs and disturbances. Table 6-4 is the program listing with sufficient comment cards included to identify significant areas of the model.

No attempt was made in this analysis to provide more complex compensation for the inner loops than was used in the single-channel analysis. However, several compensation methods were considered for use in the outer loop design. Two candidate designs are shown in Figure 6-21. The principal difference between these two is four more dB of loop gain at low frequencies. This impacts low frequency or static position accuracy. The open-loop response of the system outer loop is shown in Figure 6-22. This response was run with the more complicated compensation resulting in greater loop gain below 1 Hz. As can be seen from Figure 6-22, the phase margin is 57 degrees and the gain margin is 10.5 dB. Closed-loop actuator response is shown in Figures 6-23 and 6-24. Performance limits are included for comparison purposes.

Position error response to commanded position inputs are of interest (especially in the low frequency region). Figure 6-25 is the error frequency response and Figure 6-26 is the transient error response to a step function input. The increased loop gain becomes apparent as better error rejection and the large phase margin maintains excellent system damping which is evidenced in the same response. The transient response settling time is also very good which is brought about from adequate bandwidth and greater than 45 degrees of phase margin.

The next two responses deal with the velocity correction error performance. This run utilizes a proportional plus integral compensation scheme. The integral control was selected to eliminate steady-state velocity error, and the proportional gain was selected to aid in the compensation phase. Integral control alone adversely affects stability of the motor inner velocity loops. With the compensation selected, the comparator error response to commanded position and torque disturbance step functions are plotted in Figures 6-27

DAS-360 COMPILER

EPSN(10,1)  
EPSN(11,1)

LINEAR TWO MOTOR MODEL WITH LOAD DYNAMICS

7/22/77

POSITION LOOP COMPENSATION

G1 =  $170.43 \cdot (S/12.566 + 1) \cdot (S/29.74 + 1)$   
G2 =  $(S/904.8 + 1) \cdot (S/427.2 + 1) \cdot (S/6.283 + 1) \cdot (S/47.193 + 1)$

FIRST MOTOR PARAMETERS

G3 = 2.0  
G3 = 2.4  
G4 = 1  
G4 =  $(S/502.7 + 1)$   
G5 = 1  
G6 = .00842\*S  
G6 = .0101\*S

TACHOMETER FEEDBACK

G7 = 0.2694  
G7 = .3233  
  
G8 = 1  
G8 =  $(S/1061.9 + 1)$

SECOND MOTOR PARAMETERS

G11 = 0  
G11 = 2.0  
G11 = 1.6  
G12 = 1  
G12 =  $(S/502.7 + 1)$   
G13 = 0  
G13 = 1  
G14 = 1  
G14 = .00842\*S  
G14 = .0067\*S

TACHOMETER FEEDBACK

G15 = 0  
G15 = 0.2694  
G15 = .2155  
G16 = 1  
G16 =  $(S/1061.9 + 1)$

GEAR BOX PARAMETERS

G9 = 1/3.75  
G17 =  $1/(4 \cdot 1.50)$   
G18 = S

LOAD DYNAMICS

Table 6-4 (Sheet 1 of 4). Two-Channel EMA Model Program Testing

$G19 = 1.E6 * 0.86E6$   
 $G19 = 0.6748 * ((S/94.44) ** 2 + 0.20 * S/94.44 + 1)$   
 $G19 = 0.3374 * ((S/94.44) ** 2 + 0.20 * S/94.44 + 1)$   
 $G20 = (0.86E6 + 238 ** 2 * 1.E6) * 8. * 3.75 * 1.5$   
 $G20 = (S/7663.68) ** 2 + 0.20 * S/7663.68 + 1$

VELOCITY COMPARATOR COMPENSATION

$G21 = 0$   
 $G21 = 1$   
 $G21 = 4.48 * (S/25.13 + 1)$   
 $G22 = 1$   
 $G22 = S$   
 $G24 = 1$   
 $G24 = (S/213.63 + 1)$

CHARACTERISTIC EQUATION FOR OPEN POSITION LOOP

$GCD = G4 * G6 * G8 * G12 * G14 * G16 * G20 * G22 * G24 * G18$   
 $G65 = G12 * G14 * G16 * G20 * G22 * G24 * G18$   
 $G66 = G8 * G12 * G14 * G16 * G20 * G24 * G18$   
 $G67 = G4 * G8 * G12 * G14 * G16 * G22 * G24$   
 $G68 = G4 * G8 * G16 * G24$   
 $G69 = G4 * G6 * G8 * G20 * G22 * G24 * G18$   
 $G70 = G4 * G6 * G8 * G16 * G20 * G24 * G18$   
 $G71 = G4 * G6 * G8 * G12 * G16 * G22 * G24$   
 $G72 = G8 * G12 * G16 * G24$   
 $G77 = G20 * G22 * G24 * G18$   
 $G78 = G16 * G20 * G24 * G18$   
 $G79 = G12 * G16 * G22 * G24$   
 $G80 = G8 * G20 * G24 * G18$   
 $G81 = G8 * G12 * G16 * G24$   
 $G82 = G4 * G8 * G22 * G24$   
 $G83 = G4 * G8 * G16 * G24$   
 $GCE = GCD + G3 * G5 * G7 * G65 + G3 * G5 * G21 * G66 + G5 * G9 * G17 * G19 * G67 +$   
 $1 \quad G5 * G21 * G11 * G13 * G9 * G17 * G19 * G68 + G11 * G13 * G15 * G69 + G11 * G13 * G21 * G70$   
 $2 \quad + G13 * G9 * G17 * G19 * G71 + G13 * G21 * G3 * G5 * G9 * G17 * G19 * G72 + G3 * G5 * G7 * G77$   
 $3 \quad G11 * G13 * G15 * G77$   
 $GCE = GCE + G3 * G5 * G7 * G11 * G13 * G21 * G78 + G3 * G5 * G7 * G13 * G9 * G17 * G19 * G79$   
 $1 \quad + G3 * G5 * G21 * G11 * G13 * G15 * G80 + G3 * G5 * G21 * G13 * G9 * G17 * G19 * G81 +$   
 $2 \quad G5 * G9 * G17 * G19 * G11 * G13 * G15 * G82 + G5 * G9 * G17 * G19 * G11 * G13 * G21 * G83$

CHARACTERISTIC EQUATION FOR CLOSED LOOP RESPONSE

$GLCD = G2 * G4 * G6 * G8 * G12 * G14 * G16 * G20 * G22 * G24 * G18$   
 $G31 = G8 * G12 * G14 * G16 * G20 * G22$   
 $G32 = G4 * G6 * G8 * G16 * G20 * G22$   
 $G33 = G8 * G16 * G20$   
 $G35 = G2 * G12 * G14 * G16 * G20 * G22 * G24 * G18$   
 $G36 = G2 * G8 * G12 * G14 * G16 * G20 * G24 * G18$   
 $G37 = G2 * G4 * G8 * G12 * G14 * G16 * G22 * G24$   
 $G38 = G2 * G4 * G8 * G16 * G24$   
 $G39 = G2 * G4 * G6 * G8 * G20 * G22 * G24 * G18$   
 $G40 = G2 * G4 * G6 * G8 * G16 * G20 * G24 * G18$   
 $G41 = G2 * G4 * G6 * G8 * G12 * G16 * G22 * G24$   
 $G42 = G2 * G8 * G12 * G16 * G24$   
 $G43 = G8 * G20 * G22$

Table 6-4 (Sheet 2 of 4). Two-Channel EMA Model Program Testing

$G44 = G8 \cdot G16 \cdot G20$   
 $G45 = G16 \cdot G20 \cdot G22$   
 $G46 = G8 \cdot G16 \cdot G20$   
 $G47 = G2 \cdot G20 \cdot G22 \cdot G24 \cdot G18$   
 $G48 = G2 \cdot G16 \cdot G20 \cdot G24 \cdot G18$   
 $G49 = G2 \cdot G12 \cdot G16 \cdot G22 \cdot G24$   
 $G50 = G2 \cdot G8 \cdot G20 \cdot G24 \cdot G18$   
 $G51 = G2 \cdot G8 \cdot G12 \cdot G16 \cdot G24$   
 $G52 = G2 \cdot G4 \cdot G8 \cdot G22 \cdot G24$   
 $G53 = G2 \cdot G4 \cdot G8 \cdot G16 \cdot G24$   
 $GCEG = GLCD + G1 \cdot G3 \cdot G5 \cdot G9 \cdot G17 \cdot G31 + G1 \cdot G11 \cdot G13 \cdot G9 \cdot G17 \cdot G32 +$   
 $1 \ G1 \cdot G3 \cdot G5 \cdot G21 \cdot G11 \cdot G13 \cdot G9 \cdot G17 \cdot G33 + G1 \cdot G11 \cdot G13 \cdot G21 \cdot G3 \cdot G5 \cdot G9 \cdot G17 \cdot G33$   
 $2 + G3 \cdot G5 \cdot G7 \cdot G35 + G3 \cdot G5 \cdot G21 \cdot G36 + G5 \cdot G9 \cdot G17 \cdot G19 \cdot G37 + G5 \cdot G21 \cdot G11 \cdot$   
 $3 \ G13 \cdot G9 \cdot G17 \cdot G19 \cdot G38$   
 $GCEG = GCEQ + G11 \cdot G13 \cdot G15 \cdot G39 + G11 \cdot G13 \cdot G21 \cdot G40 + G13 \cdot G9 \cdot G17 \cdot G19 \cdot$   
 $1 \ G41 + G13 \cdot G21 \cdot G3 \cdot G5 \cdot G9 \cdot G17 \cdot G19 \cdot G42 + G1 \cdot G3 \cdot G5 \cdot G9 \cdot G17 \cdot G11 \cdot G13 \cdot G15$   
 $2 \cdot G43 + G1 \cdot G3 \cdot G5 \cdot G9 \cdot G17 \cdot G11 \cdot G13 \cdot G21 \cdot G44 + G1 \cdot G11 \cdot G13 \cdot G9 \cdot G17 \cdot G3 \cdot G5 \cdot$   
 $3 \ G7 \cdot G45 + G1 \cdot G11 \cdot G13 \cdot G9 \cdot G17 \cdot G3 \cdot G5 \cdot G21 \cdot G46$   
 $GCEG = GCEQ + G3 \cdot G5 \cdot G7 \cdot G11 \cdot G13 \cdot G15 \cdot G47 + G3 \cdot G5 \cdot G7 \cdot G11 \cdot G13 \cdot G21 \cdot G48$   
 $1 + G3 \cdot G5 \cdot G7 \cdot G13 \cdot G9 \cdot G17 \cdot G19 \cdot G49 + G3 \cdot G5 \cdot G21 \cdot G11 \cdot G13 \cdot G15 \cdot G50 + G3 \cdot G5$   
 $2 \cdot G21 \cdot G13 \cdot G9 \cdot G17 \cdot G19 \cdot G51 + G5 \cdot G9 \cdot G17 \cdot G19 \cdot G11 \cdot G13 \cdot G15 \cdot G52 + G5 \cdot G9$   
 $3 \cdot G17 \cdot G19 \cdot G11 \cdot G13 \cdot G21 \cdot G53$

#### OPEN POSITION LOOP RESPONSE

$GPLP = G1 \cdot (G3 \cdot G5 \cdot G9 \cdot G17 \cdot (G12 \cdot G14 \cdot G16 \cdot G22 + G11 \cdot G13 \cdot G15 \cdot G22 + G11 \cdot$   
 $1 \cdot G13 \cdot G21 \cdot G16) \cdot G8 \cdot G20 + G3 \cdot G5 \cdot G21 \cdot G11 \cdot G13 \cdot G9 \cdot G17 \cdot G8 \cdot G16 \cdot G20 + G11$   
 $2 \cdot G13 \cdot G9 \cdot G17 \cdot (G4 \cdot G6 \cdot G8 \cdot G22 + G3 \cdot G5 \cdot G7 \cdot G22 + G3 \cdot G5 \cdot G21 \cdot G8) \cdot G16 \cdot G20 -$   
 $3 + G11 \cdot G13 \cdot G21 \cdot G3 \cdot G5 \cdot G9 \cdot G17 \cdot G8 \cdot G16 \cdot G20) / (G2 \cdot GCE)$   
 $FREQ( \quad , \quad , .1, 1.0, .1, 1., 50., 1., GPLP, CYC)$

#### CLOSED POSITION LOOP RESPONSE

$GCL = (G1 \cdot G3 \cdot G5 \cdot G9 \cdot G17 \cdot (G12 \cdot G14 \cdot G16 \cdot G22 + G11 \cdot G13 \cdot G15 \cdot G22 + G11 \cdot$   
 $1 \ G13 \cdot G21 \cdot G16) \cdot G8 \cdot G20 + G1 \cdot G3 \cdot G5 \cdot G21 \cdot G11 \cdot G13 \cdot G9 \cdot G17 \cdot G8 \cdot G16 \cdot G20 +$   
 $2 \ G1 \cdot G11 \cdot G13 \cdot G9 \cdot G17 \cdot (G4 \cdot G6 \cdot G8 \cdot G22 + G3 \cdot G5 \cdot G7 \cdot G22 + G3 \cdot G5 \cdot G21 \cdot G8) \cdot$   
 $3 \ G16 \cdot G20 + G1 \cdot G11 \cdot G13 \cdot G21 \cdot G3 \cdot G5 \cdot G9 \cdot G17 \cdot G8 \cdot G16 \cdot G20) / GCEQ$   
 $FREQ( \quad , \quad , .1, 1.0, .1, 1., 50., 1., GCL, CYC)$

#### POSITION ERROR TO POSITION COMMAND RESPONSE

$GEEM = GCE \cdot G2 / GCEG$   
 $FREQ( \quad , \quad , .1, 1.0, .1, 1., 50., 1., GEEM, CYC)$

#### POSITION ERROR STEP RESPONSE

$GTEC = GEEM / S$   
 $TRNS( \quad , C.C, 2.0, 0.01, GTEC)$

#### POSITION ERROR RAMP RESPONSE

$GTEC = GEEM / S \cdot S^2$   
 $TRNS( \quad , C.C, 2.0, 0.01, GTEC)$

#### VELOCITY ERROR TO POSITION COMMAND

$GVEP = (G1 \cdot G3 \cdot G5 \cdot (G12 \cdot G14 \cdot G16 \cdot G18 \cdot G20 + G11 \cdot G13 \cdot G15 \cdot G18 \cdot G20 +$   
 $1 \ G13 \cdot G9 \cdot G17 \cdot G19 \cdot G12 \cdot G16) \cdot G8 \cdot G22 \cdot G24 + G1 \cdot G3 \cdot G5 \cdot G9 \cdot G17 \cdot G19 \cdot G13 \cdot G8 \cdot$

```

3 G12*G16*G22*G24 = G1*G11*G13*(G4*G6*G8*G18*G20 + G3*G5*G7*G18*G20
  + G5*G9*G17*G19*G4*G8)*G16*G22*G24 = G1*G11*G13*G9*G17*G19*G5*G4
4 *G8*G16*G22*G24)/GCEQ
FREQ( , ,.1,1.C,.1,1.,50.,1.,GREP,CYC)

```

#### VELOCITY ERROR STEP RESPONSE

```

GTRF = GREP/S
TRNS( ,C.O,2.C,0.C1,GTRF)

```

#### VELOCITY ERROR RAMP RESPONSE

```

GTRP = GREP/S**2
TRNS( ,C.O,2.5,0.1,GTRP)

```

#### VELOCITY ERROR TO TORQUE DISTURBANCE

```

GRET = ((G2*G12*G14*G16*G18*G20*G24 + G1*G11*G13*G9*G17*G16*G20 +
1 G11*G13*G15*G2*G18*G20*G24 + G13*G9*G17*G19*G2*G12*G16*G24)*G5*
2 G4*G8*G22 + G5*G9*G17*G19*G13*G2*G4*G8*G12*G16*G22*G24 +
3 G5*G9*G17*G1*G11*G13*G4*G8*G16*G20*G22)/GCEQ
FREQ( , ,.1,1.C,.1,1.,50.,1.,GRET,CYC)

```

#### VELOCITY ERROR STEP RESPONSE

```

GTRT = GRET/S
TRNS( ,C.O,2.C,0.C1,GTRT)

```

#### VELOCITY ERROR RAMP RESPONSE

```

GTRT = GRET/S**2
TRNS( ,C.O,2.C,0.C1,GTRT)

```

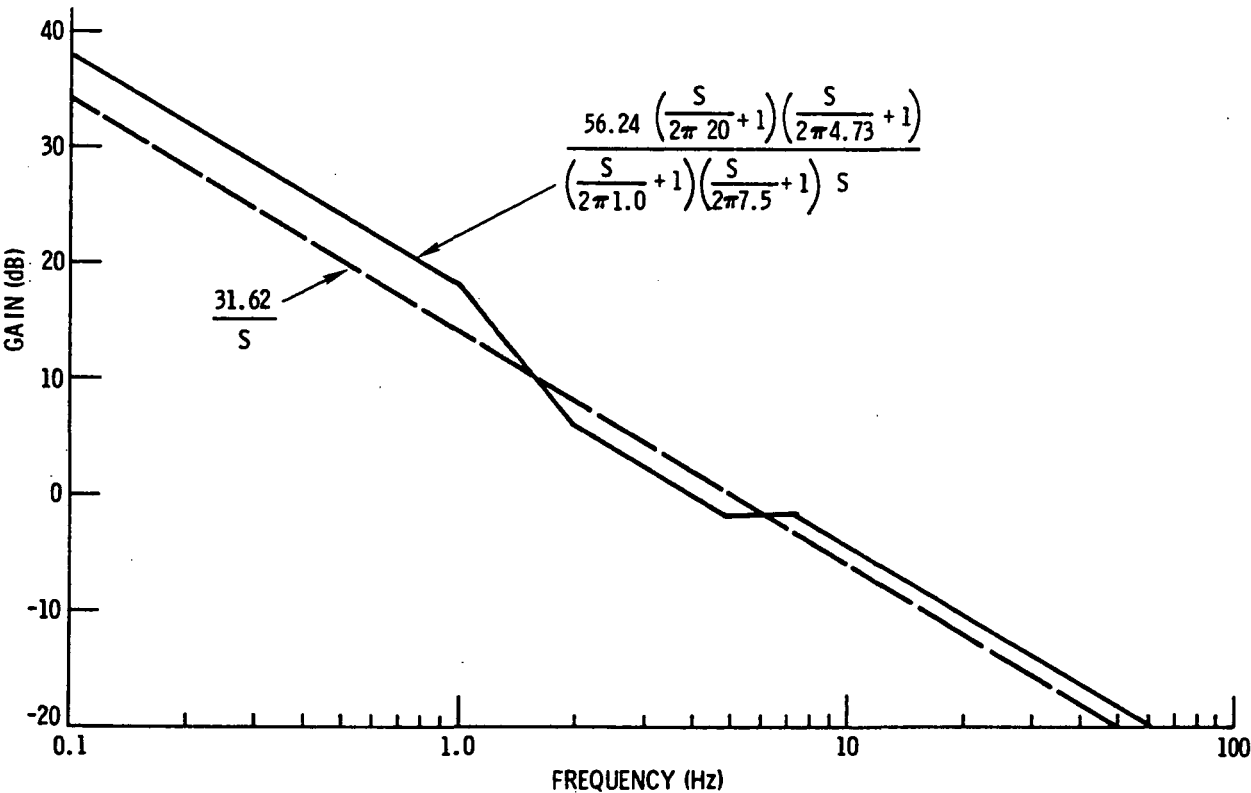


Figure 6-21. Two-Motor Model Outer Loop Compensation

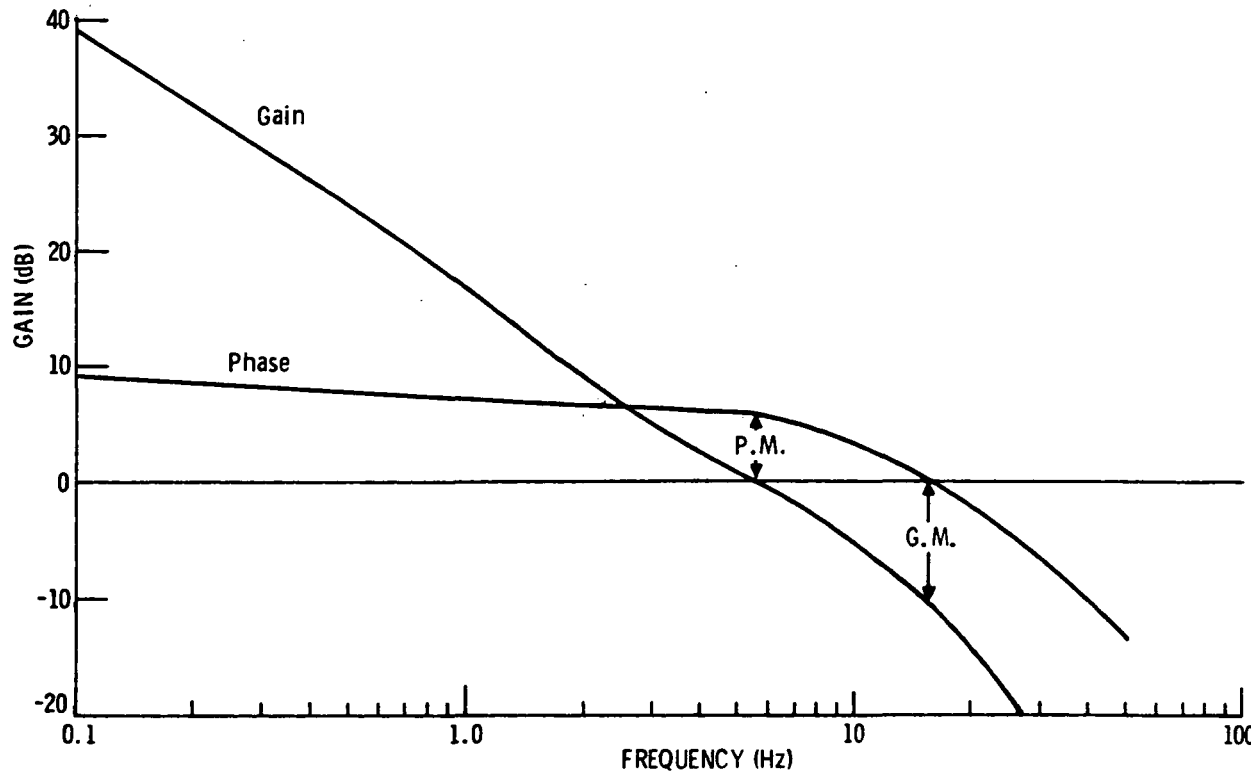


Figure 6-22. Open-Loop Position Loop

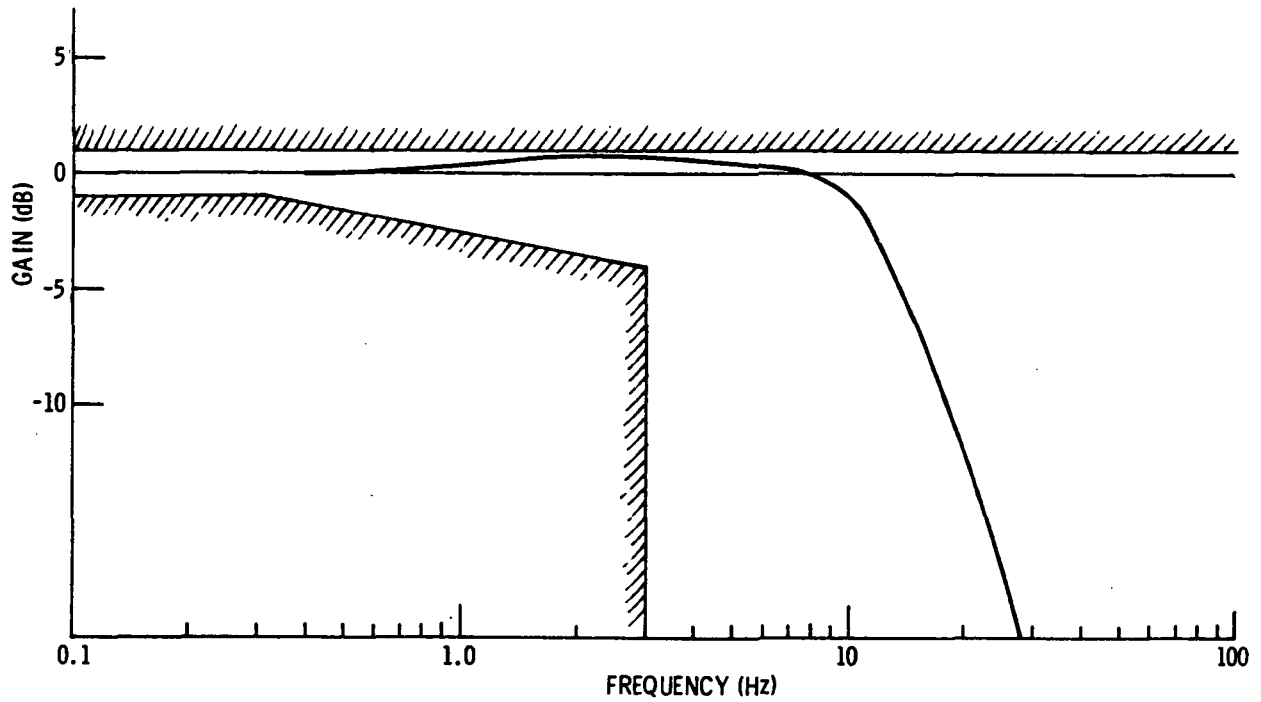


Figure 6-23. Closed-Loop Actuator Response to Position Command (Gain)

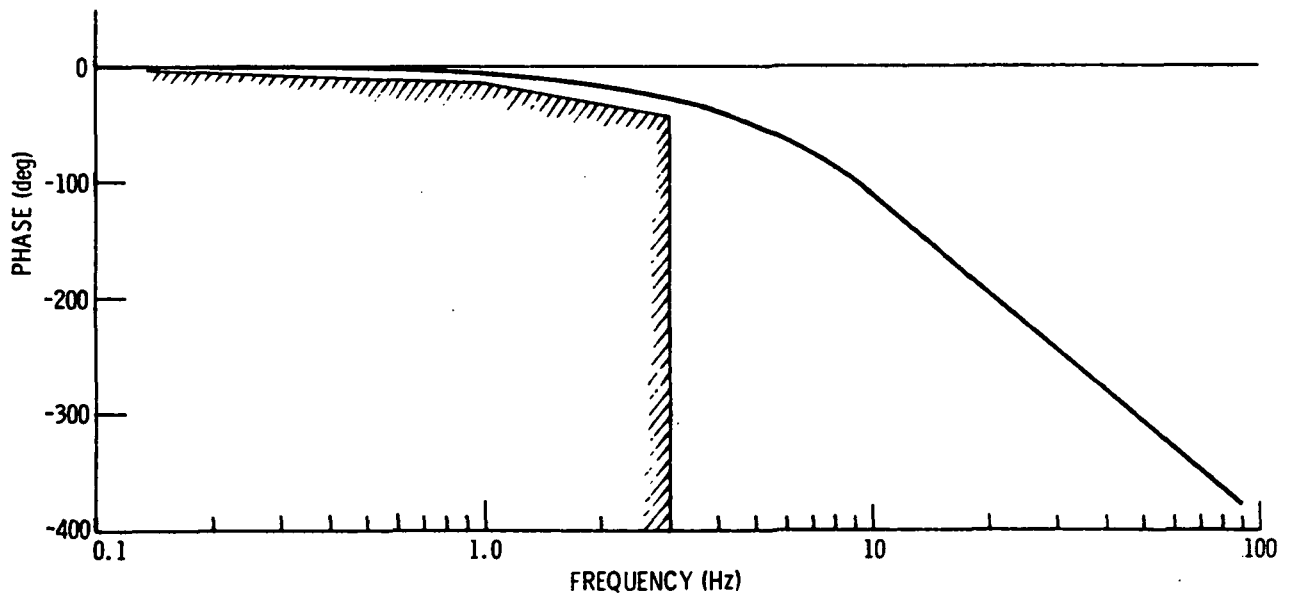


Figure 6-24. Closed-Loop Actuator Response to Position Command (Phase)



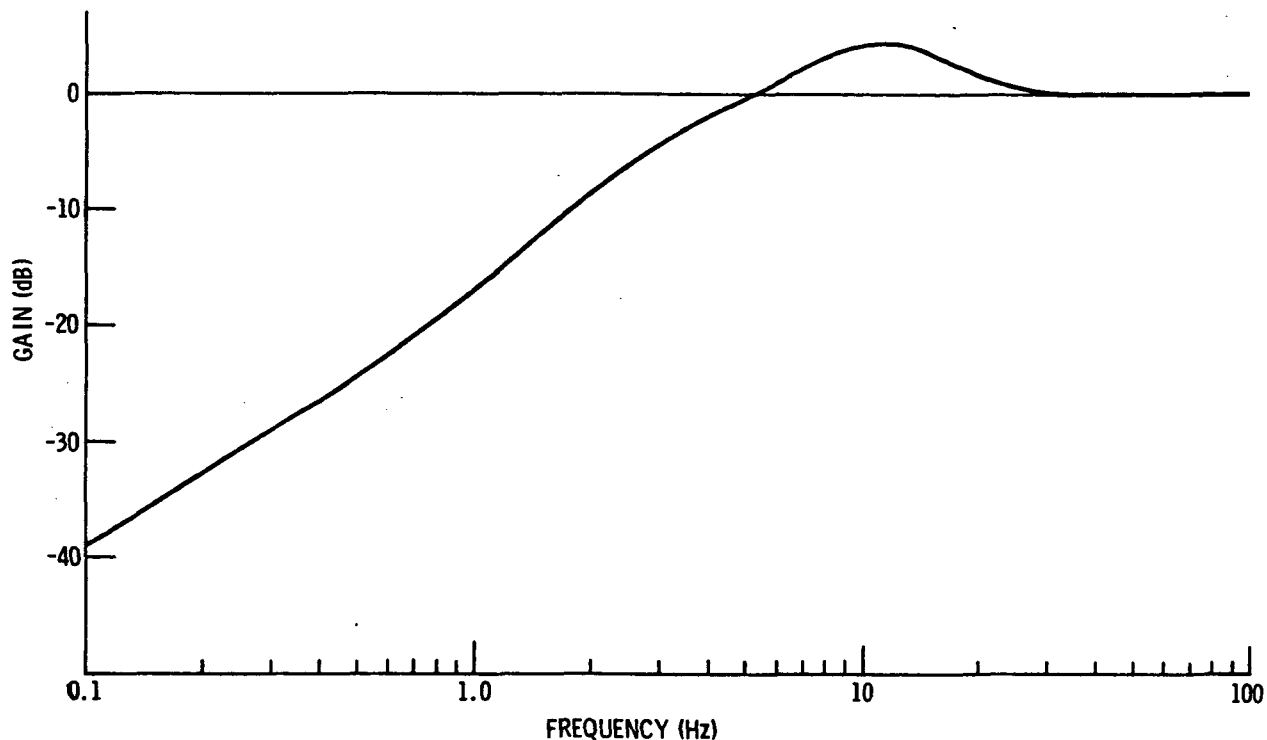


Figure 6-25. Position Error Response to Position Command

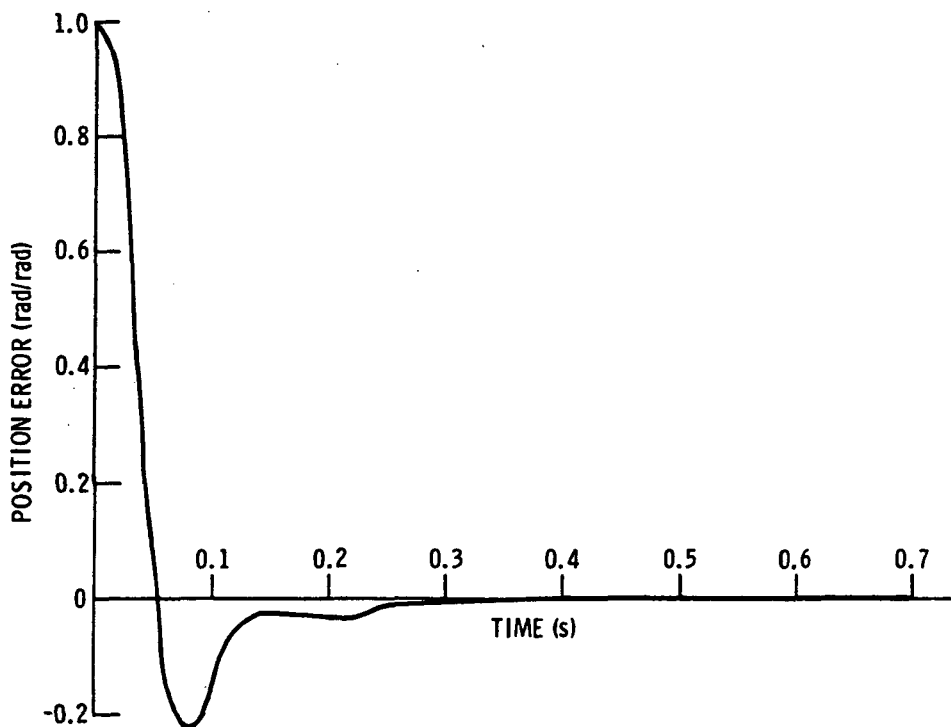


Figure 6-26. Position Error Response to Stop Position Command

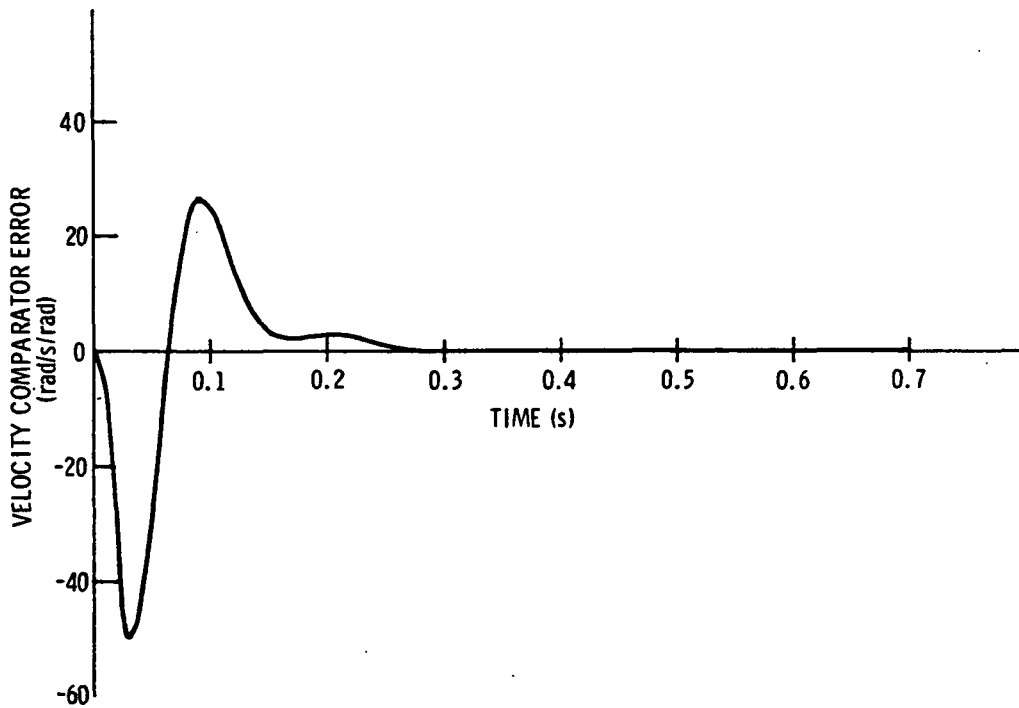


Figure 6-27. Velocity Comparator Error to Position Command Step Response

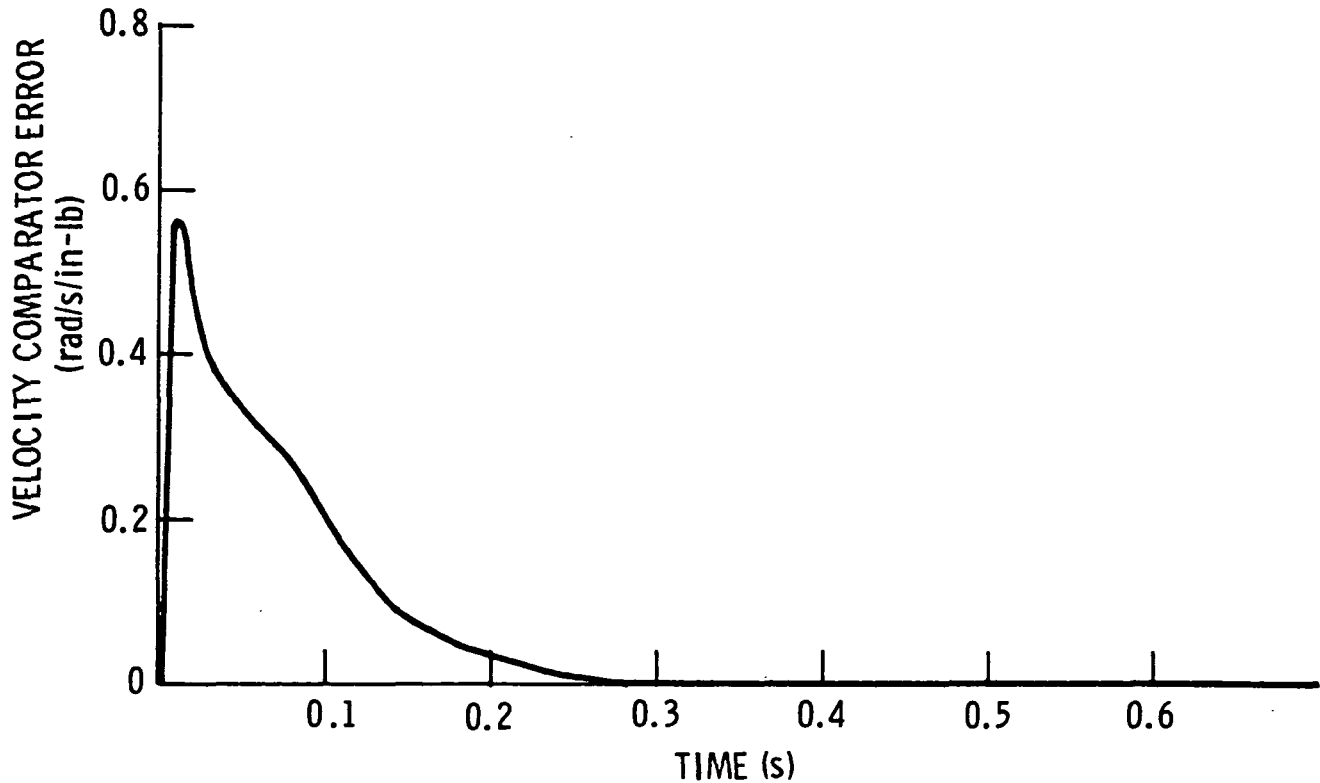


Figure 6-28. Velocity Comparator Error to Torque Disturbance Step Response

and 6-28, respectively. Both responses show settling times less than 0.3 seconds and are very well damped at all times.

To emphasize velocity tracking problems, these runs were made with variances in the two motor's inertias, torque constants, and tachometer feedback gains. One motor's parameters were increased 20% while the second motor's parameters were decreased by 20%. These are extreme changes in values and are definitely not variances tolerated in the hardware.

#### 6.2.4 SINGLE-CHANNEL NONLINEAR ANALYSIS

The preceding analysis of the linearized two-channel model is very useful in describing the small-signal linear operation of the actuator, but it is not adequate to describe the large-signal, nonlinear response characteristics. For this purpose, a simplified single-channel nonlinear model was derived. The model derivation and results are presented in the following paragraphs.

The model simplification used for this analysis is based on the results obtained from the linear two-channel model. In that study it was found that incorporating the load characteristics had virtually no effect on the EMA dynamics. This result was also verified during laboratory tests. In addition, it was found that the velocity correction loops had very little influence on the basic tachometer loop stability. For these two reasons, the nonlinear model was kept simple, using a single motor representation of the system. The single-channel model simulates the proper loop dynamics as well as the effective gear ratio which results when two motors are operating. The model block diagram is shown in Figure 6-29.

During laboratory testing of the EMA (see Paragraph 7.4) two nonlinearities were repeatedly observed: torque and velocity saturation. Since these were felt to be the dominant nonlinearities, they were incorporated in the model. In the physical hardware, velocity limiting occurs because the effective motor counter-emf becomes as large as the battery voltage, thus preventing further speed-up of the machine. Torque limiting occurs because the power converter

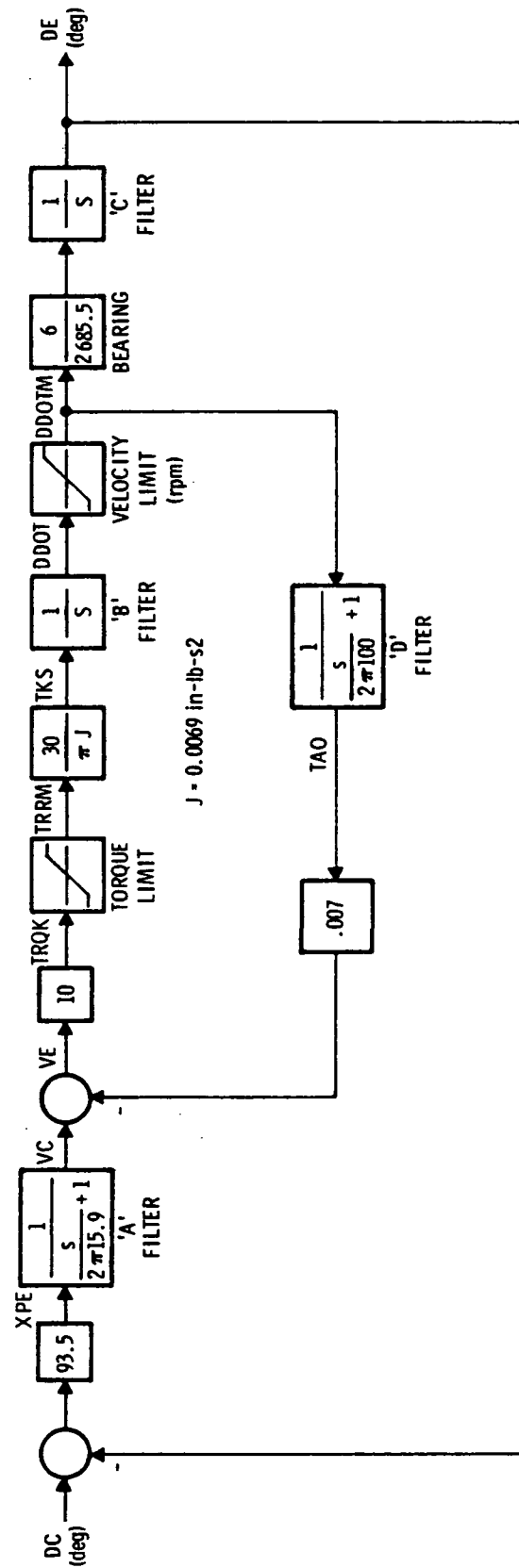


Figure 6-29. EMA Single-Channel Nonlinear Model

limits the motor current. In the case of the four-channel system, the velocity limit is about 9500 r/min (with nominal battery voltage) and the motoring current limit of 40 A limits the torque to 80 in-lb. In the single-channel power electronics breadboard the nominal current limit is 60 A, which results in a torque limit of 120 in-lb.

The nonlinear model incorporating torque and velocity limiting was simulated on the XDS Sigma 7 digital computer. Transfer functions in the control loops were converted from the s-domain to z-domain sampled data equations by means of the algebraic bilinear z-transform. The computer program listing is shown in Table 6-5. With the comment cards in the listing and the system block diagram shown in Figure 6-29, the program is largely self-explanatory. The subroutines listed in the program are for the complete list of s to z transforms normally encountered in most simulations; not all of them were needed in the model even though they are included in the program listing.

Program checkout was accomplished by opening up the torque and velocity limits to values which would assure that the solution would run in a linear manner. With a one-degree step function input, the single-channel model was run and the output compared very well with the two-channel linear step response (Table 6-6). During this run the maximum torque required was 399.6 in-lb and the maximum velocity was 10,021.6 r/min during the 1-degree step response model run. The 9500 r/min velocity limit is not very significant for a 1-degree step input, but the 80 in-lb torque limit is.

Eight cases were run with both velocity and torque limits imposed on the solution. All runs were made with a 9500 r/min velocity limit. Four of the runs were made with an 80 in-lb torque limit, and the remaining four were run with a 120 in-lb limit. Figures 6-30 through 6-33 are the responses to step commands of 2, 3, 4 and 5% of full travel (55 degrees). For comparison purposes the step response design goal envelope is plotted on each response. For the most part the runs with the 80 in-lb limit meet the system design goals. These results agree quite well with the EMA laboratory runs, as

```

1: C
2: C      SINGLE CHANNEL NONLINEAR EMA MODEL
3: C
4:      NAMEDLIST WA,WD,TRKMAX,DDTMAX,DC,DT
5:      NAMEDLIST KPRNT, TEND
6:      INPUT
7: C
8: C      INITIALIZE PARAMETERS
9: C
10:      YA1 = YAO = XA1 = XAO = 0
11:      YB1 = YBO = XB1 = XBO = 0
12:      YD1 = YDO = XD1 = XDO = 0
13:      YC1 = YCO = XC1 = XCO = 0
14:      T = 0
15:      KI = 0
16: C
17: C      CALCULATE FILTER COEFFICIENTS
18: C
19:      CALL CLWPASS(AAO,AB1,WA,1.0,DT)
20:      CALL CINTGRAL(BAO,1.0,DT)
21:      CALL CINTGRAL(CAO,1.0,DT)
22:      CALL CLWPASS(DAO,DB1,WD,1.0,DT)
23:      WRITE(108,9000)
24:      9000 FORMAT('1',T10,'EMA ONE CHANNEL NONLINEAR MODEL'//)
25:      OUTPUT WA,WD,TRKMAX,DDTMAX
26:      OUTPUT DC,DT,KPRNT,TEND
27:      OUTPUT AAO,AB1,BAO,CAO,DAO,DB1
28:      WRITE(108,9020)
29:      9020 FORMAT(/)
30:      WRITE(108,9040)
31:      9040 FORMAT(T6,'T',T15,' DE ',T30,'TRCK',T41,'TRKM',T55,'DDAT',T67,
32:      C 'DDDTM')
33:      WRITE(108,9050)
34:      9050 FORMAT(/)
35:      3000 CONTINUE
36:      KI = KI + 1
37:      IF(T.GT.TEND) GO TO 9999
38: C
39: C      POSITION LOOP EQUATION
40: C
41:      XPE = (DC - DE)*93.5
42: C
43: C      A FILTER ( SINGLE LAG )
44: C
45:      XAO = XPE
46:      YAO = AAO*(XAO + XA1) - AB1*YA1
47:      YA1 = YAO; XA1 = XAO
48:      VC = YAO
49: C
50: C      TACHOMETER LOOP EQUATION
51: C
52: C
53: C      D FILTER ( SINGLE LAG )
54: C
55:      XDO = DDO*TM
56:      YDO = DAO*(XDO + XD1) - DB1*YD1
57:      YD1 = YDO; XD1 = XDO
58:      TAO = YDO
59:      VE = VC + TAO*.007

```

Table 6-5 (Sheet 1 of 3). Nonlinear EMA Model Program Testing

```

60:      TRCK = 10.*VE
61: C
62: C      TORQUE SATURATION
63: C
64:      TRKM = TRGK
65:      IF (TRGK.GT.*TRKMAX) TRKM=TRKMAX
66:      IF (TRGK.LT.*-TRKMAX) TRKM=-TRKMAX
67:      TKS = 1383.96*TRKM
68: C
69: C      B FILTER ( INTEGRATOR )
70: C
71:      XB0=TKS
72:      YB0 = BA0*(XB0 + XB1) + YB1
73:      XB1=XB0;YB1=YB0
74:      DD0T = YB0
75: C
76: C      VELOCITY SATURATION
77: C
78:      DD0TM = DD0T
79:      IF (DD0T.GT.*DDTMAX) DD0TM=DDTMAX;YB1=DDTMAX
80:      IF (DD0T.LT.*-DDTMAX) DD0TM=-DDTMAX;YB1=-DDTMAX
81: C
82: C
83: C      C FILTER ( INTEGRATOR )
84: C
85:      XC0 = DD0TM*.002234
86:      YC0 = CA0*(XC0 + XC1) + YC1
87:      XC1 = XC0;YC1 = YC0
88:      DE = YC0
89:      IF (T.LT.DT) GO TO 1500
90:      IF (KI.EG.*KPRNT) GO TO 1500
91:      GO TO 2500
92: 1500 CONTINUE
93:      KI = 0
94: C
95: C      OUTPUT DATA
96: C
97:      WRITE (108,9100) T,DE,TRCK,TRKM,DD0T,DD0TM
98: 9100 FORMAT (T4,F5.3,T14,F8.3,T26,F9.2,T38,F8.3,T51,F9.2,T64,F7.2)
99: 2500 CONTINUE
100:      T = T + DT
101:      GO TO 3000
102: 9999 CONTINUE
103:      END

```

Table 6-5 (Sheet 2 of 3). Nonlinear EMA Model Program Testing

```

1:      SUBROUTINE CSECND(AC,B1,B2,WZ,ZETA,XK,TF)
2:      W = TAN(WZ*TF/2.); W2 = W*W; ZW = 2.*ZETA*W; D = 1. + ZW + W2
3:      AO = W2*XK/D; B1 = -2.*(1.-W2)/D; B2 = (1.-ZW+W2)/D;      RETURN
4:      ENTRY      CHIPASS(AO,B1,B2,WZ,ZETA,XK,TF)
5:      W = TAN(WZ*TF/2.); W2 = W*W; ZW = 2.*ZETA*W; D = 1. + ZW + W2
6:      AO =      XK/D; B1 = -2.*(1.-W2)/D; B2 = (1.-ZW+W2)/D;      RETURN
7:      ENTRY CRATELAG(AO,B1,WZ,XK,TF); D = 2./TF; GO TO 1
8:      ENTRY CLWPASS(AO,B1,WZ,XK,TF); D = 1.
9:      1 W = TAN(WZ*TF/2.); AC = D*W*XK/(1.+W); B1 = -(1.-W)/(1.+W); RETURN
10:     ENTRY CINTGRAL(AO,XK,TF); AO = XK*TF/2.;      RETURN
11:     ENTRY CINTLD(AO,A1,WZ,XK,TF); W=TAN(WZ*TF/2.); D=XK*TF/2.
12:     AO=D*(1.+W)/W; A1=-D*(1.-W)/W;
13:     ENTRY CRATE (AO,XK,TF); AC = 2.*XK/TF;      RETURN
14:     ENTRY LAGLEAD(AO,A1,B1,WZ1,WZ2,XK,TF); W1 = TAN(WZ1*TF/2.)
15:     W2 = TAN(WZ2*TF/2.); D = 1.+W2; W21 = W2/W1; B1 = -(1.-W2)/D
16:     AC = XK*W21*(1.+W1)/D; A1 = -XK*W21*(1.-W1)/D;      RETURN
17:     END

```

Table 6-5 (Sheet 3 of 3). Nonlinear EMA Model Program Testing



Step Magnitude (deg)	Time to Reach First Zero Error		Peak Overshoot (%)	Undershoot (%)	* Settling		Comment
	Condition (ms)	Time (ms)			Time (ms)		
Unity	65	7	1.5		110		Linear model
1.0	67	7.3	0.6		112		Nonlinear model with limits opened up
1.1	115	25	4.1		235		EMA
1.1	105	24.8	2.0		210		Model
1.65	134	29	4.7		265		EMA
1.65	125	28	2.1		245		Model
2.2	158	25.9	4.7		305		EMA
2.2	150	21.6	1.6		270		Model
2.75	187	22.4	3.8		334		EMA
2.75	175	17.4	1.2		295		Model

\* Within    5% of input

Table 6-6. Step Response Comparisons

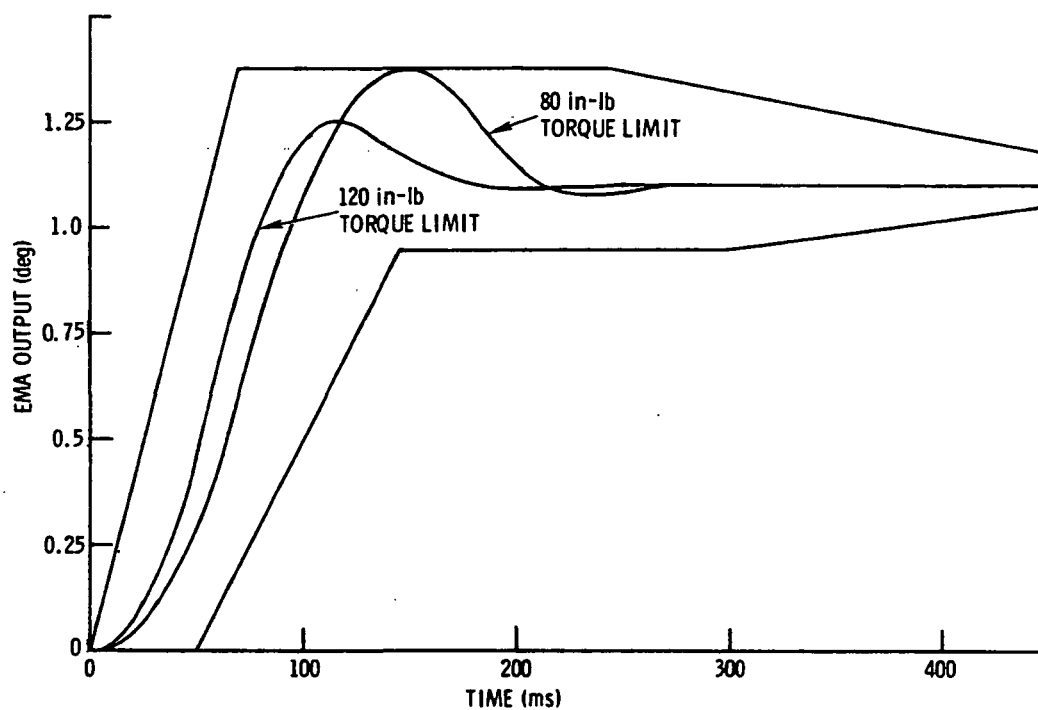


Figure 6-30. 2% FT Step Response

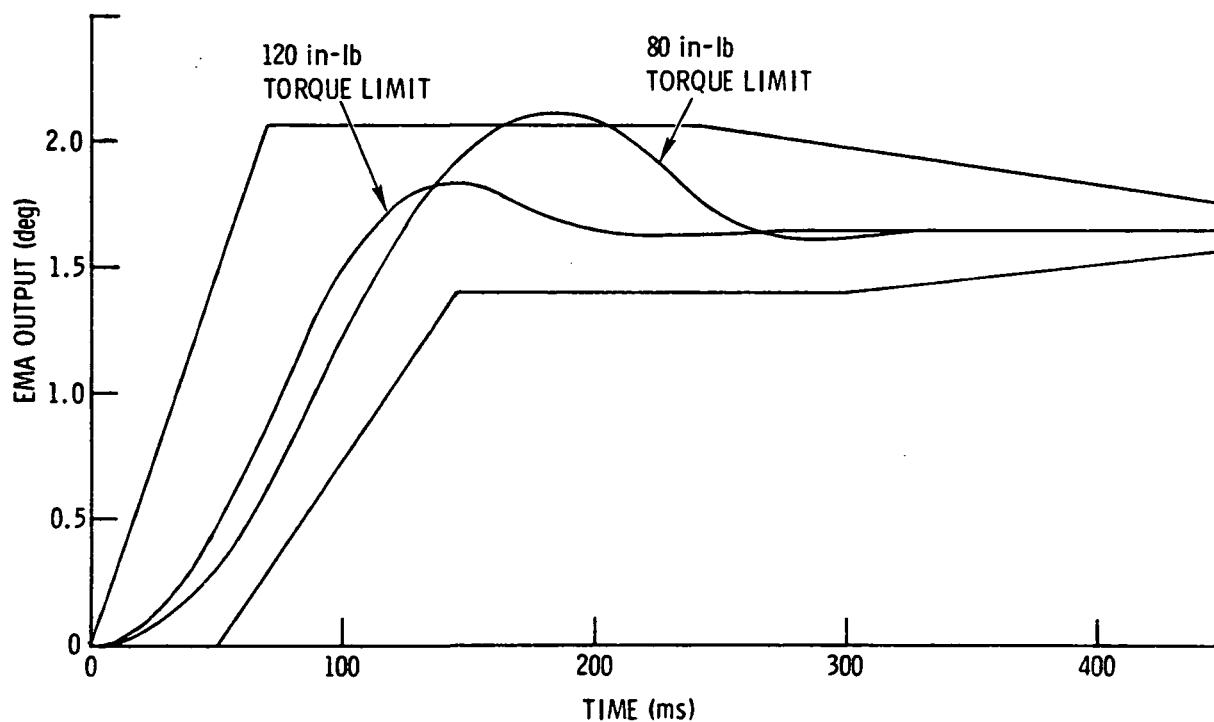


Figure 6-31. 3% FT Step Response

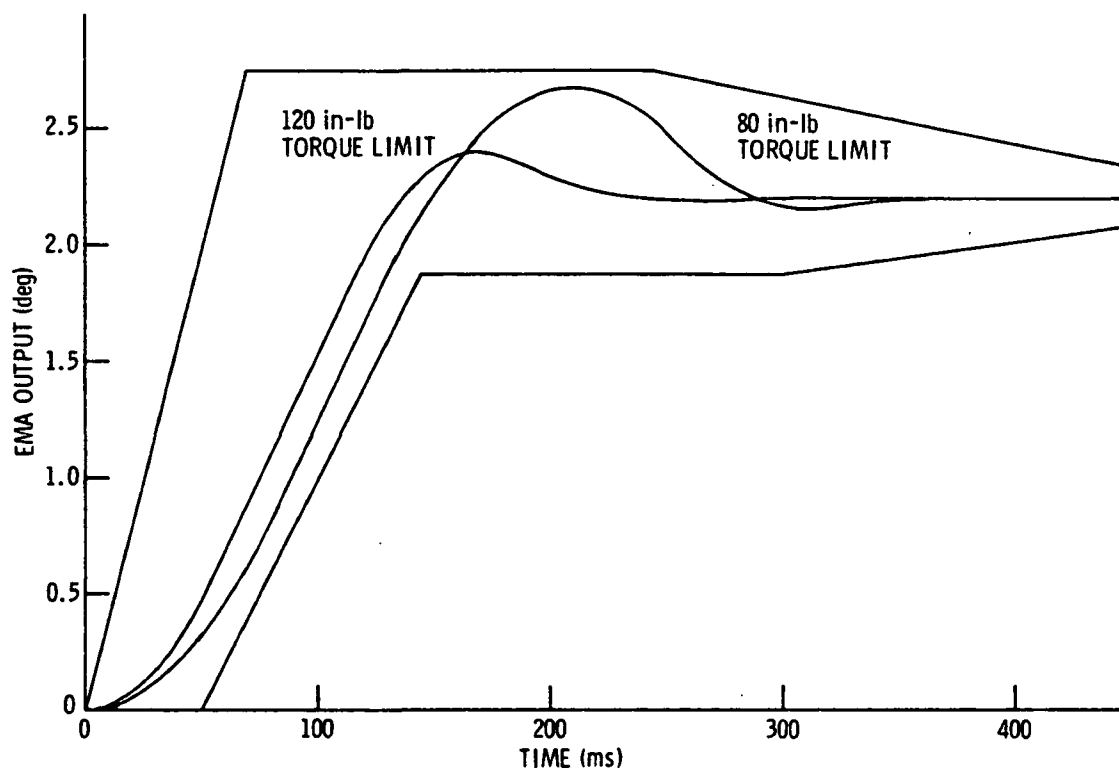


Figure 6-32. 4% FT Step Response

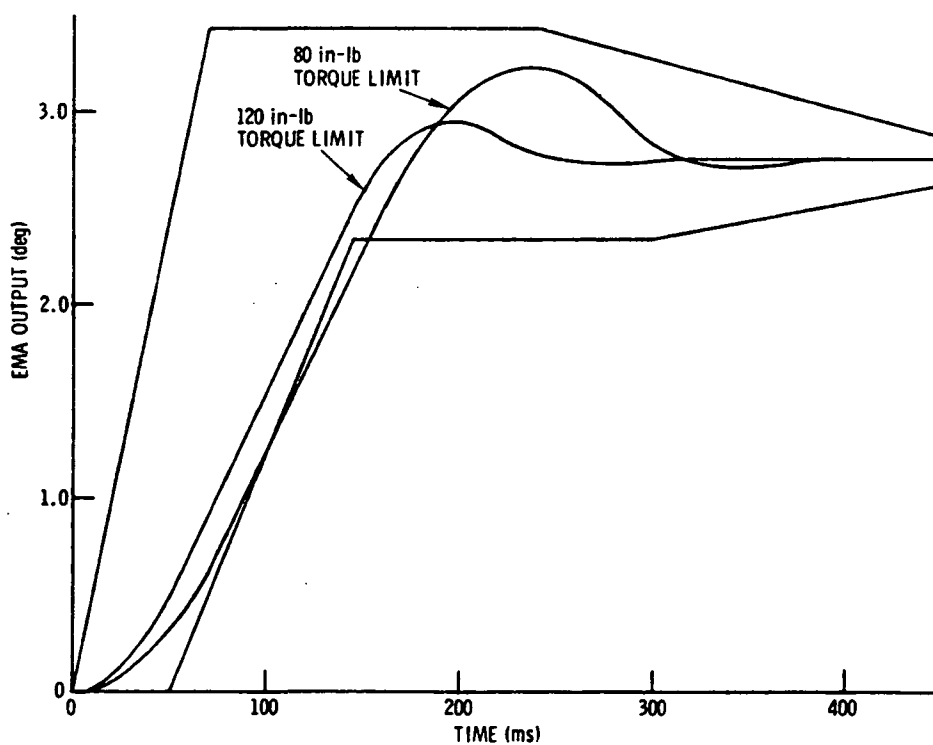


Figure 6-33. 5% FT Step Response

shown in Table 6-6. Times to reach the first zero error agree to within 8.5% and the setting times agree to within 11.5%. Several parameters can be fine-tuned to get better agreement. The 80 in-lb limit set in the model is probably slightly different from the actual torque limit set in the EMA. The value of  $0.0069 \text{ in-lb-s}^2$  for the motor inertia could be slightly different from the hardware and the actual velocity limit may be slightly different from 9500 r/min, since it is strongly dependent on the battery voltage.

In summary, the model comparison with laboratory results is very good, even though the model is somewhat simplified. It has verified laboratory observations that the two dominant nonlinearities in the EMA are torque and velocity saturation. Because the comparison came out so close to actual results, it was felt that changing the torque limit to 120 in-lb would be instructive. Based on the results in Figures 6-30 through 6-33, the 120 in-lb limit would allow the response to stay within design goal limits for step commands up to 5% of full travel.

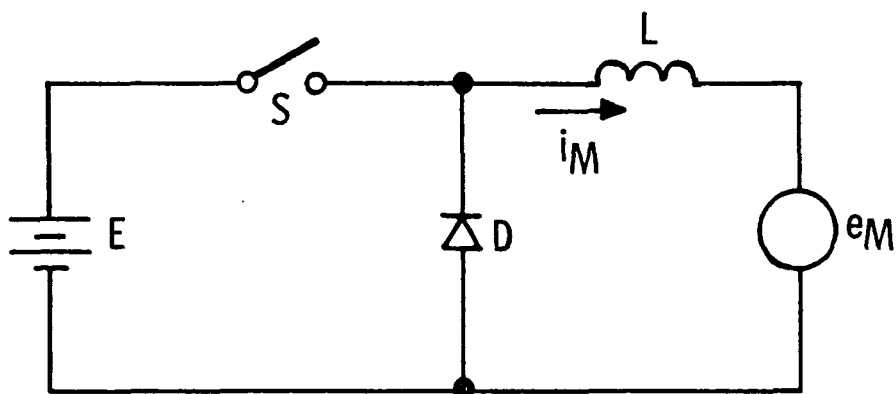
### 6.3 CHOPPER CIRCUIT ANALYSIS

One of the most important subsystems of the EMA is the chopper circuit of the power converter (which is discussed in Paragraph 5.1.2). Its operation is nonlinear, but a very informative approximate analysis of its behavior can be made using the simplified circuits of Figures 6-34 and 6-35 which show both motoring and regenerative modes of operation. Although these idealized schematics neglect the losses and parasitics of the actual circuits, they provide a convenient, straightforward means for analyzing the operation of the chopper in both the motoring and regenerative braking modes.

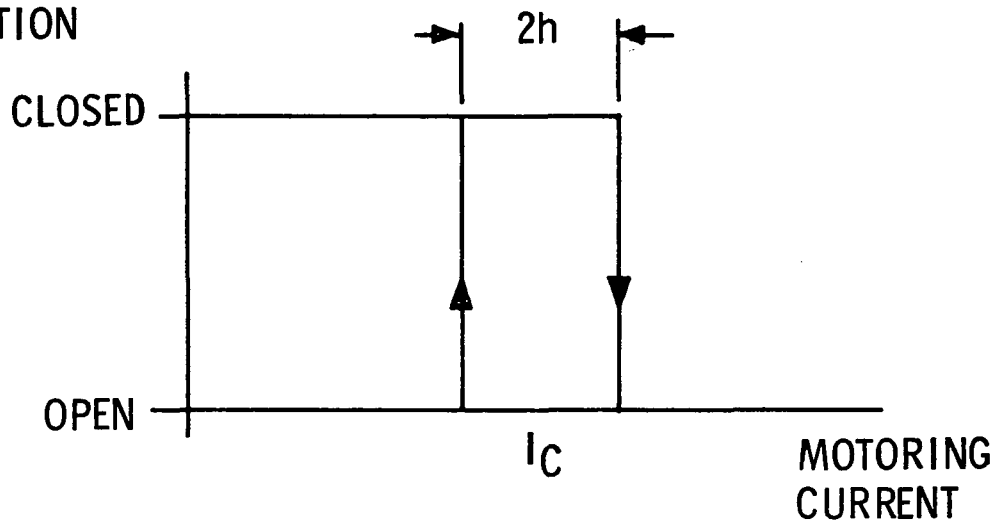
#### 6.3.1 MOTORING MODE

When the motoring mode is being used, and the chopper has settled into its normal mode of operation, the time that the switch is closed is given by

$$T_1 = \frac{2hL}{E - e_M} \quad (6-31)$$



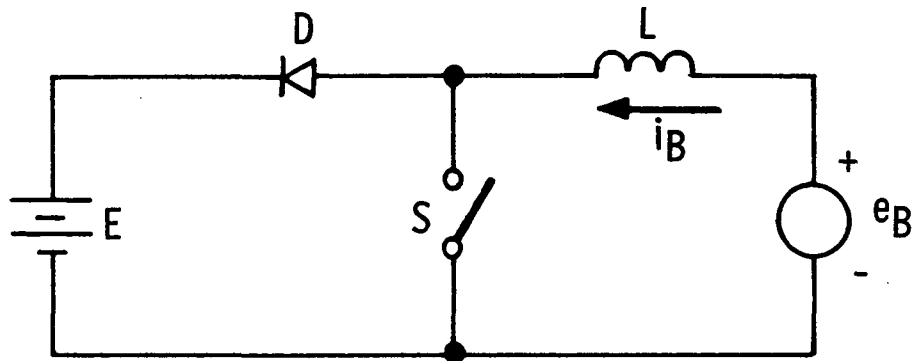
SWITCH  
CONDITION



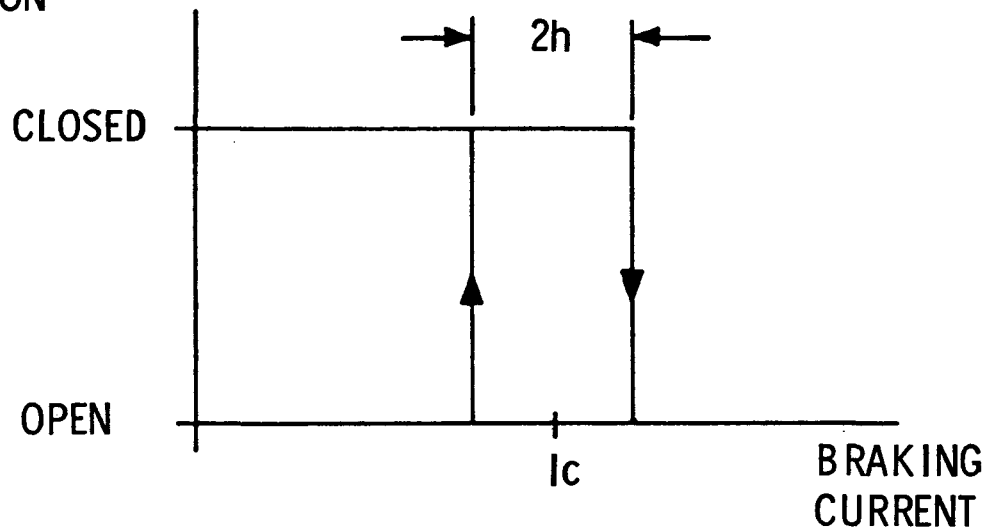
Switch Closed: 
$$\frac{di_M}{dt} = \frac{E - e_M}{L}$$

Switch Open: 
$$\frac{di_M}{dt} = \frac{-e_M}{L}$$

Figure 6-34. Chopper Operation, Motoring Mode



SWITCH  
CONDITION



Switch Closed: 
$$\frac{di_B}{dt} = \frac{e_B}{L}$$

Switch Open: 
$$\frac{di_B}{dt} = \frac{e_B - E}{L}$$

Figure 6-35. Chopper Operation, Braking Mode

The switch then opens for the interval

$$T_2 = \frac{2hL}{e_M} \quad (6-32)$$

The period of the sawtooth waveform is therefore

$$T_M = T_1 + T_2 = 2hL \left[ \frac{1}{E - e_M} + \frac{1}{e_M} \right] \quad (6-33)$$

Simplifying

$$T_M = \frac{2hLE}{e_M(E - e_M)} \quad (6-34)$$

or

$$T_M = \frac{2Lh}{a(1-a)E} \quad (6-35)$$

where a is defined to be

$$a = \frac{e_M}{E} \quad (6-36)$$

The chopper frequency is therefore

$$f_M = e_M \frac{(E - e_M)}{2hLE} \quad (6-37)$$

or

$$f_M = \frac{a(1-a)E}{2Lh} \quad (6-38)$$

Table 6-7 shows the calculated characteristics of the chopper circuit for a 270 V supply, a circuit inductance of  $0.5 \times 10^{-3}$  H, and a hysteresis setting of  $\pm 4$  A.

### 6.3.2 REGENERATIVE BRAKING MODE

For the regenerative braking mode (Figure 6-35), the switch will be closed for the time interval given by

$$T_3 = \frac{2hL}{e_B} \quad (6-39)$$

and the switch will then open for the time period

$$T_4 = \frac{2hL}{E - e_B} \quad (6-40)$$

The period of the steady-state waveform is therefore

$$T_B = T_3 + T_4 = 2hL \left[ \frac{1}{e_B} + \frac{1}{E - e_B} \right] \quad (6-41)$$

Simplifying,

$$T_B = \frac{2hLE}{e_B (E - e_B)} \quad (6-42)$$

or

$$T_B = \frac{2hL}{a(1-a)E} \quad (6-43)$$

The frequency of the chopper during braking is therefore

$$f_B = e_B \frac{(E - e_B)}{2hLE} \quad (6-44)$$

or

$$f_B = \frac{a(1-a)E}{2hL} \quad (6-45)$$

Since these equations are identical in form to the motoring equations,

Table 6-7 is also valid for braking if the following substitutions are made:

$T_4 \Rightarrow$	$T_1$
$T_3 \Rightarrow$	$T_2$
$T_B \Rightarrow$	$T_M$
$f_B \Rightarrow$	$f_M$
$e_B \Rightarrow$	$e_M$



$e_M$ (V)	$T_1$ ( $\mu$ s)	$T_2$ ( $\mu$ s)	$T_M$ ( $\mu$ s)	$f_M$ (Hz)
1	14.87	4000	4015	249.1
2	14.93	2000	2015	496.3
5	15.09	800	815.1	1227
10	15.38	400	415.4	2407
20	16.00	200	216	4630
50	18.18	80	98.18	10,185
100	23.53	40	63.53	15,740
135	29.63	29.63	59.26	16,875
170	40	23.53	63.53	15,740
220	80	18.18	98.18	10,185
250	200	16.00	216.0	4630
260	400	15.38	415.4	2407
265	800	15.09	815.1	1227
268	2000	14.93	2015	496.3
269	4000	14.87	4015	249.1

Table 6-7. Chopper Operation in Motoring Mode

Although this is a simplified analysis, it provides insight into the chopper circuit's operation. Major effects which would modify the performance include:

- The switching of power currents requires a finite amount of time, thus lowering the theoretical chopper frequency
- The comparators require some overshoot and operating time to sense that the chopper current has reached the preestablished limits; this effect also lowers the chopper frequency from the theoretical value.
- Parasitic losses cause the chopper currents to change less rapidly than the theoretical currents, again reducing the chopper frequency from its theoretical value.

#### 6.4 COMMUTATION ANALYSIS

The power converter and its control were discussed in Paragraph 5.1.2. The inverter section of the power converter performs a function similar to that of the commutator and brushes of a conventional dc motor. As the rotor turns, the motor current is sent through the proper windings of the machine by the inverter switches. To understand the transients associated with the commutation process, an analysis of the power converter and its load has been conducted. The system under consideration is shown in Figure 6-36. All semiconductors are assumed to be ideal, i.e., their forward drops during conduction are negligible, and have no leakage current when reverse biased. Losses in the circuits are neglected, and all parameters are assumed to be independent of operating conditions. Parasitic elements are neglected, and all switching actions are assumed to take place instantaneously.

The commutation instant is taken to be that shown as the electrical angle of  $0^\circ$  in Figure 6-37. Figure 6-37 shows the idealized waveforms that would appear when a commutation angle advance of  $30^\circ$  is used, and the current source is perfect. At  $t = 0$ , Q3 and Q5 are conducting. At  $t = 0+$ , Q3 is turned off and Q1 is turned on. Since the motor is inductive,  $i_C$  will continue to flow, but will now be conducted through D6. Since  $i_A$  cannot build up instantaneously,  $i_1(0+) = 0$ , and since  $i_3(0+) = 0$ ,  $i_1(0+) = 0$ . The current initially flowing through  $L_o$  must now flow through  $D_R$ . With both  $D_R$  and  $D_6$  conducting, the circuit equations for the system are:

$$E - e_A + e_B = L_m \frac{di_A}{dt} - M \frac{di_B}{dt} - M \frac{di_C}{dt} - (L_m \frac{di_B}{dt} - M \frac{di_A}{dt} - M \frac{di_C}{dt}) \quad (6-46)$$

$$0 = i_A + i_B + i_C \quad (6-47)$$

$$e_B - e_C = -(L_m \frac{di_B}{dt} - M \frac{di_A}{dt} - M \frac{di_C}{dt}) + L_m \frac{di_C}{dt} - M \frac{di_A}{dt} - M \frac{di_B}{dt} \quad (6-48)$$

Now letting,

$$A = E - e_A + e_B$$

$$B = e_B - e_C$$

$$L = L_m + M$$

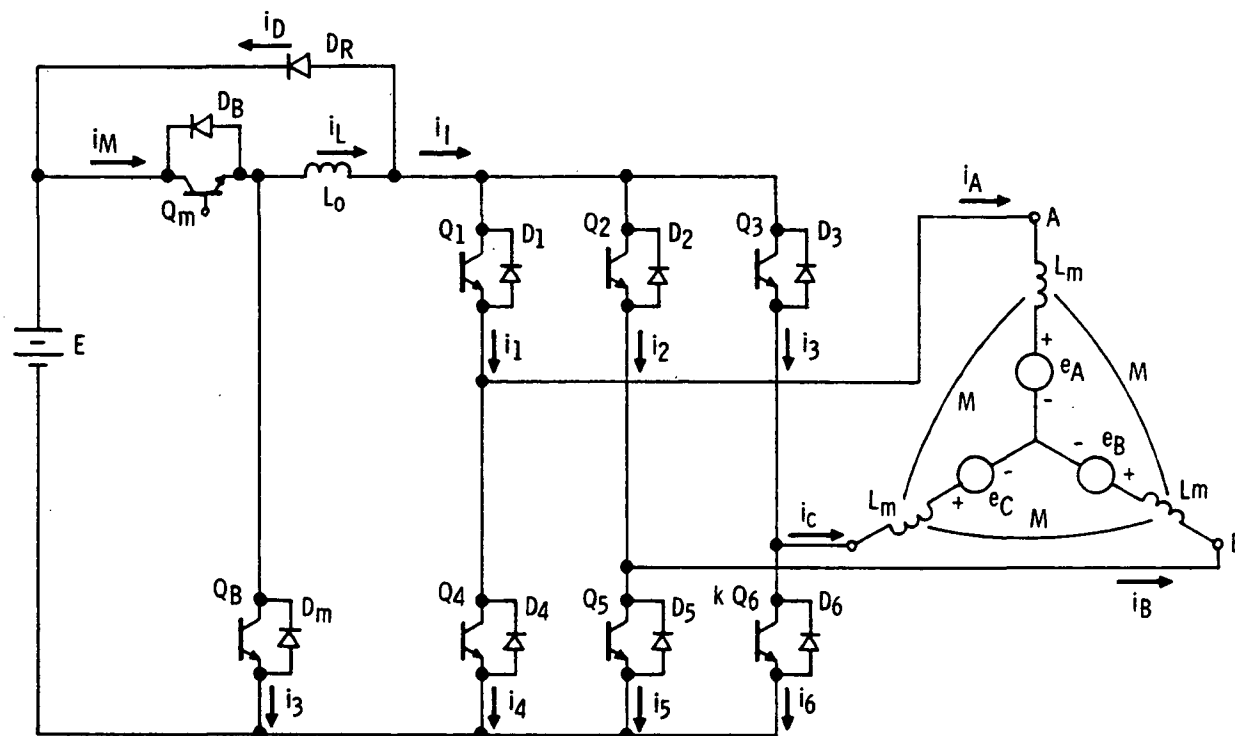


Figure 6-36. Power Circuit Schematic Diagram

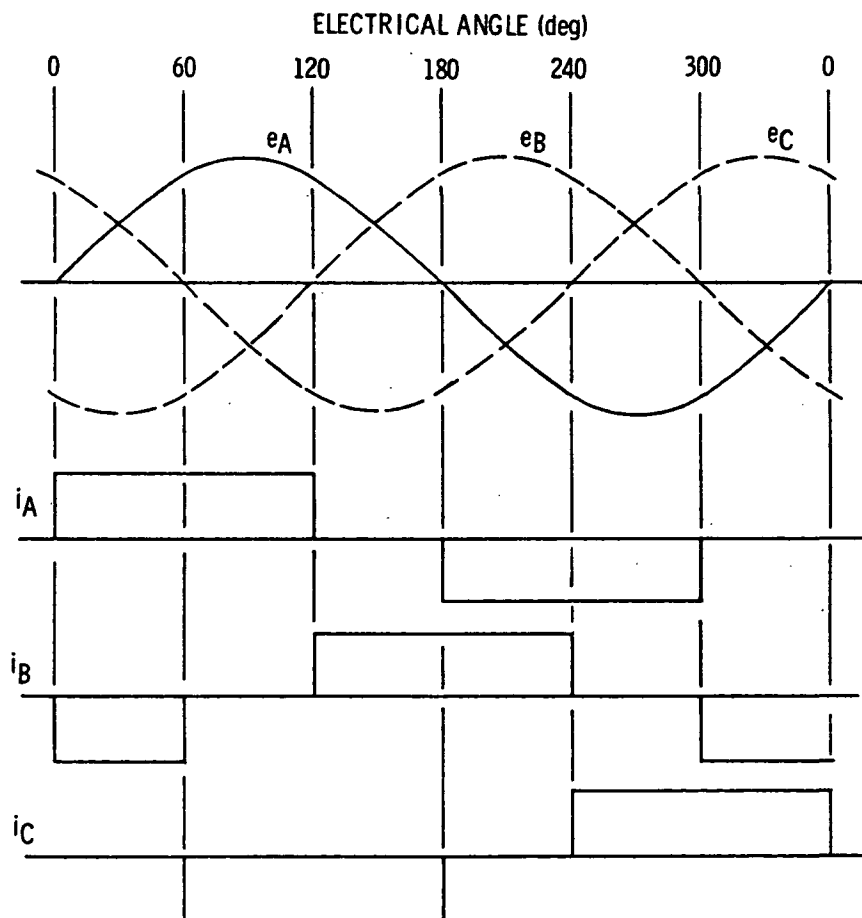


Figure 6-37. Idealized Motor Waveform

Equations 6-46, 6-47, and 6-48 can be rewritten as

$$A = L \frac{di_A}{dt} - L \frac{di_B}{dt} + 0 \quad (6-49)$$

$$0 = \frac{di_A}{dt} + \frac{di_B}{dt} + \frac{di_C}{dt} \quad (6-50)$$

$$B = 0 - L \frac{di_B}{dt} + L \frac{di_C}{dt} \quad (6-51)$$

Equations 6-49, 6-50, and 6-51 can be solved simultaneously to obtain

$$\frac{di_A}{dt} = \frac{2E - 2e_A + e_B + e_C}{3L} \quad (6-52)$$

$$\frac{di_B}{dt} = \frac{-E + e_A - 2e_B + e_C}{3L} \quad (6-53)$$

$$\frac{di_C}{dt} = \frac{-E + e_A + e_B - 2e_C}{3L} \quad (6-54)$$

For simplicity, if the counter-emf's are sinusoidal and a  $30^\circ$  commutation angle advance is used

$$e_A = E_m \sin \omega t \quad (6-55)$$

$$e_B = E_m \sin \left( \omega t - \frac{2\pi}{3} \right) \quad (6-56)$$

$$e_C = E_m \sin \left( \omega t - \frac{4\pi}{3} \right) \quad (6-57)$$

or

$$e_A = E_m \sin \omega t \quad (6-58)$$

$$e_B = E_m \left[ -\frac{1}{2} \sin \omega t - \frac{\sqrt{3}}{2} \cos \omega t \right] \quad (6-59)$$

$$e_C = E_m \left[ -\frac{1}{2} \sin \omega t + \frac{\sqrt{3}}{2} \cos \omega t \right] \quad (6-60)$$

Substituting Eqs. 6-58, 6-59, and 6-60 into Eqs. 6-52, 6-53, and 6-54

$$\frac{di_A}{dt} = \frac{2 E - 3 E_m \sin \omega t}{3 L} \quad (6-61)$$

$$\frac{di_B}{dt} = \frac{- E + E_m \left( \frac{3}{2} \sin \omega t + \frac{3\sqrt{3}}{2} \cos \omega t \right)}{3 L} \quad (6-62)$$

$$\frac{di_C}{dt} = \frac{- E + E_m \left( \frac{3}{2} \sin \omega t - \frac{3\sqrt{3}}{2} \cos \omega t \right)}{3 L} \quad (6-63)$$

Integrating these equations, and recognizing

$$i_A (0+) = 0$$

$$i_B (0+) = -I_o$$

$$i_C (0+) = I_o$$

$$i_A = \frac{2E}{3L} t - \frac{E_m}{\omega L} (1 - \cos \omega t) \quad (6-64)$$

$$i_B = -I_o - \frac{Et}{3L} + \frac{E_m}{2\omega L} \left[ (1 - \cos \omega t) + \sqrt{3} \sin \omega t \right] \quad (6-65)$$

$$i_C = I_o - \frac{Et}{3L} + \frac{E_m}{2\omega L} \left[ (1 - \cos \omega t) - \sqrt{3} \sin \omega t \right] \quad (6-66)$$

As a design example, suppose

$$I_o = 50 \text{ A}$$

$$L = 330 \text{ } \mu\text{H}$$

$$L_o = 500 \text{ } \mu\text{H}$$

$$E = 270 \text{ V}$$

$$E_m = 50 \text{ V}$$

$$\omega = 1200 \text{ rad/s}$$

Solving Eqs. 6-64, 6-65, and 6-66 with these values:

$t$ ( $\mu s$ )	$i_A$ (A)	$i_B$ (A)	$i_C$ (A)
0	0	-50.00	50.00
20	10.87	-52.81	41.94
40	21.67	-55.59	33.92
60	32.40	-58.33	25.93
80	43.05	-61.05	17.99
90	48.36	-62.39	14.04
93.11	50.00	-62.81	12.81

After  $D_R$  recovers, but with  $D_6$  still conducting, the equivalent circuit becomes as shown in Figure 6-38.

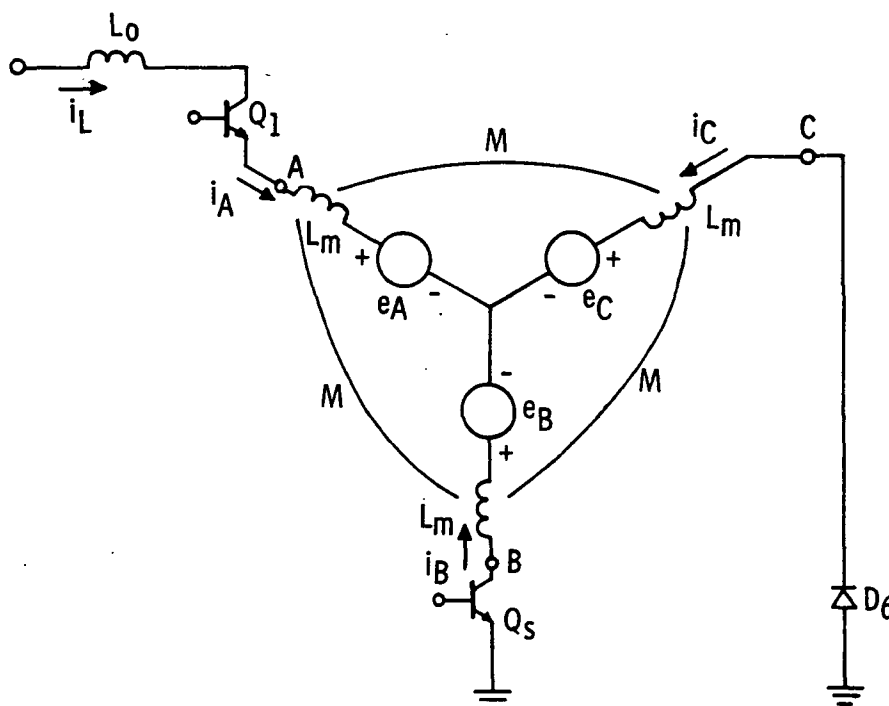


Figure 6-38. Equivalent Circuit -  $D_6$  Conducting

In Figure 6-38, assume the current source is ideal, then

$$i_L = I_L \quad (6-67)$$

$$e_B - e_C = L_m \frac{di_C}{dt} - M \frac{di_B}{dt} - (L_m \frac{di_B}{dt} - M \frac{di_C}{dt}) \quad (6-68)$$

$$0 = \frac{di_B}{dt} + \frac{di_C}{dt} \quad (6-69)$$

Solving,

$$\frac{di_B}{dt} = \frac{e_C - e_B}{2 L} = \frac{di_C}{dt} \quad (6-70)$$

Combining eqs. 6-59, 6-60, and 6-70:

$$\frac{di_B}{dt} = \frac{\sqrt{3} E_m}{2 L} \cos \omega t \quad (6-71)$$

Integrating, and recognizing  $i_B(t_1) = I_{B_1}$

$$i_B = I_{B_1} + \frac{\sqrt{3} E_m}{2 \omega L} (\sin \omega t - \sin \omega t_1) \quad (6-72)$$

$$i_A = I_L \quad (6-73)$$

$$i_C = -I_L - i_B \quad (6-74)$$

Continuing the same design example described earlier, with

$$t_1 = 93.11 \mu s$$

$$I_L = 50 \text{ A}$$

$$I_{B_1} = -62.81 \text{ A}$$

t ( $\mu$ s)	$i_B$ (A)	$i_C$ (A)
93.11	-62.81	12.81
100	-61.91	11.91
120	-59.31	9.31
140	-56.72	6.72
160	-54.14	4.14
180	-51.57	1.57
190	-50.29	0.29
192.25	-50.00	0.00

The transient currents for this case are plotted in Figure 6-39.

Although the preceding analysis covers the normal commutation transient, if  $D_6$  recovers before  $D_R$ , the equivalent circuit becomes that illustrated in Figure 6-40.

For this circuit

$$E - e_A + e_B = L_m \frac{di_A}{dt} - M \frac{di_B}{dt} - L_m \frac{di_B}{dt} + M \frac{di_A}{dt} \quad (6-75)$$

but since

$$i_B = -i_A \quad (6-76)$$

$$E - e_A + e_B = 2L \frac{di_A}{dt} \quad (6-77)$$

Combining Eqs. 6-58, 6-59, and 6-77,

$$\frac{di_A}{dt} = \frac{E}{2L} - \frac{E_m}{2L} \left[ \frac{3}{2} \sin \omega t + \frac{\sqrt{3}}{2} \cos \omega t \right] \quad (6-78)$$



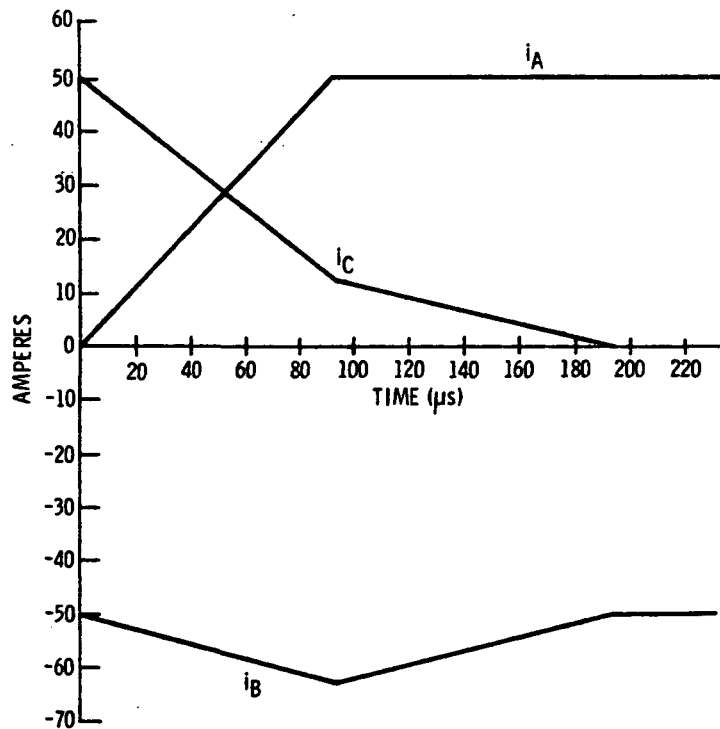


Figure 6-39. Commutation Transient with  $D_R$  Recovering Before  $D_6$

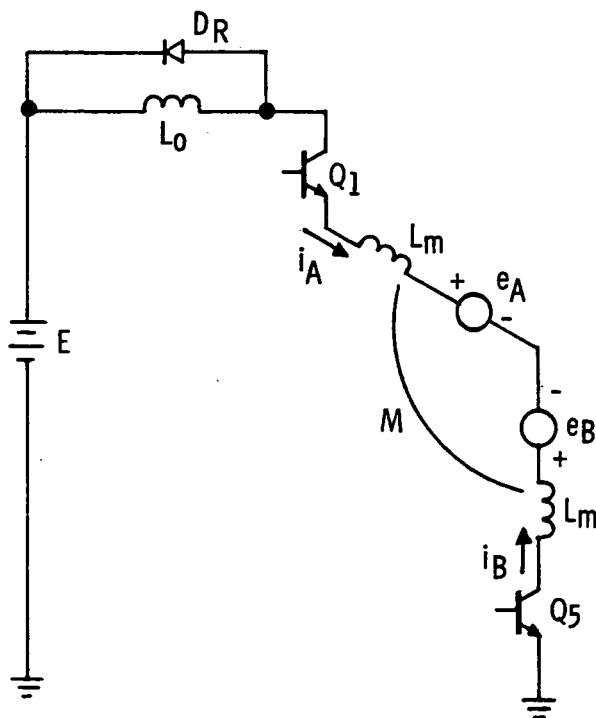


Figure 6-40. Equivalent Circuit,  $D_R$  Conducting

Integrating Eq. 6-78, and letting  $i_A(t_1) \triangleq I_{A_1}$

$$i_A = I_{A_1} + \frac{E(t-t_1)}{2L} - \frac{3E_m}{4\omega L} \left[ (\cos \omega t_1 - \cos \omega t) + \frac{\sqrt{3}}{3} (\sin \omega t - \sin \omega t_1) \right] \quad (6-79)$$

$$i_B = -i_A \quad (6-80)$$

$$i_C = 0 \quad (6-81)$$

As a design example, consider the following conditions

$$I_O = 50 \text{ A}$$

$$L = 330 \text{ } \mu\text{H}$$

$$L_O = 500 \text{ } \mu\text{H}$$

$$E = 270 \text{ V}$$

$$E_m = 125 \text{ V}$$

$$\omega = 3000 \text{ rad/s}$$

Solving Eqs. 6-64, 6-65, and 6-66 with these values

t	$i_A$	$i_B$	$i_C$
$\mu\text{s}$	A	A	A
0	0.00	-50.00	50.00
20	10.68	-48.78	38.10
40	20.91	-47.36	26.45
60	30.69	-45.77	15.08
80	40.02	-44.02	4.00
87.36	43.34	-43.34	0.00

Solving Eq. 6-79 with  $t_1 = 87.36 \mu s$  and  $I_{A1} = 43.34 A$ ,

$t$ $\mu s$	$i$ A
87.36	43.34
90	43.81
100	45.52
110	47.17
120	48.76
128.1	50.00

The transient currents for this case are plotted in Figure 6-41.

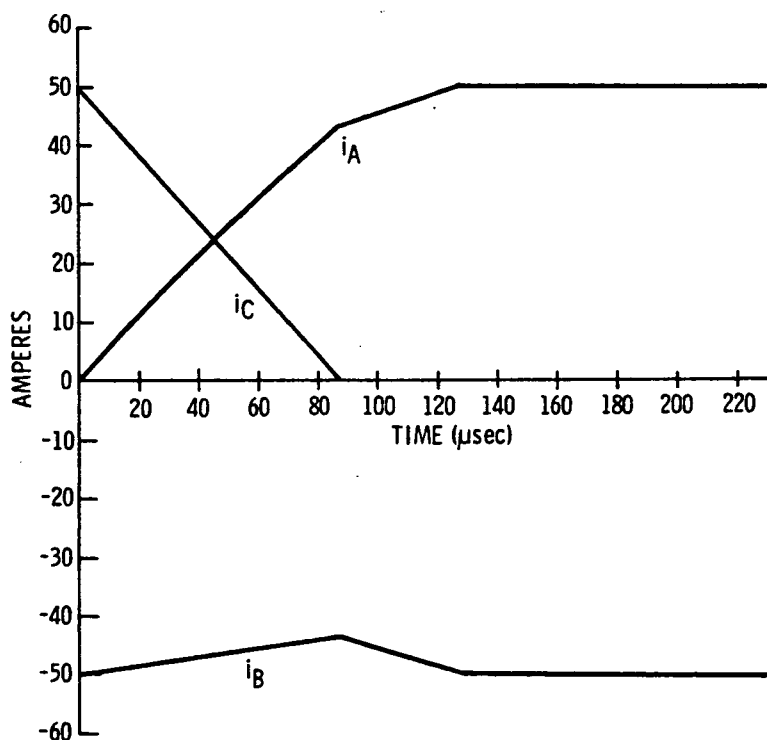


Figure 6-41. Commutation Transient with  $D_6$  Recovering Before  $D_R$

## SECTION VII

### TESTS AND TEST RESULTS

#### 7.1 MOTOR TESTS

The EMA motor was tested extensively to provide data such as:

- Winding resistance
- Winding self-inductance
- Winding mutual inductance
- Incremental inductance with dc bias
- Open-circuit voltage characteristics
- Cogging torque
- DC torque
- Short-circuited braking characteristics
- Alternator performance under load.

The tests which were conducted and the results which were obtained are summarized in Appendix E. Since virtually all of the motor characteristics are functions of the rotor position, stator currents and environmental conditions, it is necessary to review the actual data for detailed information. However, for convenience, Table 7-1 summarizes some of the typical results presented in Appendix E.

#### 7.2 EFFICIENCY TESTS

Dynamometer tests were conducted in both the motoring and regenerative braking modes to determine the efficiencies of the motor and electronic subsystems, as well as the overall system efficiency. The methods used in conducting the tests, as well as the results, are presented in Appendix F. Table 7-2 presents efficiency data in both motoring and regenerative modes for a shaft power of 8.0 hp. In general, the efficiencies improve at higher power levels, and the system is more efficient in the motoring mode than in the regenerative braking mode.

<u>Parameter</u>	<u>Value</u>
DC winding resistance, line-to-neutral	0.06 ohm
Winding line-to-neutral self-inductance	0.290 mH
Winding phase-to-phase mutual inductance	0.020 mH
Winding line-to-neutral incremental inductance	0.220 mH
Current source inductor incremental inductance	0.450 mH
Current source inductor dc resistance	0.012 ohm
Open circuit line-to-line rms voltage	0.02 V/r/min
Open circuit line-to-neutral rms voltage	0.012 V/r/min
Peak dc torque with line to neutral current	1.3 in-lb/A
Maximum short-circuited braking torque	130 in-lb

Table 7-1. Summary of Typical Motor Test Data

<u>MODE</u>	<u>MOTOR EFFICIENCY (%)</u>	<u>ELECTRONICS EFFICIENCY (%)</u>	<u>OVERALL EFFICIENCY (%)</u>
Motoring	92.7	97.0	89.9
Regenerative	91.8	91.3	83.8

Table 7-2. Efficiencies at 8.0 Shaft Horsepower

### 7.3 ELECTRONICS TESTS

#### 7.3.1 LOW-LEVEL ELECTRONICS TESTS

The low-level electronics circuits were tested extensively as part of their checkout. Each of the four channels underwent similar tests, and the results of the tests conducted on Channel D are presented in Appendix G. All channels have virtually the same characteristics.

#### 7.3.2 POWER CONVERTER TESTS

Waveform measurements were made of various voltages and currents in the power converter circuit under various motoring, plugging and regenerative braking conditions. These tests were made using Delco's dynamometer (described in Paragraph 4.1.2 and shown in Figures 4-6 through 4-8). The results of these tests are summarized in Appendix H.

### 7.4 DESIGN VERIFICATION TESTS

#### 7.4.1 DESIGN VERIFICATION TEST PLAN

The NASA Statement of Work (SOW) which is given in Appendix C established design goals for the four-channel actuator. As a part of the system tests, Design Verification Tests (DVT) were conducted. The basic DVT plan is presented in Appendix I. The plan outlines the tests to be conducted, the instrumentation to be used, and the purpose and duration of each test.

#### 7.4.2 DESIGN VERIFICATION TEST CONFIGURATION

The Design Verification Tests were conducted using the circuit configurations shown in Appendix A. The basic system gains are given by:

Position loop current gain	450 A/deg
Velocity loop current gain	15 A/deg/s
Velocity correction current gain	32 A/deg/s

These gains are given with respect to output motion at the spring load.

The current limits were set at 40 A for motoring or regenerative conditions and 25 A for the plugging conditions. The comparators for the SPDHI or SPDLO conditions have a nominal load speed setting of 0.92 deg/s (which corresponds to a motor speed of 410 r/min) with a hysteresis of  $\pm 0.25$  deg/s. The comparators for the SPDPOS and SPDNEG conditions toggle at a nominal load speed of 0.11 deg/s and have a hysteresis of  $\pm 0.12$  deg/s.

The current overload sensors are set to indicate an overload if the motor current exceeds 60 A. The hysteresis built into the motoring and braking current control comparators is  $\pm 2.1$  A. The dominant filter time constants are shown in Figure 5-2.

#### 7.4.3 DESIGN VERIFICATION TEST RESULTS

The Design Verification Test results are presented in Appendix J. For convenience, some of the more important results are summarized in the following paragraphs.

##### 7.4.3.1 Output Stroke

When mounted on the load stand, the safe maximum output travel is about  $\pm 11$  degrees. The design was therefore set to limit travel between 9 and 11 degrees in each direction. The measured travel limits were  $\pm 10.3$  degrees.

##### 7.4.3.2 Output Velocity

The maximum output velocity of the actuator under no-load conditions, and with a nominal battery voltage of 270 Vdc was 22.7 degrees/second.

##### 7.4.3.3 Output Torque

The actuator was operated in three different modes as indicated in Table 7-3. The temperature rise which was measured is also shown in the table, and did not exceed 24°C for any of the tests.

Test Cond.	Steady-state Load Spring Deflection (degrees)	Peak-to-peak Sinusoidal Motion (degrees)	Input Freq. (Hz)	Test Duration (minutes)	Measured Motor Temperature Rise ( $^{\circ}$ C)
I	8.0	1.0	2.5	26.0	24
II	6.0	4.0	1.0	5.5	12
III	6.0	4.0	1.27	1.5	3

Table 7-3. Output Torque Test Conditions

#### 7.4.3.4 Displacement Linearity

The displacement linearity tests showed that the linearity of each of the position feedback transducers was much better than the design goal of 1%. The worst-case maximum deviation was 0.22%.

#### 7.4.3.5 Threshold

The design goal for threshold is 0.0275 degree. All combinations of two active channels easily met this requirement.

#### 7.4.3.6 Position Null

The position null design goal is 0.275 degree. All combinations of two active channels easily met this requirement.

#### 7.4.3.7 Hysteresis

The design goal for hysteresis is 0.0275 degree. All combinations of two active channels easily met this requirement. The worst-case hysteresis was measured using channels C and D. This combination had a hysteresis of 0.008 degree.

#### 7.4.3.8 Cross-Channel Velocity Tracking

The cross-channel velocity tracking error under steady-state conditions has a design goal of 3% of the maximum motor speed. All combinations of two active channels met this requirement. The average of all the cross-channel velocity tracking errors was found to be 1.5% of full motor speed.



#### 7.4.3.9 Frequency Response

All six motor combinations were tested for frequency response, and all easily met the design goals for the system. The -4 dB bandwidth was typically 9.5 Hz compared with a design goal of 3.0 Hz. The  $-45^{\circ}$  phase shift frequency was typically 3.4 Hz compared to a design goal of 3.0 Hz.

#### 7.4.3.10 Step Response

The step response of the EMA was found to meet the design goal for step commands up to 2% of full travel. For larger commands, either the overshoot exceeded the design goal of 25%, or the time to reach 85% of the steady-state response exceeded the design goal of 0.145 second. A summary of the measured step response characteristics of the EMA is given in Table 7-4.

Step Command (% Full Travel)	Measured Overshoot (25% is Design Goal)	Time to Reach 85% of Steady-state Displacement (0.145 s is Design Goal)
2%	25%	0.100 s
3%	30%	0.120 s
4%	27%	0.140 s
5%	22%	0.160 s

Table 7-4. Step Response of EMA

#### 7.4.3.11 Motor Brake

During this test the EMA output shaft was locked. One at a time, each motor was operated at its full output torque to test the braking torque of the other three brakes. All brakes operated without appreciable slip during these tests.

#### 7.4.3.12 Chatter and Instability

The design goal for chatter and instability is 0.055 degrees peak-to-peak. None was observed or recorded which approached that value.

#### 7.4.3.13 Velocity Gain Test

The measured velocity gain was 0.035 A/r/min (or 15.7 A/deg/s at the load).

#### 7.4.3.14 Torque Gain Test

The measured torque gain was 427 A/degree.

### 7.5 COMPARISON OF ANALYTICAL AND TEST RESULTS

As a check on the validity of the math models which were developed for the EMA, lab test results were compared with the analytical results. In paragraph 6.2, the step response characteristics obtained in the nonlinear model were compared with the EMA lab test data. A summary of the results (Table 6-6) showed excellent agreement between the two. A comparison was also made of the frequency response characteristics of the EMA and its math model. A block diagram of the two-channel configuration is shown in Figure 7-1. Figure 7-2 is the frequency response of the inner (tachometer feedback) loop. Again, the correlation between test and analytical results is excellent. Figure 7-3 presents the open-loop response of the position loop, Figure 7-4 gives the closed-loop response gain characteristic, and Figure 7-5 shows the phase characteristic. Figure 7-6 presents the position error response to a position input command. In all instances the math models and test data show very good agreement.

### 7.6 POWER COMPONENT TESTS

Power transistor selection for the single-channel power electronics breadboard was based on the requirements and goals shown in Table 7-5. A vendor survey was conducted in an attempt to find suitable devices, with inquiries being sent to 19 manufacturers. From the responses which were received, three devices were evaluated which appeared suitable for the EMA application without requiring parallel operation:

- Westinghouse developmental unit 17B-X (predecessor to Type D60T)
- RCA type J15490 (transcendent device)
- Power Tech type PT-4503.

Tests were conducted on the candidate devices, and the test methods and results were reported in Delco Engineering Exhibit EE-22T-EMA-022. In general, all three of the transistor types tested were found to have excellent

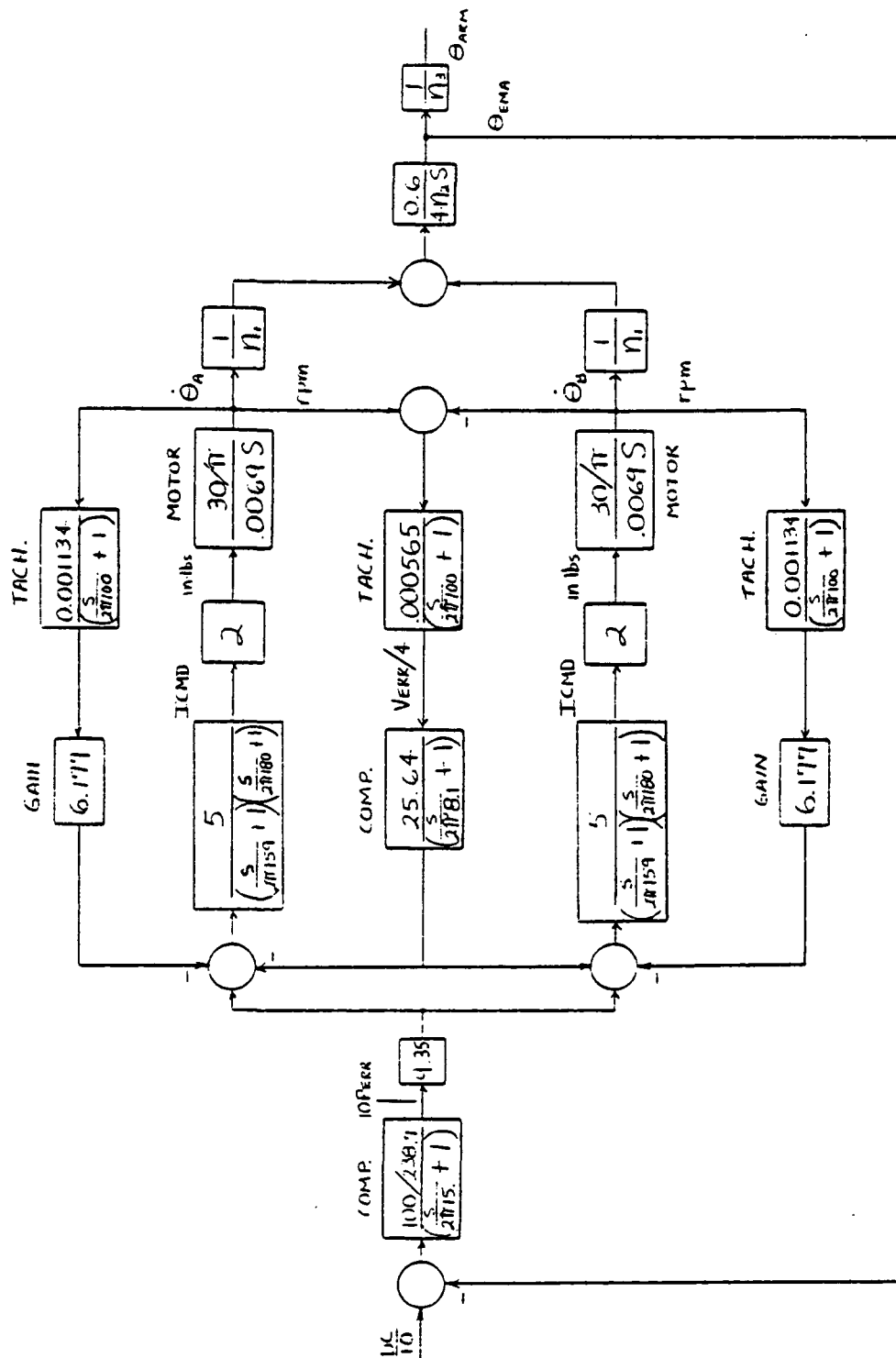


Figure 7-1. Two-Motor EMA Block Diagram

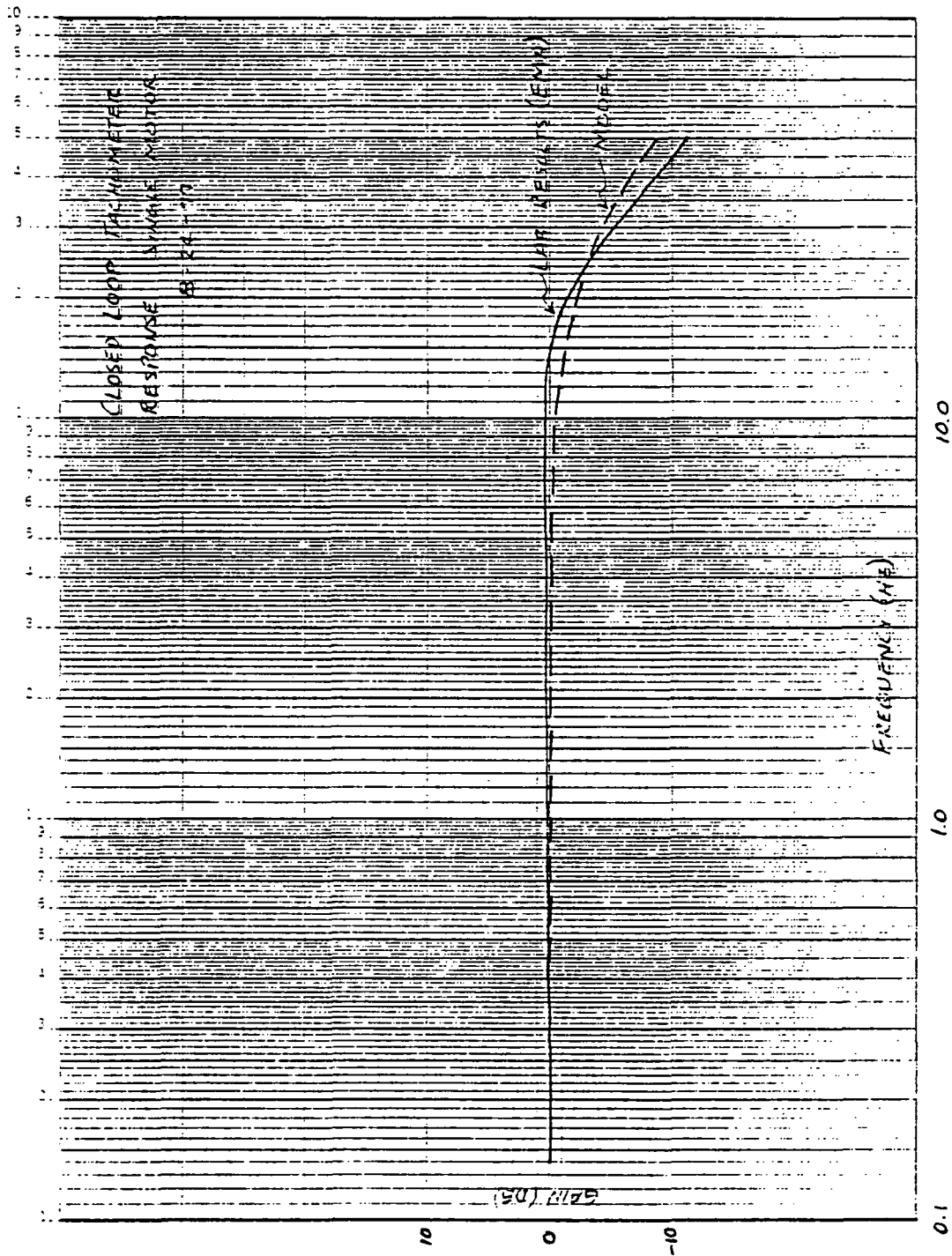


Figure 7-2. Closed-Loop Tachometer Response, Single Motor

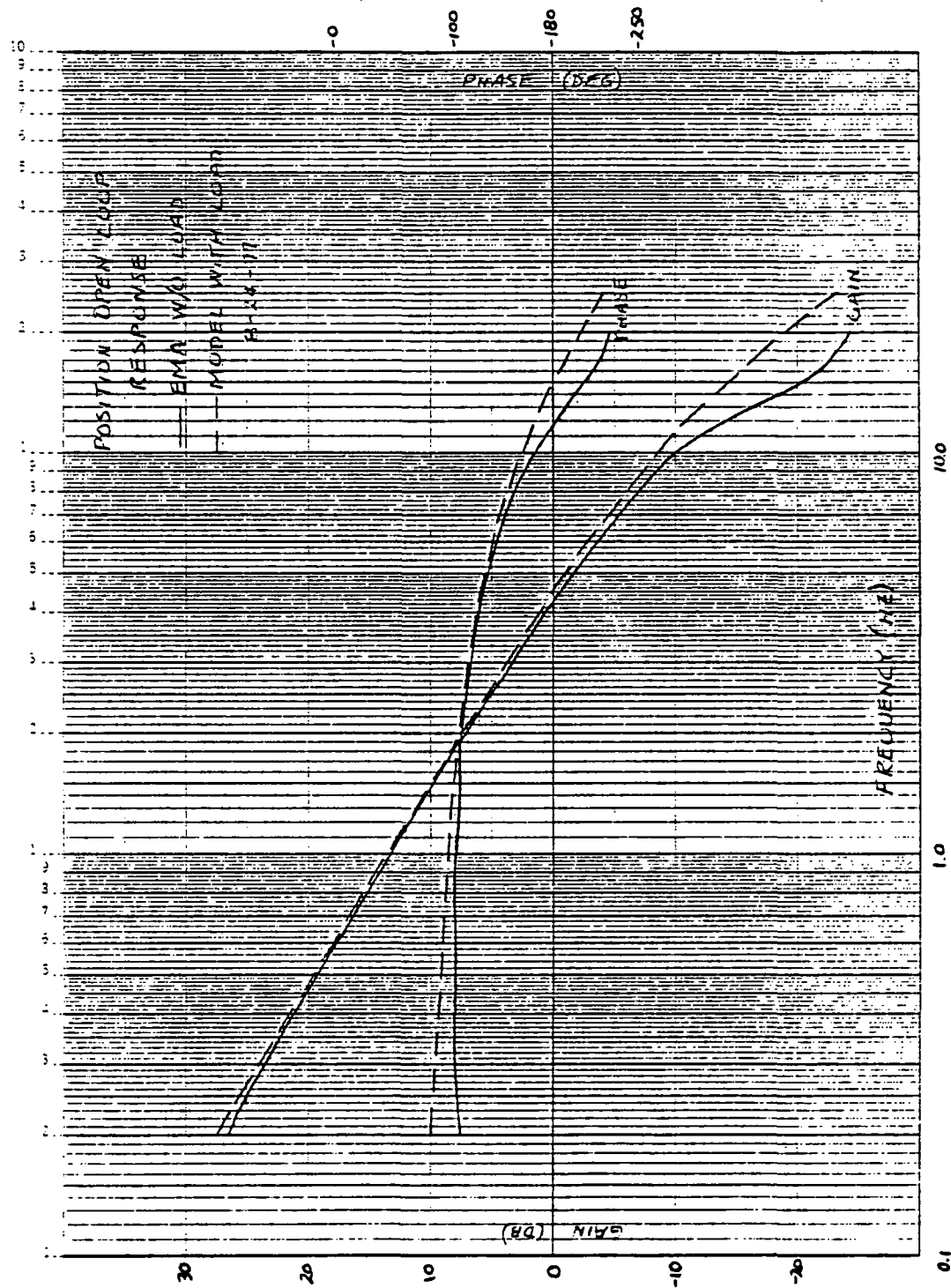


Figure 7-3. Position Open-Loop Response

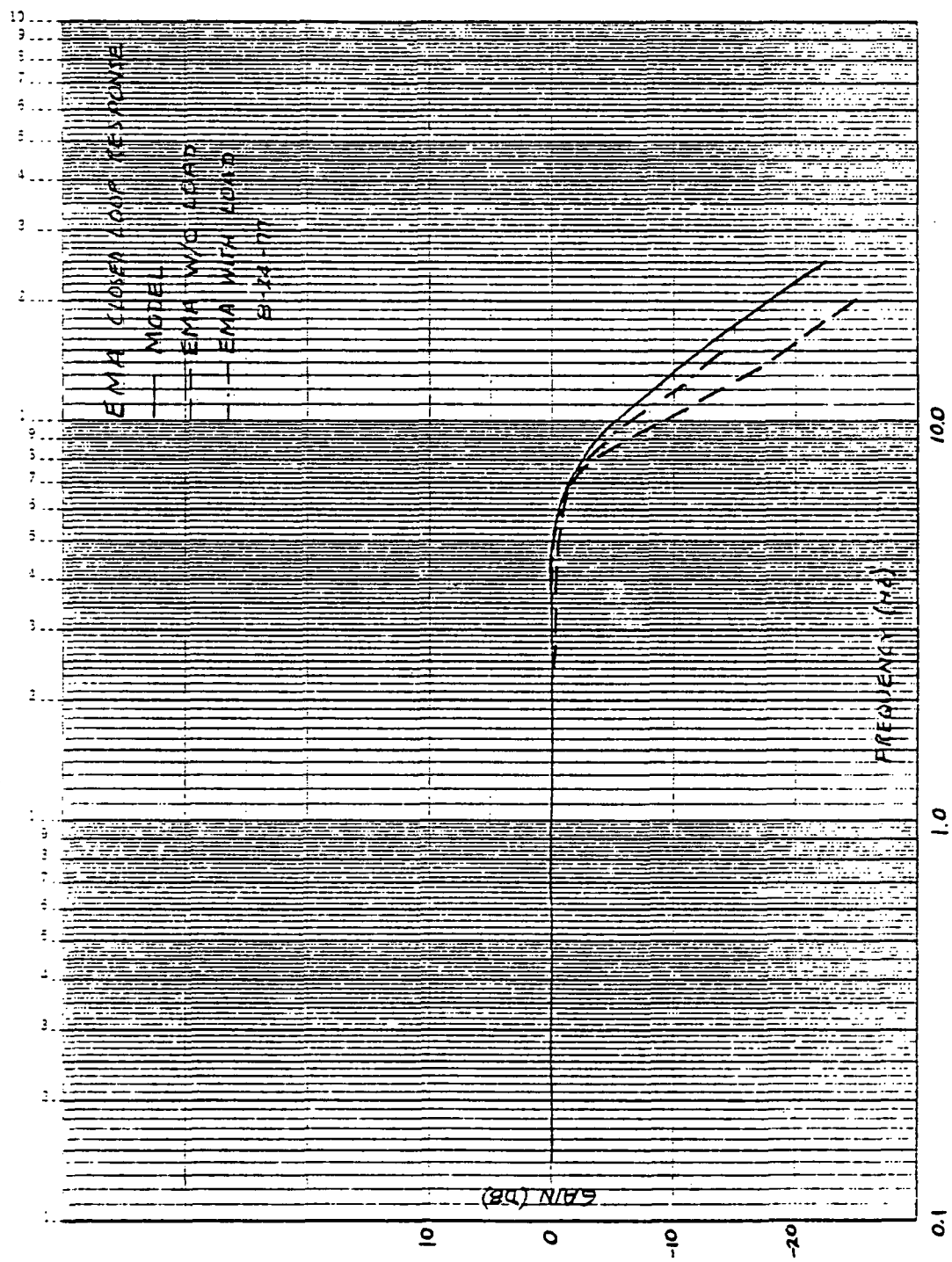


Figure 7-4. Closed-Loop Response Gain Characteristic

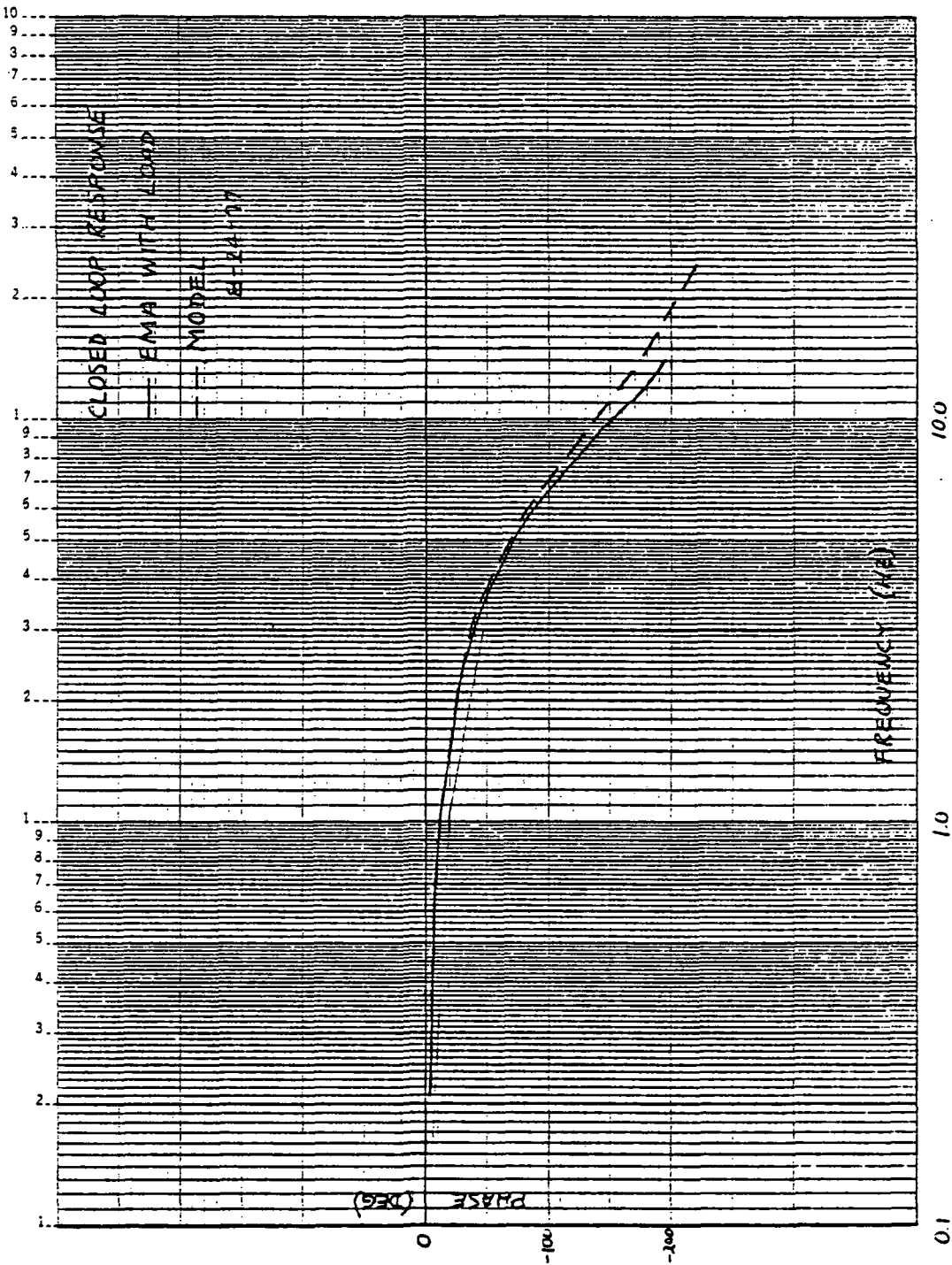


Figure 7-5. Closed-Loop Response Phase Characteristic

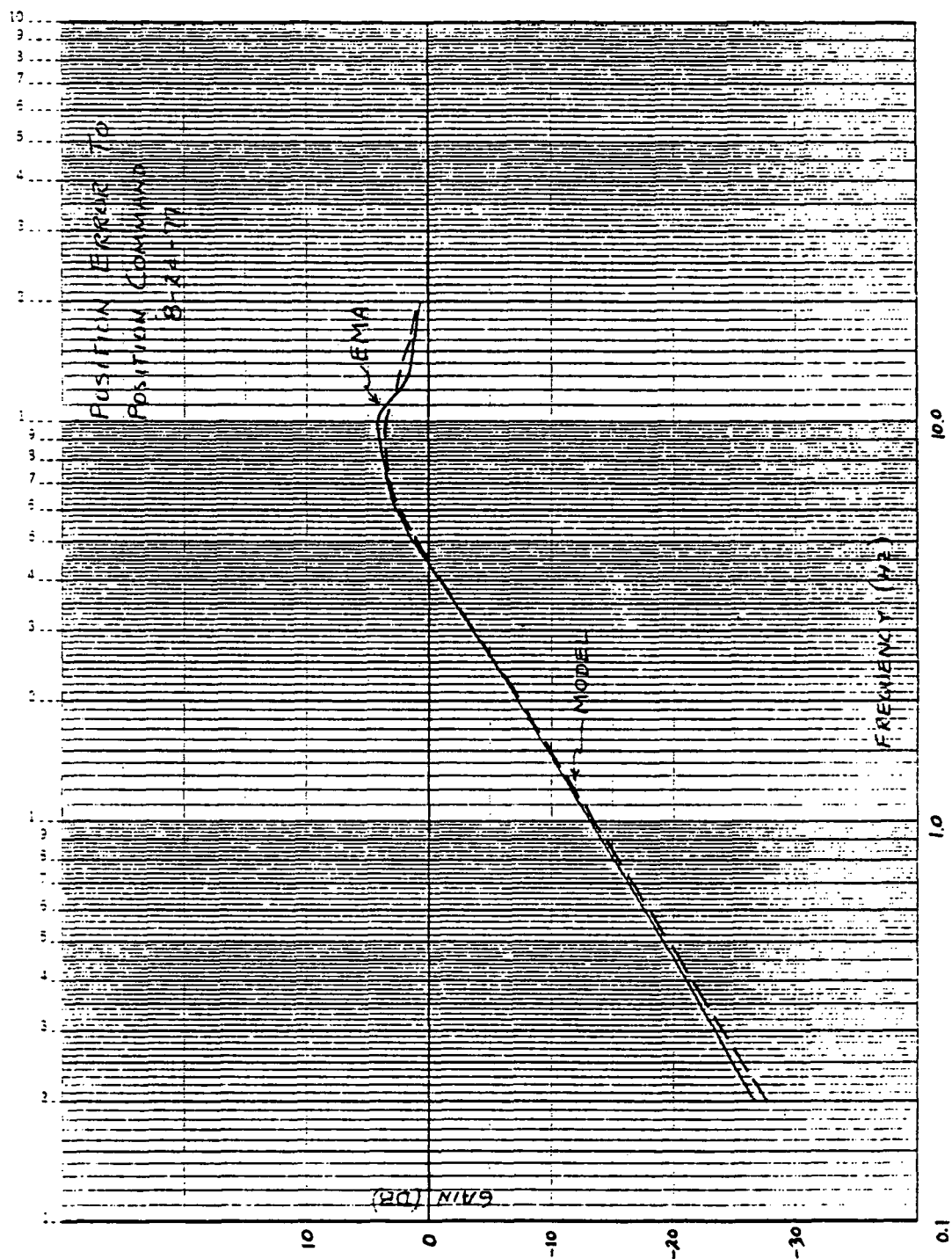


Figure 7-6: Position Error Response to a Position Error Command



<u>PARAMETER</u>	<u>REQUIREMENT</u>	<u>GOAL</u>
$V_{CEO}$ (SUS)	400 V	425 V
$I_C$	60 A	100 A
$I_{CPEAK}$	100 A	150 A
BETA AT 60 A	10 AT $V_{CE} = 1$ V	15
BETA AT 100 A	7.5 AT $V_{CE} = 1.5$ V	10
$V_{CE}$ (SAT)	1 V AT $I_C = 60$ A, $I_B = 6$ A	0.5 V
$P_D$	250 W AT $T_C = 100^\circ\text{C}$	300 W
RISE TIME	0.8 MICROSECOND	0.5
STORAGE TIME	6 MICROSECONDS	3
FALL TIME	1.2 MICROSECONDS	0.8

Table 7-5. Power Transistor Parameter Requirements and Goals

characteristics. The RCA device had superb turn-off characteristics and very low average losses. However, it did not have as much current-handling capability as either the Power Tech or Westinghouse transistors. Both Power Tech and Westinghouse devices provided adequate current and voltage margins, but the Westinghouse unit had somewhat lower losses than the Power Tech unit. Although either type would have been suitable for use in the single-channel power electronics breadboard, the Westinghouse D60T power transistor was selected, since it is an improved version of the Westinghouse 17B-6, tailored to applications such as the EMA power converter.

#### 7.7 SINGLE-CHANNEL POWER ELECTRONICS BREADBOARD TESTS

The single-channel power electronics breadboard was tested to demonstrate that it could drive the motor with a nominal current of at least 60 A using a nominal supply voltage of 270 Vdc. This was successfully accomplished, and the test results were summarized in EE-22-EMA-023 (Appendix L). The snubbers limited the collector-emitter voltages to acceptable values, and the power switch currents were within the capabilities of the power transistors used in the breadboard.

SECTION VIII

FINAL STATUS

All of the tasks which were intended to be conducted as part of this program have been completed. It was not necessary to discontinue any of the planned efforts. The four-channel electromechanical actuator has been delivered to NASA, and the power electronics breadboard has been designed, fabricated, assembled, and tested. All documentation has been delivered, and this report completes the total effort conducted under the current contract.